

University of Nottingham
UK | CHINA | MALAYSIA

Broadline ^{1}H NMR Investigations of the Mobility of Polymers Supported on Carbonaceous Particles and Silica Substrates

Genevieve Hodgins

The EPSRC Engineering Doctorate Centre in Carbon Capture and Storage and Cleaner Fossil Energy

The University of Nottingham

27 September 2019

Abstract

This research consists of two parallel investigations using solid state NMR to study the mobility of polymers adsorbed on substrates, the first is a study on the use solid state proton NMR as a testing methodology for deposit control additives, and the second is the investigation into the mobility of the carbon capture material; polyethylene imine supported on silica.

Within the transport sector increased efficiencies are required if vehicles are to meet emissions targets, unfortunately the engine development implemented can be less tolerant to engine deposits, reducing efficiencies and causing engine failure. One solution to the problem of deposit formation is the use of deposit control additives in the fuel mixture. The development of these materials is costly due to the high expense associated with testing them; therefore the development of additional lower cost testing mechanisms is advantageous to manufacturers and consumers alike. Polyisobutylene derivatives are a common deposit control additive for use with automobile fuels.

Solid state broadline proton NMR has been used to study polyisobutylene derivatives at high temperatures replicating operational conditions. This method has shown the capacity to distinguish between polyisobutylene derivatives based on their interactions with carbon black, a deposit model. A series of different polyisobutylene derivatives with different chain lengths and headgroups were investigated at loadings of 2-50 % on carbon black over 30-250 °C. The lowest loading samples often had significantly reduced mobility at operational temperatures (of 250 °C) indicating stronger interactions between the polymer and substrate, and enabling a distinction to be made between additives which may have deposit control features and those

which likely do not. This low loading is likely indicative of the monolayer adsorption of these materials on carbon black and, in combination with other findings in this study, suggests the polyisobutylene chain is interacting with the carbon surface to a greater extent than had previously been assumed. Further investigation into these materials using carbon-13 NMR in the solid state has been hindered by the presence of paramagnetism within the carbon black material, and the use of silica as an alternate substrate investigated.

The release of CO_2 into the atmosphere results in climate change which must be mitigated in order to limit devastating environmental effects. One of the most valuable mitigated technologies available is carbon capture and storage. Post combustion capture is the most mature of the carbon capture technologies and can be retrofitted to existing CO_2 sources. Most commonly liquid amines are used for this, however to combat high energy costs and issues with corrosion associated with these materials solid adsorbents are also being developed. Polyethylene imine supported on mesoporous silica is a promising material in this field.

The mobility of the silica-supported branched chain polyethylene imine is studied over the operational temperature range of 60-130 °C, in association with the kinetics of CO_2 adsorption. All of the samples show similar mobilities with little correlation between polyethylene imine molecular weight and mobility. Over the temperature range studied the mobility plateaus at approximately 80 °C which corresponds well with the maximum adsorption temperature and fastest rate of adsorption. In addition to this, the CO_2 capacity of the samples prepared has shown to be in keeping with the existing literature, with the lowest molecular weight polyethylene imine studied, FG (800 mol/g), generally showing the highest CO_2 adsorption. However a significant outlier to this trend has been noted with high CO_2 capacities of up to 22 wt. % seen by some of the longer chain PEI samples when supported on macroporous silicas, with these materials providing a potential direction for future study.

Acknowledgements

My thanks in this endeavour goes out to my supervisors, Professor Colin Snape, Dr. Lee Stevens, and Dr. Miguel Castro Dias of the University of Nottingham, and Dr. Jim Barker of Innospec Inc. for their guidance and support in this project. Your expertise and assistance has been invaluable.

I would also like to thank all of my colleges at the University of Nottingham, specifically those in the Energy Technologies Building for their patience and assistance. A special thanks goes to Professor William Meredith and Dr. Xin Liu for their help in the lab.

To the EPSRC and Innospec Inc. I extend my gratitude for funding this research, and to all the members, staff and students, of the CCS CFE CDT for making me feel at home over the past few years.

My parents have been constant source of comfort and encouragement in all aspects of my life including my studies. I would not be the person I am today without their inspiration and counsel, and for that I am eternally grateful. I would also like to express my appreciation for the company and compassion I have received from rest of my family and friends, you are all incredibly dear to me.

Most importantly, I would like to thank my husband, Joseph, for his unwavering love and understanding. Together we have grown in ways I never thought possible.

Contents

1 Introduction **33**

1.1 Motivation for Research 33

1.2 Aims and Objectives of Research 34

1.3 Thesis Organisation 36

1.4 Introduction to Polymer Adsorption and Mobility 37

1.4.1 Polymers 37

1.4.2 Solid State NMR 39

1.4.3 Applications 39

1.5 Introduction to Deposit Control 40

1.5.1 Automobile Emissions 40

1.5.2 Types of Deposit 44

1.5.3 Impacts of Deposits 46

1.5.4 Fuel Additives 47

1.6 Introduction to Carbon Capture 51

1.6.1 Post-Combustion Capture 51

1.6.2 Solid Adsorbents 52

2 Literature Review **54**

2.1 Introduction 54

2.2 Introduction to Deposits in Internal Combustion Engines 54

2.2.1 Deposit Formation 55

2.2.2 Carbon Black 57

2.3 Deposit Control Additives 58

2.3.1 Polyisobutylene Derivatives 60
2.4 Analytical Methods 67
2.4.1 Nuclear Magnetic Resonance Studies of Carbonaceous Materials 68
2.4.2 Nuclear Magnetic Resonance Studies of Polymers 69
2.4.3 Engine Tests 71
2.4.4 Adsorption Measurements 71
2.4.5 Rheology 73
2.4.6 Other Studies of Interactions Between Carbon Black and Polymers 74
2.4.7 Studies of Carbon Black and Deposits 74
2.5 Deposit Control Summary 75
2.6 Introduction to Carbon Capture 77
2.7 Carbon Capture Technologies 77
2.7.1 Pre-Combustion Capture 78
2.7.2 Post-Combustion Capture 79
2.7.3 Oxy-Fuel and Chemical Looping Combustion 83
2.8 Amine Based Carbon Capture Materials 84
2.8.1 Polyethylene Imine 85
2.8.2 Analytical Methods 91
2.9 Carbon Capture Summary 94

3 Methodologies **96**
3.1 Background and Theory 96
3.1.1 Nuclear Magnetic Resonance 96
3.1.2 Carbon-13 NMR 102
3.1.3 Proton NMR 103
3.1.4 N_2 Sorption Isotherms 104
3.1.5 Thermogravimetric Analysis 104
3.1.6 Viscometry 104
3.1.7 Electron Paramagnetic Resonance 105
3.1.8 Materials 105

3.2 Description of Techniques . . . 113
3.2.1 Sample Preparation . . . 113
3.2.2 Proton NMR . . . 116
3.2.3 Carbon-13 NMR . . . 118
3.2.4 N_2 Sorption Isotherms . . . 120
3.2.5 Thermogravimetric Analysis . . . 121
3.2.6 Viscometry . . . 123
3.2.7 Oxidation of PEI-Silica . . . 123

4 High Temperature Mobility of Deposit Control Additives 125
4.1 Introduction . . . 125
4.2 Proton NMR Optimisation and Method Development . . . 126
4.2.1 Temperature Range . . . 126
4.2.2 Error and Reproducibility . . . 127
4.2.3 Other Contributions to Signal . . . 132
4.2.4 Peak Fitting: Lorentzian vs Gaussian . . . 132
4.3 N_2 Sorption Determined Pore Structure of MicroCB . . . 133
4.3.1 Simple Calculation of Monolayer Coverage . . . 134
4.4 Thermogravimetric Analysis of PIB Derivatives . . . 135
4.5 Proton NMR Determined Mobility of PIB Derivative MicroCB Dispersions . . . 138
4.5.1 Trends in Mobility between PIB Derivatives and MicroCB over 30-250 °C . . . 139
4.5.2 Effect of Polymer Loading on Mobility over 30-250 °C . . . 145
4.5.3 Effect of Polymer Loading on Mobility at 250 °C . . . 147
4.6 Comparison of PIBSI Samples by Structure . . . 153
4.6.1 Impact of mono- and bis- Functionalisation . . . 153
4.6.2 Impact of PIB Chain Length . . . 155
4.6.3 Comparison of PIBSI with TEPA Headgroups . . . 156
4.7 Comparison of Mobility of PIB Derivatives on MicroCB at 250 °C . . . 157
4.7.1 Proton NMR Determined Monolayer Coverage . . . 157

4.7.2 Grouping of PIB Derivatives by Interaction Strength 159
4.7.3 Using Proton NMR to Investigate PIB Derivatives as Deposit Control Additives 161
4.8 Further Investigations of PIBSIs and their Dispersions using Solid State NMR 163
4.8.1 Characterisation of Liquid PIBSIs Using Solid State Carbon-13 NMR 164
4.8.2 Impacts of Carbon Black on CP MAS NMR Spectroscopy . . 166
4.8.3 The Use of Silica as a Deposit Model 169
4.9 Chapter Summary 174

5 Mobility and Kinetics of CO_2 Adsorption of PEI-Silica 176
5.1 Introduction 176
5.2 Method Development 177
5.2.1 Polyethylene Imine Samples 177
5.2.2 Moisture Content of PEI 177
5.2.3 Impregnation of Silica 180
5.3 Measurements of Repeatability 184
5.3.1 Repeatability of Thermogravimetric Analyses 184
5.3.2 Repeatability of Proton NMR Results 185
5.4 N_2 Sorption Isotherms of Silica Samples 187
5.5 Viscosity Measurements of Neat PEI 193
5.6 Thermogravimetric Analysis of Thermal Decomposition and Volatilisation of PEI 194
5.7 ^{1}H NMR Mobility Measurements of Neat PEI 196
5.8 Impact of PEI Molecular Weight on Mobility and Kinetics of PEI-Silica 197
5.8.1 Impact of Molecular Weight of PEIs supported on Silica 1 . . 198
5.8.2 Impact of Molecular Weight of PEIs supported on SBA-15 . . 201
5.8.3 Impact of Molecular Weight of PEIs supported on MCF . . . 204
5.8.4 Impact of Molecular Weight of PEIs supported on Rice Husk Silica 1 207

5.8.5 Impact of Molecular Weight of PEIs supported on Rice Husk Silica 2 . . . 210
5.9 Impact of Silica Substrate on Mobility and Kinetics of PEI-Silica . . . 212
5.9.1 Kinetics of CO_2 Adsorption at Optimum PEI-Silica Loadings . 231
5.10 Discussion of PEI-Silica Mobility and Kinetics Results . . . 233
5.10.1 Discussion of PEI and PEI-Silica Mobility . . . 234
5.10.2 Discussion of PEI-Silica Kinetics . . . 235
5.10.3 Rate of CO_2 Adsorption . . . 237
5.10.4 Relationship Between Kinetics and Mobility . . . 238
5.11 Chapter Summary . . . 243

6 Additional Investigations into PEI-Silica 244

6.1 Introduction . . . 244
6.1.1 Method Development of The Preparation of PEI-Silicas with Antioxidants . . . 244
6.2 Carbon-13 NMR Detection of Urea Formation . . . 247
6.2.1 Carbon-13 NMR of a Control Sample . . . 247
6.2.2 Carbon-13 NMR of Pilot Plant Samples . . . 249
6.2.3 Thermogravimetric Analysis of Pilot Plant Samples . . . 252
6.2.4 Determination of Urea Formation . . . 254
6.3 The Impact of Antioxidants on PEI-Silica Performance . . . 255
6.3.1 Impact of Antioxidants on the CO_2 Capacity of G100-Silica 1 256
6.3.2 Potential for Use of Antioxidants in PEI-Silcia Carbon Capture 270
6.4 Chapter Summary . . . 273

7 Conclusions 274

7.1 Studies of PIBSI Dispersions As A Model of Deposit Control Additives 274
7.1.1 Suggestions for Future Work . . . 276
7.2 Investigations of PEI-Silica As Carbon Capture Materials . . . 277
7.2.1 Conclusions of Research . . . 277
7.2.2 Suggestions for Future Work . . . 279

A Deposit Control Additives **310**

A.1 PIB Derivative Preparation 310

A.2 Example Monolayer Calculation Using the PSA Method 310

A.3 PIBSI structures 313

A.4 Supplementary Methods 315

A.4.1 Gel Permeation Chromatography Methodology 315

B Carbon Capture Materials **316**

B.1 Characterisation of Rice Husk Samples 316

B.2 Mercury Intrusion Porosimetry of Silicas by Dr. Lee Stevens 319

B.3 Supplier Specification of SBA-15 319

B.4 N_2 Sorption Isotherms for Silica Samples 319

B.5 Physisorption Isotherms and Hysteresis Loop Classifications 321

B.6 Viscosity of PEI Samples (From Specification) 323

B.7 PEI-Silica Kinetics 323

B.8 KIER Pilot Plant Samples 327

B.9 Antioxidant Loadings 328

B.10 Additional Oxidation Testing Results 328

B.11 Supplementary Methods 331

B.11.1 X-Ray Fluorescence 331

B.11.2 Elemental Analysis 331

B.11.3 University of Nottingham Strata Technology CO_2 Capture Pilot Plant 332

List of Figures

1.1 Schematic of a Direct Fuel Injection System (from RideApart)[22] . . . 41

1.2 Schematic of a multi orifice injector (courtesy of Robert Bosch LLC, from Diesel Engines)[23] . . . 42

1.3 SEM image of deposits on an injector tip at 88x and 703x magnification (image modified from Sarah Angel Smith)[34] . . . 45

1.4 Photograph of an injector tip (from Sarah Angel Smith)[34] . . . 45

1.5 Photograph of an injector needle (from Sarah Angel Smith)[34] . . . 45

1.6 Structure of PEI monomer . . . 52

2.1 Structure of PIB, PIBSA and PIBSI[57] . . . 61

2.2 Structures of PIBs produced by each catalyst . . . 61

2.3 Synthesis of PIBSA from highly substituted PIB, Diels-Alder reaction at 140-250 °C . . . 62

2.4 Synthesis of PIBSA from PIB with vinylidene end group, "ENE" reaction at 150–250 °C . . . 62

2.5 Synthesis of mono (x=1) and bis (x=2) PIBSI, 160 °C . . . 63

2.6 Comparison of Mushroom and Brush regimes (image modified from Chevalier et al. (2004))[29] . . . 65

2.7 Straight chain PIBSI and comb-like polyPIBSI[76] . . . 66

2.8 A diagram showing three types of CCS technology: post-combustion, pre-combustion and oxy-fuel capture (based off of Figeroa et al. (2008))[112] 77

2.9 Schematic of a typical absorber-stripper for a liquid amine (MEA in this case) post-combustion capture plant (from Wei et al. (2019))[119] . 80

2.10 Diagram comparing the two types of adsorption: Physisorption and Chemisorption (Global CCS)[120] 81
2.11 Basic schematic of a CCS membrane (from Global CCS)[120] 82
2.12 Structure of monoethanolamine 85
2.13 Linear and Branched PEI 85
2.14 The chemisorption of CO_2 by PEI 86
2.15 Non-reversible formation of cyclic urea from MEA 90

3.1 Simplified Diagram of an NMR Magnet 97
3.2 Figure showing net/bulk magnetisation and precessional rotation (by Thomas Wenzel)[169] 99
3.3 Free Induction Decay and Fourier Transformed Spectra (from Comprehensive Analytical Chemistry, 2018)[171] 100
3.4 Rice husk from Hunan province, China. As received from the supplier. 109
3.5 Chemical structure of sodium salicylate 111
3.6 Chemical structure of pyrogallol 111
3.7 Chemical structure of 3,3' dithiodipropionic acid 111
3.8 Chemical structure of 2,2' thiodiethanol 111
3.9 A simplified schematic of the KIER Pilot Scale Carbon Capture Facilities[166] 112
3.10 Photographs of a 5 kg batch of 50 wt. % G100-Silica 1 being prepared (Courtesy of Lee Stevens) 115
3.11 6 mm Boron Nitride Capsule with Macor screw cap, used to contain the samples in high temperature ^{1}H NMR in this study 117
3.12 Solid Echo Pulse Sequence (from the Encyclopedia of Analytical Chemistry)[178] 117
3.13 $\Delta H_{1/2}$ vs T_2 118
3.14 Chemical Structure of TKS 119
3.15 Cross Polarisation Pulse Sequence 119
3.16 Direct Excitation Pulse Sequence where x= nucleus probed 120

3.17 Example burnoff TGA thermogram demonstrating polymer loading calculation variables 121

3.18 Example CO_2 adsorption TGA thermogram demonstrating CO_2 uptake calculation variables 122

4.1 $\Delta H_{\frac{1}{2}}$ over 30-250 °C for repeat analysis of 50 wt. % PIBSI C MicroCB dispersions 129

4.2 Average $\Delta H_{\frac{1}{2}}$ over 30-250 °C for repeat analysis of 50 wt. % PIBSI C MicroCB dispersions, with error bars of one standard deviation . . 129

4.3 $\Delta H_{\frac{1}{2}}$ results for 3 samples of 50 wt. % PIBSI C MicroCB dispersions over 30-250 °C. Each sample was independently prepared in order to determine reproducibility. 131

4.4 Average $\Delta H_{\frac{1}{2}}$ over 30-250 °C for 3 samples of 50 wt. % PIBSI C MicroCB dispersions, with error bars of one standard deviation.Each sample was independently prepared in order to determine reproducibility. 131

4.5 Comparison of the $\Delta H_{\frac{1}{2}}$ values of a 20 wt. % PIBSI C MicroCB dispersion over 30-250 °C fitted with and without Gaussian component. The two data sets are almost indistinguishable. 133

4.6 TGA proximate analysis data for each of the PIB derivatives (offset of 2.5-17.5 % added to Weight (%) for visual clarity) 135

4.7 An example ^{1}H NMR spectrum of 7.5 % PIBSI C adsorbed on microCB. This spectrum was acquired at 250 °C. 138

4.8 ^{1}H NMR data for various loadings of PIBSI B on MicroCB over 30-250 °C 139

4.9 ^{1}H NMR data for various loadings of PIBSI C on MicroCB over 30-250 °C 140

4.10 ^{1}H NMR data for various loadings of PIBSI G on MicroCB over 30-250 °C 141

4.11 ^{1}H NMR data for various loadings of PIBSI I on MicroCB over 30-250 °C142

4.12 ^{1}H NMR data for various loadings of PIBSI Y on MicroCB over 30-250 °C 143

4.13 ^{1}H NMR data for various loadings of PIBSI Z on MicroCB over 30-250 °C 144

4.14 ^{1}H NMR data for various loadings of PIB on MicroCB over 30-250 °C 144

4.15 ^{1}H NMR data for various loadings of PIBSA on MicroCB over 30-250 °C145

4.16 Mobility of PIBSI B MicroCB dispersions of different loadings at 250 °C148

4.17 Mobility of PIBSI C MicroCB dispersions of different loadings at 250 °C149

4.18 Mobility of PIBSI G MicroCB dispersions of different loadings at 250 °C149

4.19 Mobility of PIBSI I MicroCB dispersions of different loadings at 250 °C150

4.20 Mobility of PIBSI Y MicroCB dispersions of different loadings at 250 °C151

4.21 Mobility of PIBSI Z MicroCB dispersions of different loadings at 250 °C152

4.22 Mobility of PIBSA 2 MicroCB dispersions of different loadings at 250 °C152

4.23 Mobility of PIB MicroCB dispersions of different loadings at 250 °C . 153

4.24 A comparison of the ^{1}H NMR $\Delta H_{\frac{1}{2}}$ for PIBSI I (bis-) and PIBSI Y (mono-) at 250 °C over 5-20 wt. % polymer loadings 154

4.25 A comparison of the ^{1}H NMR $\Delta H_{\frac{1}{2}}$ for PIBSI G (bis-) and PIBSI B (mono-) at 250 °C over 2-20 wt. % polymer loadings 154

4.26 A comparison of the ^{1}H NMR $\Delta H_{\frac{1}{2}}$ for PIBSI G (1000 M_n PIB) and PIBSI Z (750 M_n PIB) at 250 °C over 2-20 wt. % polymer loadings . 155

4.27 Comparison of PIBSI with TEPA Headgroups adsorbed on MicroCB, ^{1}H NMR performed at 250 °C 156

4.28 Comparison of PIB derivatives adsorbed on MicroCB, ^{1}H NMR performed at 250 °C 157

4.29 Comparison of PIB derivatives adsorbed on MicroCB with the potential monolayer region highlighted 159

4.30 Grouping of PIB derivatives by interaction strength 160

4.31 ^{13}C-^{1}H CP MAS NMR spectrum for PIBSI C, acquired at ambient temperature under a spinning speed of 1000 Hz, a contact time of 3000 ms, and with a spectrometer calibrated to TKS (at 3.5 ppm). The peaks at 135 and 138 ppm are likely to be the result of terminal isobutylene carbons and the peaks between 30-70 ppm are tentatively asssociated with carbons in the PIB chain. 164

4.32 ^{13}C-^{1}H CP MAS NMR spectrum for PIBSI G, acquired at ambient temperature under a spinning speed of 750 Hz, a contact time of 3000 ms, and with a spectrometer calibrated to TKS (at 3.5 ppm). The peaks at 135 and 138 ppm are likely to be the result of terminal isobutylene carbons and the peaks between 40-70 ppm may result from the carbons in the PIB chain. 165

4.33 Single pulse excitation ^{13}C NMR spectrum for PIBSI C, acquired at ambient temperature under a spinning speed of 1000 Hz, a contact time of 3000 ms, and with a spectrometer calibrated to TKS (at 3.5 ppm) 166

4.34 Single pulse excitation ^{13}C NMR spectrum for a 10 wt. % PIBSI G MicroCB dispersion, acquired at ambient temperature, under a spinning speed of 5000 Hz, a contact time of 3 ms and with the spectrometer calibrated to TKS (at 3.5 ppm). 167

4.35 Electron Paramagnetic Resonance of MicroCB, at ambient temperature 168

4.36 ^{13}C-^{1}H CP MAS NMR spectra of 50 wt. % PIBSI C mesoporous silica dispersion, acquired at ambient temperature, under a spinning speed of 5000 Hz, a contact time of 10 ms and with the spectrometer calibrated to TKS (at 3.5 ppm). 170

4.37 ^{13}C-^{1}H CP MAS spectra of 30 wt. % PIBSI G SBA-15 dispersion, acquired at ambient temperature, under a spinning speed of 5000 Hz and a contact time of 1 ms (TKS Standard at approximately 3.5 ppm). 171

4.38 ^{13}C SPE spectra of 30 wt. % PIBSI G SBA-15 dispersion, acquired at ambient temperature, under a spinning speed of 5000 Hz and a contact time of 3 ms (TKS Standard at approximately 3.5 ppm). . . . 171
4.39 ^{1}H NMR data for PIBSI G supported on SBA-15 over 30-250 °C . . . 172
4.40 ^{1}H NMR data for PIBSI G supported on SBA-15 at 250 °C, with error bars of one standard deviation 173
4.41 Comparison of PIBSI G dispersions on SBA-15 and MicroCB, at 10-40 % loading 174

5.1 TGA thermogram for 25000 PEI, highlighting moisture loss after 30 min at 100 °C 178
5.2 ^{1}H NMR data for a 25000 PEI-Silica 1 sample before and after drying in situ. Measurements acquired over 40-130 °C 179
5.3 Photograph of a sample of 60 wt. % 750000 PEI-RH2 showing solidification of the PEI-Silica on the beaker walls 180
5.4 Adsorption and desorption of CO_2 on various PEI-Silicas as found by Abu-El-Haija (A) and Alhuaybi (B), 2016, with a line indicating 75 °C.[139,140] 182
5.5 The maximum free-form loading of 25000 PEI-Silicas and the percentage loading which causes agglomeration 183
5.6 Plots of the CO_2 capacity at 75 °C against loading for 25000 PEI (HF) adsorbed onto SBA-15 (A), MCF (B), RH1 (C), and RH2 (D) . 184
5.7 $\Delta H_{\frac{1}{2}}$ over 30-150 °C for repeat analysis of 40 wt. % 5000 PEI-MCF with drying in situ at 110 °C 185
5.8 Average $\Delta H_{\frac{1}{2}}$ over 30-150 °C for repeat analysis of 40 wt. % 5000 PEI-MCF, dried in situ at 110 °C, with error bars of one standard deviation 186
5.9 Example ^{1}H NMR spectra of PEI-Silica (40 wt. % 25000 PEI on Silica 1 at 80 °C) 187
5.10 Inkbottle (A) vs channel (B) type pore shapes. Note that ink-bottle pores are not exclusively terminal as is shown in this image. 190
5.11 N_2 sorption isotherm for SBA-15 (at 200 °C) 190

5.12 N_2 sorption isotherm for Rice Husk Silica 2 (at 200 °C) 191

5.13 Viscosity measurements of PEI over 25-130 °C 194

5.14 Burnoff TGA results for neat PEI samples under N_2/air 195

5.15 Proximate TGA results for neat PEI samples under N_2 195

5.16 ^{1}H NMR data for different neat PEI samples over 30-100 °C 196

5.17 Maximum CO_2 capacity of different 40 wt. % PEI-Silica 1 samples over 30-100 °C, derived from TGA thermograms 199

5.18 t_{30} of CO_2 adsorption on different 40 wt. % PEI-Silica 1 samples over 30-100 °C, derived from TGA thermograms 199

5.19 t_{60} of CO_2 adsorption on different 40 wt. % PEI-Silica 1 samples over 30-100 °C, derived from TGA thermograms 200

5.20 t_{90} of CO_2 adsorption on different 40 wt. % PEI-Silica 1 samples over 30-100 °C as determined by TGA 200

5.21 ^{1}H NMR data for different PEI-Silica 1 samples over 30-130 °C . . . 201

5.22 Maximum CO_2 capacity of different 50 wt. % PEI-SBA15 samples over 30-100 °C, derived from TGA thermograms 202

5.23 t_{60} of CO_2 adsorption on different 50 wt. % PEI-SBA15 samples over 30-100 °C, derived from TGA thermograms 202

5.24 t_{90} of CO_2 adsorption on different 50 wt. % PEI-SBA15 samples over 30-100 °C, derived from TGA thermograms 203

5.25 ^{1}H NMR data for different 50 wt. % PEI-SBA15 samples over 30-130 °C 204

5.26 Maximum CO_2 capacity of different 50 wt. % PEI-MCF samples over 30-100 °C, derived from TGA thermograms 205

5.27 t_{60} of CO_2 adsorption on different 50 wt. % PEI-MCF samples over 30-100 °C, derived from TGA thermograms 206

5.28 t_{90} of CO_2 adsorption on different 50 wt. % PEI-MCF samples over 30-100 °, derived from TGA thermogramsC 206

5.29 ^{1}H NMR data for different 50 wt. % PEI-MCF samples over 30-130 °C 207

5.30 Maximum CO_2 capacity of CO_2 adsorption on different 50 wt. % PEI-RH1 samples over 30-100 °C as determined by TGA 208
5.31 t_{60} of different CO_2 adsorption on 50 wt. % PEI-RH1 samples over 30-100 °C as determined by TGA 208
5.32 t_{90} of CO_2 adsorption on different 50 wt. % PEI-RH1 samples over 30-100 °C as determined by TGA 209
5.33 ^{1}H NMR data for different 50 wt. % PEI-RH1 samples over 30-130 °C 209
5.34 Maximum CO_2 capacity of different 60 wt. % PEI-RH2 samples over 30-100 °C, derived from TGA thermograms 210
5.35 t_{60} of CO_2 adsorption on different 60 wt. % PEI-RH2 samples over 30-100 °C, derived from TGA thermograms 211
5.36 t_{90} of CO_2 adsorption on different 60 wt. % PEI-RH2 samples over 30-100 °C, derived from TGA thermograms 211
5.37 ^{1}H NMR data for different 60 wt. % PEI-RH2 samples over 30-130 °C 212
5.38 Maximum CO_2 capacity of different 800 molecular weight PEI-Silica samples over 30-100 °C, derived from TGA thermograms 214
5.39 t_{60} of CO_2 adsorption on different 800 molecular weight PEI-Silica samples over 30-100 °C, derived from TGA thermograms 214
5.40 T_{90} of CO_2 adsorption on different 800 molecular weight PEI-Silica samples over 30-100 °C, derived from TGA thermograms 215
5.41 ^{1}H NMR data for different 800 molecular weight PEI-Silica samples over 30-130 °C, including neat PEI 215
5.42 Maximum CO_2 capacity of different 1300 molecular weight PEI-Silica samples over 30-100 °C, derived from TGA thermograms 217
5.43 t_{60} of CO_2 adsorption on different 1300 molecular weight PEI-Silica samples over 30-100 °C, derived from TGA thermograms 217
5.44 t_{90} of CO_2 adsorption on different 1300 molecular weight PEI-Silica samples over 30-100 °C, derived from TGA thermograms 218
5.45 ^{1}H NMR data for different 1300 molecular weight PEI-Silica samples over 30-130 °C, including neat PEI 218

5.46 Maximum CO_2 capacity of different 2000 molecular weight PEI-Silica samples over 30-100 °C, derived from TGA thermograms 219
5.47 t_{60} of CO_2 adsorption on different 2000 molecular weight PEI-Silica samples over 30-100 °C, derived from TGA thermograms 220
5.48 t_{90} of CO_2 adsorption on different 2000 molecular weight PEI-Silica samples over 30-100 °C, derived from TGA thermograms 220
5.49 ^{1}H NMR data for different 2000 molecular weight PEI-Silica samples over 30-130 °C, including neat PEI 221
5.50 Maximum CO_2 capacity of different 5000 molecular weight PEI-Silica samples over 30-100 °C, derived from TGA thermograms 222
5.51 t_{60} of CO_2 adsorption on different 5000 molecular weight PEI-Silica samples over 30-100 °C, derived from TGA thermograms 223
5.52 t_{90} of CO_2 adsorption on different 5000 molecular weight PEI-Silica samples over 30-100 °C, derived from TGA thermograms 223
5.53 ^{1}H NMR data for different 5000 molecular weight PEI-Silica samples over 30-130 °C, including neat PEI 224
5.54 Maximum CO_2 capacity of different 25000 molecular weight PEI-Silica samples over 30-100 °C, derived from TGA thermograms 225
5.55 t_{60} of CO_2 adsorption on different 25000 molecular weight PEI-Silica samples over 30-100 °C, derived from TGA thermograms 226
5.56 t_{90} of CO_2 adsorption on different 25000 molecular weight PEI-Silica samples over 30-100 °C, derived from TGA thermograms 226
5.57 ^{1}H NMR data for different 25000 molecular weight PEI-Silica samples over 30-130 °C, including neat PEI 227
5.58 Maximum CO_2 capacity of different 750000 molecular weight PEI-Silica samples over 30-100 °C, derived from TGA thermograms 228
5.59 t_{60} of CO_2 adsorption on different 750000 molecular weight PEI-Silica samples over 30-100 °C, derived from TGA thermograms 229
5.60 t_{90} of CO_2 adsorption on different 750000 molecular weight PEI-Silica samples over 30-100 °C, derived from TGA thermograms 229

5.61 ^{1}H NMR data for different 750000 molecular weight PEI-Silica samples over 30-130 °C, including neat PEI 230

5.62 TGA determined t_{30} of CO_2 adsorption onto the highest capacity PEI-Silica materials with respect to the molecular weight of the PEI . 231

5.63 TGA determined t_{60} of CO_2 adsorption onto the highest capacity PEI-Silica materials with respect to the molecular weight of the PEI . 232

5.64 TGA determined t_{90} of CO_2 adsorption onto the highest capacity PEI-Silica materials with respect to the molecular weight of the PEI . 232

5.65 Rate of Adsorption, shown by t_{30}, against Mobility, shown by $\Delta H_{\frac{1}{2}}$, for 50 wt. % 5000 PEI-RH1 with the temperature of each measurement noted. 239

5.66 Rate of Adsorption, shown by t_{60}, against mobility, shown by $\Delta H_{\frac{1}{2}}$, for 50 wt. % 5000 PEI-RH1 with the temperature of each measurement noted. 239

5.67 Rate of Adsorption, shown by t_{90}, against Mobility, shown by $\Delta H_{\frac{1}{2}}$, for 50 wt. % 5000 PEI-RH1 with the temperature of each measurement noted. 240

5.68 Comparison of ^{1}H NMR mobility and TGA maximum CO_2 adsorption and kinetics (t60) data of PEI-Silicas (Silica 1) over 20-120 °C 242

6.1 Solubility Test for (from left to right) Sodum Salicylate, 2,6-Di-tert-butyl-4-(dimethylaminomethyl)phenol, Pyrogallol and Pentaerythritol tetrakis(3,5-di-tert-butyl-4-hydroxyhydrocinnamate). 246

6.2 CP MAS ^{13}C-^{1}H NMR spectra of 40 % G100-Silica 1. The spectrum was acquired at a spinning speed of 5000 Hz and a contact time of 1 ms. The spectrometer was calibrated to TKS at 3.5 ppm. 248

6.3 SPE MAS ^{13}C-^{1}H NMR spectra of neat G100, with a spinning speed of 1000 Hz. The spectrum was acquired at a spinning speed of 5000 Hz and a contact time of 3 ms. The spectrometer was calibrated to TKS at 3.5 ppm. 249

6.4 CP MAS ^{13}C-^{1}H NMR spectra of adsorbed (Top/Red) and regenerated (Bottom/Blue) PEI-Silica samples from the KIER pilot scale plant. Peaks are at 164 ppm (C=O), 50 ppm (PEI) and the reference peak is at 3.5 ppm (TKS). The spectrum was acquired at a spinning speed of 5000 Hz and a contact time of 1 ms. 250

6.5 CP MAS ^{13}C-^{1}H NMR spectra of adsorbed (Top), regenerated (Middle) and desorbed-regenerated (Bottom) PEI-Silica samples from the KIER pilot scale plant. Peaks are at 164 ppm (C=O), 50 ppm (PEI) and the reference peak at 3.5 ppm (TKS). The spectrum was acquired at a spinning speed of 5000 Hz and a contact time of 1 ms. 255

6.6 Oxidation results for a G100-Silica 1 sample with no added antioxidant 257

6.7 Labelled structure of sodium salicylate 258

6.8 CP MAS ^{13}C-^{1}H NMR spectrum of 10 % sodium salicylate functionalised 40 wt. % G100-Silica 1 (top), 40 wt. % G100-Silica 1 (middle) and sodium salicylate (bottom). The spectrum was acquired at a spinning speed of 5000 Hz and a contact time of 1 ms. The spectrometer was calibrated using TKS at 3.5 ppm. 259

6.9 TGA determined maximum CO_2 capacity of G100-Silica 1 functionalised with 0.0, 0.25, 0.50, 0.75 and 1.0 % sodium salicylate, over 10 days under oxidation conditions[148] 260

6.10 TGA determined maximum CO_2 capacity of G100-Silica 1 functionalised with 0, 4, 6, 8 and 10 % sodium salicylate, over 10 days under oxidation conditions[148] 260

6.11 Pyrogallol impregnated G100-Silica 1 using minimal added water (left) and using an additional 5 g added water (right). 261

6.12 Labelled structure of pyrogallol 262

6.13 CP MAS ^{13}C-^{1}H NMR spectrum of 10 % pyrogallol functionalised 40 wt. % G100-Silica 1 (top), 40 wt. % G100-Silica 1 (middle) and pyrogallol (bottom). The spectrum was acquired with spinning at 5000 Hz and a contact time of 1 ms. The spectrometer was calibrated to TKS at 3.5 ppm. 263

6.14 TGA determined maximum CO_2 capacity of G100-Silica 1 functionalised with 0, 0.5 1 and 6 % pyrogallol, over 10 days under oxidation conditions[148] 263

6.15 TGA determined maximum CO_2 capacity of G100-Silica 1 functionalised with 0, 10 and 14 % pyrogallol, over 10 days under oxidation conditions[148] 264

6.16 Labelled structure of 3,3' dithiodipropionic acid 265

6.17 CP MAS ^{13}C-^{1}H NMR spectrum of 10 % 3,3' dithiodipropionic acid functionalised 40 wt. % G100-Silica 1 (top), 40 wt. % G100-Silica 1 (middle) and 3,3' dithiodipropionic acid (bottom). The spectrum was acquired with spinning at 5000 Hz and a contact time of 1 ms. The spectrometer was calibrated to TKS at 3.5 ppm. 266

6.18 TGA determined maximum CO_2 capacity of G100-Silica 1 functionalised with 0, 0.25, 0.5, 0.75 and 1 % 3,3' dithiodipropionic acid, over 10 days under oxidation conditions 267

6.19 Labelled structure of 2,2' thiodiethanol 268

6.20 Liquid ^{13}C NMR spectrum of 2,2' thiodiethanol, with a TMS standard. From SpectraBase.com, courtesy of Bio-Rad Laboratories Inc.[196] 268

6.21 CP MAS ^{13}C-^{1}H NMR spectrum of 40 wt. % G100-Silica 1 (top) and 10 % 2,2' thiodiethanol functionalised G100-Silica 1 (bottom). The spectrum was acquired with spinning at 5000 Hz and a contact time of 1 ms. The spectrometer was calibrated to TKS at 3.5 ppm. 269

6.22 TGA determined maximum CO_2 capacity of G100-Silica 1 functionalised with 0.5, 1.0, 2.0, and 4.0 % 2,2' thiodiethanol, over 10 days under oxidation conditions 269

A.1 Total surface area of PIBSI G and MicroCB at different polymer loadings of 1 g sample 313
A.2 Structure of tetraethylenepentamine (TEPA), head group of PIBSI B and G 314
A.3 Structure of aminoethylethanolamine (AEEA), head group of PIBSI C 314
A.4 Structure of ethylenediamine (EDA), head group of PIBSI I 314
A.5 Structure of ethanolamine 314

B.1 Burnoff thermogravimetric analysis of Rice Husk under a nitrogen/air atmosphere 317
B.2 Proximate thermogravimetric analysis of Rice Husk under a nitrogen atmosphere 317
B.3 N_2 sorption isotherm for Silica 1, at 200 °C 320
B.4 N_2 sorption isotherm for 40 nm Silica, at 200 °C 320
B.5 N_2 sorption isotherm for Rice Husk Silica 1, at 200 °C 320
B.6 Classification of physisorption isotherms[189] 321
B.7 Classification of hysteresis loops[189] 322
B.8 T_{30} of different PEI-SBA15 dispersions over 30-100 °C 324
B.9 T_{30} of different PEI-MCF dispersions over 30-100 °C 325
B.10 T_{30} of different PEI-RH1 dispersions over 30-100 °C 325
B.11 T_{30} of different PEI-RH2 dispersions over 30-100 °C 325
B.12 TGA determined maximum CO_2 capacity of G100-Silica 1 functionalised with 0, 2, 6, 8 and 10 % 3,3' dithiodipropionic acid, over 10 days under oxidation conditions 329
B.13 TGA determined maximum CO_2 capacity of G100-Silica 1 functionalised with 0, 12, 14, 16 and 20 % 3,3' dithiodipropionic acid, over 10 days under oxidation conditions 329

B.14 TGA determined maximum CO_2 capacity of G100-Silica 1 functionalised with 0, 6, 8, 10 and 12 % 2,2' thiodiethanol, over 10 days under oxidation conditions 330
B.15 TGA determined maximum CO_2 capacity of G100-Silica 1 functionalised with 0, 14, 16, 18 and 20 % 2,2' thiodiethanol, over 10 days under oxidation conditions 330

List of Tables

1.1 Some important types of fuel additives[37] 49

1.2 Challenges related to biofuel usage 50

2.1 PEI-Silica properties and loadings from the literature, the majority obtained at operational levels of CO_2 at 2.5-15 % except those noted * which were at 95-100 % CO_2. Wt% values were either provided in the text or calculated from mg g^{-1} values. N/a refers to data not reported in the literature. 89

3.1 Polymer chain information on PIB derivative samples 106

3.2 Information on PIB derivative samples 107

3.3 PEI average molecular weights and concentrations as received (*concentration determined by burnoff TGA) 108

3.4 Silica sample properties 110

3.5 Weights used to prepare 1 g of PEI-Silica by impregnation 114

4.1 Polymer chain information on PIB derivative samples 126

4.2 Information about pore size for MicroCB as determined by N_2 sorption isotherms and as provided by Sigma Aldrich 133

4.3 Atomic Contributions to PSA (# denotes a triple bond) 134

4.4 Predicted Monolayer Coverage 135

4.5 Moisture content of PIB derivatives, as determined by TGA 136

4.6 PSA predicted monolayer coverage and NMR Determined monolayer coverage 158

4.7 Grouping of PIB derivatives by interaction strength, including approximate PIB chain length and headgroup information 161

4.8 Comparison of supplier provided data on the pore structure of MicroCB and potential silica analogue 169

5.1 PEI average molecular weights, as provided by the supplier. No information on error bands was provided. 177

5.2 TGA determined moisture content of PEI samples. * denotes that the moisture content may be inaccurate due to the inhomogeneous nature of the sample 179

5.3 PEI Loading of 25000 PEI on SBA15 (Dry Basis), *indicates an agglomerated sample 181

5.4 The maximum loading (wt.%) values at which 25000 PEI-Silica remains a free-form powder, and the loading at which these samples have the highest maximum CO_2 adsorption at 75 °C 183

5.5 The N_2 sorption data for each of the silica samples obtained at 200 °C (^{a} determined using t-plot model with Harkins Jura correction, ^{b} determined using BJH model with Harkins Jura correction, ^{c} Average Pore size using Total Pore Volume using adsorption isotherm and ^{d} Next/Window Pore size using Total Pore Volume using desorption isotherm data) 192

6.1 Solubility of Antioxidants. * denotes liquid sample 246

6.2 Ratio of CO_2 peak integral (approx. 164 ppm) to PEI peak integral (approx. 50 ppm) displayed as a percentage for sample set 1 251

6.3 Ratio of CO_2 peak integral (approx. 164 ppm) to PEI peak integral (approx. 50 ppm) displayed as a percentage for sample set 2 252

6.4 Maximum CO_2 adsorption of the adsorbed and regenerated samples, as determined by TGA at 75 °C and 15 % CO_2, for sample set 1 . . . 252

6.5 Maximum CO_2 adsorption of the adsorbed and regenerated samples, as determined by TGA at 75 °C and 15 % CO_2, for sample set 2 . . . 253

6.6 Impact of the addition of antioxidant materials to 40 wt. % G100-Silica on the maximum CO_2 capacity as determined by TGA at 75 °C, under a 15 % CO_2 atmosphere 270
6.7 Cost per kg Antioxidant, from Sigma-Aldrich as of July 2019 271

A.1 Weights used to prepare 1 g of PIB derivative dispersions (not considering moisture content) 310
A.2 Atomic Contributions to PSA of PIBSI G 311
A.3 Example calculation of monolayer coverage for a 1 g sample of PIBSI G-MicroCB 312
A.4 PIBSI Headgroup Structures 313

B.1 Elemental composition of rice husk 318
B.2 Average concentrations of significant species ($\geq$ 0.5 %) in Rice Husk sample, as determined by XRF 318
B.3 Porosity data of Rice Husk Silica 2 and Silica 1 as determined by mercury intrusion porosimetry. This method has an intrusion accuracy of $\pm$ 1 %. Further data on error is unavailable. 319
B.4 Specification of SBA-15 as supplied by Sigma Aldrich 319
B.5 Viscosity measurements of PEI samples (*according to the product specification, $^{(1)}$measurement taken at 30 °C) 324
B.6 The maximum CO_2 capacity of each PEI-Silica material and its associated adsorption temperature 326
B.7 Date of sample extraction (in 2017) and sample name 327
B.8 Weight percent of antioxidant in antioxidant functionalised PEI-Silicas 328

Abreviations

$\Delta H_{1/2}$ peak half width.

η* viscosity.

^{13}**C** carbon-13.

AEEA aminoethylethanolamine.

AES auger electron spectroscopy.

AFM atomic force microscopy.

ATC Additive Technical Committee.

BET Brunauer-Emmett-Teller.

BJH Barrett-Joyner-Halenda.

CCDs combustion chamber deposits.

CEC Co-ordinating European Council.

CLC chemical looping combustion.

CO_2 carbon dioxide.

CP cross polarisation.

CP MAS cross polarisation magic angle spinning.

CPMG Carr, Purcell, Meiboom, Gill.

DCA deposit control additive.

DEA diethanolamine.

DI direct injection.

DISI direct injection spark ignition.

EDA ethylenediamine.

EPR electron paramagnetic resonance.

FAME fatty acid methyl esters.

FID free induction decay.

GHGs greenhouse gases.

GPC gel permeation chromatography.

GTDI gasoline turbo direct injection.

hpdec high powered decoupled.

IR infra-red spectroscopy.

Kel-F chlorotrifluoroethene.

KIER Korean Institute of Energy Research.

MAS magic angle spinning.

MDEA methyl-di-ethanolamine.

MEA monoethanolamine.

MiP mercury intrusion porosimetry.

MOF metal organic framework.

MPFI multi-port fuel injector.

NMR nuclear magnetic resonance.

NO_x nitrogen oxides.

ORI octane requirement increase.

PD polydispersity.

PEI polyethylene imine.

PIB polyisobutylene.

PIBSA polyisobutylene succinic anhydride.

PIBSI polyisobutylene succinimide.

ppm parts per million.

PSA polar surface area.

PVC poly(vinyl chloride).

RDE real driving emissions.

REMPI ToF MS resonant enhanced multiphoton ionization combined with time of flight mass spectrometry.

RF radiofrequency.

SEM scanning electon microscopy.

SPE single pulse excitation.

STM scanning tunnelling microscopy.

T_1 spin-lattice relaxation time.

$T_1\rho$ spin-lattice relaxation in the rotating frame.

TEM transmision electron microscopy.

TEOS tetraethyl orthosilicate.

TEPA tetraethylenepentamine.

TGA thermogravimetric analysis.

THF tetrahydrofuran.

TKS tetrakis(trimethylsilyl)silane.

TMB 1,3,5-trimethylbenzene.

UV-Vis Ultraviolet-visible spectroscopy.

XPS x-ray photon spectroscopy.

XRF X-Ray fluorescence.

Chapter 1

Introduction

1.1 Motivation for Research

The mitigation of carbon dioxide (CO_2) release into the environment is a key issue for mankind. CO_2 is the main contributor to global climate change which has the potential for devastating effects on earth's physical geography, and consequently on human, animal and plant life.[1] To limit these effects, it is widely agreed that global temperature increase should be limited to 2 °C.[2] In order to achieve this limitation, the release of CO_2 into the atmosphere must be reduced, eliminated entirely or brought into the realm of negative emissions; power generation, industry and transport are the three of the main sources of global CO_2 emissions, and thus form the main targets for curtailing planet-wide temperature increases.

Within the transport sector, diesel and petrol (gasoline) powered engines used for both private and commercial purposes are required to increase efficiency in order to reduce emissions if they are to meet increasingly stringent emissions targets (i.e. Regulation (EC) 443/2009). With these efficiency gains that reduce CO_2 emissions come challenges in engine design and a reduced tolerance to carbonacous deposit build up on internal engine surfaces (further information on deposits can be found in Section 1.5.2) Without effective deposit control which both protects against build-ups and effectively removes them, these efficiency gains are reduced and ultimately cause engines to fail. Fuel additives are a common solution to this issue, however

their design and testing can cost tens of thousands of pounds and take several days for one sample, therefore it is desirable to develop alternative laboratory scale test methods. Solid-state nuclear magnetic resonance (NMR) of additives (specifically polyisobutylene derivatives) adsorbed onto carbon black (an imitation engine deposit) has previously shown promising results (this is outlined in Section 2.4.2).

In addition to this, CO_2 is produced through power generation and industry processes. Carbon capture has the potential to be a very powerful technique in preventing emissions from these processes. During the course of this study a further application of high temperature solid state NMR on a carbon capture material, PEI-Silica (polyethyleneimine absorbed onto silica), was investigated and a collaboration with the Korean Institute of Energy Research KIER undertaken in parallel to the initial aims of the project. PEI-Silica is used in post-combustion carbon capture, adsorbing CO_2 from flue gases. In order to bring the process up to a commercial scale it is necessary to optimise several process variables and test different materials, with high temperature studies replicating real world conditions.

Solid state broadline proton NMR is a useful non-destructive technique to apply to both of these fields, as it is able to probe the molecular motion of materials while maintaining the surface interactions of interest, which may be altered if these materials were entered into solution. The capacity of this method to operate at high temperature enables measurements which reflect operational conditions, and the relative speed of the individual experiments allows measurements at regular temperature intervals whilst maintaining a constant heating rate.

In this thesis, discussion of both branches of the project will generally be kept separate, as although the key techniques and research methodologies are the same, the insight gained is distinct for each material.

1.2 Aims and Objectives of Research

On the initial undertaking of this research the singular goal was to develop a more affordable testing method, using solid state broadline proton NMR at elevated temperatures, for polyisobutylene derivatives as deposit control additives in automobile

fuels. As the project progressed the scope widened and its the aims developed to include other areas of research. In addition to developing broadline NMR as a method to investigate these materials, the project grew to encompass using more resolved NMR techniques, specifically cross polarisation magic angle spinning carbon-13 NMR, to investigate their mobilities at a sub-molecular level. In branching out further into investigations of other polymer-substrate materials (specifically silica supported polyethylene imine), new research goals of determining what, if any, relationship exists between polymer mobility and CO_2 adsorption kinetics of these materials, were found.

In order to achieve these aims the following objectives were determined:

Investigation of polyisobutylene derivatives:

- To prepare a range of PIB derivative microCB dispersions and measure the mobility of these dispersions over 30-250 °C using broadline proton NMR
- To compare the mobility of these PIB derivative dispersions at operational temperatures
- To investigate the applicability of CP MAS carbon-13 NMR as a testing method for these dispersions

Investigation of silica supported polyethylene imine:

- To prepare a range of PEI-Silicas with different molecular weight PEIs and different silica pore structures
- To investigate the mobility of these materials over their CO_2 adsorption temperature
- To measure the kinetics of CO_2 adsorption of these materials and compare with the mobility measurements
- To investigate CO_2 adsorption using carbon-13 NMR

- To investigate the impact of the addition of antioxidants to these materials on CO_2 capacity

1.3 Thesis Organisation

This thesis is divided into seven chapters, an introduction, literature review, methodologies, three results chapters and a conclusions chapter. Each Chapter, bar Chapters 1 and 7 is summarised at the end.

The remainder of the current chapter, Chapter 1: Introduction, will introduce some of the main topics of this research and provide a general background. Chapter 2: Literature Review, discusses the relevant literature and is split into two halves. The first half discusses literature relevant to deposit control additives and polyisobutylene derivatives while the second half discusses the relevant literature to carbon capture and storage and silica supported polyethylene imine. The 3rd chapter on experimental methodologies is also split into two halves, with the first half providing a theoretical background on the techniques called upon over the course of this study and the second half describing the specific conditions, parameters and equipment used to obtain the results of this work.

The 4th, 5th and 6th Chapters present and discuss the results of this study. With Chapter 4 focusing on polyisobutylene derivatives and Chapter 5 and 6 on polyethylene imine silica. Each of these Chapters takes a somewhat chronological approach, discussing first the development of the methods used and then presenting the results obtained. These chapters are followed by Conclusions in Chapter 7, where the key findings are summarised, the novelty of research discussed and paths for future work suggested. At the end of this thesis two appendices can be found, with Appendix A and B containing information pertinent to the research into polyisobutylene derivatives and polyethylene imine silica, respectively.

1.4 Introduction to Polymer Adsorption and Mobility

1.4.1 Polymers

Polymers are molecules with a structure consisting of repeating monomers.[3] Polymers often have high molecular masses, with Rudin and Choi (2013) suggesting most polymers have a molecular weight of greater than 5000, however they concede that there is no real lower limit on polymer size.[3] Polymers can be considered to be from two major categories: natural and synthetic. Naturally occurring polymers include DNA and rubbers while plastics are a common type of synthetic polymer.

The structure of polymers can vary with linear polymers having long straight chains, and branched polymers having secondary chains branching off of the linear backbone. A third structure can be seen in cross-linked polymers where cross-linkages connect polymer chains to one another.[3]

As polymers are large molecules they are often solids or vicious liquids at room temperature, generally the larger the molecule the less fluid the bulk polymer. The uses of polymers will depend on the properties of that polymer, with the monomer, chain type and linkage, and any end groups impacting those properties. For instance polyethylene is commonly a weak material used in plastic bags ans household goods, however when the molecular weight is increased to 3.5-7.5 million the strength increases such that it can be used in orthopaedic implants.[4]

In this study the two types of polymer investigated, polyisobutylene (PIB) and polyethylene imine (PEI), are both organic synthetic polymers. PIB is also known as butyl rubber and can be used in inner tubes as well as use in fuel additives after further synthesis.[5] PEI has uses in personal care products and food packaging in addition to the carbon capture use case discussed in this study.[6]

Polymer Adsorption

Adsorption of polymers onto surfaces is the result of the attractive interactions between the polymer and the surface being greater than the repulsion caused through

the restriction of chain mobility. Stronger adsorption is therefore often the result of stronger interactions between the surface and the polymer.[7] However the capacity for a polymer to adsorb onto a substrate will be impacted not only by the interactions present, be they Van der Waals forces or stronger site specific interactions but also by the shape and size of the polymer compared to the pore shape and size.

Common measurements of polymer size include the molecular weight (often M_n, the number average or M_w, the weight average) and the radius of gyration, a measure of the size of the coil.[8] The molecular weight can be determined through chromatography (e.g. GPC) and the radius of gyration by light scattering (e.g. X-ray scattering). Molecular weight gives an basic understanding of the overall size of the polymer however provides little information of conformation, however the radius of gyration will also depend on the amount of branching of the molecule.[8]

Polymer adsorption can occur through the interaction of the entire polymer chain, or only parts of the polymer chain (for example headgroups) which leads to different chain conformations. The adsorption of sub-chains or parts of polymer chains can be thought of as in three categories: trains, where the entire chain in interacting with the substrate; loops, where the chain is interacting with the substrate at two ends; and tails, where the chain is only interacting with the substrate at one end and the other end is not adsorbed.[9]

Polymers may also interact with each other, in what is known as chain entanglement. This is a phenomenon in which a polymer chain may cross-link with other chains restricting movement.[10] For a chain to have enough flexibility for entanglement to occur the chain length must be greater than some critical number of monomers, this is seen in both bulk and adsorbed polymers.[11] In the case of the adsorbed polymers studied in this work, this may restrict the mobility of the polymer chains and if chain entanglement occurs between particles, may result in agglomeration of the particles. Chain entanglement may be expected to increase at greater than monolayer coverage due to the increased number of adsorbed polymer molecules, and the increased likelihood of these molecules to form loops and tails.[9]

1.4.2 Solid State NMR

Broadline solid state proton NMR can be used to determine the spin-spin relaxation time (T_2) of a sample. This is related to the mobility of the sample. This technique has been used extensively in the past to study coal and other carbonaceous material. It was first used in 1979 by Sanada et al. in a study of coal and pitch.[12] Since then it has been used by several different studies to investigate various coals and carbonaceous materials, including those monitoring the mobility of fluid entities forming in coal and biomass upon pyrolysis.[13–15] In addition studies investigating polymers have also been performed, specifically those investigating the relationship between chain mobility and thermal degradation.[16,17]

Polymer Mobility

The mobility of polymers adsorbed onto substrates will be impacted by the strength of interaction between the polymer and the substrate, as well as the conformation of the polymer. A polymer that is adsorbed chemically, with covalent bonding, would be expected to have a lower mobility than one bonded by physical forces (e.g. Van der Waals forces). Therefore by comparing the broadline NMR results of similar polymers adsorbed onto the same substrates, or to the bulk polymer, the strength of interactions can be inferred.

1.4.3 Applications

In this study, the mobility of two groups of adsorbed polymers were investigated: a carbon capture agent (polyethylene imine supported on silica), and a fuel additive (polyisobutylene succinimide).

1.5 Introduction to Deposit Control

1.5.1 Automobile Emissions

Because of global climate changes resulting from the anthropogenic release of greenhouse gases (GHGs) into the atmosphere, increasingly stringent controls on the emission of GHGs and pollutants from vehicles have been enacted as a means to restrict and mitigate global warming. The European Union has limited emissions from petrol and diesel engines through the Euro Emissions Standards, which currently limit new diesel and petrol vehicles to 500 mg/km and 1000 mg/km of carbon monoxide; 180 mg/km and 60 mg/km of NO_x, respectively and 5 mg/km of particulates (for direct injection (DI)) for both; hydrocarbon emissions are also limited.[18] In addition to this, EU regulation (EC) 443/2009 set mandatory CO_2 targets of 130 g/km from 2015 for car manufacturers, this will be decreased from 2021 to 95 g/km.[19] However actual driving emissions can be very different, thus in 2017 the European commission introduced the Real Driving Emissions RDE tests in addition to current lab tests.[20]

To meet changing legislation and the expectations of consumers, manufacturers must find ways to reduce emissions from engines through engine design changes. These changes include the narrowing of DI orifices and tend to result in engines more susceptible to the formation of, and lower tolerance for engine deposits. The presence of these deposits can also, in turn, increase emissions levels as well as reducing engine performance. A solution to minimise these deposits is the use of fuel additives which control and restrict the aggregation of carbon particles in internal combustion engines, thereby protecting against deposit formation and removing pre-existing deposits from internal engine surfaces.

A new generation of fuel additives has also been required for the replacement of existing, effective, additives that contain pollutants (e.g. the sulfur and phosphorous containing additive Zinc dialkyldithiophosphate, ZDDP[21]) and can no longer be used.

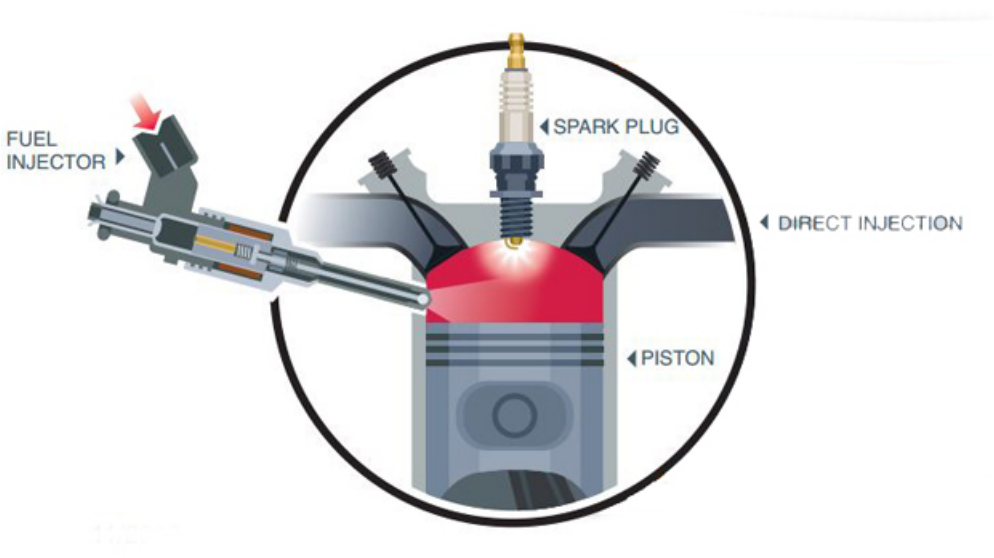


Figure 1.1: Schematic of a Direct Fuel Injection System (from RideApart)[22]

Fuel Injection Equipment

Previously, gasoline engines used carburettors which were less sensitive to deposit formation. With the development of gasoline engine technologies, direct fuel injection systems have become the norm. In a diesel engine there has also been a shift with the majority of vehicles using common rail injection. With this development of fuel injection equipment, injection orifices have been narrowed and engines have been fine tuned to specific air-fuel mixtures. These changes have left modern engines susceptible to performance loss in the presence of deposits. A schematic of a direct injection system and an injector can be seen in Figures 1.1 and 1.2.

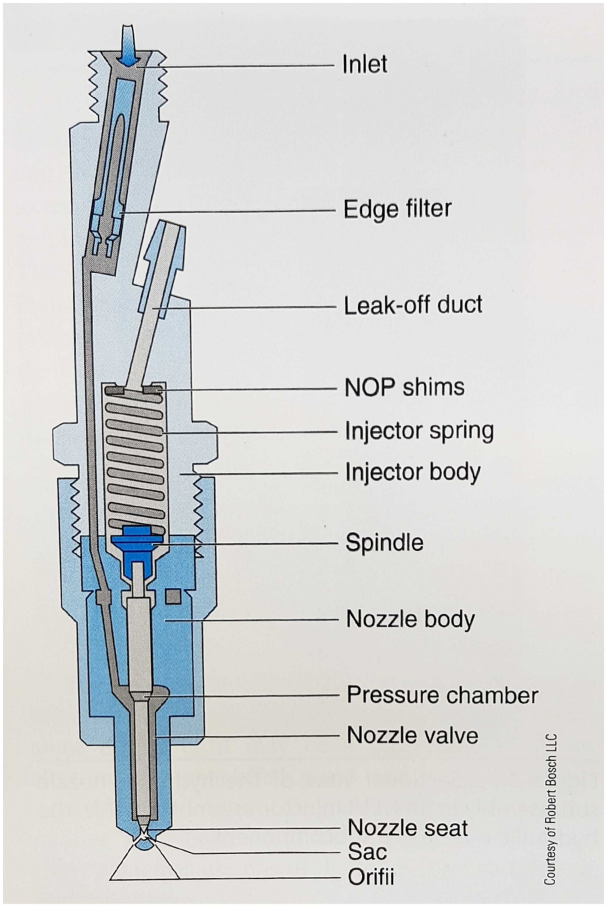


Figure 1.2: Schematic of a multi orifice injector (courtesy of Robert Bosch LLC, from Diesel Engines)[23]

Current Testing Methods

Current testing methods for the efficacy of fuel additives include several tests on different scales, starting with bench tests, and then progressively increasing in size and complexity until full engine tests.

Initial testing is commonly done on a small scale through characterisation of the adsorption characteristics, and tests to determine the stability of particulate suspensions, such as calorimetry.[24] Further testing can then be achieved through rig or engine tests, in which engine operation is emulated through a series of runs and soaks (runs referring to the time the engine is in operation and soaks being a resting period). These engine tests are designed to facilitate the formation of deposits and represent a worst-case scenario. Many of these engine tests are developed for or by standards agencies in order to be used by industry as standard tests. An example would be the Co-ordinating European Council (CEC) DW10C direct injector test, which is currently in the process of becoming a standard test (to replace the currently used DW10B).[25] The CEC DW10C is as follows:

- A diesel direct injector engine test consisting of 8 cycles (of 12 steady state conditions giving a total cycle time of 3600 s) followed by a 4 hour soak.
- Exhaust gas temperatures are recorded prior to and after the test.
- If the test is completed once it provides "8 hour data", twice gives "16 hour data" etc., cycles are performed for 32 hours total or until engine failure.[26]

Further testing may include vehicles on dynamometer rigs and/or field/road tests using a fleet of real vehicles on the road. There are reasonable correlations between results in lab and field tests with lab-scale tests giving an indication of the efficacy of different fuel additives and helping determine the appropriate treatment rates.[27] Many of these real-world tests are expensive so it is key that initial laboratory scale testing is as accurate and representative of additive efficacy as possible.

Although few of these tests can claim to be truly representative of real engine operation, it is important to note the difference in results and deposits types seen between similar engines and tests.[28]

1.5.2 Types of Deposit

Carbonaceous deposits are formed from the incomplete combustion of polyaromatic species that are present in fuel.[29] These deposits and carbon aggregates in engines are known as 'sludge' in petrol engines and 'soot' in diesel engines.[30] The exact chemical composition of deposits varies but deposits tend to be mixtures of graphitic carbon and more complex carbon structures (such as aromatic, polyaromatics, and chains) as well as some inorganic features including sodium (as NaOH and Na_2SO_4), calcium, and potassium ions.[31]

Engine deposits can be categorised into 'fuel system', 'intake system', and 'combustion chamber' deposits. Fuel system deposits include those in the fuel injector system (or carburettor).[32]

- Fuel System Deposits

  Fuel system deposits are those that form in the fuel injection system, with specific areas of interest being those on injector needles and tips. Carburettors are also part of the fuel system; however, as carburettors are now rarely used in western automobile engines, they will not be considered here.

  - Injector Deposits

    Injector deposits restrict the fuel flow rate and can cause spray distortion in direct injection engines. These issues are not easy to compensate and can result in reductions to fuel economy and increased emissions.[33] An image of a deposit on the injector tip of a direct injection diesel engine can be seen in Figure 1.3 and images of a used injector needle and tip can be seen in Figures 1.4 and 1.5. From these figures, the presence of deposits on the surfaces can be seen. These injectors were supplied to a previous member of this group by Innospec Inc.

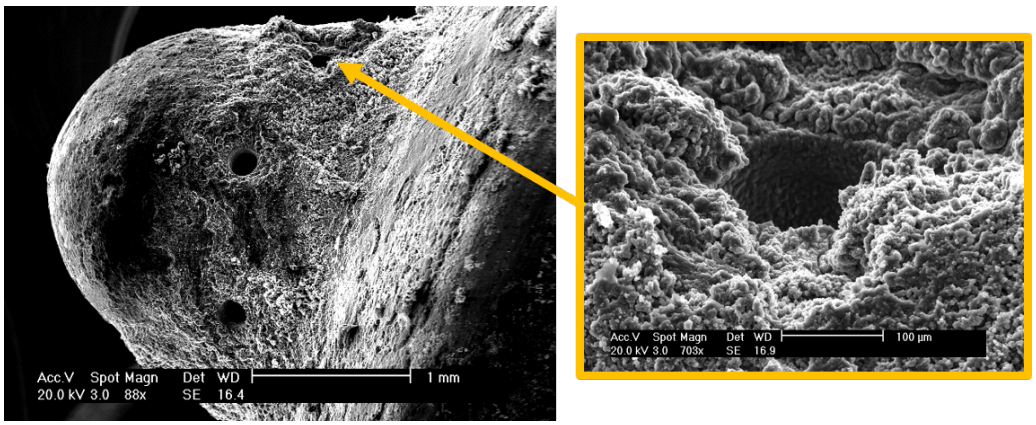


Figure 1.3: SEM image of deposits on an injector tip at 88x and 703x magnification (image modified from Sarah Angel Smith)[34]

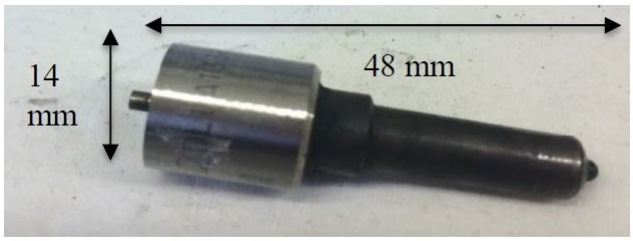


Figure 1.4: Photograph of an injector tip (from Sarah Angel Smith)[34]

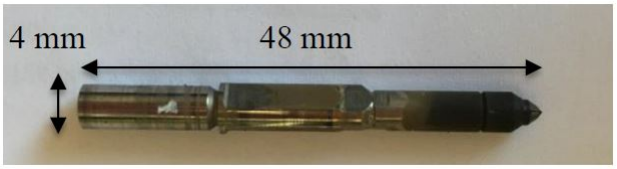


Figure 1.5: Photograph of an injector needle (from Sarah Angel Smith)[34]

- Intake System Deposits

  Deposits form on the surfaces of the intake manifold, the intake port, and the intake valve. In severe cases these deposits can prevent the intake valve from closing, or can cause it to stick open in the cold, leading to engine malfunction and damage.[32] Other deposits in the intake system (manifold) can result in reduced heat transfer to the fuel affecting cold-start driveability, and port deposits which can increase the octane requirement. Deposits that restrict the air flow into the engine can also result in a loss of power (acceleration) and an increase in NO_x emissions (due to the change in air-fuel ratio).

1.5.3 Impacts of Deposits

Deposits can and do form on many surfaces of an engine, having a multitude of effects. The impacts of engine deposits are detrimental to engine performance and can also actively damage the engine. The impacts of engine deposits are summarised below:

- Octane Requirement Increase

  Octane requirement increase (ORI) is the variation of octane requirement with distance/engine operating time. ORI is predominantly caused by combustion chamber deposits with some influence from inlet system deposits (due to chemical and thermal effects).

- Increase in Exhaust Emissions

  Deposits formed on many internal engine surfaces result in an increase in NO_x, CO and hydrocarbon emissions from the engine (unless removed by post combustion processes).

- Changes in Fuel Economy

  An improvement in fuel economy can be seen with the presence of combustion chamber deposits due to reduced heat loss to coolant. However, deposits

in other regions of the engine can reduce fuel economy due to, for example, maintaining the flow rate from fuel injectors.

- Reduced Driveability and Power

  Deposits which affect the air and fuel flow, for example those in fuel injection and air intake system, will have an impact on the engine performance as the air:fuel ratio will be changed and combustion of fuel will be affected.

- Combustion Chamber Deposits

  Combustion chamber deposits (CCDs) result in knock, a characteristic knocking sound that occurs as a result of deposits on the cylinder head contacting with deposits on the piston squish area.[35] CCDs also increase octane requirement. Combustion chamber deposits can vary considerably, as the combustion chamber covers many regions from the piston to the spark plugs. CCDs have been shown to increase hydrocarbon emissions due to the adsorption of hydrocarbons by the deposit preventing combustion and an increase in NO_x emissions resulting from increased cylinder temperature.[28,36] The development of engines also leads to different issues with regards to deposits. For example, the evolution in engine design away from carburettors and over to fuel injection has changed the type of deposits seen.

1.5.4 Fuel Additives

The Additive Technical Committee (ATC) estimates that over 95 % of diesel and gasoline for road use is treated with performance additives.[37] The dosage of additives is typically in low ppm (mg/kg) range and there are many different types of fuel additives, designed to serve many different purposes. Most additives are used in conjunction with others to create multi-functional additive packages, which combat several issues simultaneously. Some common additive types and their effects can be seen in Table 1.1.

Some important benefits of fuel additives include:[37]

- Petroleum conservation

- Biofuel use
- Increased fuel economy
- Reduced emissions
- Improved Health and Safety
- Reduced engine maintenance[38]

Prior to the commercial utilisation of lead compounds in 1923, fuel additives were not used in gasoline engines (diesel ignition improver additives were deployed at a similar time). Since then a vast array of different additives, serving a multitude of purposes, have been developed and employed. Additives can be categorised as refinery products, distribution system products, and automotive performance enhancement products depending on their point of impact. Deposit control additives are an important type of automotive performance enhancement product, and are often included in both gasoline and diesel multi-functional additive packages (alongside a corrosion inhibitor and demulsifier), although the specific composition of these packages will depend on the customers' needs and regional specifications.

As vehicle/engine demands have developed, additives have been important in assisting manufacturers in meeting new requirements. Important demands include:

- Reduced emission of pollutants and GHGs
- Increased power output
- Increased fuel efficiency
- Increased reliability

The development of new fuel injection systems (specifically gasoline direct injection and high pressure common-rail diesel injection) has created further demand for additives due to changes in tolerance and design. Modern injection equipment has smaller orifices which are more susceptible to and less tolerant of deposits.[39] With the increase in demand for alternative fuels and 'greener' engines, the use of biofuels

Point of Impact	Additive Type	Example
Refinery Products	Antioxidants	Aromatic diamines
	Stability Improver Additives	Cyclohexylamine
	Octane Enhancing Additives	Ferrocene
	Cold Flow Improver Additives	Ethyl vinyl acetate
	Dyes	Anthraquinone
	Metal Deactivator Additives	N,N'-disalicylidene-1,2-propanediamine
Distribution System Products	Corrosion Inhibitor	Additives Thiadiazoles
	Anti-Static Additives	Quaternary ammonium Salts
	Pipeline Drag Reducing Additives	Polyacrylamide
Automotive Performance Products	Deposit Control Additives	PIB amine
	Cetane Improvers	2-Ethylhexyl Nitrate
	Lubricity Additives	Oleic Acid
	Friction Modifiers	Glycerol Mono-Oleate
	Anti-Foam Additives	Polydimethylsiloxane
	Corrosion Inhibitors	Dodecenyl Succinic Acid
	Demulsifiers	Phenolic resin alkoxylate

Table 1.1: Some important types of fuel additives[37]

Gasoline/Bioethanol Mixtures	Diesel/FAME mixtures
Increased deposits	Increased deposits
Increased corrosion	Reduced oxidation stability[39]
Increased intake valve sticking	Altered cold flow characteristics[29]
Reduced fuel economy	Increased contamination (of microbes)

Table 1.2: Challenges related to biofuel usage

has increased. This has also resulted in further issues within the engine system. Challenges created through the increased use of biofuels are shown in Table 1.2.

Many of these biofuel-specific issues can be reduced or negated through the use of fuel additives. When any additive or package is released into circulation, it must not, in solving one problem, create more issues when used. This is the principle of 'no harm', and has resulted in stringent testing for additives to prove the absence of adverse effects. Such as tests for intake valve sticking, and for the the deposit forming tendencies of lubricants. In this vein, it is also important that fuel additives are designed to retain efficacy under internal engine conditions.

Some of the key requirements of any fuel additive are as follows:

- High performance at low concentration
- Low cost
- Complete, ashless, combustion in engine with no pollutants produced
- No additional harm caused, or other engine problems created

Ultimately, fuel additives and deposit residues should be completely combusted in the engine, resulting in a negligible change in exhaust gas composition.

1.6 Introduction to Carbon Capture

Carbon Capture and Storage (CCS) is a method of mitigating climate change by restricting the release of carbon dioxide into the atmosphere through capture and storage.[40]

Carbon dioxide can be captured from power stations and large industry, such as cement manufacture, and then pressurised into a supercritical liquid and transported, either through pipelines or on ships, to storage sites (often offshore) to be permanently stored in geological formations.[41] There are several other storage mechanisms, e.g. chemical storage and oceanic storage, but geological storage is currently the most mature and viable.[40] Most potential geological storage sites, in the UK, are offshore in depleted oil beds, but storage in other suitable geological formations (such as saline aquifers) is also possible.[42]

There are several different capture mechanisms for the combustion of fossil fuels: post-combustion capture, where carbon dioxide is separated from flue gases after conventional combustion; pre-combustion capture, where the fuel is chemically separated into hydrogen and carbon dioxide and only the hydrogen burned and oxyfuel-combustion capture, where the fuel is burned only in oxygen so the dry flue gases consist only of carbon dioxide.[40,41] In cement manufacture, only oxyfuel and post-combustion capture are viable as the majority of CO_2 produced is from the calcination of limestone rather than the combustion of hydrocarbon fuel.[43]

1.6.1 Post-Combustion Capture

Post-combustion capture of CO_2 is a promising technology for battling global warming and reducing greenhouse gas (GHG) emissions. For this many technologies have been developed with the most common (commercially) being amine adsorption using a liquid amine.[44,45] However this process has a high energy penalty due to the high-energy regeneration process, and also suffers from foaming issues and corrosion as well as amine loss. One potential solution to some of the issues faced by this technology is that of using solid adsorbents rather than a liquid amine scrubber, as solid adsorbents are more energy efficient, and do not face many of the same issues

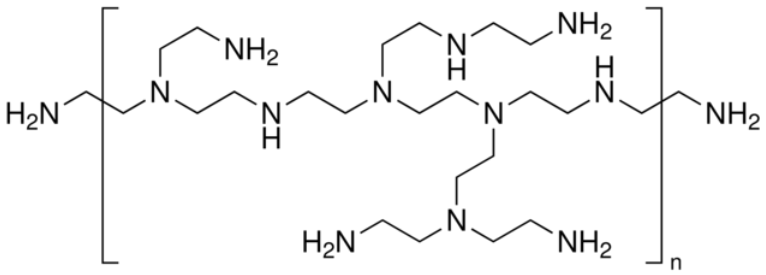


Figure 1.6: Structure of PEI monomer

as the liquids (e.g. corrosion and amine evaporation).[46,47]

1.6.2 Solid Adsorbents

Zeolites, MOFs, alkaline earth metal oxides, and activated carbons are all possible solid adsorbents, but many of these have low CO_2 adsorption, low selectivity, or tolerance to moisture or energy intensive regeneration or adsorption all of which are unideal.[45,47–49]

Another potential CO_2 capture medium are amines (such as PEI) supported on silica. These adsorbents have high CO_2 sorption capacity, selectivity and a relatively low energy demand.[45,50]

There are three common synthesis routes for amine-silicas: impregnation, direct condensation, and grafting. Impregnation results in higher adsorption capacity than the others.[47,51–54]

Different amine-silicas have been investigated for use as carbon capture materials. Amines of interest include tetraethylenepentamine (TEPA), monoethanolamine (MEA), diethanolamine (DEA) etc., however, the most promising amine has been PEI due to its good thermal stability which enables operation at higher temperatures.[46,55]

Branched PEIs have been shown to be a good material for CO_2 capture (when compared to 10 other types of organic amines, branched PEIs were the most suitable) and low molecular weight PEIs have performed better as CO_2 capture materials than those of higher molecular weights, perhaps due to the higher primary amine percentage or higher molecular mobility (although these do have lower thermal stability

than the higher weight PEIs).[56] However, although PEI-silica shows good potential, there are still issues with degradation in the long term.

Chapter 2

Literature Review

2.1 Introduction

Due to few areas of overlap in the literature between automobile deposits and their additives and post-combustion carbon capture materials, this chapter is divided into two sections. The first half of the chapter is in regard to deposits and deposit control and the second half (Section 2.6 onward) to carbon capture.

2.2 Introduction to Deposits in Internal Combustion Engines

In the automobile industry, reduction in engine performance over a vehicles lifetime is a key concern. With carbonaceous deposit build up on engine surfaces being a major factor in engine deterioration, especially in modern engines which are increasingly intolerant to deposits. Additives in fuel packages (specifically premium fuels) are an important way in which users can reduce and control deposit formation and therefore maintain engine performance. This can be especially valuable to vehicle fleets (e.g. taxi fleets) used in businesses, where engine/vehicle lifetime may relate to profitability.

The development of fuel additives is constantly evolving, with new testing methods which reduce cost and improve accuracy being valuable to the industry. The

use of solid state NMR is being considered for the characterisation of specific PIB derivative fuel additives in order to determine performance. Much of the previous research into PIB derivatives as additives has been performed at ambient temperature, a condition which does not represent the operational environment, and previous work by Sam Bailey (In "A Study of Polyisobutylene and it's Derivatives at High Temperature", 2016) as a member of this group in association with Innospec Inc. has focused on Diesel engines and fuels.[57]

2.2.1 Deposit Formation

Deposits are formed through the day to day action of an engine as it operates, however the exact mechanism of formation is not completely clear. Chevalier states that deposits are formed as high molecular mass polyaromatics (gums) adsorb onto internal engine surfaces and are combusted incompletely forming a polymeric varnish which turns into thicker carbonaceous deposits over time and with repeated use.[29]

The morphology of deposits can vary greatly depending on several chemical and environmental factors. One study by Tupa and Koeheler in 1988 found two main types of intake valve deposits in internal combustion engines: a thin varnish or lacquer type of deposit and a thick porous 'sponge-like' deposit which may be oily.[28] Daly also found two distinct morphologies in a study of combustion chamber deposits in 1994.[35] In a 1986 study of multiport fuel injector deposits 2 distinct layers were also seen by Benson through visible inspection with a microscope (a thin varnish and a thick over-layer were seen).[58] It is therefore important that deposit control measures (including additives) can effectively deal with different types of deposit.

The morphology and structure of deposits may also influence the extent of the effects and damage caused. With more porous deposits having a large surface area and interacting differently with fuels and additives than non-porous deposits, potentially adsorbing fuel.[59] The quantity and chemistry of deposits can also influence the impact on the engine with damage increased by higher levels of deposits but also by harder and more polar deposits.[60] In 1986, Tupa and Koehler noted that the rate of injector plugging (in a port fuel injector, PFI) is 'primarily effected by

hydrocarbon composition of the fuel and the presence of DCAs'; they also note that deposits which reduce flow by greater than 10 % result in reduced driveability due to the air:fuel ratio becoming lean.[61] The same authors later found, in a different paper, that multi-port fuel injector (MPFI) are more sensitive to deposit formation than carburettors due to the richer air/fuel ratios to which carburettors are tuned.[28]

The formation of deposits is influenced by the fuel mixture and impurities therein and therefore, as fuels have developed, the deposits formed in engines have also changed. For example, when leaded fuels were common, spark plug fouling due to deposits was considerably more of an issue than in more modern vehicles which use unleaded fuels (however in a study by Tupa and Koehler, no difference in intake valve deposit levels was noted between leaded and unleaded fuels).[28]

The T_{90} (The temperature where 90 % of fuel is vapour) of fuels has been found to be critical to the formation of injector deposits, with higher T_{90}s resulting in lower flow loss due to deposits.[33] The presence of olefins in fuels also results in higher levels of deposits and the presence of sulfur in fuels results in less deposit formation.[33] The impact sulfur has on deposits has been seen through increases in deposit formation with the rise in ultra-low sulfur fuels.

The presence of polar compounds (e.g. oxygenated hydrocarbons) in the fuel mixture has also been shown to form deposits as has the presence of olefins (specifically in MPFI engines).[62] The aromatic content of fuels has not been seen to influence deposit formation, however, and neither does the addition of alcohol into the fuel mixture in small quantities.[61] However, the use of a high ethanol-petrol fuel mixture (E85, 85 % ethanol and 15 % gasoline) has been found to result in higher levels of intake valve deposits than is found using 100 % gasoline fuel.[63] The increase in deposit formation was partially deemed to be due to the presence of sulfates in the ethanol resulting in sulfate salt deposits on the fuel injector valves. The increase in deposits was seen to be controlled by the use of deposit control additives (including a PIB derivative).[63]

In a comparison of soots from diesel and gasoline engines, where the gasoline soot originated from a gasoline turbo direct injection (GTDI) engine, both of the

soots were found to have similar morphologies and sizes (particle sizes in the order of 10 nm) but with somewhat different compositions. The gasoline soot was seen to have more additive elements and other materials than the diesel soot including calcium containing compounds and iron oxides.[60] This study also found more disordered carbonaceous particles in diesel engines, these particles are more reactive, competing more effectively with polar additives for adsorption on the metal surface and increasing deposit formation and wear.[60] Diesel engines also tend to generate more soot than gasoline engine due to less efficient fuel-air mixing and higher levels of incomplete combustion

It is worth noting that the fuel type, the lube oil type, and the presence or absence of fuel additives all seem to influence deposit formation in port fuel injection engines and direct injection engines in the same ways.[36]

2.2.2 Carbon Black

Carbon black is the product of incomplete combustion of hydrocarbons; it is most commonly made commercially from aromatic hydrocarbon oil using the oil furnace method.[24,64,65] It has been used by several different groups and organisations to model and represent engine deposits, soots and sludges.[24] It is a low cost material used commercially for several purposes including printing ink, air and liquid purification and as a filler material.[24]

The composition of carbon black is mostly, as the name would suggest, elemental carbon. It forms 'parallel stacked layers of polyaromatic planes' in colloidal particles.[24] There are many types of carbon black (referred to generically as carbon blacks) with different properties depending on the combustion material used in its creation and the conditions under which it was made, with many of the surface properties (and therefore the chemical behaviours it exhibits) controlled by surface elements and species especially oxygen/oxides.[24,66]

Carbon black is used to model carbonaceous deposits due to similarities in the formation processes for both materials, as deposits are created through the oxidation and incomplete combustion of impurities and other species in the fuel mixture.[24]

The morphology of carbon blacks and soot was seen to be similar in a study on soots from used lubricating oil gathered from diesel exhausts and engines, however the surface chemistry had significant differences.[67] The compositional differences between carbon blacks and deposits stem from the proportion of carbon found in each substance: in carbon black, the carbon content is typically higher than that of soots (97 % vs. approximately 60 %),[68] and none of the polar organic species present in soots are present in carbon blacks. This may influence the potential wear and agglomeration seen when using carbon black to model deposit behaviour.

Despite differences in composition and chemistry, certain carbon blacks may mimic the behaviour, specifically aggregation, of soots and deposits in engines.[67] Clague et al. concluded that carbon blacks with a surface area of approximately 300 m^2g^{-1}, of intermediate primary particle size (10-100 nm) and possessing some surface polarity may be used to mimic the behaviour of soots in oils.[67]

2.3 Deposit Control Additives

As briefly discussed in the previous chapter, the use of deposit control additives are the most common method for removal and prevention of deposits within the fuel injection system and other engine surfaces, alongside control of engine conditions (e.g. temperature). These additives, most commonly dispersants, are known in the industry as detergents.[37] Before deposit control additives were introduced it was necessary to manually remove engine deposits, which necessitated a lengthy engine disassembly process to accomplish.

Deposit control additives are fuel additives which prevent deposit formation on engine walls.[29] They are generally similar for diesel and gasolines engines, although the specific chemistry differs between for additives designed for specific engine types.[37] One key type of DCA are PIB derivatives, which will be introduced in the next section.

DCAs (including PIB derivatives) consist of a polar head and hydrocarbon tail, the polar head interacts with the deposit or the deposit precursor and the hydrocarbon/polymer tail ensures the solubility of the additive. They are commonly

described as detergents, although chemically behave more similarly to dispersants and are not legally considered detergents (in the same way as one might refer to household cleaning agents).[37] The purpose of DCAs is to keep the fuel system clean and prevent deposit formation which, if left unchecked, would ultimately result in damage to the engine and reduced engine performance.

Other fuel additives can also be used to impact deposit formation. Antioxidant additives, for example, can assist with increasing the stability and reducing the oxidation of the fuel, thus reducing deposit formation.[30,37] On the other hand, metal containing detergents, although they also have a dispersant effect, can degrade into insoluble solid salts which add to the sludge problem and therefore render them undesirable for use.[30,69]

All fuel additives must also work at the high engine operating temperature; combust completely in the engine (i.e. be 'ash-less'); be non-toxic; and be economical. Commonly used DCAs are polyisobutylene derivatives, including PIB amines, polyisobutylene succinimide (PIBSI) and polyisobutylene succinic anhydride (PIBSA). Not only do PIB derivatives meet the above criteria, they are also chosen due to the reactivity of PIB with potential head groups thereby facilitating synthesis, as well as their thermal stability, and the solubility of PIB in hydrocarbon fuel. Two other DCA types are polyether amines and Mannich's detergents (some Mannich detergents may also be PIB derivatives), with the Mannich detergents being the more effective.[33] Carburettor detergents were introduced in the 1950s but were initially fairly ineffective at clean-up (deposit removal).[38] Additives for use in carburettor engines work in much the same was as more modern detergent/dispersant additives, although in the past several different types of additives have been used commercially including phosphorus and boron containing compounds.[39]

DCAs work in three ways:

- Preventing the aggregation of particles
- Forming a protective layer on engine surfaces; and
- Dispersing aggregates and deposits

DCAs overcome attractive interactions (such as Van der Waals forces and London interactions) between particles to prevent aggregation, through the adsorption of the additive on to surface of deposit particles. Due to the importance of steric repulsion in this process polymers are chosen as DCA to create a sufficiently thick layer around the particle. DCAs need an affinity for the solid particle as well as for the medium, hence the polar head and polymer tail. Additive effectiveness tends to increase with concentration and some additives have the potential for single or occasional use in large doses to clean-up engines.[27,70]

Unfortunately, one side effect of some potential DCAs, specifically those designed for intake valve deposits and port valve injector deposits, is their propensity to increase levels of combustion chamber deposits, thereby reducing the benefits of the use of these additives. Additives such as these would not pass 'no harm' tests and are therefore not commercially used.[71,72]

2.3.1 Polyisobutylene Derivatives

PIB derivatives are an important group of molecules used as deposit control additives due to PIB reactivity with head groups in synthesis, thermal stability and solubility in fuel. PIB is a polymer hydrocarbon that provides solubility and structure for DCAs when combined with a polar head group. Two of the most common types of PIB derivatives are PIBSA, polyisobutenylsuccinic anhydride, and PIBSI, polyisobutenylsuccinimide. PIBSA is commonly synthesised through reaction of PIB with maleic anhydride and can be converted to PIBSI through condensation with an amine (with at least one primary nitrogen).[26,73]

As there can be many variations of head and tail groups, the terms PIB, PIBSA and PIBSI are all used to represent groups of compounds with similar structures and properties. Commonly PIBSI additives have a molecular weight of 1000-3000 g/mol.[74]

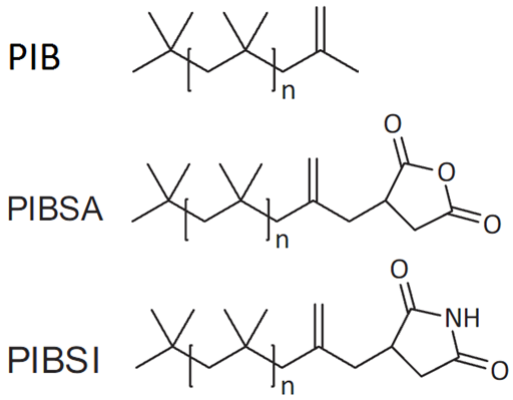


Figure 2.1: Structure of PIB, PIBSA and PIBSI[57]

Synthesis of PIB Derivatives

PIB is synthesised by catatonic vinyl polymerisation using either $AlCl_3$ or BF_3 as a catalyst. The use of BF_3 gives vinylidene end groups while the use of $AlCl_3$ results in more highly substituted end groups (see Figure 2.2).[75]

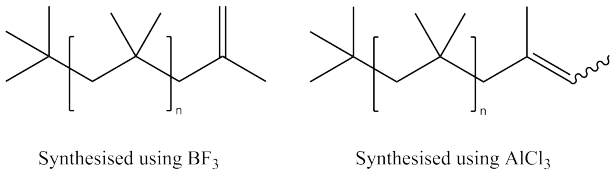


Figure 2.2: Structures of PIBs produced by each catalyst

PIBSA can be synthesised from PIB and maleic acid at high temperatures. The two synthetic routes depend on the PIB used, i.e. whether it has been synthesised by the $AlCl_3$ or the BF_3 process, and are respectively an Alder-ene (Diels-Alder) reaction and an "ENE" process shown in Figures 2.3 and 2.4, respectively.[75]

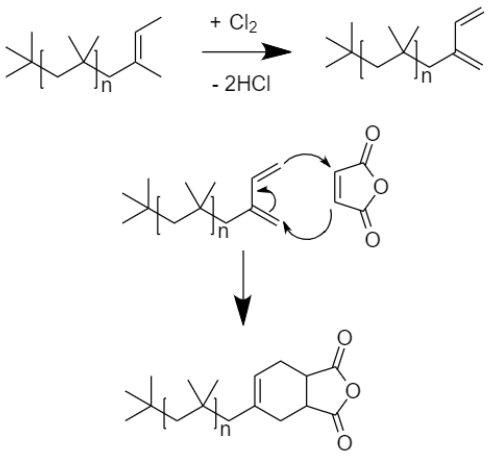


Figure 2.3: Synthesis of PIBSA from highly substituted PIB, Diels-Alder reaction at 140-250 °C

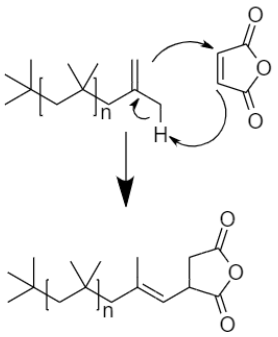


Figure 2.4: Synthesis of PIBSA from PIB with vinylidene end group, "ENE" reaction at 150–250 °C

The PIBSA can then be converted to a mono- or bis- PIBSI through a 1:1 or 1:2 reaction with a polyamine (often ethyleneamines) as shown in Figure 2.5.[75]

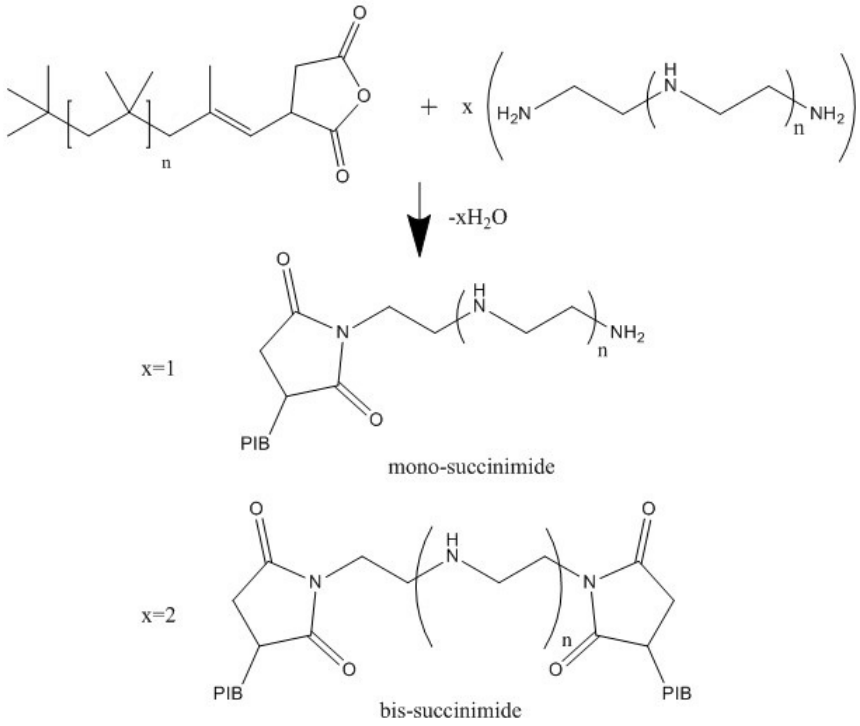


Figure 2.5: Synthesis of mono (x=1) and bis (x=2) PIBSI, 160 °C

Mechanism of Action

The polar (often polyamine) head groups in PIB derivatives allow for the adsorption on to engine surfaces and carbon particles (as well as other acidic surfaces), while the PIB tail allows for solubility in the hydrocarbon medium (i.e. the fuel mixture).[29]

The polar surface area of PIB derivatives and the number of nitrogen containing groups in the head group, specifically primary and tertiary amines, has been shown to increase the affinity of the molecule for adsorption onto surfaces and carbon particles, thereby resulting in increased amounts of adsorbance and increased enthalpy of adsorption.[24] Several studies have reported the occurrence of greater than monolayer coverage (hemi-micelles) from both direct evidence in the form of adsorption isotherms and indirect evidence through enthalpies of adsorption.[76–78]

The stability of particulate dispersions is dependent on the forces of repulsion between particles being greater than those of attraction. When the attractive forces between particles are greater than the repulsive forces, agglomeration occurs and the particles drop out of solution, in this case forming deposits. To control this, polymers additives are introduced to the solution, to adsorb onto the surface of the

particles and increase the repulsive forces between particles.

For submicron sized particles, precipitation from the fuel mixture is not an issue as particles of this size remain in suspension due to Brownian forces and the circulation of the fuel.[30]

There is some disagreement amongst the literature as to which forces play important roles in the dispersion of carbonaceous particles by deposit control additives. In 2001, Cox at al. commented on the disagreement by other groups (Pugh et al., Kornbrekke et al. and Georges et al.)[79–82] on the importance and presence of electrostatic forces in PIBSA/PIBSI-carbon particle interactions, and notes that it would not be expected for monolayer coverage of these polymers to provide enough of steric hindrance to overcome the strong attractive forces and prevent all aggregation/flocculation of particles.[83] Cox then found evidence for multilayer coverage with good steric stabilisation, in support of Kornbrekke and Georges. Tomlinson et al. (2000), also found evidence from adsorption isotherms of PIBSI adsorbing beyond monolayer coverage in multilayer coverage.[30] Kozak et al, however, suggest that sterics are not enough to give stable dispersions and that electrostatics are also needed to prevent aggregation.[24] Kozak suggests that primary and secondary amines groups in the DCA head group may be undergoing proton exchange with acidic sites, resulting in electrostatic repulsion between particles and increased number of primary and secondary amines in the head group increases the electrostatic repulsion.[24] Overall, from the literature, it seems that steric repulsion is the dominant force preventing aggregation in polymer stabilised particles in a hydrocarbon medium. However electrostatic forces as a result of proton transfer may still play a role in some situations.[79,80] This is in contrast to the importance of electrostatic forces in aqueous media.[29]

In low concentrations the isotherm for di-block co-polymers is similar to that of small molecules but as the concentration grows the isotherm curves downwards due to repulsive lateral interactions between the polymer tails hindering adsorption. The initial regime (at low concentration) is termed the mushroom regime and the latter is the brush regime. The brush regime is not to be confused with the plateau

found for molecules at high concentration due to the entirety of the surface being covered by the adsorbing molecule.[29]

As the polymers are extended in the brush regime the adsorbed layer is thicker resulting in greater steric repulsion between molecules. Therefore, it was suggested that to get optimum performance from deposit control additives the concentrations must be high enough to enter brush regime. However, fuel additive concentrations are low, so the low concentration regime may be the more important for studies of DCAs. It was suggested that the lateral repulsions which increase the energy cost of the brush regime could be overcome through the use of comb-like polymers (which have multiple tails) as the conformation is already prepared. The brush regime is also reached more quickly for longer polymers due to them taking up more active sites. Increasing the number of amino groups generally increases the number of sites that can be occupied, and the strength of the adsorption of the macromolecule.[29]

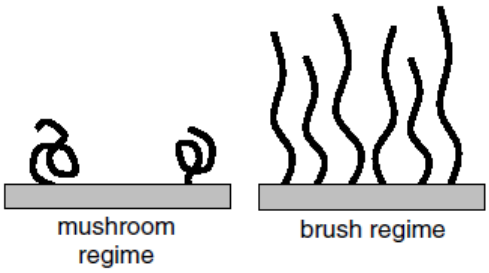


Figure 2.6: Comparison of Mushroom and Brush regimes (image modified from Chevalier et al. (2004))[29]

Regimes similar to the brush and mushroom regimes were also found by Dubois-Clochard in 2001 who saw an increase in strength of adsorption for comb-like polymers (over di-block polymers).[76] They found that comb-like polymers resulted in a denser monolayer which was more stable.

Tomlinson also notes that adsorption occurs within the porous structure of the carbon, and that the length and structure of the hydrocarbon tail has an impact on the ability of the polymer to adsorb on the internal surfaces as well as impacting on the stability of the particles. A long and rigid tail is most favourable for both the adsorption and stability, as it prevents access to inner pores and produces a higher

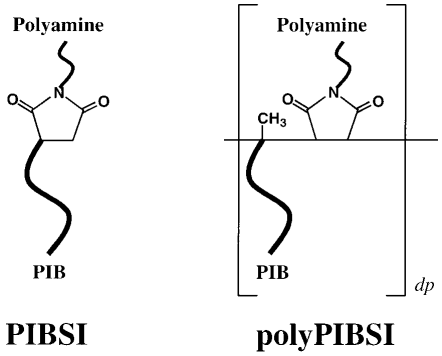


Figure 2.7: Straight chain PIBSI and comb-like polyPIBSI[76]

steric influence.[30]

Studies of detergents designed to reduce deposit formation (in intake valves and port fuel injectors) have been shown to significantly increase the levels of combustion chamber deposits compared the use of gasoline without such detergents.[71,72,84] However, other polymer additives, designed for the purpose, have also been shown to reduce combustion chamber deposits and impact on the microstructure of these deposits, reducing the overall deposit surface area through reducing the number of pores. This is perhaps due to deposit fragments filling the pores.[59]

Examples of PIBSIs as Deposit Control Additives

For this study Innospec Inc. provided a series of PIB derivates. The PIBSI samples provided each contained one of the following headgroups: ethylenediamine (EDA), aminoethylethanolamine (AEEA), and tetraethylenepentamine (TEPA). Due to the proprietary nature of these materials and their function in commercial enterprises, specific information in the literature is limited. The following examples of PIBSIs with these headgroups have been found in the literature and patents.

An Innospec Inc. patent originally filed in 2010 contains examples of mono PIBSIs of M_n 1000 with functionalised AEEA and M_n 750 with TEPA for use in deposit reduction in diesel fuel engines.[85] In addition to this EDA, AEEA, TEPA are mentioned in several patents relating to use as fuel additives in different ways, e.g. friction modifiers.[86]

In a study of different PIBSI dispersants/detergents as a part of an additive pack-

age, PIBSIs with TEPA and EDA headgroups with a 1300 M_n PIB tail were shown to have the best deposit control qualities out of 13 potential additives, although alone they did not have the equal function as a commercial additive in the same package.[87] In 2015, Kim et al., studied a series of PIBSI samples as deposit control additives for aviation fuel (Jet A-1). Of these one of the PIBSIs studied was similar to PIBSI B, in that it had a PIB tail with a M_n of 920 and a TEPA headgroup prepared at a 1.2:1 ratio (mono functionalised). Each of the PIBSIs studied by this group, including the PIBSI B analog, were found to be effective at deposit control.[88] In 2015, a patent filed by Afton Chemical, calls upon an example of a TEPA PIBSI as a deposit control additive, showing power recovery when used for an 8 hour clean up test on a DW10 engine.[89] A similar finding is also reported by Bubalik et al. in 2009, using the same type of test engine.[90] In a patent filed in 1994, TEPA is stated as a preferable headgroup for deposit control PIBSIs, compared to EDA and several other amine headgroups.[91]

Although limited, the amount of information in literature suggests there may be slightly more interest in the TEPA PIBSIs than the other PIBSIs available for this study. However there is no specific information in the available literature of the efficacy of bis functionalised PIBSIs, although the conditions for bis functionality are within the scope of several different patents.[85,91,92]

2.4 Analytical Methods

In this section, analytical methods used in the literature to investigate relevant carbonaceous materials and polymers will be discussed. NMR will be the focus of this part of this study as there is an interest in developing this technique for use with PIB derivatives.

2.4.1 Nuclear Magnetic Resonance Studies of Carbonaceous Materials

Engine Deposits

Solution state ^{13}C NMR has been used to study the composition of engine deposits.[35] In 1994, Takei et al. studied the composition of combustion chamber deposits from gasoline engines under the influence of different deposit control additives.[71] These studies showed that combustion chamber deposits are influenced by additives designed for elsewhere in the engine, and the presence of these additives was seen in the NMR spectra of the CCDs. High resolution solid state ^{13}C NMR (with magic angle spinning, MAS, and cross polarisation, CP) has been used to study various engine deposits, especially combustion chamber deposits. It can also be used to determine the levels of aromaticity within the deposits.[72,93] Additionally, proton inverse recovery has also been used to look at CCDs in a gasoline DI engine.[94]

Low resolution studies have been performed as information on T_2 relaxation time can be related to the mobility and information on the proportions of aliphatic and aromatic carbons can still be gleaned from broad peaks. More in depth measurement, for example on T_1 (spin-lattice) relaxation times requires higher resolution studies (for example using MAS and proton decoupling) as T_2 is significantly smaller than T_1.[94] When considering solid state NMR in reference to polymer dispersions (as is the case with fuel additives), it is important to look at the mobility of the polymer, as this provides information on the relative amounts of adsorbed versus free polymer.

In 1999, Clague et al. used solid state ^{13}C NMR (MAS, proton decoupling) to examine soots from diesel engines (lubricant), which had different polymeric additives.[67] They observed that the additive structure was visible in the spectra of the soots (with a PIB additive showing peaks at 60, 39 and 32 ppm additional to aliphatic peaks), and that a non-additised carbon black sample showed no signal under the same conditions. This suggests that the spectra from the soots are due to the additives and other surface species. This inference was further supported after

solvent extraction significantly reduced the signal, also suggesting the additives bind physically instead of chemically. The species extracted were also studied by solution state ^{13}C NMR to provide more information about their chemical makeup.

Other Carbons

Solid state ^{1}H NMR has been widely used to study the relaxation times of coals. In 1984, Ripmeester et al. conducted T_1 measurements on bituminous coals over an 80-500 K range using a $90° - \tau - 90°$ pulse sequence and in 2004 Steel et al. looked at coal coking pressure, specifically focusing on T_2 relaxation time (T_2 is proportional to $\Delta H_{1/2}$) as a measure of fluidity (^{1}H mobility).[13,95]

2.4.2 Nuclear Magnetic Resonance Studies of Polymers

PIB Derivatives

The use of ^{1}H NMR (by Pirouz) to characterise PIBSI derivatives has been attempted, although hydrogen bonding within PIBSI (between succinimide and secondary amine groups) has been shown to complicate and distort the spectra resulting in difficulty in quantitative analysis.[69]

Other Polymers

Solid state NMR has been widely used to study relaxation times in polymers for a variety of purposes.

- In 2001, Separovic et al. used T_1 relaxation times to study changes in dynamics as a result of weather on polymer coatings (both ^{13}C and ^{1}H)[96]
- Lee et al., 2007, studied the structure and local proton mobility of poly(vinyl phosphoric acid). The proton mobility was determined through line width measurements (T_1).[97]
- Lam et al., 2001, studied proton mobility in proteins (T_1, $T_1\rho$) using ^{1}H-^{13}C cross polarisation magic angle spinning (CP MAS) ^{13}C NMR.[98]

- T_1 and T_2 measured for gels undergoing phase transitions, showing a decrease in both during the transition. T_1 was measured by inversion recovery and T_2 by Carr, Purcell, Meiboom, Gill (CPMG).[99]

- Molecular motion measured using T_1 for PVC and poly(ether-ester).[100]

- Solid state ^{13}C NMR has been used to study the mobility of polysaccharides. Single pulse excitation (SPE) can be utilised to find information about very mobile molecules (with very short relaxations) where other methods (e.g. CP MAS) may not be appropriate.[101]

T_1 times of PIB derivatives (and other polymers) have also been used to study conductivity.[102]

Previous Work

Previous work at the University of Nottingham conducted by Sam Bailey in association with Innospec Inc., using low resolution solid state proton NMR, determined the general principles upon which this work is founded. This work studied PIBSAs and PIBSIs adsorbed onto carbon black and found there to be two categories/groups of PIB derivatives: those with low polar surface areas and weak interactions with carbon black (Group 1); and those with high polar surface areas and stronger interactions (Group 2).[57] This study compared the peak half width ($\Delta H_{1/2}$) of polymer carbon black dispersions, whilst varying the concentrations and temperature. The study also employed rheology which will be discussed in Section 2.4.5.

The Group 1 polymers showed more consistent $\Delta H_{1/2}$ (with temperature) due to the higher mobility of the polymer, whilst, the Group 2 polymers exhibited a greater increase in $\Delta H_{1/2}$ with decreasing polymer concentration as less of the polymer was free in solution. There was a weak to medium correlation of increase in polar surface area to increase in $\Delta H_{1/2}$ at 250 °C which suggests that polar surface area is the most dominant influence on the strength of interactions as opposed to length of polymer chain.

Other details of note:

- Carbon blacks with fewer oxygen atoms and those with the highest proportion of surface carbon give the lowest mobility results
- More ordered (rather than amorphous) carbons are better distinguished by ^{1}H NMR
- The carbon black studied which showed the strongest interactions with the PIB derivatives was microCB, a mesoporous carbon sourced from Sigma-Aldrich

2.4.3 Engine Tests

A DISI injector fouling test was developed by China and Rivere in 2003 to measure the effectiveness of additives in reducing injector fouling and was designed to replicate similar conditions to those of normal operation. This test did not show changes in fouling associated with exhaust gas recirculation, air intake temperature, or blow by; however, higher cooling fluid temperature and fuel temperature have both been seen to increase injector fouling.[103]

In 2011 Ramadhas et al. used the CEC F-20-A-98 test for intake valve cleanliness to determine the impact of multifunctional gasoline additives on deposit formation and used a "weigh and scrape" method to determine CCD formation.[84]

Using the CECs DW10C engine test, Barker et al., 2014, found that low molecular weight PIBSI's were unsuitable as DCAs as they resulted in increased injector sticking following previous work, using the XUD9 test which found that they increased flow loss.[26,104] This work highlights the importance of maintaining quality in fuel additives.

2.4.4 Adsorption Measurements

Many previous studies of the interactions between PIB derivatives and surfaces have considered three key factors in determining the efficacy of the polymer. These are the amount of polymer adsorbed onto the surface; the strength of this adsorption; and the stability of the dispersion.[24] The first of these factors can be determined using adsorption isotherms.

Adsorption is commonly studied by using UV-Vis spectroscopy to determine the concentration of surfactant left free in a solution of surfactant and carbon black at equilibrium. Desorption can then be found by removing the remaining surfactant and replacing with solvent, redispersing the particles and tumbling. The adsorption and desorption can then be displayed as an isotherm (graph) comparing adsorption to concentration of surfactant used in the initial solution.

The comparison of adsorption isotherms, with variation of a secondary variable can give information on how the adsorption is influenced by other factors, for example temperature, or type of surfactant used. Dubois-Clochard et al. determined the adsorption through titration with an acidic indication before and after adsorption.[76] This was followed with UV-Vis spectroscopy. Pirouz et al., in 2015, used a pH indicator to determine the adsorption (through concentration of secondary amines).[69]

Kozak et al., in 2009, found, from adsorption isotherms, that increasing the number of tertiary amine groups in the head group of PIBSA (from 0 to 4) increases the maximum adsorbed amount (Γ_{max}) of surfactant. Similar results were also found by the same group for PIBSA adsorption of stainless steel using ellipsometry.[24] Their results also suggest a less than monolayer coverage, through from comparison of A_{exp} (from Γ_{max} to A_{theor}) values, and that adsorption of polymer on the surface is also strong and effectively irreversible. Enthalpy results from the same study also supported that the coverage was less than monolayer.

To determine the strength of adsorption, calorimetry has been utilised to determine the enthalpy of adsorption and desorption (through measurement of heat changes associated with the processes).[24]

Chevalier et al. found that the efficacy of linear polyaromatics as DCAs in diesel fuels followed the strength of the polymers adsorption on carbon black when used as a model of carbon deposits on cylinder walls and injector orifice.[29] However, with gasoline, the trend is not as simple; significant departures from the trend of carbon black occur as problems are the result of varnishes on admission valves (valve sticking).

Stability of the dispersion can be measured by light transmission measurements (on sonicated dispersions), flocculation tests and kinetic aggregation using time-resolved light scattering.[24,29]

2.4.5 Rheology

In previous work by this group, PIB derivative- Carbon black mixes were studied in a temperature dependent rheological study.[57] Viscosity (η^*) was used as a measure of the strength of interaction between polymer and carbon black, with an increase in viscosity showing a stronger interaction (η^* was also seen to increase with increasing carbon black content). The study compared a series of different PIB derivatives, finding that PIBSI interacted more strongly with carbon black than unaltered PIB and was able to distinguish between even very chemically similar PIBSIs.

In 2007, Yang performed a temperature dependent rheological study of carbon nanotubes stabilised by PIBSI, which found an increase in viscosity due to flocculation at temperatures of 75 °C, but noted no significant adsorption change associated with this viscosity change. The flocculation was deemed to be partially due to a reduction in PIBSI chain length at high temperature (with a secondary effect of nanotube-PIBSI networks forming) resulting in less steric hindrance to agglomeration of particles.[105]

Rheological testing by Won et al. (2005) showed an increase in attraction between PIBSI stabilised carbon black particles with temperature, which, when combined with adsorption isotherms suggesting little temperature dependence of amount or strength of adsorption, indicates that deformation of PIBSI chains at high temperature may decrease its efficiency as a fuel additive.[106] The temperature at which the effect is seen is only 65 °C (for the polyamine PIBSI studied) which is below engine operating temperatures.

In 2014, Yasin et al. also employed rheology to investigate carbon black-polymer dispersions finding that viscosity was decreased at optimum dispersant concentration. This is a result of excess free polymer increasing the viscosity of the solution and low polymer concentrations resulting in aggregation.[107]

2.4.6 Other Studies of Interactions Between Carbon Black and Polymers

In a 2014 study by Yasin et al., atomic force microscopy (AFM) was utilised to determine the strength of interactions between carbon black particles in the presence of polymeric dispersants.[107] By positioning carbon black on both sides of AFM in solution and measuring the resistance (and therefore attraction) as the carbon blacks are separated, strengths of attraction and repulsion can be compared between carbon blacks in different solutions. The study found the solution containing PIBSI resulted in repulsive forces between the carbon black particles in reduced attractive forces between carbon black particles compared to attractive forces seen in solutions without dispersant. The PIBSI derivative used had a block copolymer head. In previous work by the same author conductivity was used to determine interaction forces between polymers (including PIBSI) and carbon black.[108] Small-angle neutron scattering has also been used to study the structure of and measure the thickness of the adsorbed layer.[109]

2.4.7 Studies of Carbon Black and Deposits

Several different techniques have been used to study both engine deposits and carbon blacks used as deposit models. The more common characterisation methods include:

- Microscopy (TEM, SEM, STM) to study the structure of deposits[36,58,60,67]
- Elemental analysis (AES, XPS)[37,39,62]
- Raman spectroscopy to determine levels of amorphous and graphitic carbons[36,60]
- TGA and IR studies of composition/morphology[35,36,58,67]
- Gas adsorption studies of surface area[24,36]
- Weight of deposit formed (weigh and scrape)[84]

Alongside the above, many other methods have been used in studies of deposits.

Specially designed laboratory methods have also been used; for example, a laboratory test involving heating of a pressurised injector and rail assembly was used to study deposit formation, and showed that deposit formation is not dependant on combustion products.[58]

Some studies have focused on specific features of the deposits, for instance in 2015 Lau et al. used thermodesorption resonant enhanced multiphoton ionization combined with time of flight mass spectrometry (REMPI ToF MS) to measure the presence of aromatics in injector deposits in common rail injector diesel engines. The study considered the injection temperature, pressure, fuel amounts, and fuel composition, finding that the addition of PIBSI to a diesel fuel reduced the amount of aromatics seen. They also saw that increasing temperature increased the amounts of aromatics in the deposits.[110] Hydropyrolysis has also been used to characterise carbonaceous materials including fuel injector deposits (diesel engines).[31]

2.5 Deposit Control Summary

- Deposits forming on internal engine surfaces lead to a myriad of efficiency losses and engine operation complaints
- Deposits vary depending on engine and fuel type, however can be experimentally modelled using carbon black
- Deposit control additives are commonly used to combat and prevent deposits. They are dispersants, with a polar head and polymer tail. One type of DCA is PIB derivatives, specifically PIBSI.
- The polar succinimide head group of PIBSI interacts with deposit particles and internal engine surfaces, while the hydrocarbon tail is soluble in fuels. Head groups with a greater number of amines interact more strongly.
- NMR has been used to study carbonaceous materials and polymers including PIB derivatives. However it is only in preliminary work that it has been used

to investigate the interactions between carbon black and PIB derivatives.

- Traditional methods for testing potential deposit control additives are expensive and lengthy, whereas NMR is rapid and cheap

2.6 Introduction to Carbon Capture

Carbon capture technologies enable the burning of conventional fuels (including fossil fuels and biomass) without the release of the greenhouse gas CO_2 into the atmosphere. This is accomplished through the separation of carbon (in the form of CO_2) from the fuel at some stage in the combustion process; this CO_2 is then sequestered, stored, or utilised.

2.7 Carbon Capture Technologies

There are three main types of carbon capture: pre-combustion capture, post-combustion capture, and oxy-fuel capture.[111] Each of these will be discussed in more detail in this section and a basic schematic can be seen in Figure 2.8.

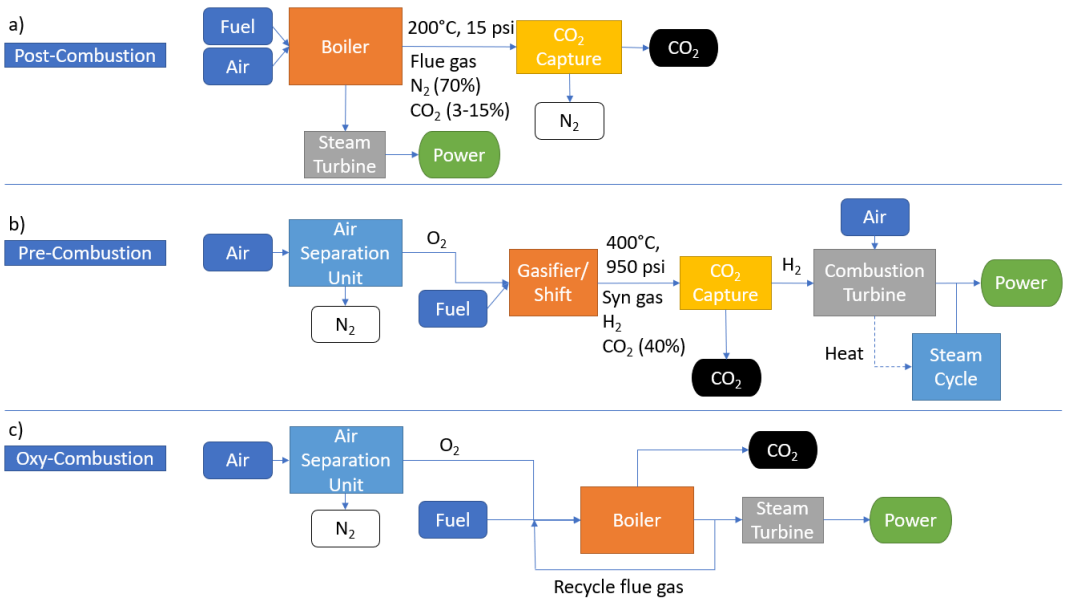


Figure 2.8: A diagram showing three types of CCS technology: post-combustion, pre-combustion and oxy-fuel capture (based off of Figeroa et al. (2008))[112]

In addition to these methods, a newer method, chemical looping combustion (CLC), is also being investigated as a carbon capture method.[113–117] This method is similar to Oxy-fuel combustion in that oxygen is separated from air before combustion.

2.7.1 Pre-Combustion Capture

Pre-combustion carbon capture removes CO_2 from fuel prior to combustion by converting the fuel into hydrogen and CO_2 (see Figure 2.8 b). This occurs through the reaction of the fuel with oxygen, air or steam, resulting in syngas. Syngas is a mixture of mostly CO and H_2, the CO is then converted to CO_2 by reacting with steam, producing further H_2. The CO_2 is then captured and the H_2 used as fuel.[41]

The two main routes to create syngas are steam reforming and partial oxidation for liquid and gas fuels, and gasification for solid fuels. Steam reforming uses steam according to Equation 2.1,[118]

$$C_xH_y + xH_2O \Longleftrightarrow xCO + (x + \frac{y}{2})H_2 \tag{2.1}$$

and partial oxidation and gasification use oxygen, per Equation 2.2; this can be done with or without a catalyst.

$$C_xH_y + \frac{x}{2}O_2 \Longleftrightarrow xCO + \frac{y}{2}H_2 \tag{2.2}$$

It is also possible to use both steam and oxygen, called auto-thermal reforming, in which the endo- and exothermic reactions (steam reforming and partial oxidation respectively) balance.[118] The conversion of CO to CO_2 in the syngas occurs through a water-gas shift, as shown in Equation 2.3.[118]

$$CO + H_2O \Longleftrightarrow CO_2 + H_2 \tag{2.3}$$

The CO_2 can then be captured for storage. There are additional purification steps for the gas produced from oil and coal fuels in order to remove ash and other impurities. The CO_2/H_2 separation generally involves a liquid solvent which adsorbs the CO_2 either chemically or physically. Some processes include both physical and chemical sorbents. A common chemical sorbent is methyl-di-ethanolamine (MDEA). Pre-combustion capture has a lower energy penalty and water usage than post-combustion capture, however is not suitable for retrofitting onto conventional power plants and comes at a higher capital cost, the cost of pre-combustion is comparative

with the expected costs of oxy-fuel combustion.[111]

2.7.2 Post-Combustion Capture

Post-combustion capture is the separation and capture of CO_2 from flue gases that exist as a result of fossil fuel combustion in air (see Figure 2.8 a). These flue gases consist of N_2, CO_2, water and O_2 as well as impurities such as SO_x NO_x and ash. The majority of impurities are removed using technologies such as FGD and SCR as standard. The separation of CO_2 could potentially be done in several ways: including absorption, where CO_2 is dissolved in a bulk material; adsorption, including both physisorption, where the CO_2 is adsorbed onto a surface using only van der waals forces and chemisorption, which involves the chemical reaction of CO_2 with a binding site or chemical substance; and through the use of membranes. The most common of these is absorption, a technique which is widely used in other industries.

One of the main benefits of post-combustion capture over other capture technologies is the potential to retrofit existing powerplants with this technology, however this is at a cost of a loss of 30 % power.[111]

Absorption

There are several potential absorption based capture technologies for post-combustion capture with the majority relying on aqueous amines in an absorber-stripper configuration (as in Figure 2.9). This method often uses a temperature swing or pressure swing system.

In a typical temperature swing absorber-stripper system, flue gases pass through the desulphurisation unit (if necessary e.g. for solid fuel flue gases) and then into the absorber column, where they mix with the solvent at temperatures of 40-60 °C and the CO_2 is chemically adsorbed by the solvent. The remaining flue gases (N_2 and H_2O) exit the absorber and pass through a clean-up system before release into the atmosphere. The solvent is then pumped from the bottom of the column through the heat exchanger and into the desorber/stripper column. Heat (100-140 °C) is

applied to this column and the solvent is regenerated through the desorption of CO_2. The CO_2 produced passes through a condenser, removing any moisture, and is then depressurised before being transported, used, or stored. The solvent is then pumped back into the absorber through the heat exchanger, and the cycle begins again.

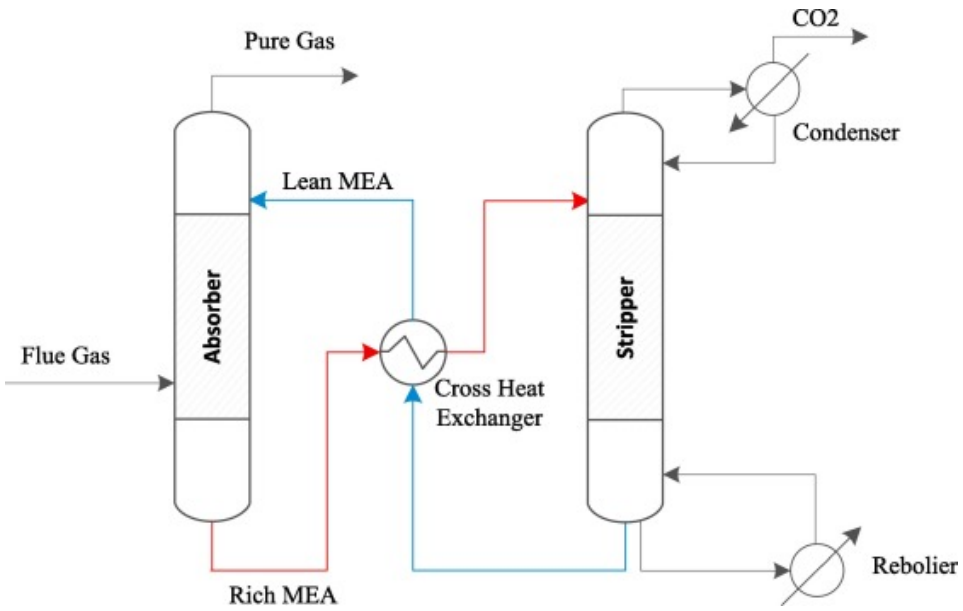


Figure 2.9: Schematic of a typical absorber-stripper for a liquid amine (MEA in this case) post-combustion capture plant (from Wei et al. (2019))[119]

One of the most commercially viable technologies over the past 30 years is aqueous monoethanolamine (MEA).[120] Some other technologies include KS-1 solvent (used in the MHI KM-CDR process) which claims to have lower energy requirements for CO_2 adsorption and desorption; ACAP (Alstom's Chilled Ammonia Process) which uses the ammonia to capture CO_2, and is resistant to degredation under both high temperature and SO_x/NO_x exposure; and Cansolv Absorbent DC 101, a diamine which can be utilised in combination with Cansolvs SO_2 stripper Cansolv Absorbent DS.[120]

Adsorption

Where *ab*sorption refers to the uptake of CO_2 *into* the liquid absorbent, *ad*sorption is the uptake of CO_2 *onto* the surface of the adsorbent (a solid). This can occur

in two ways: chemisorption, where the adsorbate (in this case CO_2) is chemically bound to surface sites; and physisorption, where the adsorbate is held on the surface with Van der Waals forces. Chemisorption tends to be higher efficiency, so is more commonly used for carbon capture than physisorption. It is also possible for the adsorption mechanism to be a combination of chemi- and physisorption.

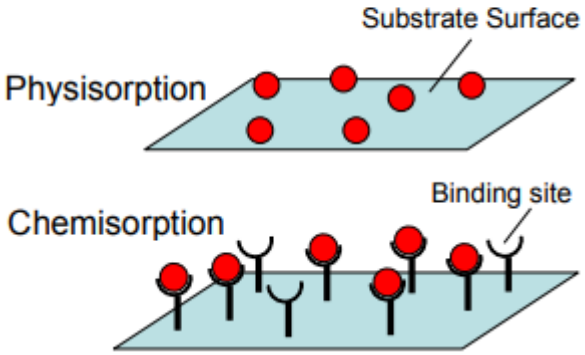


Figure 2.10: Diagram comparing the two types of adsorption: Physisorption and Chemisorption (Global CCS)[120]

One of the commonly cited disadvantages, of using a liquid (often aqueous) solvent, is that the regneration of the solvents is highly energy intensive.[121] The heat requirement of solid sorbents is lower than that of liquid sorbents, which means that in theory solid sorbents should be more energy efficient in temperature swing methods, although this logic does not consider the many other impacts of solid vs liquid sorbents.[122] Solid sorbents also benefit from lower levels of corrosion,[123] but still face several issues in their use in large scale processes, for example amine leaching from silica supports.[124]

Currently there are several types of adsorbent undergoing research at institutions around the globe; some common interests are metal organic frameworks (MOFs), zeolites and carbonaceous materials (e.g. activated carbons).[120,123,125] These materials may also be functionalised with other materials (e.g. impregnating with nitrogen containing compounds) to aid in carbon capture.[126] In this research, silica impregnated with polyethylene imine (PEI) has been the sorbent of choice.

Supported amine adsorbent materials can be categorised into three classes (1, 2 and 3). This grouping is related to the preparation method and interaction type of the adsorbent. Class 1 refers to amines impregnated into pores, with non-covalent interactions between the amine and the support. Class 2 materials consist of molecular amines bound covalently to the support surface and class 3 materials are amines which are polymerised in situ such that both covalent and non-covalent bonds tie the polymer to the surface.[127] Of these categories PEI-Silica is a prime example of Class 1.

Membranes

Membranes can be used to separate CO_2 from flue gases (see Figure 2.11, however it can difficult due to the similar molecular sizes of CO_2 and N_2. If CO_2 has a higher permeability than the rest of the flue gases and there is a pressure gradient across the membrane then the CO_2 will selectively permeate through the membrane, separating it from the flue gas. To achieve this, the membrane can be altered chemically to increase its selectivity and increase the flue gas pressure and/or apply a vacuum on the other side of the membrane.[120]

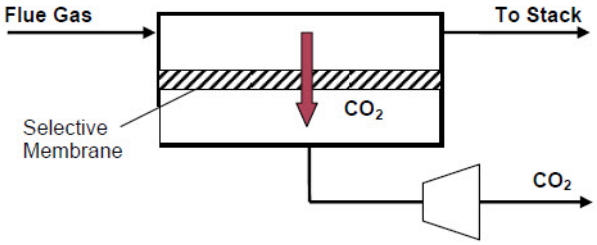


Figure 2.11: Basic schematic of a CCS membrane (from Global CCS)[120]

Some examples of membranes that may be used for post-combustion carbon capture are: polymeric solution-diffusion membranes, porous inorganic membranes (e.g. silica and zeolite membranes) and MOFs.[128] Membranes can also be used in pre-combustion capture and oxyfuel capture. Membranes that are selective for CO_2 or H_2 can be used to separate the gases after or during the shift process in pre-combustion capture, whereas membranes that are O_2 selective can be used for air separation in both pre-combustion and oxyfuel processes.[126]

2.7.3 Oxy-Fuel and Chemical Looping Combustion

Oxy-Fuel Combustion

In oxy-fuel combustion, N_2 is removed from the air before combustion (see Figure 2.8 c). This results in a flue gas consisting of approximately 90 % CO_2 which, depending on regulation, may be stored without purification.[129] Oxy-fuel plants consist of an air separation unit (APU), which separates oxygen from the air prior to combustion, followed by a combustion system similar to that found in a standard air-fired plant, and a CO_2 purification unit (CPU) for drying and compressing the flue gases (this may also include higher levels of purification).[129] The flue gases may also be recycled in order to manage temperature, thereby increasing efficiency. If further purification is required, this can be achieved through decreasing the temperature to selectively condense out the CO_2. If using partial condensation to purify the CO_2, up to 10 % of the CO_2 will likely be lost unless additional processes such as absorption and membrane separation are utilised.[129] Oxy-fuel capture also has the potential for utilisation in cement manufacture.[43]

Oxy-fuel combustion plants cannot be retrofitted to existing power stations and use a considerable amount of land, thus require the higher capital investment when compared to pre- and post- combustion capture. The energy loss from Oxy-fuel is 25 % of that of traditional power generation, and it is expected that the cost of CO_2 capture would be comparable to both pre- and post-combustion capture. The primary benefit of this method is the potential for ultra-low levels of other pollutants emissions at little (or no) extra cost.[130]

Chemical Looping Combustion

Similar to oxy-fuel combustion, chemical looping separates oxygen from the air gas mixture before combustion of the fuel creating a flue gas stream of CO_2 and H_2O. For this process either a solid or gaseous fuel can be used, generally coal and natural gas.

This process uses an oxygen carrier, usually a transition metal, which is oxidised in air and then reacted with the fuel, reducing it back to its non-oxidised form.[113,114]

This takes place in two reactors an oxidising reactor and reducing reactor, which are usually fluidised beds. Some metals potentially used by this process include iron, copper, nickel and combined oxides.[113,115] Using Me to represent the oxygen carrier the basic reaction schematics can be seen in Equations 2.4 (oxidisation) and 2.5 (reduction).[113]

$$2Me + O_2 \rightarrow 2MeO \tag{2.4}$$

$$\begin{aligned} 2MeO + C &\rightarrow 2Me + CO_2 \\ MeO + H_2 &\rightarrow Me + H_2O \end{aligned} \tag{2.5}$$

As the oxidisation reaction is exothermic and the reduction is endothermic, generally occurring at temperatures of 600-900 °C and 700-1000 °C respectively, heat transfer can be used to minimise energy penalty.[113] In addition, the gas stream produced by CLC is simply CO_2 and water the purification process only consists of condensing out the moisture to produce and almost pure CO_2 stream, further reducing energy cost compared to other methods. There is little NO_x impurity due to the lack of N_2 in the combustion reactor. The reduced energy penalty results in lower cost operation, and as the CO_2 capture is potentially 100 % from this method CLC is economically competitive with the other methods discussed.[114]

Like oxy-fuel and pre-combustion capture this method presents barriers with respects to retrofitting to existing power stations as the key features of the process occurs before combustion, however it has been shown to be possible to retrofit to existing pulverised coal power plants.[116] Some potential issues that this technology faces include the difficulties associated with carrier stability and lifetime, especially with solid fuels where ash removal also removes the carrier.[117]

2.8 Amine Based Carbon Capture Materials

Amines have been widely used for post-combustion carbon capture with the most widely used being MEA (see Figure 2.12). MEA is utilised as an aqueous solution

in an absorber-stripper system, and it loosely bonds to CO_2 through the amine centre forming a carbamate species; this is typical for amine-based carbon capture materials. Other amines used for carbon capture include: piperazine, mixtures of piperazine and 2-aminomethylpropanol or 2-methylpiperazine, and methyl diethanolamine.[131] As an alternative to aqueous solutions, amines may be adsorbed onto inert substrates such as silica. A promising amine-silica in this regard, is PEI-silica.

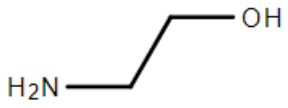


Figure 2.12: Structure of monoethanolamine

2.8.1 Polyethylene Imine

PEI is a polymer used commercially in various industries. It is used in detergents, adhesives, cosmetics, to name but three amongst many other applications.[132] PEI can also be used to capture and release CO_2.

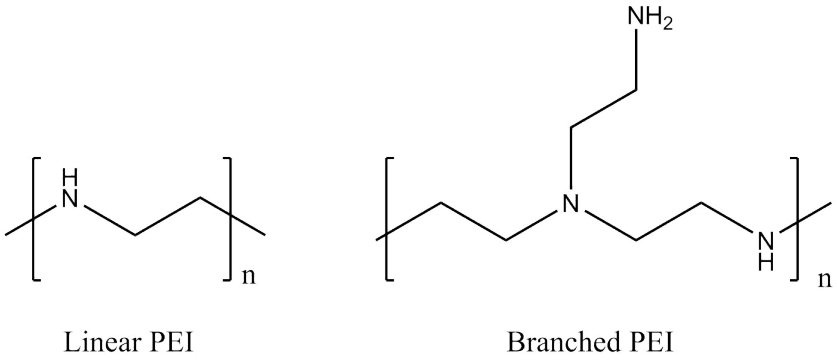


Figure 2.13: Linear and Branched PEI

PEI can be linear or branched as shown in Figure 2.13, with the linear polymer consisting of secondary amines while the branched polymer contains primary, secondary and tertiary amine groups. PEI can adsorb CO_2 through a chemical reaction (chemisorption) between the amine centres of the PEI and the carbon in CO_2 (as seen in Figure 2.14). The mechanism for the adsorption is debated with formation

via a zwitterion intermediate being the likely mechanism over a single step reaction.[133] Primary and secondary amines are able to react with CO_2 in dry conditions, where tertiary amines require the presence of H_2O.[132] PEI is most commonly used for carbon capture when immobilised on a solid substrate, where it has shown to have higher CO_2 capacity than in its pure form,[134] although PEI may also be added to membranes for membrane separation.

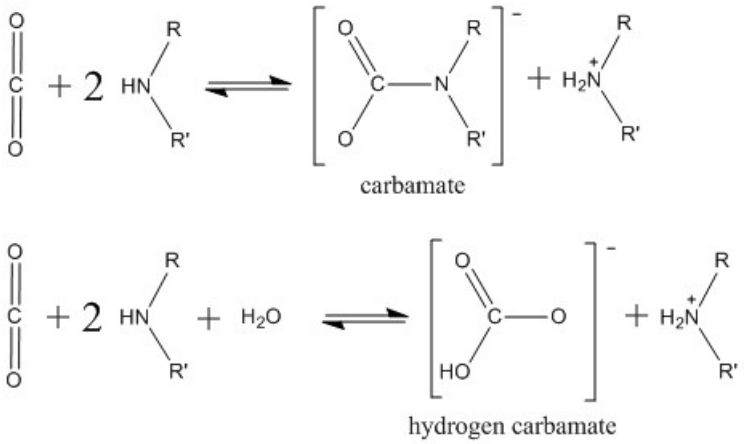


Figure 2.14: The chemisorption of CO_2 by PEI

Regenerable CO_2 adsorption by PEI immobilised on a solid substrate was first reported by Tsuda and Fujiwara in 1992, where the PEI was adsorbed on to a silica gel.[135] Since then there has been extensive work on immobilised PEI for carbon capture purposes, including HSC+, a PEI immobilised on a polymethyl methacrylate support, which has been used by NASA to remove CO_2 on the space shuttle.[136] Other potential substrates include zeolites and various types of nanotubes (e.g. carbon, TiO_2).[132]

PEI is used as the carbon capture amine, in these cases, for a variety of reasons. PEI is fairly inexpensive, it is easy to synthesise and, importantly, has a high thermal stability in comparison to other potential amine choices such as MEA.[132] The thermal stability of a carbon capture material is important due to the high temperatures of flue gases. The adsorber-desorber system for PEI-silica is similar to a typical solution state absorber-stripper, but as the adsorber is a solid, the system uses a solid transport system and bubbling fluidised bed reactors. PEI silica was also seen by Chen et al. to be more resistant to leaching in a comparison of PEI-silica

to TEPA-silica.[137]

PEI-silica has also been investigated for capturing CO_2 from ambient air (5 % CO_2) in a similar style reactor (with a circulating fluidised bed adsorber and bubbling fluidised bed desorber).[138] With uptakes of 7.3 w% for fresh PEI-silica and 5.2 wt% for PEI-silica that had previously undergone 20 adsorption and regeneration cycles under flue gas conditions (15 % CO_2).

In previous work in this group and in collaboration with KIER, Nadine Abu-El-Haija and Zaid Alhulaybi investigated the effects of loading and PEI molecular weight (using two silica samples) on carbon capture performance, measured by CO_2 uptake and adsorption kinetics using TGA. These investigations found the optimum loading of PEI on silica was dependent on the silica surface area and pore size, with the lower surface area (and smaller pore size) silica resulting in a higher CO_2 capacity. A general trend of decreasing absorption capacity with molecular weight was also seen.[139,140] This work determined that the optimum PEI loading (for CO_2 adsorption and desorption) of a series of PEIs (M_ws of 800-750000) on silica with a pore size of 24 nm (surface area of 266 m^2 g^{-1} and pore volume of 1.5 mL g^{-1}) to be approximately 40 % with a CO_2 capacity of 10.5-12.5 wt%.

A loading of 40 % PEI (hyperbranched M_w=1800) on a silica with a pore diameter of 20 nm (surface area of 250 m^2 g^{-1} and pore volume of 1.7 mL g^{-1}) was used by Zhang et al. in a larger scale study of PEI silica (discussed in Section 2.8.2).[46] In this study an adsorption capacity of 10.6-11.1 % was observed, with breakthrough capacity of 7.6-8.2 %. A further study found that at temperatures of 55-85 °C PEI with lower molecular weight (M_w=800) at loadings of up to 75 or 80 % gave increased CO_2 capacity, however at lower temperatures of 25 °C higher M_w PEI (M_w=25000) shows the highest capacity. These samples from the study used silica with a pore diameter of 24 nm (surface area 688 m^2 g^{-1} and pore volume of 4.2 mL g^{-1}).[141] This study also found that using these samples an increase in capacity with loading up until the pores are filled, as did Son et al.[134] This trend can also be seen in data from Chen et al.[137,142]

In a 2011 study, Subagyono et al. prepared samples of PEI-Silica (linear PEI

M_w=2500 and branched PEI M_w=1200) with one pore volume of PEI. The silica used in this was SBA-15, loading of 50 %, and mesocellular siliceous foam, loading of 70 %.[143] This study found that the siliceous foam samples showed a higher adsorption capacity (151 vs 107 mg g^{-1}) and working capacity than SBA-15 samples and that of a commercial zeolite.

A separate study on mesocellular siliceous foam samples, used 50 % loading of a low molecular weight PEI on 3 samples with similar pore diameter (23-24 nm) and varying surface area (532-811 m^2 g^{-1}) and window size (5.0-11.3 nm). This study found the sample with the largest window size (and smallest surface area) to have the highest CO_2 uptake, both per gram sample and per gram PEI.

Increased PEI content has also been shown to increase CO_2 capacity in a study of 800 M_w PEI on SBA-15, although increased loading does decrease the efficiency per unit PEI. The study in question used loadings of 10, 30, 50 and 70 %, and found that at 45 °C and 1 bar, the 70 % loading sample had a capacity of 88.2 mg g^{-1}. Increasing the pressure was also seen to increase the capacity and increacing the temperature over 25-75 °C showed an increase in capacity for the 50 % sample.[144]

The data from these studies suggests that the optimum loading is dependant on the silica pore size with increased surface area resulting in higher loadings, and smaller pore width and volume limiting loading. Reports of a maximum CO_2 capacity occurring when pores are filled but not blocked are common. In this data, it can also be seen that lower molecular weight branched PEI consistently outperform higher molecular weight linear samples. However the comparison of data between studies is difficult due to the different methods, conditions and materials used. A summary ofthe data can be seen in Table 2.1.

Silica			PEI				
Pore Width nm	Surface Area $m^2\ g^{-1}$	Pore Volume $mL\ g^{-1}$	M_w $g\ mol^{-1}$	Chain Type	Loading %	Max. CO_2 Capacity $wt\%^{-1}$	Ref.
24	266	1.5	800 - 750000	branched	40	10.5 - 12.5	139,140
20	230	1.7	1800	hyper-branched	40	10.6 - 11.1	46,138
24	688	4.2	25000	branched	75 - 80	23*	141
			800			26.5*	
6.8	723	0.89	1200	branched	50	5.23	143
			2500	linear		1.59	
2.23 - 2.26	509 - 732	2.25 - 2.50	1300	branched	70	8.07 - 8.22	
			2500	linear		1.17 - 1.22	
8.9	775	1.1	800	branched	70	8.82	144
3	950	3.2	n/a	n/a	65	16.5	137
2.8	952	0.82	600	linear	60	11.5*	142
9.8	1123	1.37				18.4*	

Table 2.1: PEI-Silica properties and loadings from the literature, the majority obtained at operational levels of CO_2 at 2.5-15 % except those noted * which were at 95-100 % CO_2. Wt% values were either provided in the text or calculated from mg g^{-1} values. N/a refers to data not reported in the literature.

Solvent Degradation

One of the issues facing amine-based carbon capture materials including PEI-Silica is degradation of the adsorbent, which can contribute significantly to CCS cost. This degradation can be oxidative or thermal degradation. Solid materials can also suffer from steam-induced degradation of the supports; this can be limited through careful substrate selection.[145]

Thermal degradation often pertains to the formation of urea, a non-reversible reaction of the amine and CO_2, with the use of more highly substituted amines inhibiting the reaction.[146] The basic process can be seen in Figure 2.15 with MEA, an amine with 2 primary amines.

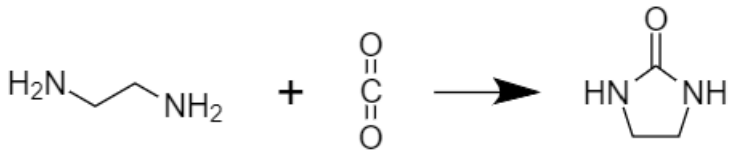


Figure 2.15: Non-reversible formation of cyclic urea from MEA

Oxidative degradation pathways include autoxidation and oxidation in the presence of metal ions (catalysts).[145,147] Structural changes in the adsorbent can be used to make it more resilient to oxidation, for example hydroxy groups. This has been achieved in PEI-Silica through functionalisation with 1,2-epoxybutane, which in combination with the addition of chelators to the support (which combat metal ions, thereby preventing oxidation) achieved a decrease in deactivation rate of approximately 50 times.[145] Linear PEI has also been shown to be more resistant to oxidation than branched PEI.

Antioxidants

Antioxidant materials inhibit oxidation slowing oxidation rates. There have been a vast number of studies of antioxidants in a variety of fields, however no existing literature on antioxidants has been found other than the work previously done by this group.[148] There has however been some examples of stabilising MEA against

oxidation with specialised inhibitors, although some of this work has found standard antioxidants to be ineffective.[149,150] Unfortunately the literature on this subject is limited, likely a result of these materials and blends being proprietary. Therefore, in order to find more examples of antioxidants which may be useful for PEI-Silicas, antioxidants used in fuels were considered, as antioxidants are commonly and successfully used in this industry. Due to immediate availability pyrogallol and sodium salicylate, were investigated in this study. Pyrogallol is an antioxidant that has been shown to stabilise biofuels and salicylates are antioxidant commonly used in fuels and also utilised in the medical field.[151,152] In addition several further general antioxidants were selected.[153]

Silica

Many different silicas can be used as substrates for amines for CCS purposes. Some of the most commonly used include: MCM-41, MCM-48 and SBA-15.[132] Larger pore sizes have been seen to increase CO_2 capacity, due to the great accessibility of the amine and amine loadings.[134,154] However it is worth noting that, completely filled pores result in a lower capacity. Son et al. (2008) found that loadings over 50 % resulted in the PEI covering the external structure and filling the pores of the silica (MCM-41, MCM-48, SBA-15, SBA-16 and KIT-6).[134] Whereas Chen et al. (2010) found they could increase loadings up to 60 % when using a hexagonal mesoporous silica with textural mesopores without a loss of sorption capacity.[142]

2.8.2 Analytical Methods

Many studies of PEI-Silica and other carbon capture materials have been performed around the globe. Initial investigations into potential materials are usually performed in small scale laboratory settings on bench equipment. This lab-based analysis is also used to optimise materials before moving on to more expensive, larger scale testing, and to develop understanding of chemical processes and interactions. Larger scale investigations then build on these data.

Bench Scale Methods

PEI-Silica has been characterised using several analytical methods, with some of the most commonly used methods including:

- Nitrogen adsorption/desorption (BET); to determine the surface area and pore volume;
- Thermogravimetric analysis (TGA); to determine the thermal stability;
- Scanning electron microscopy (SEM); to investigate the surface structure of the silica (SEM generally has a maximum resolution of around 10 nm);
- Infra-red spectroscopy (IR); to observe CO_2 adsorption.

In addition to characterisation of PEI-Silica, lab scale methods can also be used to simulate plant activity and determine CO_2 uptake/capacity and regeneration. This has been done in several different ways. For example, in 2013, Wang et al. used a fixed bed flow adsorber to separate a moist CO_2 and N_2 mixture, using gas chromatography (GC) on the inlet and outlet gas to determine adsorption.[44] Previously, in 2010, Zhu et al had used a static volumetric method, where the amount of CO_2 adsorbed is found through the change in amount of gas (CO_2) in a closed system using pressure, temperature and volume measurements.[155] TGA, a gravimetric method, can also be used for this purpose, with a CO_2 or mixed gas stream adsorption of CO_2 over the desired temperature range can be determined through the change in weight of the sample.[134,156,157] One benefit of this method is the low sample amounts of 10-20 mg required, however as TGA measures the mass gain of the sample rather than the CO_2 concentration it cannot be used to determine the "breakthrough capacity" (the point at which 90 % CO_2 is captured - a common performance indicator). TGA can also be used to determine the loading of PEI on silica when performed under an inert (N_2) atmosphere as the PEI volatilises/decomposes at temperatures where the silica is stable.

Solid State NMR

In addition to the common use of solution state NMR to analyse and characterise all types of materials including PEI and other liquid polymers, solid state NMR has been used in the literature to characterise PEI adsorbed onto (or interacting with) solid materials.

- J. Moore studied PEI-Silica (SBA-15) using static ^{13}C NMR as part of a doctoral thesis in 2015, along-side studies of other carbon capture materials.[158] This investigation used NMR to show the presence of CO_2 in the sample. This study also investigated the T_1 (spin-lattice) relaxation time of the samples and took broadline measurements of the peak half width at 20, 70 and 100 °C, with these results both showing increasing mobility with temperature.[158] In a separate part of this study, ^{29}Si NMR was also employed, though not on PEI or SBA-15 but rather on an amorphous silica layer present on the surface of forsterite particles.

- Andreoli et al., in 2014, used ^{13}C and ^{14}N CP MAS NMR to characterise PEI-C_{60} (PEI with C_{60} as a cross linkage).[159]

- Dillon et al., in 2008, also used solid state ^{13}C NMR to characterise PEI-functionalised single wall carbon nanotubes.[160]

Larger Scale Testing

In 2014, Zhang et al. investigated PEI-Silica for carbon capture at the kg scale for post combustion CCS using a bubbling fluidised bed reactor, and ambient air CCS using a combination of a bubbling fluidised bed desorber and a circulating fluidised bed adsorber.[46,138] In these studies, the PEI was supported on a mesoporous silica at 40 % amine loading and desorption occurred at 130 °C. The adsorption temperatures were 50-70 °C and ambient temperature respectively, with 70 °C seeing the maximum CO_2 capacity. The equilibrium CO_2 capacities seen were 9.4-11.1 wt% (with breakthrough capacity of 8.2 wt%) for the PCC capture experiments and up to 7.3 wt% for ambient condition tests. These investigations show great promise for

the use of PEI-Silica in the future of CCS with estimated costs for PCC competitive to other potential methods, although longer experiment lengths are required.

In 2015 Norcem and Heidelberg Cement Northern Europe in collaboration with the European Cement Research Europe presented the results of an investigation into the use of 4 carbon capture technologies in their plant in Brevik, Norway. The technologies tested were a liquid amine, a solid amine (PEI-silica from RTI International), a membrane technology, and a calcium looping technology.[161] In this study, over 300 cycles PEI-Silica showed a CO_2 capacity of 5-7 wt%.[162] Although PEI-Silica was found to be competitive in cost, in this case the liquid amine provided by Aker Solutions was selected for further research.[162–164]

The liquid amine selected for this project was able to easily capture 90 % of the CO_2, and it is predicted to be possible for up to 85 % CO_2 to be captured using only waste heat.[165] The final stage of the study is due to be published in August 2019, and if successful may result in construction of a commercial carbon capture facility at Brevik, with operation in 2024.[164]

The Korean Institute for Energy Research has a pilot scale facility using PEI-Silica as a solid carbon capture adsorbent, this facility is in partnership with this work.[166]

2.9 Carbon Capture Summary

- There are 3 categories of carbon capture technology: pre-combustion, post-combustion and oxyfuel. Post-combustion is the only one of the three capable of retrofitting to existing technology and thus is the most viable in the short term.

- Within the field of post-combustion capture, the use of amines as a carbon capture material is popular. Liquid amine systems have several downsides that can be combatted by using amines adsorbed onto solid substrates (e.g. PEI-Silica) including corrosion and high heat transfer energy penalty.

- PEI-silica is a promising solid post-combustion capture material due to it's

high thermal stability.

- Lower molecular weight branched PEI tends to show the higher CO_2 uptake compared to linear or higher molecular weight samples.
- PEI loading on silica is dependant on total surface area and pore width and volume, with greater surface areas and pore sizes resulting in a higher possible loading before pores become blocked. Higher loadings tend to result in higher CO_2capacity.
- PEI-silica has been previously investigated using a range of techniques, such as TGA and BET, however few investigations utilising proton NMR have been performed.

Chapter 3

Methodologies

In this chapter, the experimental methodologies used in this study will be described. The first half of this chapter, Section 3.1, will focus on the theory behind each of the methods and descriptions of the raw materials used. The second half, Section 3.2, will describe the detail of how these methods were performed in this study, including the specific parameters used. Description of the sample preparation used in this study can also be found in Section 3.2.

3.1 Background and Theory

In this section the background theory of each of the methods used will be explained, methods with a greater importance to the main outcomes of the study, namely NMR, will have a greater focus on detail.

3.1.1 Nuclear Magnetic Resonance

NMR is a resonance technique that utilises the magnetic shielding caused by electron density around nuclei to enable the detection of different nuclear environments of isotopes with spin-$\frac{1}{2}$ and greater. An external static magnetic field of known strength is induced using a superconducting magnet to align the nuclear spin; radio frequency (rf) pulses are then used to observe the transitions between the parallel and anti-parallel spin states.

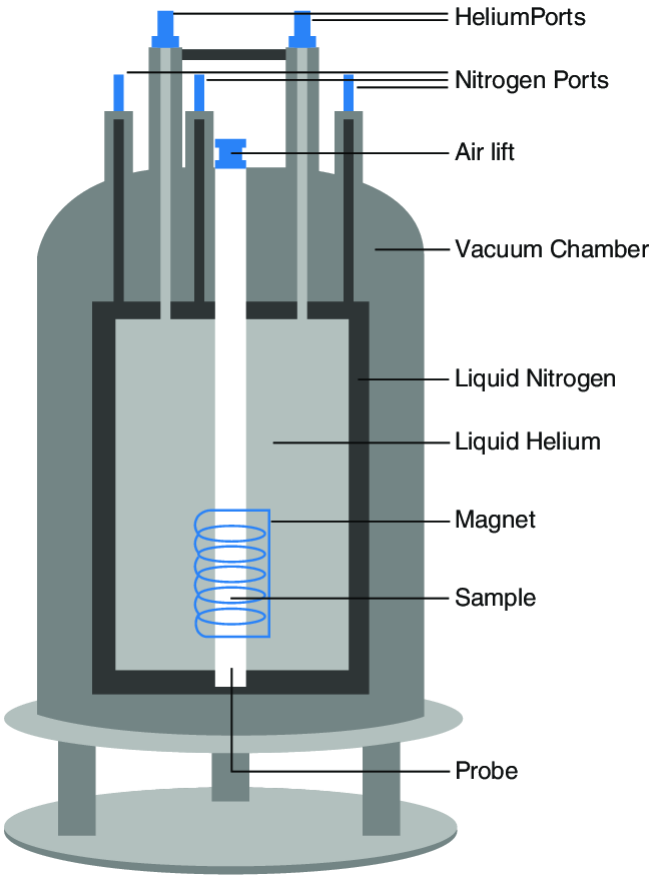


Figure 3.1: Simplified Diagram of an NMR Magnet

NMR is most commonly used on solution state systems due to the isotropic nature of the molecules in solutions, giving an average peak and a distinct spectrum.[167] In the solid state, NMR can have low resolution and extended experiment times which are unfavourable, however, it does provide information on the crystal structure and solid-state properties which cannot be determined from solution state studies.

Chemical Shift

The chemical shift is the resonance frequency of the nucleus in question; it is relative to a reference material with a known shift. The value of the chemical shift is determined by the nucleus itself and the electronic environment surrounding it.[167] The motion of electrons surrounding a nucleus will induce a second, internal, magnetic field which opposes the external magnetic field, B_0. Therefore if a nucleus is in an

electron rich environment it is shielded from the magnetic field by these electrons and has a lower, or "upfield", chemical shift, and conversely a nucleus in an electron poor environment is deshielded and has a higher, or "downfield", chemical shift.

The shielding, σ, can be described by the shielding tensor in Equation 3.1 which is diagonalised to give the principle components, σ_{xx}, σ_{yy}, σ_{zz}. The shielding tensor is necessary as the induced field is not necessarily parallel to B_0.

$$\sigma = \begin{bmatrix} \sigma_{xx} & \sigma_{xy} & \sigma_{xz} \\ \sigma_{yx} & \sigma_{yy} & \sigma_{yz} \\ \sigma_{zx} & \sigma_{zy} & \sigma_{zz} \end{bmatrix} \tag{3.1}$$

The principal components are sometimes written σ_{11}, σ_{22}, and σ_{33} (as in Figure 23), where σ_{11} is the least shielded and σ_{33} is the most and can be written in terms of the chemical shift, δ (as in Figure 22). One way of describing the chemical shift is using the shielding, as in Equation 3.2.[168]

$$\delta \approx 10^6(\delta_{ref} - \delta_{sample}) \tag{3.2}$$

However the chemical shift is usually calculated from the absolute resonance frequencies, ν, which depends on the external magnetic field, B_0. By using a reference to calculate chemical shift, it is not dependant on B_0 and therefore comparable to other measurements from other spectrometers with different strength fields. See Equation 3.3

$$\delta = \frac{\upsilon_{sample} - \upsilon_{ref}}{\upsilon_{ref}} 10^6 \tag{3.3}$$

Chemical shift is either measured in Hz or parts per million, ppm. The latter is most commonly used and is the unit of output of the two equations above.

Spin

Nuclear spin is a form of angular momentum intrinsic to elementary particles and therefore atomic nuclei, as nuclei are made of the elementary particles, protons and neutrons. Nuclei which contain on odd number of protons and/or neutrons have a

non-zero nuclear spin. In theory any isotope with a non-zero nuclear spin can be used for NMR, however the most common isotopes studied are proton (^1H) and carbon-13 (^{13}C), both spin 1/2.[168]

Vector Model

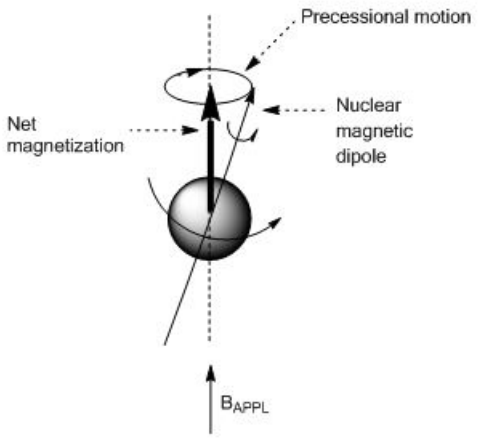


Figure 3.2: Figure showing net/bulk magnetisation and precessional rotation (by Thomas Wenzel)[169]

The vector model is a common way of conceptualising the magnetic moments of nuclei in a NMR experiment. The magnetic moments of the nuclei are not randomly aligned and as such result in bulk magnetisation, which is represented by the vector. This vector is aligned with the direction, z, of the applied field, B_0.[170]

A radio frequency pulse is able to alter the bulk magnetisation in such a way that it precesses (rotates) around z in a cone; this is Larmor precession, which has a frequency, ω_0 in rad s^{-1} or ν_0 in Hz, related to B_0 by Equations 3.4 and 3.5, where γ is the gyro-magnetic ratio.

$$\omega_0 = -\gamma B_0 \tag{3.4}$$

$$\omega_0 = -\frac{1}{2\pi}\gamma B_0 \tag{3.5}$$

The signal is the x component of the Larmour frequency, and is received as a free induction decay (FID).

Free Induction Decay

The FID is the observable signal produced when performing NMR signals. It must be Fourier transformed (i.e. transformed from a function of time into its constituent frequencies) in order to show a distinguishable spectrum (see Figure 3.3).

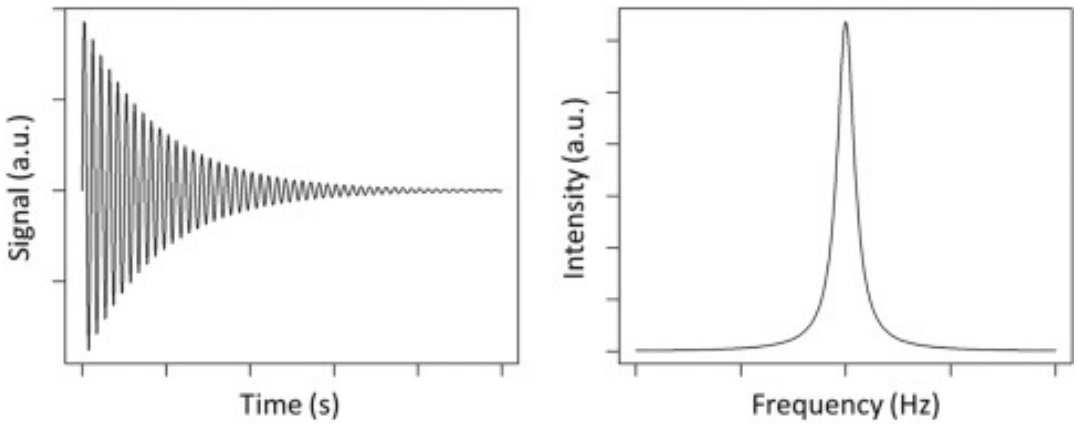


Figure 3.3: Free Induction Decay and Fourier Transformed Spectra (from Comprehensive Analytical Chemistry, 2018)[171]

Pulses

In NMR, radiofrequency (RF) pulses are calibrated such that they either rotate the magnetisation by 90 ° or by 180 °, and are as such referred to as 90 ° and 180 ° pulses. These are often displayed as lines or blocks in the schematics of pulse programs.

Relaxation

Relaxation is the process through which the spins return to equilibrium (i.e. having a Boltzmann distribution of energy levels, with no transverse magnetisation and coherences). Relaxation times (spin-spin, T_2; spin-lattice, T_1; and spin-lattice relaxation in the rotating frame, $T_1\rho$) can provide information about the molecular dynamics of species and characterise the physio-chemical environment of molecules being studied, with individual motions in a molecule having the potential to display distinct relaxation times.[167,172]

Spin-Lattice Relaxation (T_1)

T_1 relaxation is the amount of time required for excited spins to return most of the way (63 %) to their equilibrium states after a 90 ° RF pulse. T_1 is also referred to as longitudinal relaxation because it shows the rate at which the z component of the magnetisation decays. It is commonly determined using inversion recovery and saturation recovery experiments.[173]

This relaxation occurs through several mechanisms; some of those important for spin 1/2 nuclei include:[173]

- Paramagnetic species:

  Paramagnetic species are particularly effective at promoting relaxation due to the electrons' large magnetic moment.

- Dipolar mechanism:

  Interactions between adjacent spins results in the transfer of magnetisation between them, changes in orientation are most strongly responsible for relaxation (rather than changes in distance between nuclei). Dipolar effects on relaxation tend to be primarily of a spin-lattice, T_1, nature, as spin-spin effects would not by nature bring about equilibrium.

- Chemical shift anisotropy mechanism:

  The magnetic field experienced by a molecule depends on its orientation; as only the transverse fields impact the populations, these variations will result in relaxation. This is not usually significant in protons.

Spin-Spin Relaxation (T_2)

T_2 relaxation is the amount of time taken for the transverse (xy) magnetisation to decay by a factor of e (exponentially). In addition to the mechanisms that result in T_1 relaxation (these also result in T_2 relaxation), the following mechanisms are also present for spin 1/2 nuclei:

- Local variation in the magnetic fields (transient magnetic fields), so as molecular motion slows (lower molecular mobility) T_2 decreases.
- Chemical exchanges also result in T_2 relaxation.

Instrumental problems (e.g. Tuning) and sample problems (e.g. inhomogeneity, temperature gradients) can also have an effect on both types of relaxation.

T_2 relaxation times are smaller (kHz) (probing slower motions such as chain-wagging)[174] than T_1 relaxation times (MHz), and are commonly determined through Hahn-echo pulse sequence and CPMG (Carr, Purcell, Meiboom, Gill).[175]

T_2 and Line-width

Fast exchanges (as seen in protons) result in line broadening of a single spectrum. T_2 can be seen through line broadening of a sample (for protons it is often between 1 and 10 s), and is related to the half peak width by Equation 3.6 (for Lorenzian distributions only).[13]

$$T_2 = \frac{1}{\pi \Delta H_{\frac{1}{2}}} \tag{3.6}$$

Magnetic inhomogeneity may also result in changes in line width, however for a well shimmed and stabilised spectrometer the contribution is only approximately 0.1 Hz.

3.1.2 Carbon-13 NMR

In this study, two types of ^{13}C NMR experiments or pulse sequences were utilised. These are cross polarisation magic angle spinning (CP MAS), and high powered decoupled (hpdec); for both experiments MAS was used. Schematics for these pulse sequences can be seen in Section 3.2.3, in Figures 3.15 and 3.16 respectively.

Magic Angle Spinning

To observe an isotropic, solution-like, peak would be very useful and enable much easier interpretation of the spectra. To accomplish this, a technique known as magic

angle spinning (MAS) is used. MAS is the physical spinning of the sample at a specific, magic, angle, β_R, of 54.7 ° relative to the static magnetic field, B_0, induced by the superconducting magnet.[170] The anisotropy is removed as the magic angle is such that the relevant term in the motionally averaged Hamiltonian, $H_{\frac{1}{2}}$, (the Hamiltonian is an operator which represents the energy of the system) is scaled to zero (see Equations 3.7 and 3.8). In Equation 3.8, β refers to another angle relating the internuclear displacement to the magnetic field.

$$cos^2(\beta_R) = \frac{1}{3} \tag{3.7}$$

$$H\frac{1}{2} = \frac{1}{2}(3cos^2\beta_R - 1)(3cos^2\beta - 1) \tag{3.8}$$

Therefore at the magic angle the $(3cos^2\beta_R - 1)$ term is reduced to 0 thus removing the anisotropic interaction from the Hamiltonian, and therefore from the spectrum, scaling all but the isotropic part of the data to zero.[170]

MAS also removes the dipolar coupling in the same way. The $(3cos^2\theta - 1)$ term in the coupling Hamiltonian, H_D, is also reduced to zero at 54.7 °. This can be seen in the heteronuclear coupling Hamiltonian (Equation 3.9).

$$H_D = -\frac{d}{2}(3cos^2\theta - 1)2I_zS_z \tag{3.9}$$

I_z represents the spin of the nuclei being sampled; S_z is the spin of the coupling nuclei; d is the decoupling constant which is inversely proportional to r^3, where r is the internuclear distance; θ is the angle between I, S and B_0.

Magic angle spinning (MAS) or the spinning of the sample at 54.7 ° is a common technique in solid state NMR.

3.1.3 Proton NMR

In this study, a singular ^{1}H NMR experiment was utilised; a standard solid echo pulse sequence (see Figure 3.12 in Section 3.2.2). This was a broadline experiment, with no MAS. The resulting spectrum is therefore a single molecularly averaged peak.

3.1.4 N_2 Sorption Isotherms

N_2 Sorption Isotherms measures surface area by physical adsorption by van der Waals forces of a gas onto the surface of a solid sample, usually a powder. The amount of gas adsorbed is measured and with the monolayer value determining the surface area. The Brunauer-Emmett-Teller, Barrett-Joyner-Halenda (BJH) and T-plot models are used to determine the BET specific surface area, mesopore and macropore volume and size distribution, and micropore volume respectively.

3.1.5 Thermogravimetric Analysis

Thermogravimetric analysis (TGA) is a form of experimental analysis which measures weight of a material as a function of temperature under a controlled atmosphere, providing both the amount and rate of change. This method is used to determine the thermal stability of a sample and the percentage of volatiles within a sample.

The sample is contained on a pan, suspended by a precision balance, within a furnace with a gas flow controlling the sample conditions. This gas can be either inert or reactive depending on experiment design (e.g. N_2 or CO_2), with the flow rate also determined by the operator.

3.1.6 Viscometry

This equipment measures the viscosity, shear stress, and shear rate of a liquid, with the option to control the temperature. The sample liquid sits in a static cylindrical container with a spindle lowered into it, resulting in the sample sitting between the spindle and container wall. The spindle then rotates at a set speed, the required torque for this motion is a function of the liquids viscosity as can be seen in Equations 3.10, 3.11 and 3.12.

$$Shear\ Stress = 1/3r_a^2 H \times Torque \tag{3.10}$$

$$Shear\ Rate = \frac{2r_i^2 r_o^2}{r_a^2(r_o^2 - r_i^2)} \times Angular\ Velocity \tag{3.11}$$

$$Viscosity = \frac{Shear\ Stress}{Shear\ Rate} \tag{3.12}$$

Where H is the cylinder height, $r_a = \frac{r_i + r_o}{2}$, and r_i r_o are the inner and outer radius respectively.

3.1.7 Electron Paramagnetic Resonance

Electron paramagnetic resonance (EPR) spectroscopy is a method analogous to NMR, however, instead of exciting nuclei spins, electron spins are excited. As electrons are paired spin up-spin down, only materials with unpaired electrons will show signal as paired electrons orbital and spin moments equal zero. EPR is therefore used to detect free radicals and other unpaired electrons.

In EPR a variable magnetic field is applied to the sample along with fixed frequency microwave radiation. This is the opposite of NMR where the magnetic field is fixed and the radio waves are variable. The magnetic field is then increased, which in turn increases the gap between electron spin states, until it is resonant with the microwave frequency (i.e. it matches the energy of the microwaves). At this point the electrons can change spin states; as the lower spin state is more heavily occupied due to Maxwell-Boltzmann distributions, there is a net gain in energy by the sample. This can then be detected and displayed as a signal on a spectrum. The most common way to display the spectra is as a first derivative.[176]

3.1.8 Materials

PIB Derivative Samples

The PIB derivative samples (PIB, PIBSA and PIBSI) used in this study were supplied by Innospec Inc. The polymers were synthesised using a thermal synthetic "ENE" reaction. Tables 3.1 and 3.2 display the structural properties of these polymers. The basic structure of these polymers can be seen in Figure 2.1 in Section

2.3.1, more detailed polymer structures can be found in Appendix A.3.

The M_n (number average molecular weight), M_w (weight average molecular weight) and polydispersity of the PIB derivatives, as well as the PIB-M_n (number average molecular weight of the PIB tail) were determined with gel permeation chromatography by Dr. Jim Barker at Innospec Inc (See Appendix A.4.1 for methodology). The PIB Funct. refers to the number of PIB tails on the headgroup.

Table 3.1: Polymer chain information on PIB derivative samples

Polymer	PIB-M_n ($gmol^{-1}$)	PIB Funct.	Head group
PIBSA 2	1000	mono	Succinic Anhydride
PIBSI B	1000	mono	Succinimide with TEPA
PIBSI C	750	mono	Succinimide with AEEA
PIBSI G	1000	bis	Succinimide with TEPA
PIBSI I	750	bis	Succinimide with EDA
PIBSI Y	750	mono	Succinimide with EDA
PIBSI Z	750	bis	Succinimide with TEPA

Where TEPA = tetraethylenepentamine, AEEA = aminoethylethanolamine and EDA = ethylenediamine

Table 3.2: Information on PIB derivative samples

Polymer	M_n (g mol^{-1})	M_w (g mol^{-1})	PD
PIB	771	1075	1.4
PIBSA 2	904	1170	1.3
PIBSI B	1740	2648	1.5
PIBSI C	748	1794	2.4
PIBSI G	1921	3473	1.8
PIBSI I	1490	2055	1.4
PIBSI Y	1285	2059	1.6
PIBSI Z	1125	1797	1.5

Carbon Black Materials

The carbon black sample was purchased from Sigma-Aldrich (now Merck). This sample is a mesoporous carbon black with an average pore size of 10 nm. This carbon was selected due to it's use in previous work where it shows good interactions with PIB derivatives.[57]

PEI Samples

The PEI samples used in this study were purchased from BASF and are referred to by their designated codes. Seven PEI samples were investigated in total, with average molecular weights ranging from 800 to 1000000 g mol^{-1}, however the highest molecular weight sample (PN 50) was not used in the full range of investigations in this study due to low performance and issues with viscosity and solubility. The weights can be seen in Table 3.3 and the monomer structure of PEI can be seen in Figure 1.6.

Name	M_w (g mol^{-1})	Concentration*
FG	800	96 %
G20	1300	53 %
G35	2000	53 %
G100	5000	52 %
HF	25000	56 %
PS	750000	37 %
PN 50	1000000	49-67 %

Table 3.3: PEI average molecular weights and concentrations as received (*concentration determined by burnoff TGA)

Silica Samples

Silica substrates were selected based on their pore size (surface area, pore diameter and pore volume).

The silica known as Silica 1 was purchased from PQ Corporation. This sample is a synthetic amorphous silica with a pore size of 24 nm. Silica 3 is an analogous silica, used in scale-up at the KIER facilities.

The silica SBA-15 was purchased from Sigma-Aldrich (now Merck). This sample was a mesoporous silica with a particle size of less than 150 μm, a pore size of 8 nm and hexagonal pore morphology.

The MCF was produced with the help of Dr Xin Liu and Mr. Suleiman Sani at the University of Nottingham using a method based on microemulsion templating as reported by Schmidt-Winkel et al. (2000).[177] This method is as follows.

The structure directing agent P123 (8 g) was dissolved in HCl (23.7 g, 37 %) and deionised water (130 ml) with stirring at 40 °C in an autoclave reactor. Once complete dissolution was achieved, 1,3,5-trimethylbenzene (TMB) (8 g) was added and stirred for 2 hours (at 40 °C), at which point tetraethyl orthosilicate (TEOS) (18.4 ml, 17.3 g) was added. At this stage hydrolysis occurs lasting for 20 hrs (with continued stirring and heating), then 92 mg NH_4F dissolved in water (10 ml) was added. The mixture was heated to 160 °C (5 °C min^{-1}) for 24 hrs and then the



Figure 3.4: Rice husk from Hunan province, China. As received from the supplier.

white precipitate collected by vacuum filtration and washing. The precipitate was dried in air and calcined in air (1 L min^{-1}, 5 °C min^{-1}) at 550 °C for 8 hours.

The two silica made from rice husk, known as RH1 and RH2, were prepared from rice husk from a farm in the Hunan Province of China. It is not a commercial product. An image of the rice husk as received can be seen in Figure 3.4. The rice husk has a moisture content of 7.6 % and an ash content of 12.3 % on a wet basis or 13.3 % on a dry basis. Further analysis using elemental analysis and XRF can be seen in Appendix B.1.

The rice husk was initially dried by heating in air at 110 °C for 72 hours. It was then acid washed before ashing by boiling in 4 M HCl for 2 hours. The husk was then filtered and ashed at 700 °C for 2 hours with a 5 °C /min heating rate under 3 L/min flow of compressed air. The ash (5 [RH2] or 10 g [RH1]) was then dissolved 150 ml 1 M NaOH at 50 °C with stirring for 24 hrs, after which the sediment was separated from the sodium silicate solution by centrifuge. This was then prepared into mesoporous silica by a similar method to the MCF.

The preparation of Rice Husk Silica 1 and 2 is as follows. The structure directing agent P123 (8 g) was dissolved in deionised water (130 ml) with stirring at 40 °C in an autoclave reactor. After 24 hrs, 1,3,5-trimethylbenzene (TMB) (8 g) was added and stirred for 2 hours (at 40 °C), at which point a 1.28 ratio of NH_4F to Silica was added, along with the sodium silicate solution (150 ml) with stirring for 5 min. The sample was aged at 40 °C for 24 hrs and then at 100 °C for an additional 24 hrs. The

sample was filtered and the precipitate was calcined in air (1 L min^{-1}, 1 °C min^{-1}) at 550 °C for 6 hours. The preparation of these silica was performed by Hui Deng at the University of Nottingham.

All of the silica samples were characterised by gas sorption. In addition to this, the sample Rice Husk Silica 2 was characterised by Dr. Lee Stevens at the University of Nottingham using mercury intrusion porosimetry due to the presence of macro pores larger than 140 nm, and SBA-15 data were obtained from specification provided from the supplier. A general categorisation of these silica can be seen in Table. 3.3 with further information in Section 5.4.

Name	Pore Types
Silica 1	mesoporous
SBA 15	micro and mesoporous
MCF	mesoporous
RH1	meso and macroporous
RH2	meso and macroporous

Table 3.4: Silica sample properties

Antioxidant Samples

The antioxidants investigated in this study were: sodium salicylate, pyrogallol, 3,3' dithiodipropionic dcid and 2,2' thiodiethanol. All purchased from Sigma Aldrich (now Merck). Their structures can be seen in Figures 3.5, 3.6, 3.7 and 3.8.

Pilot Plant Samples

The pilot plant PEI-Silica samples were provided by KIER. These samples had been run through a lab scale unit at the KIER facilities for a number of cycles simulating plant scale adsorption, regeneration and degradation. The regenerated samples were taken after the desorption reactor and the adsorbed samples taken after the sorption reactor. A schematic of the bench scale unit can be seen in Figure 3.9. These samples were all 40 wt. % G100-Silica.

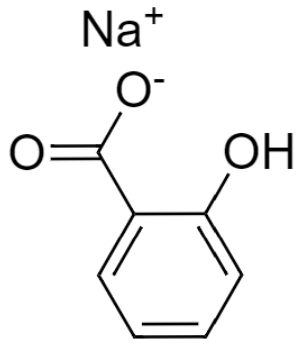


Figure 3.5: Chemical structure of sodium salicylate

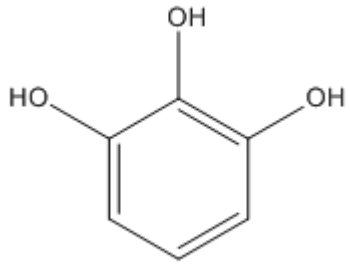


Figure 3.6: Chemical structure of pyrogallol

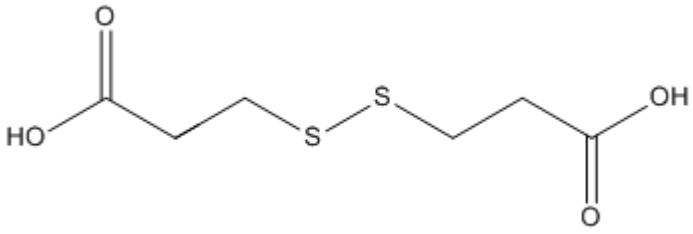


Figure 3.7: Chemical structure of 3,3' dithiodipropionic acid

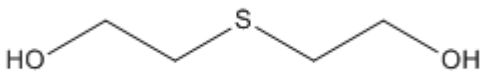


Figure 3.8: Chemical structure of 2,2' thiodiethanol

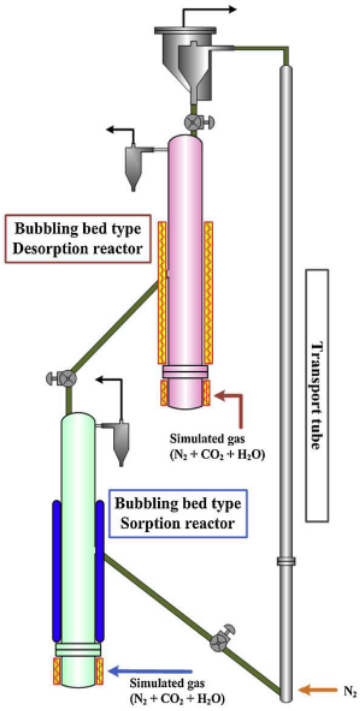


Figure 3.9: A simplified schematic of the KIER Pilot Scale Carbon Capture Facilities[166]

The unit used consists of bubbling fluidised bed adsorption and desorption reactors connected by a transport tube for recycling the PEI-Silica particles. There is a cyclone for separating the PEI-Silcia from the gases. A rotary valve for controlling the circulation of the PEI-Silica and an IR analyser for measuring the concentrations of the constituent gasses in the intake and output gas mixtures.

The bubbling beds are both 1 m tall with a 0.1 m internal diameter, with a perforated-plate-type gas distributor in the bottom. Cooling of the gas on injection into the reactor was minimised with a heater, temperature controller and heat exchanger. The gas used in the adsorber was a simulated flue gas mixture of N_2, CO_2 and H_2O. This gas was passed through a bubbler to generate vapour, to better replicate coal-fired flue gases. Where as the gas used to fluidise the desorber was a N_2, H_2O mix. The transport tube was a fast fluidised bed with a 0.02 m internal diameter and a height of 4 m, using N_2 gas. Temperature loss was prevented by preheating before the transfer pipe. Solid particles were separated from the gas using a cyclone before the desorber.

Solvents

Hexane(>95 %, BP. 69 °C) acquired from Sigma Aldrich (now Merck) was used as a solvent in the preparation of PIB derivative - carbon black dispersions. Where water was used as a solvent, it was deionised.

3.2 Description of Techniques

In this section each of the techniques are described as used in this study, for a more general description and background information on the techniques see the previous section, Section 3.1.

3.2.1 Sample Preparation

PIB Derivative Dispersions

The dispersions used in both the ^{1}H and ^{13}C NMR experiments and the other techniques were prepared by adding approximately 10 mL of solvent (hexane) to the desired mass of polymer (PIB, PIBSA, PIBSI) and mixing until completely dissolved. The desired mass of substrate (carbon black or silica) was then added to the solution and stirred continuously for approximately 24 hours at approximately 50 °C. The dispersion was then allowed to settle, and the solvent evaporated under N_2 flow. The samples were then ground to a fine powder using a mortar and pestle. The dispersions were prepared using a total mass of substrate and polymer of 1 g (as seen in Appendix A.1). This methodology was developed by Dr. Sam Bailey and Dr. Miguel Castro Diaz, and modified for this study in collaboration with Dr. Jim Barker.

PEI-Silica Impregnation

The PEI-Silica samples were prepared by dissolving the desired amount of PEI (depending on loading, see Table 3.5) in approximately 0.8 mL of water and stirred briefly. The desired amount of silica was then added, along with a small amount (approx. 2 mL) of water if necessary, to achieve incipient wetness. The sample was

then stirred at 40 °C for 24 hrs. The dry samples were then ground to a fine powder using a mortar and pestle, and dried further at 40 °C under a vacuum for 24 hrs. If samples were agglomerated or gel-like in nature and could not be ground they were dried under vacuum without grinding.

Desired Loading	Silica (g)	Aqueous PEI (g)		
		FG(96 %)	G20(53 %)	G35(53 %)
30 %	0.7	0.31	0.57	0.56
40 %	0.6	0.42	0.76	0.75
50 %	0.5	0.52	0.95	0.94
Desired Loading	Silica (g)	Aqueous PEI (g)		
		G100(52 %)	HF(56 %)	PS(37 %)
30 %	0.7	0.58	0.54	0.82
40 %	0.6	0.77	0.71	1.09
50 %	0.5	0.96	0.89	1.36

Table 3.5: Weights used to prepare 1 g of PEI-Silica by impregnation

Although this work does not directly include any scale-up, the samples provided by KEIR were part of a larger batch than prepared in this study and future work will likely include larger batch production of these materials. Therefore the scaled-up method for 50 wt. % G100-Silica 1 is as follows. The weights used in this method are different to those for the bench scale method due to the bulk G100 sample used having a different water content to the sample used for bench work. When this method is repeated it is adjusted for the water content of the samples used.

PEI (4 kg, G100) was dissolved in deionised water (1810 g) in a 7 L plastic bucket. Silica 1 (3 kg) was added slowly with stirring with a PDD 1/2 Portable Mixer from Greaves at ambient temperature. The mixture was stirred until dry and then the PEI-silica was dried further at low temperature using double cone vacuum dryers by Mitchell Dryers Ltd., Carlisle.

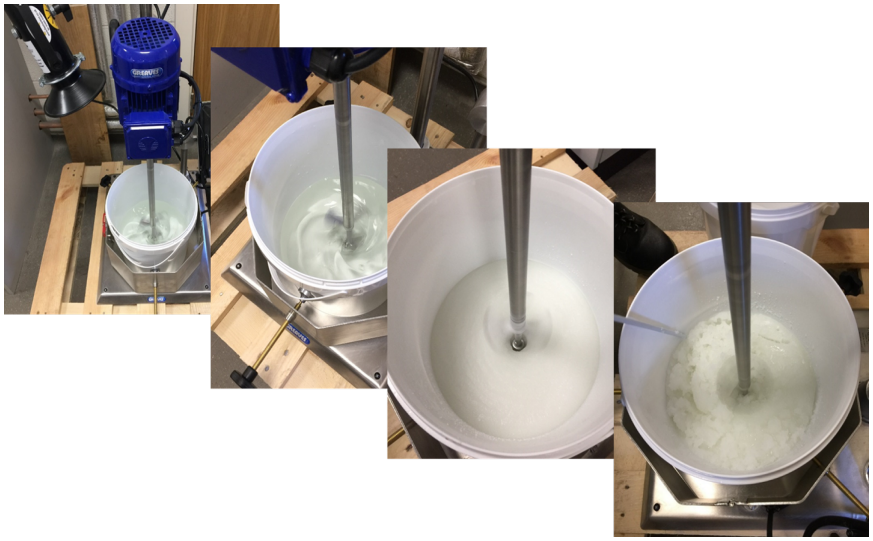


Figure 3.10: Photographs of a 5 kg batch of 50 wt. % G100-Silica 1 being prepared (Courtesy of Lee Stevens)

Preparation of antioxidant functionalised PEI-silica

The preparation of the functionalised PEI-silica is much the same as the non-functionalised. G100 was selected for functionalisation as it is the sample used by the pilot scale facility at KIER, at 40 % loading on Silica 1.

The samples were prepared by dissolving 0.77 g PEI in approximately 0.8 mL of water and stirred briefly. The desired amount of antioxidant was then added (see Table B.8 in Section 6.3.1) and stirred for 10 minutes until dissolved. 0.6 g of silica was then added, along with a small amount (approx. 2 mL) of water if necessary, to achieve incipient wetness. The sample was then stirred at 40 °C for 24 hrs. The dry samples were then ground to a fine powder using a mortar and pestle, and dried further at 40 °C under a vacuum for 24 hrs.

Moisture Removal

Moisture was removed from neat PEI samples using a horizontal tube furnace. Approximately 10 g of sample was heated to 50 °C under a nitrogen atmosphere (1 bar, 1 L min^{-1}) for 48 hours, and then cooled to room temperature in the inert atmosphere. The samples were analysed immediately to prevent water absorption.

This method was used to prepare the neat PEI for viscosity measurements and

^{1}H NMR.

Carbon Dioxide Removal

Carbon dioxide was removed from PEI-silica samples using a horizontal tube furnace. Approximately 10 g of sample was heated to 150 °C under a nitrogen atmosphere for 30 minutes, and then cooled to room temperature in the inert atmosphere. The samples were analysed immediately to prevent CO_2 adsorption from the air. This method was used to check that the C=O signal on ^{13}C NMR spectra was indicative of adsorbed CO_2 rather than urea formation, in Section 6.2.

3.2.2 Proton NMR

A high-temperature Doty 200 MHz NMR probe was used in conjunction with a Bruker MSL300 instrument. A flow of 35 L min^{-1} of dry nitrogen was used to transfer heat to the samples and remove volatile substances. A flow of 65 L min^{-1} of dry air was used to control the temperature below the sample region and protect the electrical components and a flow of 20 L min^{-1} of dry air was used to control the temperature in the region between the top bell Dewar and the outer side of the probe. The sample temperature was monitored with a thermocouple in contact with the sample container.

For all ^{1}H NMR experiments, approximately 100 mg of sample was packed into a 6 mm ceramic (boron nitride) capsule, with a macor (glass-ceramic) screw cap (see Figure 3.11. The cap has a small hole for the release of volatiles, which exit the spectrometer with the nitrogen flow.

When necessary the probe tip was cleaned through ultra-sonication in tetrahydrofuran (THF) for approximately 10 min.



Figure 3.11: 6 mm Boron Nitride Capsule with Macor screw cap, used to contain the samples in high temperature ^{1}H NMR in this study

$\Delta H_{1/2}$ and T_2 Determination

Spectra were acquired using a standard solid echo pulse sequence (90 ° − τ−90 °). The sequence had a pulse length of 3.50 μs, a recycle delay of 0.3 s, and 100 scans. Acquisition time used was 0.005 s as standard but was varied up to 10 s for experiments at very low concentrations of PIBSI. The sample was heated to 250 °C from ambient temperature with a heating rate of 3 °C min^{-1}, with spectra taken at 10 or 20 degree increments.

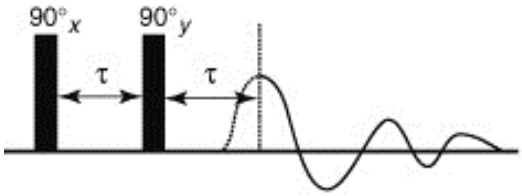


Figure 3.12: Solid Echo Pulse Sequence (from the Encyclopedia of Analytical Chemistry)[178]

The free induction decay (FID) obtained from the acquisition were Fourier transformed resulting in single peak spectra which are entirely Lorentzian, these were then fitted to calculated peaks using an iterative numerical programme (glfit2.2 by Robin G. Graham) and the peak width at half height ($\Delta H_{1/2}$) determined.

$$T_2 = \frac{1}{\pi \Delta H_{1/2}} \qquad \text{(3.6 revisited)}$$

The $\Delta H_{1/2}$ is related to the spin-lattice relaxation time (T_2) through Equation 3.6, Figure 3.13 also shows the relationship between the two units. However, in this study $\Delta H_{1/2}$ has been used to display the mobility.

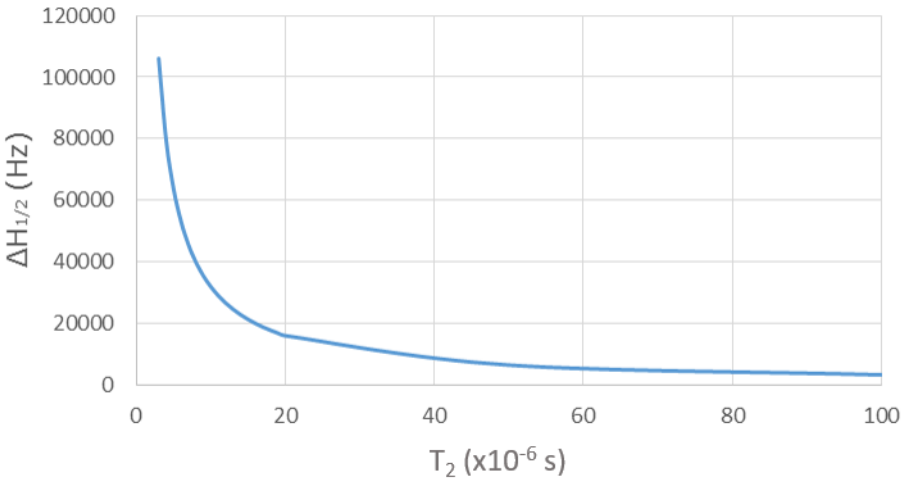


Figure 3.13: $\Delta H_{1/2}$ vs T_2

3.2.3 Carbon-13 NMR

Ambient temperature CP and SPE experiments were performed on a Bruker MSL300 instrument, with a Bruker 200 MHz CP MAS probe (dual channel). The sample container was a cylindrical (7 mm) zirconia rotor with a chlorotrifluoroethene (Kel-F) cap.

The standard used in this study was tetrakis(trimethylsilyl)silane (TKS) which presents a strong singlet peak at 3.5 ppm. Figure 3.14 shows the structure of TKS.

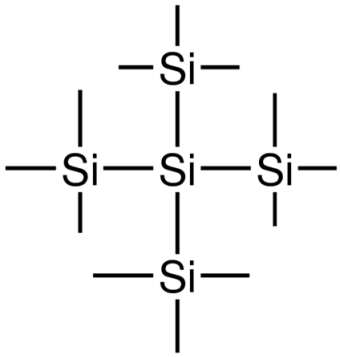


Figure 3.14: Chemical Structure of TKS

Cross Polarisation

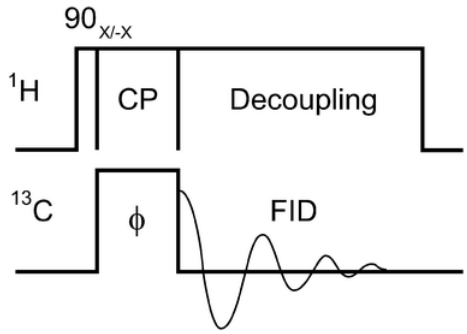


Figure 3.15: Cross Polarisation Pulse Sequence

A CP pulse sequence (shown in 3.15) was utilised in conjunction with MAS at ambient temperature. Each experiment consisted of 20000 scans, which were performed with an acquisition time of 0.03 s, a relaxation delay of 30 s, a spinning rate of between 0-5000 Hz (at 54.7 °) and a contact time of between 1000-10000 μs. This sequence includes heteronuclear (proton) decoupling.

Single Pulse Excitation

A standard direct excitation with heteronuclear (proton) decoupling pulse sequence (shown in 3.16) was utilised in conjunction with magic angle spinning (MAS) at ambient temperature. Unless stated otherwise, each experiment consisted of 20,000 scans, which were performed with an acquisition time of 0.03 s, a relaxation delay of 30 s, a spinning rate of 5000 Hz (at 54.7 °).

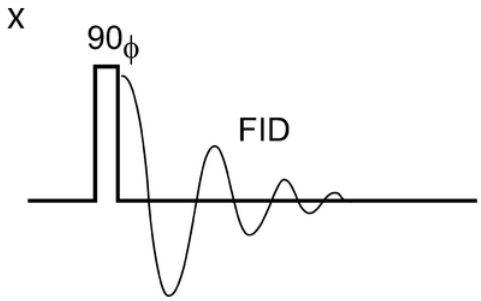


Figure 3.16: Direct Excitation Pulse Sequence where x= nucleus probed

3.2.4 N_2 Sorption Isotherms

N_2 sorption isotherms were acquired on a Micromeritics ASAP 2420 analyser. For this analysis, 0.2 g of sample (adsorbent) was used, and N_2 was the adsorbate gas for all samples.

The BET model was used to calculate surface area and the t-plot method with Harkins-Jura and BJH (Barrett-Joyner-Halenda) models were used to calculate micropore and mesopore volumes, respectively. The average pore diameter was calculated from the surface area and total pore volume using Equation 3.13, where D is the average pore diameter, V is total pore volume and SA is total surface area.

$$D = 4\frac{V}{SA} \times 1000 \tag{3.13}$$

The sample was heated to 120 °C in the case of the carbon blacks or 200 °C for the silica for 15 hrs under high vacuum to allow the removal/desorption of residual moisture and adsorbed gases. The isotherm was taken from 0.001-0.998 p/p_0 and the Brunauer-Emmett-Teller model taken from 0.05-0.20 p/p_0 gave a positive BET 'C' constant/parameter (meaning that this model is valid at this range). The BJH (Barrett-Joyner-Halenda) model with Harkins-Jura thickness correction gave the pore size and volume distribution analysis in the meso and macropore pore range. T-plot model with Harkins-Jura correction was used to determine the mircopore volume.

3.2.5 Thermogravimetric Analysis

TGA measurements of PEI, PEI-Silica and PIB derivatives were performed on a TA Instruments Q500 thermogravimetric analyser. This analyser has a weighing precision of ±0.01 %, a sensitivity of 0.1 μg, a temperature accuracy of ±1 °C and a temperature precision of ±0.01 %. The samples were all approximately 15-20 mg, and the system was initially purged of air. Three different programmes were used, "burnoff", "proximate", and "CO_2 Adsorption".

"Burnoff" Thermogravimetric Analysis

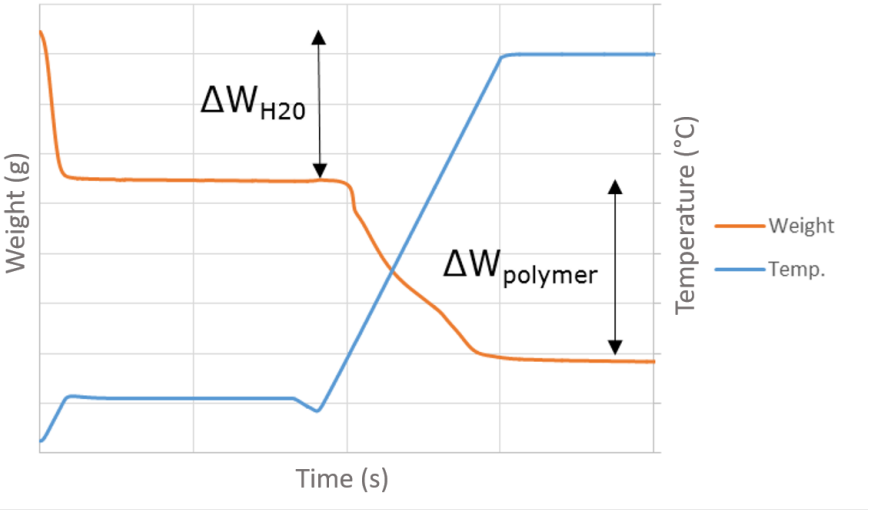


Figure 3.17: Example burnoff TGA thermogram demonstrating polymer loading calculation variables

To determine the polymer loading and/or water content of the sample a standard burnoff program was used. This consisted of heating the sample to 110 °C (at 30 °C/min) under N_2 (at 100 mL min^{-1}, 1 bar) for 30 minutes to remove moisture, the temperature was then reduced to 50 °C, the gas changed from N_2 to air (at 100 mL min^{-1}, 1 bar) and the temperature increased to 800 °C (at 30 °C/min) where it was held for 30 minutes. The weight change over the first stage of the process corresponds to the moisture content of the sample and the weight change over the second stage, the polymer loading (as can be seen in Figure 3.17. This can be calculated on a dry basis using Equation 3.14 where $\Delta W_{polymer}$ and ΔW_{H_2O} are

the changes in weight at stage 1 (moisture removal) and stage 2 (polymer burnoff) respectively.

$$Polymer = \frac{\Delta W_{polymer}}{100 - \Delta W_{H_2O}} \times 100\ \% \tag{3.14}$$

This method was also used to determine the ash content of the Rice Husk.

"Proximate" Thermogravimetric Analysis

To determine the thermal stability of samples a proximate analysis TGA was performed. This program consists of the same water removal step as the burnoff analysis followed by heating the sample to 800 °C (at 30 °C/min) under N_2 (at 100 mL min^{-1}, 1 bar). The weight change seen in this case will be the result of thermal decomposition and volatilisation of the sample. This is followed by changing the gas to air (at 100 mL min^{-1}, 1 bar) for 30 minutes to combust any remaining material.

"CO_2 Adsorption" Thermogravimetric Analysis

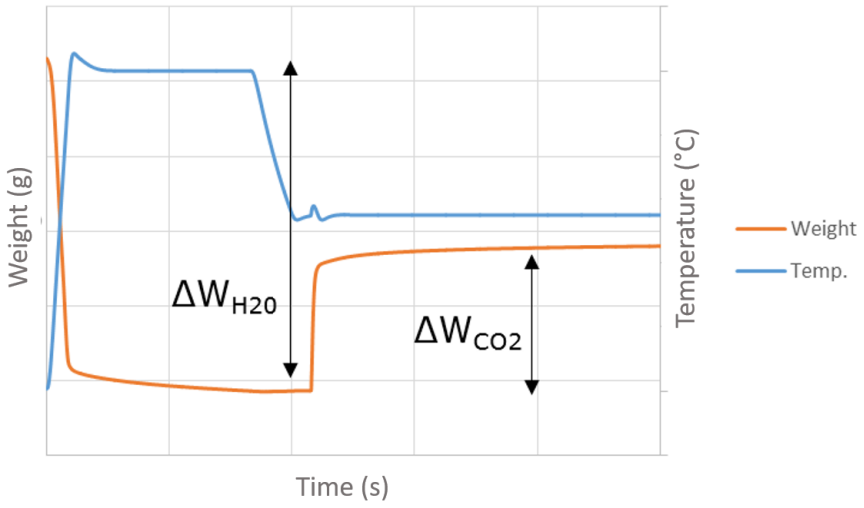


Figure 3.18: Example CO_2 adsorption TGA thermogram demonstrating CO_2 uptake calculation variables

For determining the CO_2 uptake of the carbon capture adsorbents, the program included the same moisture removal step as in the polymer loading program; this was then followed by cooling to 75 °C (the adsorption temperature) and the gas

changed to 15 % CO_2 with the remainder being N_2 (at 100 mL min^{-1}, 1 bar). The temperature was held for 1 hour in order to reach equilibrium, this length of time was sufficient for each of the samples studied to reach a plateau in adsorption. The CO_2 uptake was calculated on a dry basis using Equation 3.15 where ΔW_{CO_2} and ΔW_{H_2O} are the changes in weight at stage 1 (moisture removal) and stage 2 (CO_2 uptake) respectively. A diagram of this can be seen in Figure 3.18. This program will be referred to as a CO_2 loading program in this thesis.

$$CO_2 = \frac{\Delta W_{CO_2}}{100 - \Delta W_{H_2O}} \times 100\ \% \tag{3.15}$$

This method can also be used to determine adsorption kinetics by calculating the time taken to reach 30, 60 and 90 % of the full CO_2 uptake by weight (referred to as t_{30}, t_{60} and t_{90} respectively).

3.2.6 Viscometry

The measurements were carried out on a AMETEK Brookfield Rheometer DV3T instrument with an in-built temperature controller. The method is based off of the BSI and AASHTO standard methods for determining viscosity of bitumen.[179,180]

The neat PEI samples were heated in a horizontal tube furnace at 70 °C under a 1 bar, 1 L min^{-1} N_2 flow for 48 hrs to remove excess water. Approximately 10 g of sample were loaded into the sample cell, and a 34 spindle attached. The sample was heated to the desired temperature (measurements were taken at room temperature and then in 20 degree increments from 30 to 130 °C), and after an equilibration time of at least 10 minutes the spindle speed was increased until the torque was stabilised at approximately 50 %, then measurements of shear stress, rate and viscosity (as calculated by the equipment) were recorded. The units for viscosity are cP (centipoise) which is analogous to mPa·s.

3.2.7 Oxidation of PEI-Silica

Oxidation of PEI-Silica samples was accelerated by heating approximately 0.1 g of sample to 75 °C in a conventional oven for 1-10 days. The PEI-silica was ground

into a powder prior to heating to ensure a homogeneous sample, and even exposure to the air.

Chapter 4

High Temperature Mobility of Deposit Control Additives

4.1 Introduction

This chapter will present and discuss the data obtained over the course of this study on PIB derivatives, carbon blacks and their interactions. Initially the development of the individual methods will be discussed including the repeatability of the experiments. This is followed by the results of the supplementary methods (N_2 adsorption, TGA) and the main focus of this chapter, the proton NMR mobility results. Towards the end of this chapter a brief investigation into the use of silica as an alternate substrate will be shown.

The figures displayed in this section are predominantly to aid in the visualisation of the data by the reader, for this reason lines between points have been included although these are not representative of further data points. In addition, error bars have not been included in most of the graphs for readability, however the majority of the data points were performed in multiples.

For ease of reference over this chapter, Table 3.1 from Section 3.1.8, which contains information on the PIB derivatives used in this study, has been reproduced below as Table 4.1.

Table 4.1: Polymer chain information on PIB derivative samples

Polymer	PIB-M_n ($gmol^{-1}$)	PIB Funct.	Headgroup
PIBSA 2	1000	mono	Succinic Anhydride
PIBSI B	1000	mono	Succinimide with TEPA
PIBSI C	750	mono	Succinimide with AEEA
PIBSI G	1000	bis	Succinimide with TEPA
PIBSI I	750	bis	Succinimide with EDA
PIBSI Y	750	mono	Succinimide with EDA
PIBSI Z	750	bis	Succinimide with TEPA

Where TEPA = tetraethylenepentamine, AEEA = aminoethylethanolamine and EDA = ethylenediamine

4.2 Proton NMR Optimisation and Method Development

The method used was based upon one developed by Sam Bailey, Dr. Jim Barker and Dr. Miguel Castro-Diaz, and the carbon black chosen, MicroCB is the same as used in that study.[57]

The initial measurements of $\Delta H_{\frac{1}{2}}$ were performed as described in Section 3.2.2. To investigate repeatability and reproducibility samples of 50 wt. % PIBSI C on MicroCB were investigated.

To determine error as a result of the equipment a single sample of 20 wt. % PIBSI C on MicroCB was investigated.

4.2.1 Temperature Range

The temperature range used in this study was 30-250 °C, unless stated otherwise. The heating rate used was approximately 3 °C min^{-1}. This rate was based on the speed of the temperature controller and time required to tune/match the probe between acquisitions.

In this study temperatures over 250 °C have not been investigated due to the increased likelihood of volatilised polymer escaping the capsule and contaminating the probe, as indicated by TGA results. As the operating temperature of these polymers is approximately 250 °C, this limit was deemed appropriate for the experiment.

4.2.2 Error and Reproducibility

As with any experimental technique, there are many potential sources of error in these ^{1}H NMR tests. These include: errors associated with the manual control of the heating rate and inherent error within the heating and temperature monitoring systems; the potential for non-homogeneous samples; variation in sample amounts inside the capsules; and variation in the processing.

Overall the greatest error introduced in this method is in the preparation of the sample, as shown in the high reproducibility error. This error is thought to be mostly due to residual solvent at low temperature, but is still significant at high temperature. This error is considered when drawing conclusions, with an expected error of 5 % at 250 °C.

Repeatability of a Single Data Point

To determine error as a result of the equipment, tuning or processing the repeatability of a single arbitrary data point was investigated (20 wt. % PIBSI C). The signal was acquired three times in succession under the same tuning/matching conditions (i.e. without re-tuning) and processed using the same parameters. The greatest deviation from the mean in the resulting $\Delta H_{\frac{1}{2}}$ values was 42 Hz (from a mean of ¿ 4000 Hz), and the relative standard deviation was 0.78 %. The tuning/matching was then adjusted slightly to simulate human error in the tuning/matching process and the signal was acquired under these conditions, this was performed a total of two times. When comparing these to the initial signal the greatest deviation from the mean was 63 Hz, and the relative standard deviation was 1.06 %. To determine the error in processing, the initial signal was processed two further times, with small variations in phasing and baseline correction. The maximum deviation

from the mean seen in these results was 25 Hz, and the relative standard deviation was 0.14 %. For each of these experiments the error is shown to be minimal, with a relative standard deviation of 0.74 % over 9 experiments, when comparing and distinguishing between different polymers.

Repeatability over 30-250 °C

In order to determine the repeatability, the same sample (PIBSI C 50 wt. %) was run in triplicate. The greatest deviation from the mean was 301 Hz (relative standard deviation of 5.44 %) at 100 °C. However at high temperatures (230-250 °C), the greatest deviation from the mean was on average only 68 Hz (relative standard deviation of 2.02 %). On average over the whole range the error is 102 Hz, and the relative standard deviation is 2.86 %. Figure 4.1 shows the $\Delta H_{\frac{1}{2}}$ of each of these samples over 30-250 °C, and Figure 4.2 shows the average with an error bar of one standard deviation. The higher errors at lower temperatures (100 °C) may be due to residual hexane present in the sample which evaporates from the sample at higher temperatures.

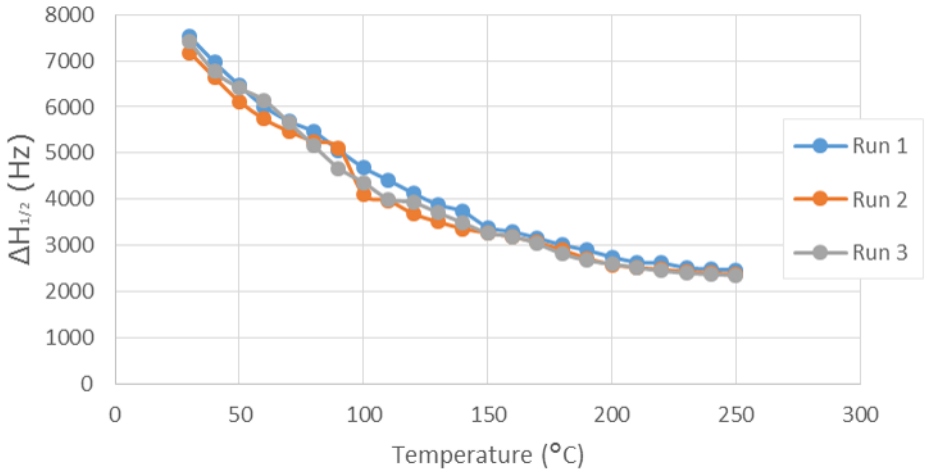


Figure 4.1: $\Delta H_{\frac{1}{2}}$ over 30-250 °C for repeat analysis of 50 wt. % PIBSI C MicroCB dispersions

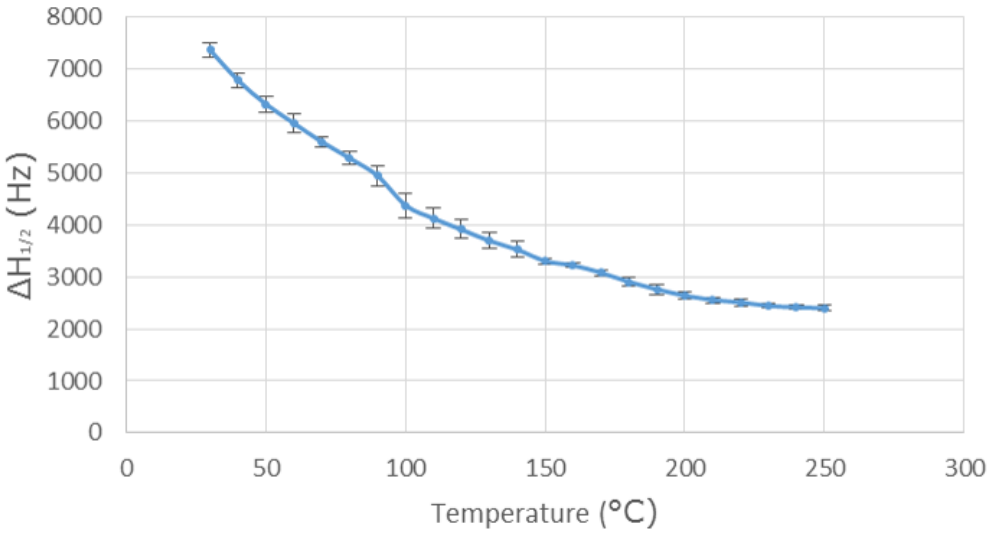


Figure 4.2: Average $\Delta H_{\frac{1}{2}}$ over 30-250 °C for repeat analysis of 50 wt. % PIBSI C MicroCB dispersions, with error bars of one standard deviation

Reproducibility

Reproducibility was investigated through the preparation of two additional samples of 50 wt. % PIBSI C using the same method, as opposed to the repeatability investigation which performed multiple tests on the same sample. Figure 4.3 shows the $\Delta H_{\frac{1}{2}}$ of each of these samples and the average of the existing sample from the previous section over 30-250 °C, and Figure 4.4 shows the average with an error bar of one standard deviation.

The difference in $\Delta H_{\frac{1}{2}}$ between these samples is larger than the error seen in the repeatability test, particularly at low temperatures. This is likely due to differences in the samples caused by changes in sample preparation. The large error at low temperature is likely due to the samples having different levels of residual solvent, although visually the samples appeared very similar. Variation in weight of sample used, volume of solvent used, moisture and solvent content of the samples and inhomogenity of the carbon black or PIBSI sample may also introduce additional error.

The largest deviation from the mean of 1485 Hz (relative standard deviation of 18.84 %) is seen at 30 °C. This large an error means that the data obtained at low temperatures is not very reproducible and should be considered as with reservations. The relative standard deviation is reduced to under 10 % by 100 °C, and under 5 % by 170 °C. The greatest deviation from the mean at the highest temperatures (230-250 °C) is 116 Hz (relative standard deviation of 3.45 %). On average over the whole range the error is 335 Hz (relative standard deviation of 8.34 %).

Obviously the variation in $\Delta H_{\frac{1}{2}}$ is much larger for duplicate samples, especially at low temperatures where the residual solvent (hexane) has not evaporated, than for repeated tests on the same samples. Fortunately the area of interest in this study is the high temperature region, where the error is much smaller. However, in order to reduce the error resulting from residual solvent as much as possible, great care was taken throughout the study to ensure a fully dried and homogeneous sample.

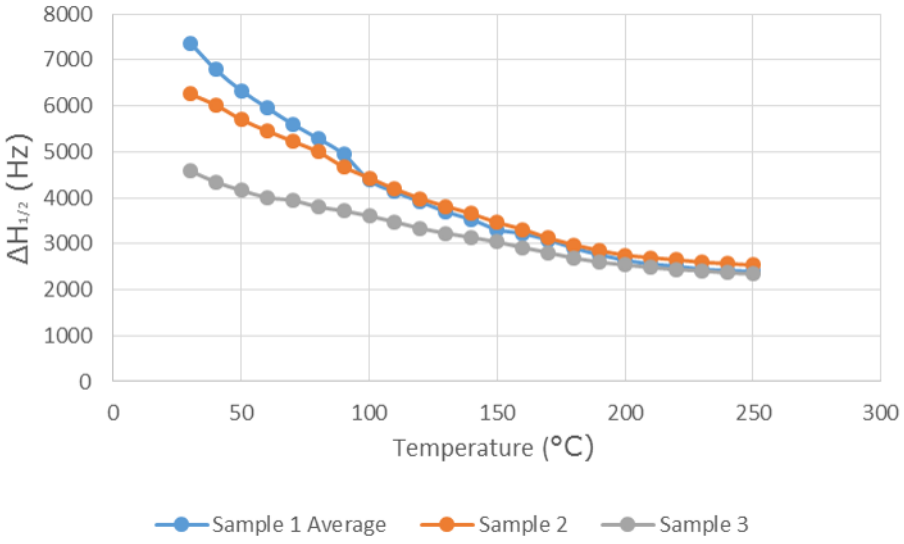


Figure 4.3: $\Delta H_{\frac{1}{2}}$ results for 3 samples of 50 wt. % PIBSI C MicroCB dispersions over 30-250 °C. Each sample was independently prepared in order to determine reproducibility.

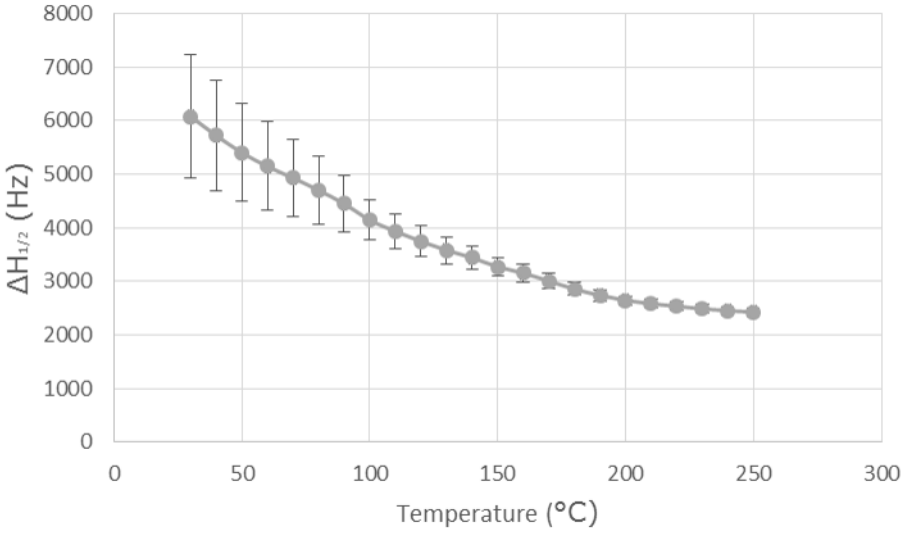


Figure 4.4: Average $\Delta H_{\frac{1}{2}}$ over 30-250 °C for 3 samples of 50 wt. % PIBSI C MicroCB dispersions, with error bars of one standard deviation.Each sample was independently prepared in order to determine reproducibility.

4.2.3 Other Contributions to Signal

A series of ^{1}H NMR tests were performed to investigate the contribution of other factors, than the PIB derivatives to the signal. Tests of the empty probe, a blank capsule and a capsule containing only carbon black showed no discernible signal at ambient temperature or 250 °C. This determined there not to be any other interfering signal.

4.2.4 Peak Fitting: Lorentzian vs Gaussian

The ^{1}H NMR spectra consist almost exclusively of Lorentzian peaks. However to ensure the negligible impact of any Gaussian functions within the spectra, a series of spectra were also fitted to include Gaussian functions. A comparison of the $\Delta H_{\frac{1}{2}}$ data using both pure Lorentzian and mixed fitting for an example spectra (20 wt. % PIBSI C) can be seen in Figure 4.5 (The jump in $\Delta H_{\frac{1}{2}}$ at 120 °C seen in this figure is likely due to inconsistent heating). This figure shows that there is very little variation between the two fittings (the maximum deviation is 1 Hz, with rigid protons functions making up less than 0.05 % of the signal). Therefore it is safe to assume that Gaussian functions, and rigid protons, do no have any meaningful influence on the value of $\Delta H_{\frac{1}{2}}$.

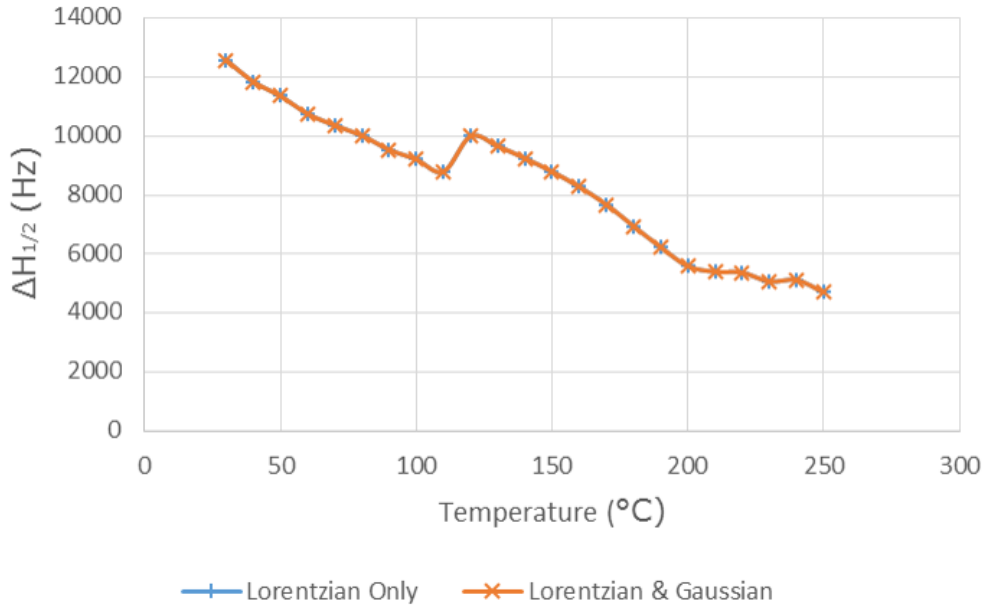


Figure 4.5: Comparison of the $\Delta H_{\frac{1}{2}}$ values of a 20 wt. % PIBSI C MicroCB dispersion over 30-250 °C fitted with and without Gaussian component. The two data sets are almost indistinguishable.

4.3 N_2 Sorption Determined Pore Structure of MicroCB

Using N_2 sorption isotherms the surface area, total pore volume and average pore diameter were determined for MicroCB. The data can be seen in Table 4.2 alongside the data provided by Sigma Aldrich. The N_2 sorption data corresponds well with the product specification, though the pore diameter is somewhat smaller.

	N_2 sorption data	Sigma Aldrich data
Surface area (m^2 g^{-1})	214 ± 1.1	150-250
Total Pore Volume (cm^3 g^{-1})	0.46 ± 0.005	0.5
Average Pore Diameter (nm)	8.5 ± 0.04	10

Table 4.2: Information about pore size for MicroCB as determined by N_2 sorption isotherms and as provided by Sigma Aldrich

4.3.1 Simple Calculation of Monolayer Coverage

The polar surface area (PSA) of each headgroup was calculated through the sum of the atomic contributions, that can be found in Table 4.3, of the individual atoms in the headgroup.[181] This method has been previously applied to PIBSIs by Kim et al. in 2015.[88] This was compared to the BET calculated surface area of MicroCB, to determine a theoretical monolayer coverage for each of the PIBSIs. An example of this process can be seen in Appendix A.2

Atom Type	PSA Contribution (Å^2)
N#R	23.8
NHR_2	12.0
NH_2R	26.0
OR_2	9.2
OHR	20.2

Table 4.3: Atomic Contributions to PSA (# denotes a triple bond)

Monolayer coverage is assumed to be when the surface area of headgroup of the polymer equals the total surface area of the carbon black. An equation expressing this can be seen in Equation 4.1. The results can be seen in Table 4.4.

$$\frac{PolymerMass \times N_a \times PSA}{PolymerM_n} = CBSA \times CBMass \tag{4.1}$$

Where PolymerMass and CBMass refers to the mass of Polymer and MicroCB, respectively, at monolayer coverage, CBSA refers to the BET determined MicroCB surface area and N_a is Avogadro's number.

Table 4.4 shows the calculated monolayer coverage using Equation 4.1 is generally around 40 wt. %, however this is using a model based on comb-like adsorbance and is the maximum value for monolayer coverage. It would therefore be expected, and is seen in the results, that monolayer coverage would be lower if the polymer tail has any contact with the MicroCB surface (e.g. mushroom configuration). PIBSA has a much higher predicted monolayer percentage than the PIBSIs, this is due to the much smaller headgroup.

Table 4.4: Predicted Monolayer Coverage

PIB Derivative	PIB Headgroup	PSA	Predicted Monolayer
PIBSI B	TEPA	88.0	43 ± 0.5 %
PIBSI C	AEEA	58.2	30 ± 0.5 %
PIBSI G	TEPA	88.0	43 ± 0.5 %
PIBSI I	EDA	52.0	40 ± 0.5 %
PIBSI Y	EDA	52.0	40 ± 0.5 %
PIBSI Z	TEPA	88.0	43 ± 0.5 %
PIBSA	N/A	9.2	85 ± 0.5 %

4.4 Thermogravimetric Analysis of PIB Derivatives

Thermogravimetric analysis was performed on each of the PIB derivative samples using a proximate analysis method (as described in Section 3.2.5). This method is primarily performed under nitrogen flow, so shows volatilisation and decomposition rather than combustion. A section of the results of this analysis can be seen in Figure 4.6.

The difference in moisture content between the samples can be seen by the initial difference in weight between the PIB derivatives on Figure 4.6, this weight

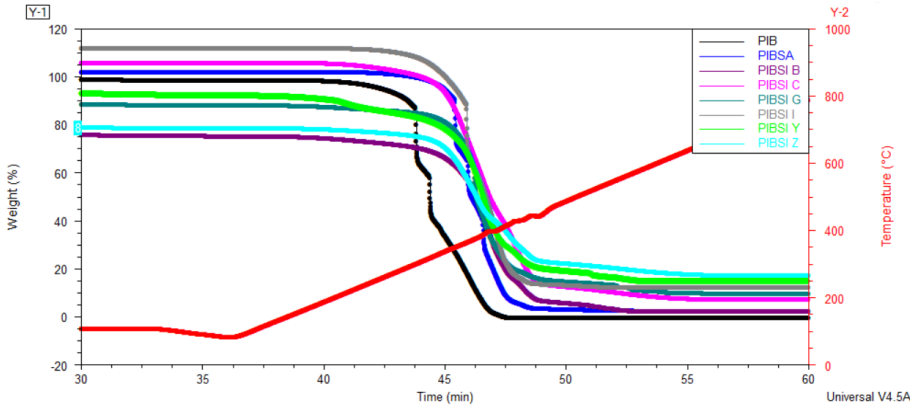


Figure 4.6: TGA proximate analysis data for each of the PIB derivatives (offset of 2.5-17.5 % added to Weight (%) for visual clarity)

loss occurs at 100 °C and is not included on this figure. PIBSI Z has the highest moisture content, PIBSI B, Y and G have a moderate moisture content, and PIB, PIBSA, PIBSI C and PIBSI I have very little moisture content (see Table 4.5 for values). The moisture content does not seem to have any correlation with any of the properties of the PIB derivatives, i.e. molecular weight and headgroup, however as the samples were prepared at different times, the moisture content may be due to differences in synthesis and/or storage conditions. Preparation of PIBSI-MicroCB dispersions accounts for the moisture content.

PIB Derivative	Moisture Content (wt. %)
PIB	1 ± 0.5
PIBSA	1 ± 0.5
PIBSI B	27 ± 0.5
PIBSI C	1 ± 0.5
PIBSI G	22 ± 0.5
PIBSI I	1 ± 0.5
PIBSI Y	23 ± 0.5
PIBSI Z	39 ± 0.5

Table 4.5: Moisture content of PIB derivatives, as determined by TGA

From Figure 4.6, it can be seen that the PIB derivatives have similar volatilisation rates, with PIB volatilising sooner, and therefore, at a lower temperature than the other samples. There is a small weight loss of approximately 10 wt. % of PIB at around 100 °C which is attributed to volatilisation of the sample, this is followed by almost complete weight loss (approximately 90 wt. %) occurring between 300 and 400 °C, which is thought to be the result of thermal decomposition. The other PIB derivatives begin to volatilise at around 150-250 °C, with significant weight loss of 80-90 wt. % (thermal decomposition) between 325-375 and 425-450 °C depending on sample. This is likely due to the lower molecular weight of PIB compared to the other samples (1075 M_w vs 1170-3473 M_w), and the lack of a headgroup which will increase electrostatic and van der Waals forces between the molecules. Any

remaining sample is generally lost by 600 °C.

PIBSI Y is distinct from the rest of the samples in that the weight loss that occurs between 200 °C and 350 °C is more significant that the other PIB derivatives, this is may indicate a higher proportion of free EDA (the headgroup) remaining in the PIBSI sample after synthesis.

PIBSA and PIB also seem to volatilise in stages, this may be a result of different molecular weight fractions of the sample having different volatilisation points. This is not really seen for any of the PIBSI samples.

With all of the samples the vast majority of the weight loss occurs before 600 °C degrees, and decomposition is seen at around 350 °C. As all of the experimental work performed on the PIB derivative samples is at or below 250 °C, the chance of significant thermal decomposition of the samples is low. However, there is some volatilisation below 250 °C, which may have some impact on the results of other techniques.

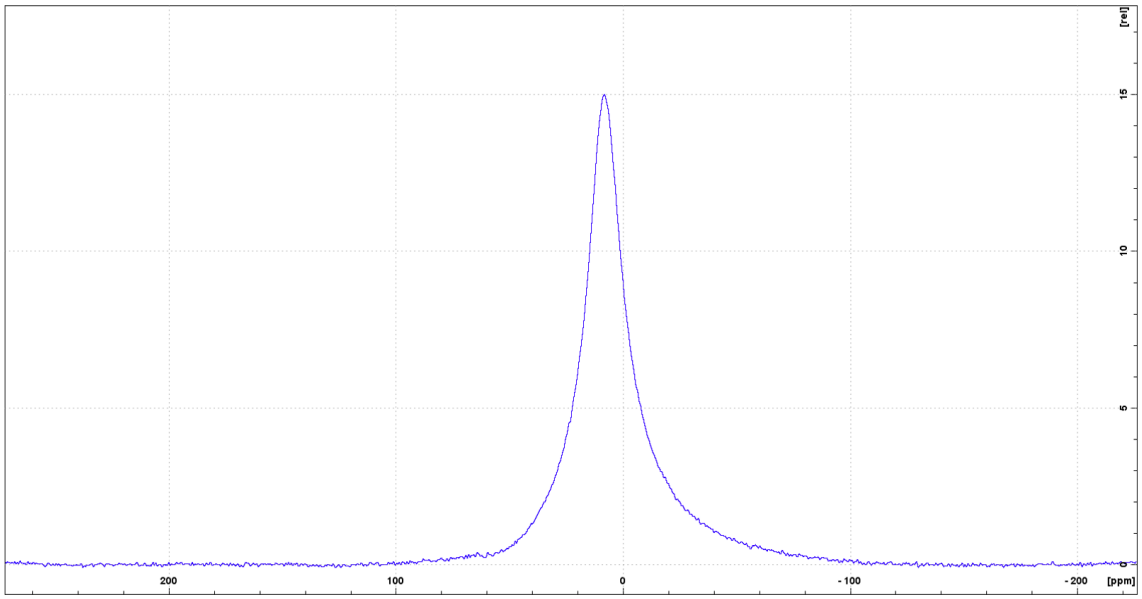


Figure 4.7: An example ^{1}H NMR spectrum of 7.5 % PIBSI C adsorbed on microCB. This spectrum was acquired at 250 °C.

4.5 Proton NMR Determined Mobility of PIB Derivative MicroCB Dispersions

The mobility of protons in molecules can be inferred from the peak half width ($\Delta H_{\frac{1}{2}}$) of the singular peak in the broadline ^{1}H NMR spectrum. An exemplar ^{1}H NMR spectrum can be seen in Figure 4.7. The mobility is inversely related to $\Delta H_{\frac{1}{2}}$, which is the unit used to display the mobility here. In this section the mobility data for dispersions of PIB derivatives and MicroCB is presented, the use of MicroCB as the substrate determined through prior work finding it to have the strongest interactions with PIB derivatives. The results presented here have a specific focus on the operational temperature of deposit control additives.

In this section the average ^{1}H NMR $\Delta H_{\frac{1}{2}}$ results for each PIB derivative MicroCB dispersion over the entire temperature range studied for that dispersion are shown followed by a comparison of the data of all of the PIB derivative dispersions at 250 °C. $\Delta H_{\frac{1}{2}}$ is inversely proportional to mobility and spin-spin relaxation time (T_2).

4.5.1 Trends in Mobility between PIB Derivatives and MicroCB over 30-250 °C

In this section the data from each of the PIB derivative MicroCB dispersions are presented individually and then compared. The PIBSI samples are listed in alphabetical order followed by the PIBSA and PIB samples. The data obtained at 250 °C is examined in more detail in Section 4.5.3 and the discussion of the key findings from this data can then be found in Section 4.7.

PIBSI B

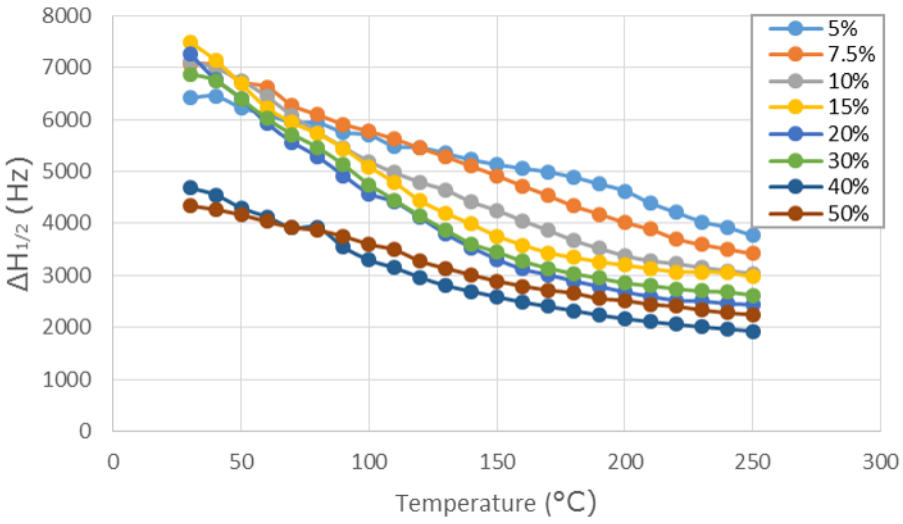


Figure 4.8: ^{1}H NMR data for various loadings of PIBSI B on MicroCB over 30-250 °C

PIBSI B has is a mono- functionalised PIBSI with TEPA headgroup and a PIB chain length with a M_n of approximately 1000.

The ^{1}H NMR spectra for PIBSI B MicroCB dispersions, at loadings of 5-50 wt. %, were acquired over 30-250 °C. The mobility data over this temperature range for each of the loadings can be seen in Figure 4.8. The mobility tends to increase ($\Delta H_{\frac{1}{2}}$ decreases) with temperature, this is expected due to the increase in kinetic energy of the molecules would result in increased movement and mobility. This trend is seen by all loadings although the 5 wt. % sample increases at a slower gradient than the other lower loading samples.

There is also a general trend of increasing mobility with increasing polymer loading, other than 20 wt. % and 30 wt. % which are very similar, and 5 wt. % below 150 °C.

PIBSI C

PIBSI C has is a mono- functionalised PIBSI with AEEA headgroup and a PIB chain length with a M_n of approximately 750.

The ^{1}H NMR spectra for PIBSI C MicroCB dispersions, at loadings of 5-50 wt. %, were acquired over 30-250 °C. The mobility data over this temperature range for each of the loadings can be seen in Figure 4.9. Much of trends are in common with the other PIBSIs studies with the mobility tending to increase ($\Delta H_{\frac{1}{2}}$ decreases) with temperature. This is expected as the increase in kinetic energy of the molecules results in increased molecular movement and therefore increased mobility. This trend is seen by all loadings except for 5 wt. %, which generally decreases with temperature, with a small increase at 170 °C.

The general trend of increasing mobility with increasing polymer loading is also seen with this PIBSI, with the exception being 5 wt. %, and 10 wt. % at temperatures above 160 °C.

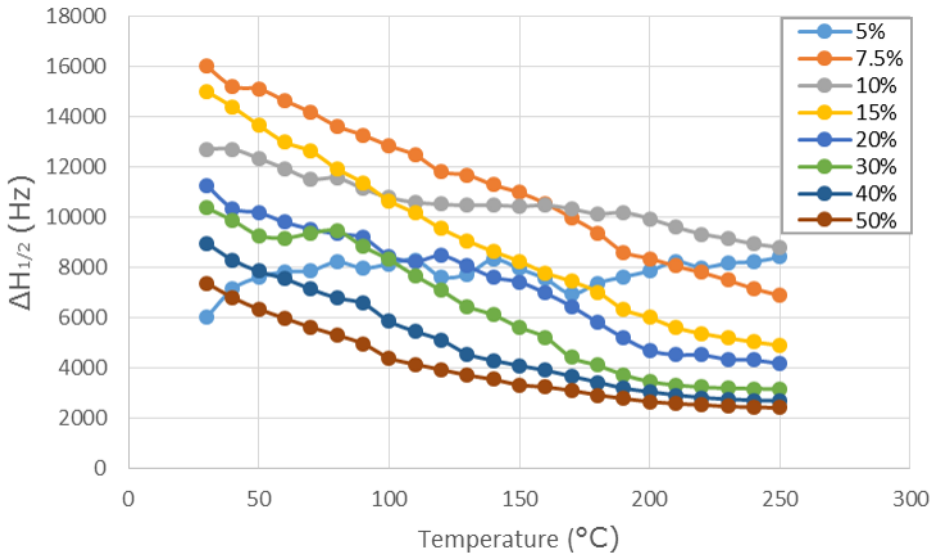


Figure 4.9: ^{1}H NMR data for various loadings of PIBSI C on MicroCB over 30-250 °C

PIBSI G

PIBSI G has is a bis- functionalised PIBSI with a TEPA headgroup and a PIB chain length with a M_n of approximately 1000 $gmol^{-1}$.

The ^1H NMR spectra for PIBSI G MicroCB dispersions, at loadings of 5-50 wt. %, were acquired over 30-250 °C. The mobility data over this temperature range for each of the loadings can be seen in Figure 4.10. Here the mobility also tends to increase ($\Delta H_{\frac{1}{2}}$ decreases) with temperature. This trend is seen for all loadings although there is some deviation at low temperatures for the 15 wt. % sample which has a small decrease in mobility at 50 ° at and the mobility of the 7.5 wt. % sample remains stable over the middle part of the temperature range (100-150 °C).

Again, there is a general trend of increasing mobility with increasing polymer loading for loadings under 20 wt. % (20 wt. %, 30 wt. % and 40 wt. % all have very similar mobilities over the majority of the temperature range), except for 7.5 wt. % which shows a higher mobility under 200 °C than the 10 wt. % sample (and at points the 15 wt. % sample). The 5 wt. % sample shows a significantly lower mobility than the other samples over the whole temperature range.

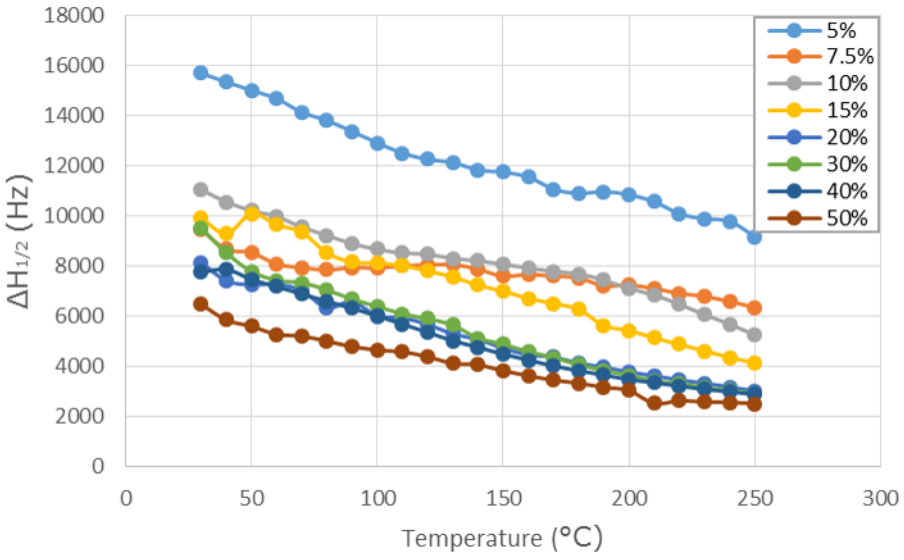


Figure 4.10: ^1H NMR data for various loadings of PIBSI G on MicroCB over 30-250 °C

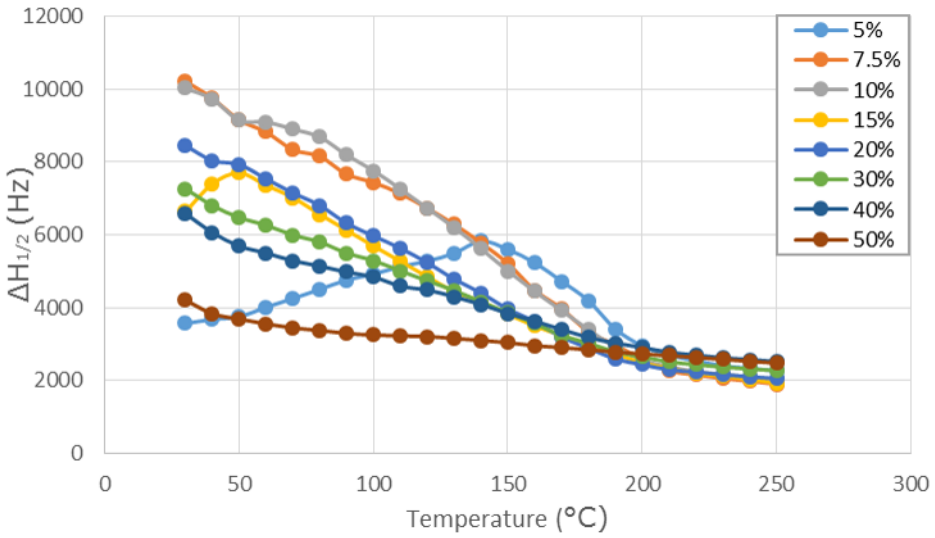


Figure 4.11: ^{1}H NMR data for various loadings of PIBSI I on MicroCB over 30-250 °C

PIBSI I

PIBSI I has is a bis- functionalised PIBSI with a EDA headgroup and a PIB chain length with a M_n of approximately 750 gmol^{-1}. The ^{1}H NMR spectra for PIBSI I MicroCB dispersions, at loadings of 5-50 wt. %, were acquired over 30-250 °C. The mobility data over this temperature range for each of the loadings can be seen in Figure 4.11. This sample shows lower distinctions in mobility at higher temperatures and a less consistent trend of increasing mobility with temperature, with 5 wt. % and 15 wt. % deviating from this trend. The mobility of the 5 wt. % sample decreases between 30-140 °C and then increases for the remainder of the temperature range, and the mobility of the 15 wt. % sample initially decreases until 50 °C.

At temperatures of below 150 °C, the trend of increasing mobility with increasing loading that is seen with the other samples is seen with the 20-50 % samples, however at low loadings or higher temperatures this trend is not observed.

All of the polymer loadings have very similar mobilities between 200 and 250 °C.

PIBSI Y and Z

In addition to the aforementioned PIBSIs: B, C, G and I, two further PIBSI samples were also investigated, as a comparison to the existing data set. These were PIBSI Y and Z. PIBSI Y has a 750 M_n PIB tail and an EDA headgroup. PIBSI Z also has a 750 M_n PIB tail but has a TEPA headgroup in bis configuration (two PIB tails). The spectra for PIBSI Y and Z were acquired in 50 degree intervals, from 50 to 250 °C due to time constraints and can be seen in Figures 4.12 and 4.13.

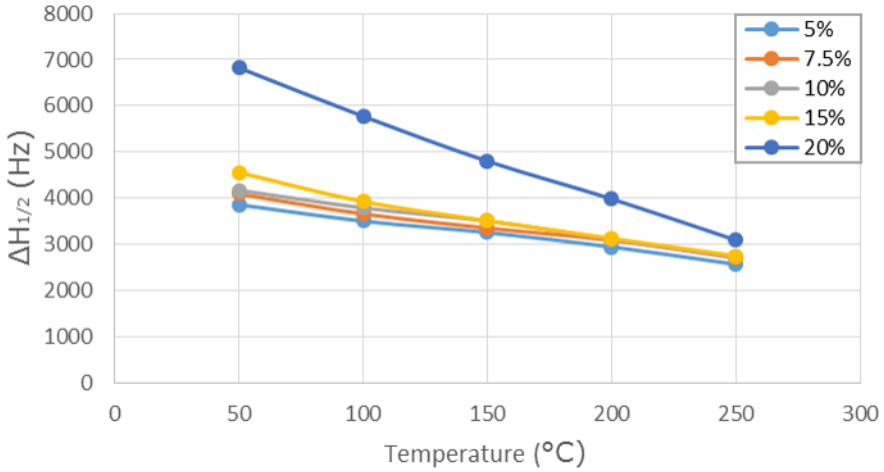


Figure 4.12: ^{1}H NMR data for various loadings of PIBSI Y on MicroCB over 30-250 °C

For both the PIBSI Y and PIBSI Z dispersions, there is a general trend of increasing mobility with temperature for all samples, as is seen in many of the other PIBSI samples. PIBSI Y also shows a trend of increasing mobility with decreasing molecular weight. This has not been seen in any of the other samples. PIBSI Z, however, shows little consistent relationship between loading and mobility. The two higher loading samples for PIBSI Z show a considerably steeper increase in mobility with temperature from 50-150 °C than the other 3 loadings.

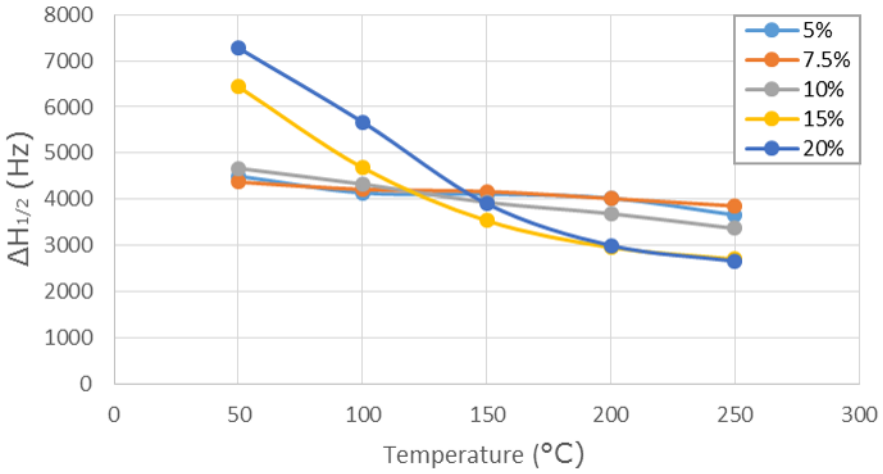


Figure 4.13: ^{1}H NMR data for various loadings of PIBSI Z on MicroCB over 30-250 °C

PIBSA and PIB

In addition to PIBSI samples, a sample of both PIBSA and PIB were investigated. These were a PIBSA with an approximately 1000 M_n tail and an approximately 750 M_n PIB.

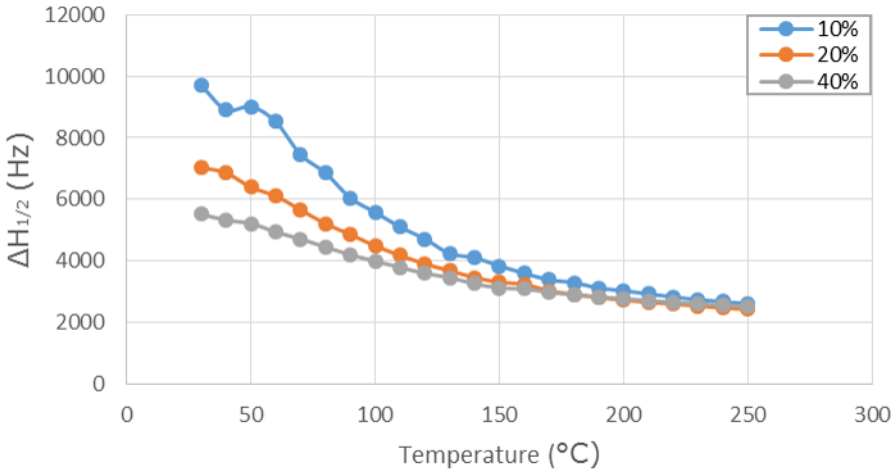


Figure 4.14: ^{1}H NMR data for various loadings of PIB on MicroCB over 30-250 °C

The ^{1}H NMR spectra for PIB MicroCB dispersions, at loadings of 10, 20 and 40%, were acquired over 30-250 °C. The mobility data over this temperature range

for each of the loadings can be seen in Figure 4.14. Again, there is a trend of increasing mobility with temperature for all three samples and the mobility increases with polymer loading. All of the samples show very similar $\Delta H_{\frac{1}{2}}$ values between 200-250 °C.

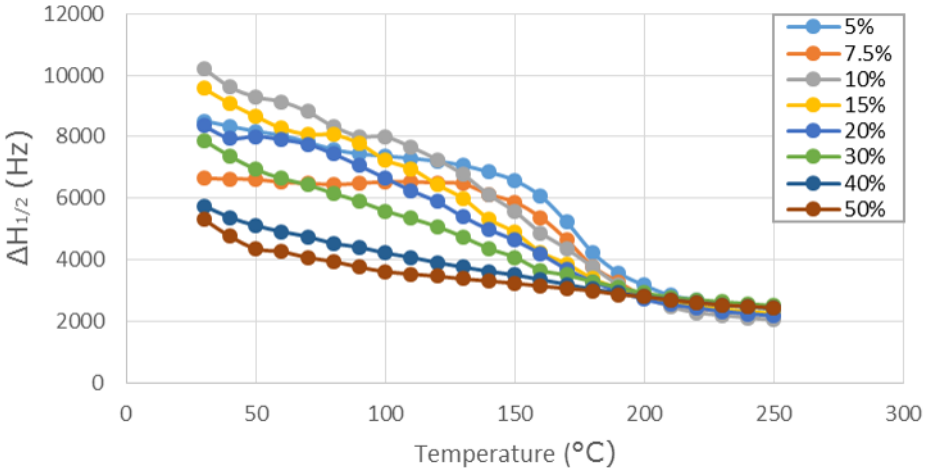


Figure 4.15: ^{1}H NMR data for various loadings of PIBSA on MicroCB over 30-250 °C

The ^{1}H NMR spectra for PIBSA MicroCB dispersions, at loadings of 5-50%, were acquired over 30-250 °C. The mobility data over this temperature range for each of the loadings can be seen in Figure 4.15. The general trend of increasing mobility with temperature for all samples is also seen with the PIBSA sample and the mobility tends to increase with polymer loading. All of the samples show very similar $\Delta H_{\frac{1}{2}}$ values between 200-250 °C.

4.5.2 Effect of Polymer Loading on Mobility over 30-250 °C

The effect of the loading of PIB derivatives on MicroCB was investigated across PIBSI B, C, G, I and PIBSA 2 from 5 to 50 wt. % loading; PIBSI Y and Z, from 5 to 20 wt. % loading; PIB from 10 to 40 wt. % loading. The results can be seen in Figures 4.8, 4.9, 4.10, 4.11, 4.15, and 4.14.

Generally speaking, the overall trend seen is a decrease in $\Delta H_{\frac{1}{2}}$ with both temperature and loading, however several of the 5 wt. % loadings were separate from

the trend.

Decreasing $\Delta H_{\frac{1}{2}}$ relates to an increase in mobility, thus it is expected that the trend of decreasing $\Delta H_{\frac{1}{2}}$ with rising temperature would be seen. This is due to the increased energy of the molecules, resulting in increasing movement and mobility. A similar trend was also found in a 1998 study of poly(methyl acrylate) adsorbed on silica.[182]

Increased mobility (decreased $\Delta H_{\frac{1}{2}}$) with increasing polymer loading was also seen across many of the samples. This likely results from an increased proportion of the polymer being free in the pores rather than directly interacting with the carbon surface, resulting in an increased average mobility. It is for this reason that it is hypothesised that the most accurate measure of dispersant strength will occur at monolayer coverage, which is closer to the operational nature of the deposit control additive. Those samples which did not see this trend, specifically those of PIBSI Y, may have a different adsorption configuration or may have been unsuited to the impregnation method used. As PIBSI I, a similar PIBSI to Y just with a longer PIB chain, also did not seem to follow this trend it is possible that it is related to the headgroup, EDA, used in these PIBSIs.

Several of the 5 wt. % loading samples follow the aforementioned downwards trend between $\Delta H_{\frac{1}{2}}$ and temperature less strongly than the other loadings. In addition to this all of the 5 wt. % samples but that of PIBSI G and some of the 7.5 wt. % have lower data points (higher mobility) at low temperature than would be expected, when considering the general trend between loading and $\Delta H_{\frac{1}{2}}$. This may result from the loading of these samples being at or below monolayer coverage. At low temperatures the molecules will have less energy and be less mobile, this means that the impact of interactions with the carbon surface will have a much lower impact on mobility, but the effects of entanglement between polymer molecules will still be present. This results in the low loading samples having an unexpectedly high mobility compared to those with higher loadings. As temperature increases the impact of the molecules interacting with the surface rather than "floating" free in the pore cavity will be more pronounced and the samples at lower loadings will be

relatively less mobile than those with a greater proportion of polymer free to move within the pores.

4.5.3 Effect of Polymer Loading on Mobility at 250 °C

In this section the $\Delta H_{\frac{1}{2}}$/mobility of each of the PIB derivative MicroCB dispersions at 250 °C is displayed against the polymer loading. The PIBSI samples are listed in alphabetical order, followed by the PIBSA and PIB samples.

PIBSI B

The ^{1}H NMR spectra for PIBSI B MicroCB dispersions, at loadings of 2-50 wt. %, were acquired over 30-250 °C. The mobility data for 250 °C can be seen in Figure 4.16. The mobility is initially fairly high at 2 wt. % loading with a $\Delta H_{\frac{1}{2}}$ of 2436 Hz, then decreases at 5 wt. % loading with a $\Delta H_{\frac{1}{2}}$ of 3764 Hz. After this the mobility tends to increase with loading percentage. This increase in mobility may be associated with increasing free PIBSI in the MicroCB pores and the peak in $\Delta H_{\frac{1}{2}}$ at 5 wt. %, may correspond with monolayer coverage.

The 2 wt. % values for each of the PIBSIs are significantly lower than those at 5 wt. %. This may be an experimental artifact as at low loadings the error would be expected to increase. However the loading of PIBSI on MicroCB was monitored and the experiments repeated in triplicate, with the results maintaining an acceptable level of consistency.

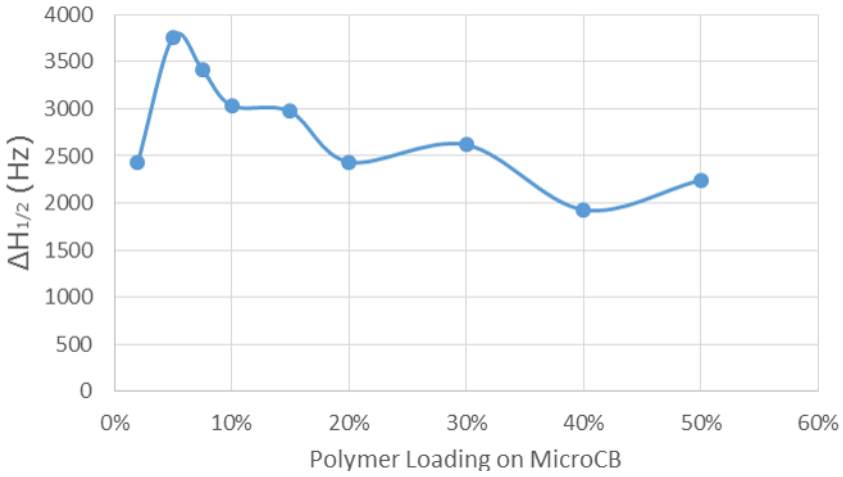


Figure 4.16: Mobility of PIBSI B MicroCB dispersions of different loadings at 250 °C

PIBSI C

The ^{1}H NMR spectra for PIBSI C MicroCB dispersions, at loadings of 2-50 wt. %, were acquired over 30-250 °C. The mobility data for 250 °C can be seen in Figure 4.17. The mobility is initially high at 2 wt. % loading with a $\Delta H_{\frac{1}{2}}$ of 4812 Hz, then decreases at 5 wt. % loading to a $\Delta H_{\frac{1}{2}}$ of 8406 Hz and after which stabilises over 7.5-10 wt. % (6873-6816 Hz) and then increases with loading percent. The increase in mobility between after 10 wt. % may be associated with increasing free PIBSI in the MicroCB pores and the peak in $\Delta H_{\frac{1}{2}}$ at 5 wt. %, may correspond with monolayer coverage.

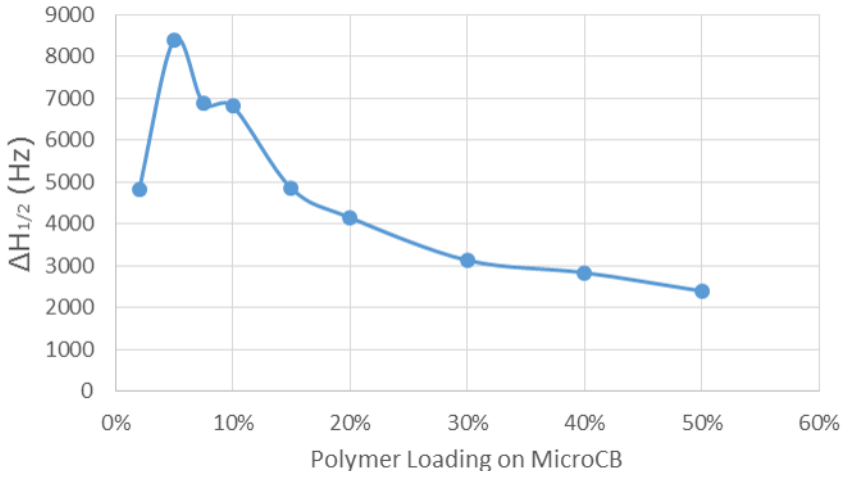


Figure 4.17: Mobility of PIBSI C MicroCB dispersions of different loadings at 250 °C

PIBSI G

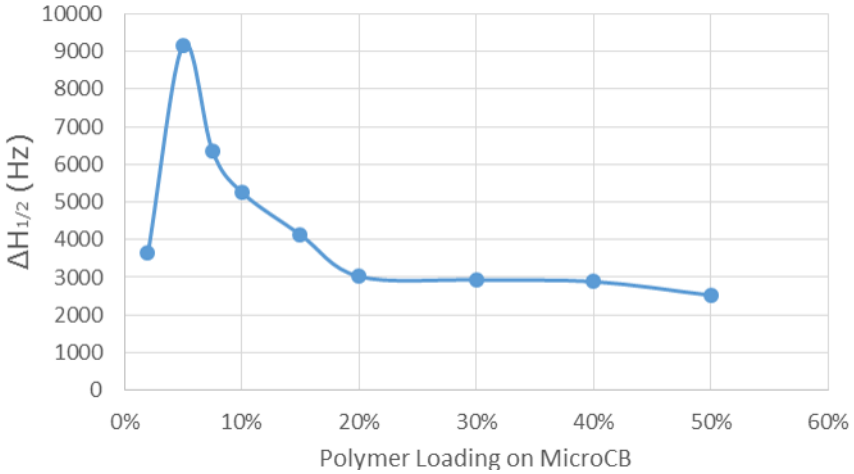


Figure 4.18: Mobility of PIBSI G MicroCB dispersions of different loadings at 250 °C

The ^{1}H NMR spectra for PIBSI G MicroCB dispersions, at loadings of 2-50 wt. %, were acquired over 30-250 °C. The mobility data for 250 °C can be seen in Figure 4.18. The mobility is initially high at 2 wt. % loading with a $\Delta H_{\frac{1}{2}}$ of 3640 Hz, then decreases significantly at 5 wt. % loading to a $\Delta H_{\frac{1}{2}}$ of 9172 Hz and after which it increases with loading percent. The increase in mobility between after 5 wt. % may be associated with increasing free PIBSI in the MicroCB pores and the peak in $\Delta H_{\frac{1}{2}}$ at 5 wt. %, may correspond with monolayer coverage. It is believed that this peak corresponds with monolayer coverage as one would expect the polymer molecules

directly interacting with the surface to be less mobile than those free in the pores or interacting in a multi-layer fashion. In addition, at monolayer coverage, compared to sub-monolayer coverage, the polymer will be more tightly packed on the surface and thus less mobile. It therefore logically follows that the least mobile polymer would be found, on average, at monolayer coverage. This feature is also seen in several of the other PIBSI dispersions.

PIBSI I

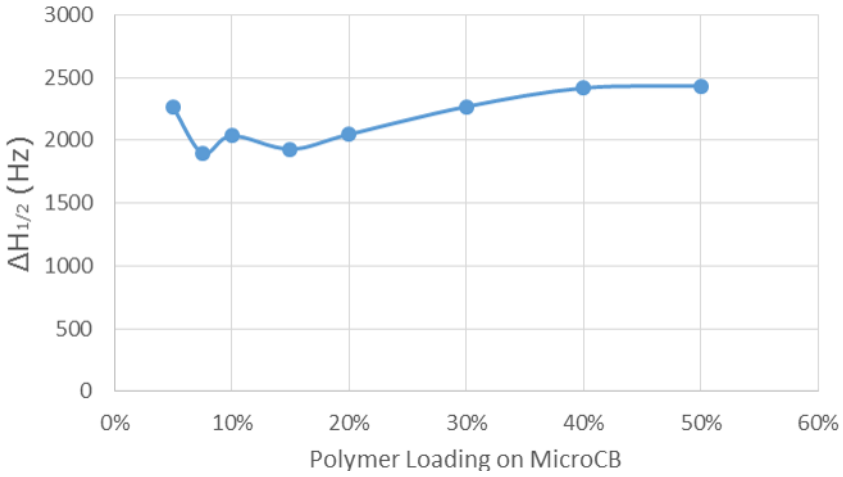


Figure 4.19: Mobility of PIBSI I MicroCB dispersions of different loadings at 250 °C

The ^{1}H NMR spectra for PIBSI I MicroCB dispersions, at loadings of 5-50 wt. %, were acquired over 30-250 °C. The mobility data for 250 °C can be seen in Figure 4.18. The mobility is consistently high (1900-2400 Hz) but seems to decrease at very low loading (5 wt. %) and higher loadings (40 and 50 wt. %). The peak in $\Delta H_{\frac{1}{2}}$ at 5 wt. %, may correspond with monolayer coverage and the increasing $\Delta H_{\frac{1}{2}}$ after 15 wt. % is unexpected when compared to the other samples. This increase corresponds to a decreasing mobility with loading, which is not generally seen by the other samples at high temperatures. However it is seen by many of the other samples at low temperature, and is likely just a reflection of the low interaction strength between PIBSI I and MicroCB.

PIBSI Y

The ^{1}H NMR spectra for PIBSI Y MicroCB dispersions, at loadings of 5-20 wt. %, were acquired over 50-250 °C. The mobility data for 250 °C can be seen in Figure 4.20. The mobility is consistently high (2400-3100 Hz) and decreases with polymer loading percentage, however the entire range of values is only around 500 Hz.

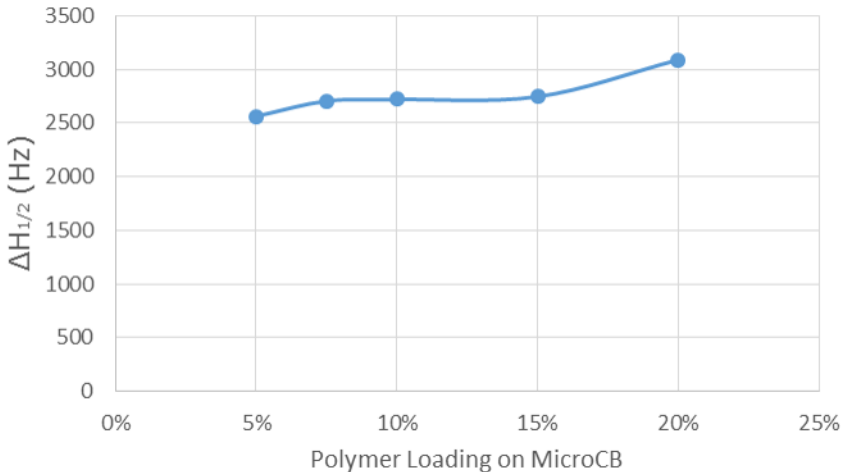


Figure 4.20: Mobility of PIBSI Y MicroCB dispersions of different loadings at 250 °C

PIBSI Z

The ^{1}H NMR spectra for PIBSI Z MicroCB dispersions, at loadings of 2-20 wt. %, were acquired over 50-250 °C. The mobility data for 250 °C can be seen in Figure 4.20. The mobility is initially high, decreasing from 2 to 7.5 wt. % (2029 to 3825 Hz) and then increasing with polymer loading percentage. The peak in $\Delta H_{\frac{1}{2}}$ at 7.5 wt. % loading may indicate the monolayer coverage.

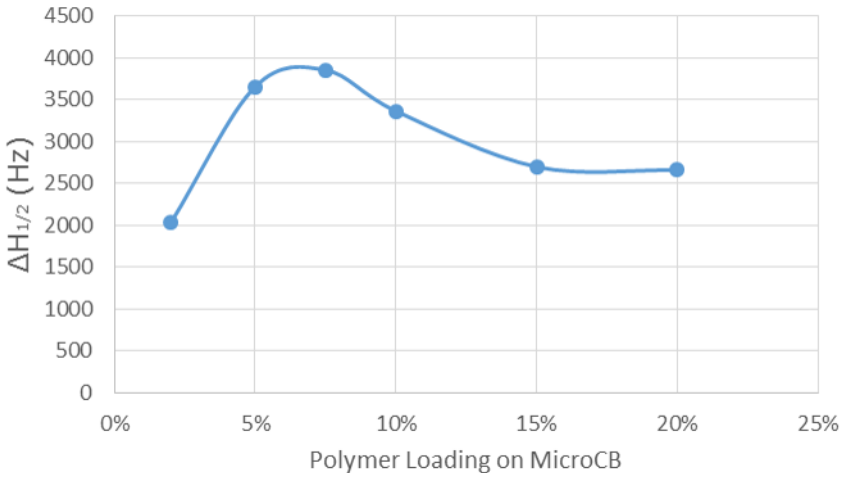


Figure 4.21: Mobility of PIBSI Z MicroCB dispersions of different loadings at 250 °C

PIBSA

The ^{1}H NMR spectra for PIBSA MicroCB dispersions, at loadings of 2-50 wt. %, were acquired over 30-250 °C. The mobility data for 250 °C can be seen in Figure 4.22. The mobility is high (2000-2500 Hz), with fairly constant values of $\Delta H_{\frac{1}{2}}$, in a range of approximately 500 Hz.

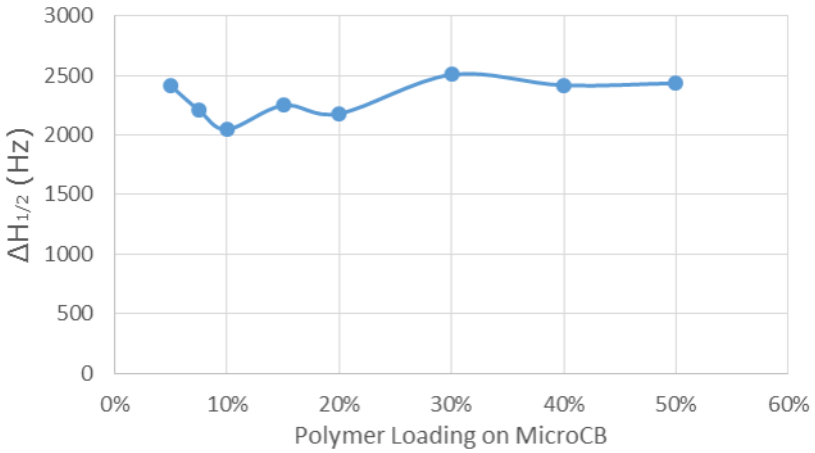


Figure 4.22: Mobility of PIBSA 2 MicroCB dispersions of different loadings at 250 °C

PIB

The ^{1}H NMR spectra for PIB MicroCB dispersions, at 10, 20 and 40 wt. % loadings, were acquired over 30-250 °C. The mobility data for 250 °C can be seen in

Figure 4.23. The mobility is high, with fairly constant values of $\Delta H_{\frac{1}{2}}$, in a range of approximately 200 Hz (2400-2600 Hz).

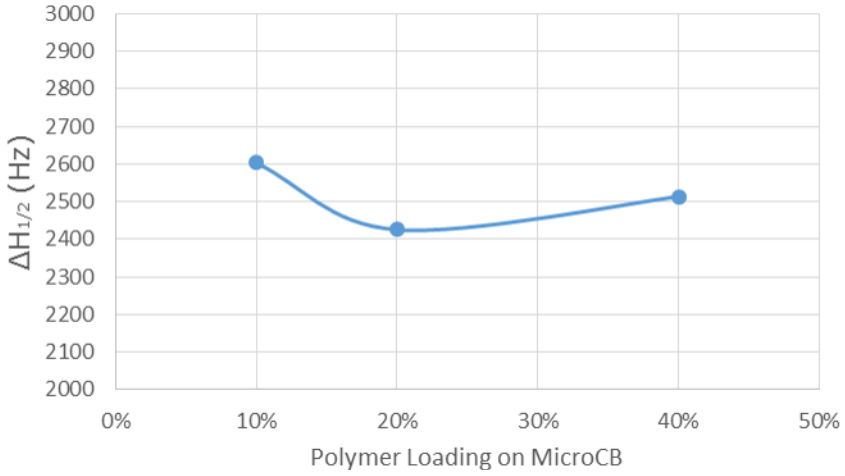


Figure 4.23: Mobility of PIB MicroCB dispersions of different loadings at 250 °C

4.6 Comparison of PIBSI Samples by Structure

In this section PIBSIs with similar structures will be compared in order to determine the impact of individual structural changes on mobility.

4.6.1 Impact of mono- and bis- Functionalisation

PIBSI Y was selected in contrast to PIBSI I as they have the same headgroup (EDA) and tail length but different functionalisations, with Y being mono and I being bis-functionalised. In Figure 4.24, the difference in $\Delta H_{\frac{1}{2}}$ between the two PIBSIs can be seen from 5-20 wt. % loading. PIBSI I has consistently higher $\Delta H_{\frac{1}{2}}$, and lower mobility, at loading greater than 10 wt. %. This is likely due to entanglement related to the additional polymer tail. At 5 wt. % loading, $\Delta H_{\frac{1}{2}}$ is similar for both Y and I, this may correspond with monolayer coverage.

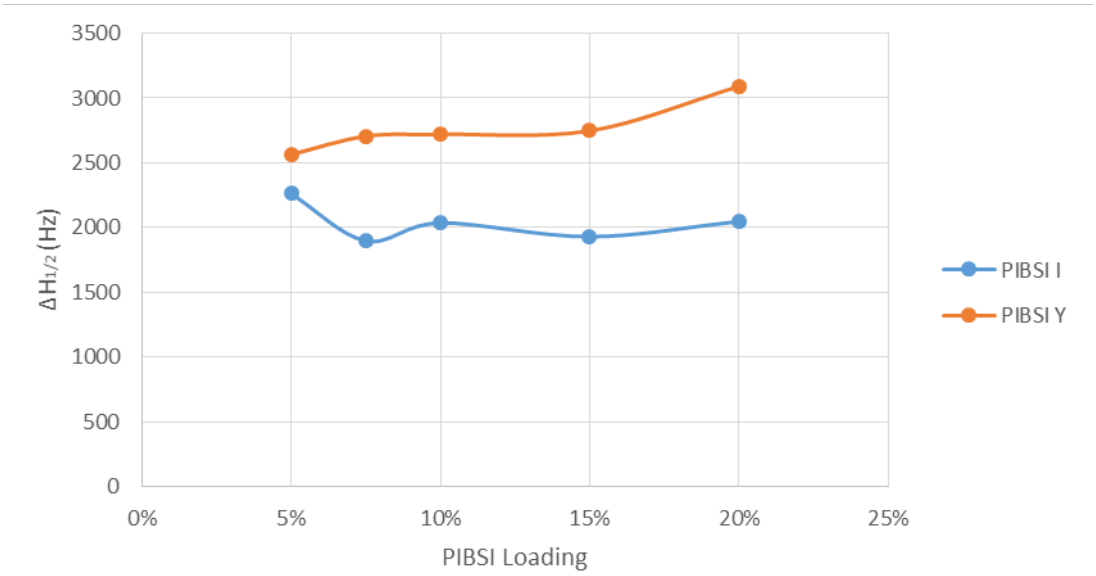


Figure 4.24: A comparison of the ^{1}H NMR $\Delta H_{\frac{1}{2}}$ for PIBSI I (bis-) and PIBSI Y (mono-) at 250 °C over 5-20 wt. % polymer loadings

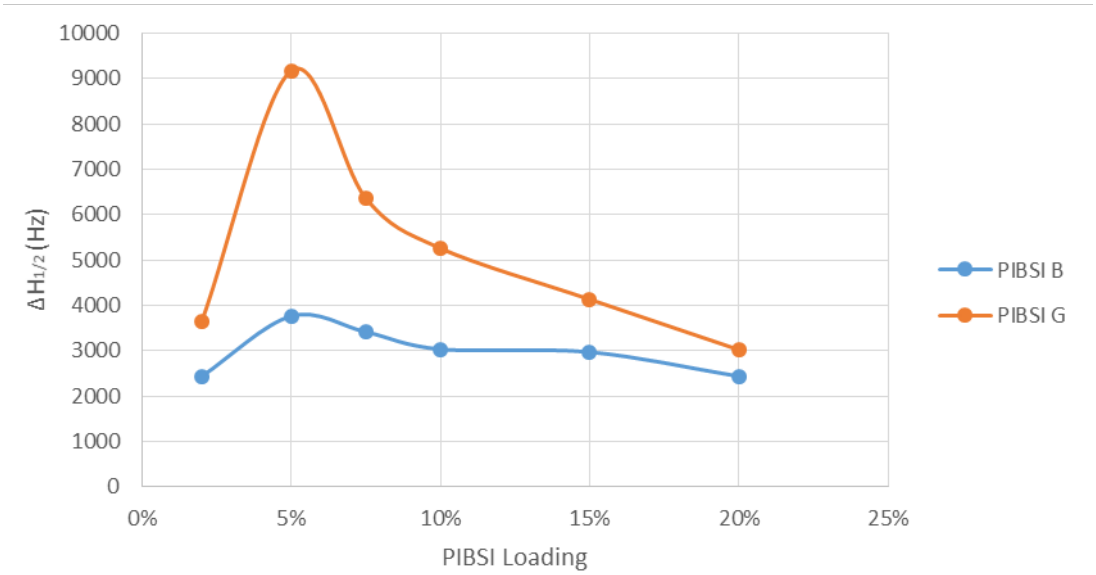


Figure 4.25: A comparison of the ^{1}H NMR $\Delta H_{\frac{1}{2}}$ for PIBSI G (bis-) and PIBSI B (mono-) at 250 °C over 2-20 wt. % polymer loadings

PIBSI B and G both have a TEPA headgroup and 1000 gmol^{-1} M_n tail length, B has mono- functionality and G has bis- functionality. From Figures 4.25 and 4.28, it is clear that at low loading $\Delta H_{\frac{1}{2}}$/mobility differs vastly between the two polymer dispersions. The bis- PIBSI, G, shows much lower mobility (higher $\Delta H_{\frac{1}{2}}$) than the mono- PIBSI, I. This is a much larger contrast than is seen in PIBSI I and Y. The mobility of the two polymers is similar at higher (30-50 wt. %) loadings.

Although the mobility is very different between the two PIBSIs at low loading, both show a peak in $\Delta H_{\frac{1}{2}}$ at a similar loading of 5 wt. %.

4.6.2 Impact of PIB Chain Length

PIBSI Z was selected to contrast to PIBSI G, as they have the same headgroup (TEPA) and bis- functionality but different PIB chain lengths. PIBSI Z has a PIB of 750 M_n gmol^{-1}, where as PIBSI G has a longer chain of 1000 gmol^{-1}. In Figures 4.28 and 4.26, the difference in mobility between the different chain length can be seen, with the longer chain length resulting in a significantly lower mobility.

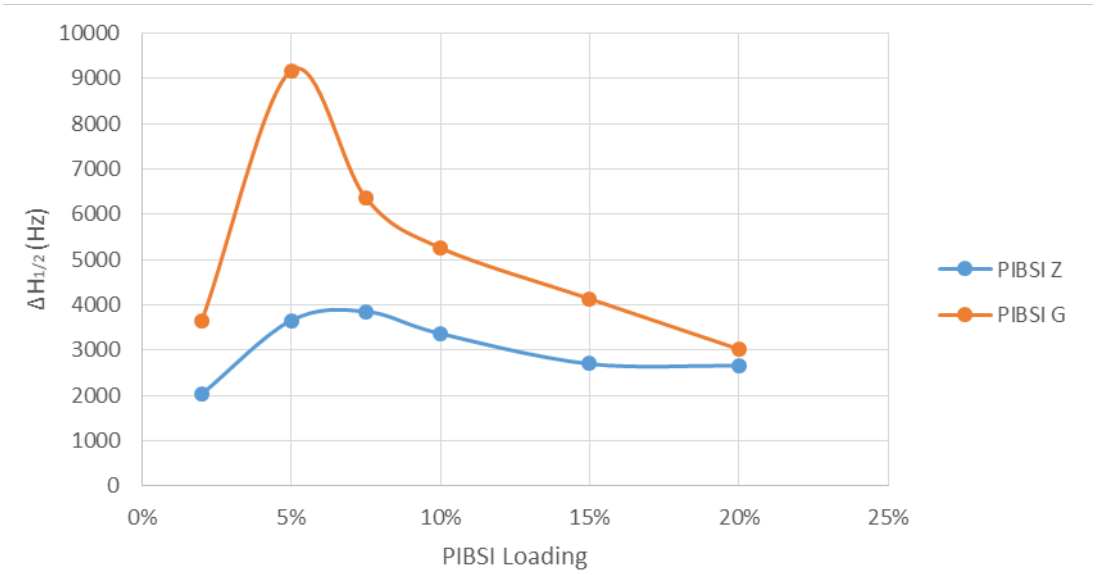


Figure 4.26: A comparison of the ^{1}H NMR $\Delta H_{\frac{1}{2}}$ for PIBSI G (1000 M_n PIB) and PIBSI Z (750 M_n PIB) at 250 °C over 2-20 wt. % polymer loadings

As seen with PIBSI G and B in Section 4.6.1, although the mobility is very different between the two PIBSIs at low loading, both show a peak in $\Delta H_{\frac{1}{2}}$ at a

similar loading (5 wt. % and 7.5 wt. % respectively).

4.6.3 Comparison of PIBSI with TEPA Headgroups

In Sections 4.6.1 and 4.6.2, PIBSI G has been compared to PIBSIs B and Z respectively, the $\Delta H_{\frac{1}{2}}$ for all three PIBSIs at 250 °C can be seen in Figure 4.27. In Figure 4.27 PIBSI G shows a significantly lower mobility at low polymer loading, with the values beginning to converge at 20 wt. % loading. The mobility for PIBSI B and Z are very similar with the lowest mobility for each occurring at 5 wt. % and 7.5 wt. % respectively.

As discussed in previous sections, the chain length and bis/mono functionality of the PIBSI seems to impact the mobility to a significant degree, suggesting a greater influence of the PIB chain on the mobility than initially thought.

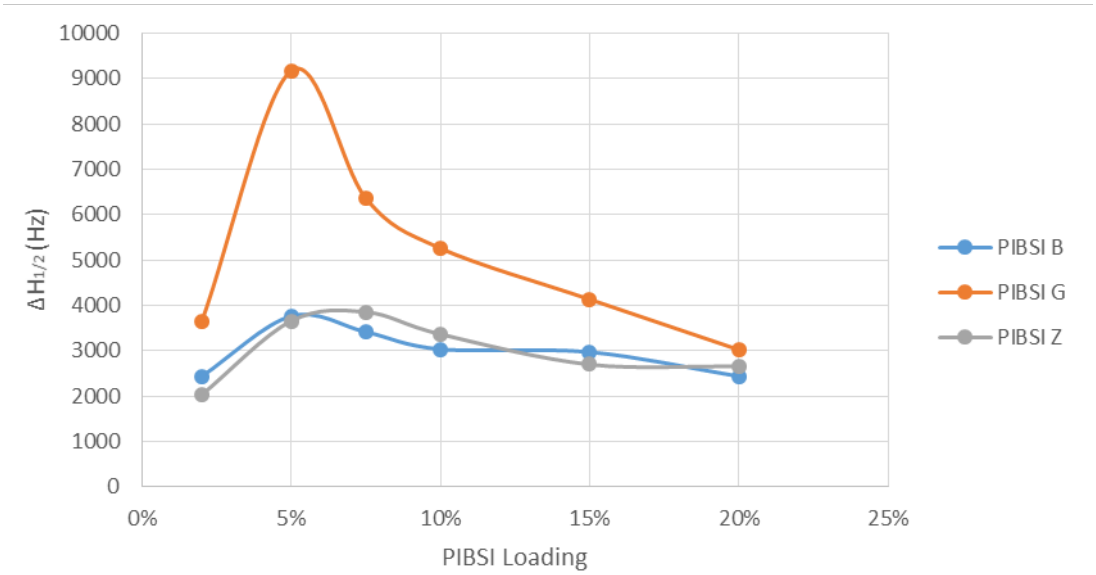


Figure 4.27: Comparison of PIBSI with TEPA Headgroups adsorbed on MicroCB, ^{1}H NMR performed at 250 °C

4.7 Comparison of Mobility of PIB Derivatives on MicroCB at 250 °C

Figure 4.28 displays the data collected for each polymer and loading at 250 °C. This includes, in addition to the data presented in the previous section (Section 4.5.1), the data for spectra that were acquired at 250 °C for 2 wt. % loading for PIBSIs G, C, B, and Z. From this data it can be seen that the PIB derivative dispersions all have similar $\Delta H_{\frac{1}{2}}$ values for the higher loadings investigated in this study, specifically 30-50 wt. %. However at lower loadings, especially around 5-10 wt. %, there is significant variation in the values of $\Delta H_{\frac{1}{2}}$ and thus the mobility of these samples.

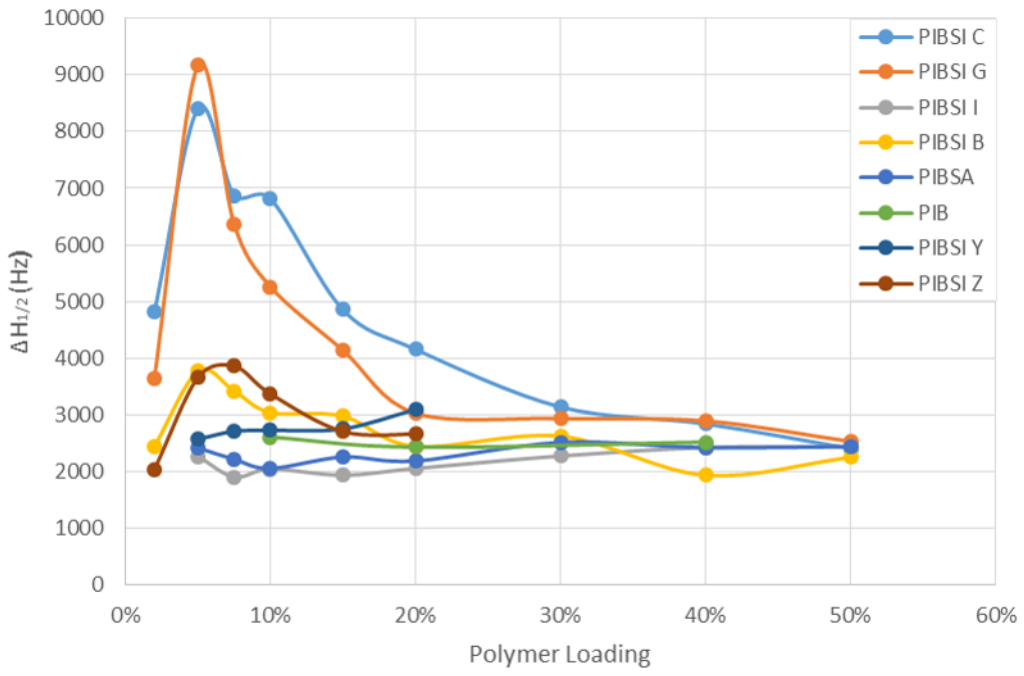


Figure 4.28: Comparison of PIB derivatives adsorbed on MicroCB, ^{1}H NMR performed at 250 °C

4.7.1 Proton NMR Determined Monolayer Coverage

As previously discussed, it might be expected that monolayer coverage would correspond with a minimum in the sample mobility (a peak in $\Delta H_{\frac{1}{2}}$). In Figure 4.29,

a region has been highlighted (5-7.5 wt. %), where the mobility tends to be lowest, to give a visual representation of a possible monolayer region. When compared to the theoretical monolayer determined using the PSA in Section 4.3.1, the monolayer loading of PIBSI G, C, B and Z appears at a much lower percentage loading than predicted (see Table 4.6). This indicates that there is significant interaction between the polymer tail and the the surface, rather than just between the headgroups and the surface. Therefore PSA is not a relevant method for determining the monolayer coverage of these PIB derivatives on MicroCB. It is however possible that the PSA monolayer coverage is more accurate for the other PIB derivatives.

Table 4.6: PSA predicted monolayer coverage and NMR Determined monolayer coverage

PIB Derivative	PSA	Monolayer (%)	
		PSA Predicted	NMR Determined
PIBSI B	88.0	43	5
PIBSI C	58.2	30	5
PIBSI G	88.0	43	5
PIBSI Z	88.0	43	7.5

This information also suggests that the adsorption does not occur for these materials in a comb regime, but rather a more complex configuration, for example a mushroom regime (see Figure 2.6), or with the polymer chain adsorbing closer to horizontal on the carbon surface. It may be the case that the strongly interacting polymers have a greater level of chain-surface interactions than the more weakly interacting ones.

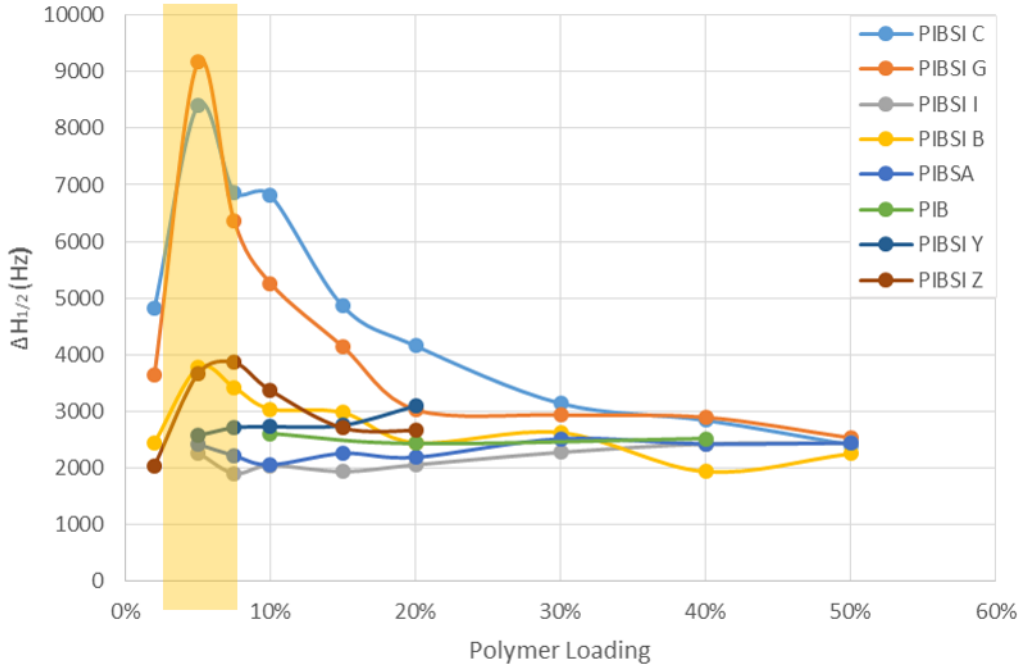


Figure 4.29: Comparison of PIB derivatives adsorbed on MicroCB with the potential monolayer region highlighted

4.7.2 Grouping of PIB Derivatives by Interaction Strength

In previous work by Sam Bailey, two groupings of PIB derivatives (Groups 1 and 2) were suggested. Group 1 being strongly interacting and Group 2 being weakly interacting, distinguished by high and low $\Delta H_{\frac{1}{2}}$ respectively (above and below 4000 Hz).[57]

Furthering the categorisation method initially suggested by Bailey, the PIB derivatives have been categorised into 3 categories, Group 1, 2 and 3, by the $\Delta H_{\frac{1}{2}}$ value at monolayer coverage or 5 wt. % polymer loading. These groups are thought to correspond with how strongly the PIB derivative is interacting with the MicroCB surface. Group 3 consists of very strongly interacting DCAs with a $\Delta H_{\frac{1}{2}}$ at 5 wt. % loading of greater than 6000 Hz. Group 2 consists of less strongly interacting polymers at around 4000 Hz (3000-6000 Hz) and Group 1 consists of very weakly interacting at less than 3000 Hz.

The addition of a 3rd category, is to highlight those PIB derivatives which interaction strength is no stronger than PIB or PIBSA, and thus the headgroups are

having no impact on interaction strength.

When drawing these groupings the reproducibility errors seen in Section 4.2.2 were considered. None of the PIB derivatives categorisations would be expected to change, even with an error of 5-10 %

These distinctions are highlighted in Figure 4.30 and Table 4.7.

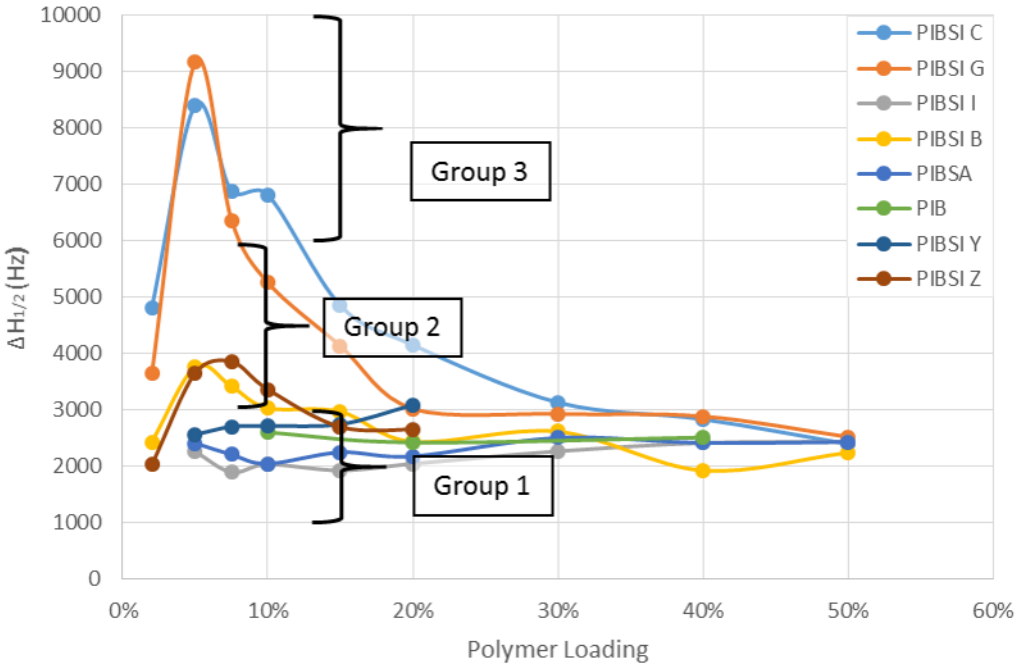


Figure 4.30: Grouping of PIB derivatives by interaction strength

PIB Derivative	Chain Length ($gmol^{-1}$)	Headgroup	PIB Funct.	Group
PIB	750	none	n/a	1
PIBSA	1000	Succinic Anhydride	mono	1
PIBSI B	1000	Succinimide with TEPA	mono	2
PIBSI C	750	Succinimide with AEEA	mono	3
PIBSI G	1000	Succinimide with TEPA	bis	3
PIBSI I	750	Succinimide with EDA	bis	1
PIBSI Y	750	Succinimide with EDA	mono	1
PIBSI Z	750	Succinimide with TEPA	bis	2

Table 4.7: Grouping of PIB derivatives by interaction strength, including approximate PIB chain length and headgroup information

4.7.3 Using Proton NMR to Investigate PIB Derivatives as Deposit Control Additives

From the mobility of the samples, insight into the efficacy of the samples as deposit control additives can be gleaned. Lower mobility indicates a stronger interaction between the PIB derivative and the surface, restricting the motion of the adsorbed molecule. A strong interaction between the carbon surface and the PIB derivative is necessary for an effective deposit control additive as the additive must be able to bind with carbonaceous materials and remove them from engine surfaces or prevent the deposition of the particles onto engine surfaces.

However considering that the NMR determined monolayer coverage does not align with the PSA calculated monolayer (as seen in Table 4.6), for the samples which provided a clear peak in $\Delta H_{\frac{1}{2}}$, it is important to question the nature of the adsorption of these PIB derivatives onto the carbon surface and how this impacts the action as a deposit control additive. Not only must the DCA adsorb on to the carbonaceous material, it must then dissolve effectively into the fuel mixture. If not only the polar headgroup but also the PIB tail is strongly interacting with the surface it is possible that the solubility of these dispersions in fuel will be reduced. This was not

seen when preparing the samples in hexane, where all of the dispersions maintained suspension at 50 °C while mixing and when left to stand for short amounts of time. However this aspect was not actively investigated.

Considering PIB and PIBSI as constants, as they are known to have little impact as deposit control additives, and the grouping suggested previously, it would be expected for PIBSI I and Y to perform poorly as deposit control additives, for PIBSIs B and Z to show some deposit control, and for PIBSIs C and G to perform very well.

To gain some insight into the accuracy of this, examples of similar PIBSIs were found in the literature. The closest analogue to one of the PIBSIs studied was a PIBSI similar to B, which had a similar PIB chain length and the same headgroup configuration. This PIBSI has been shown to be an effective deposit control additive.[88] PIBSI B falling into the "less strongly interacting" Group 2, with stronger interactions with MicroCB than those of PIB/PIBSA, and being effective as a deposit control additive suggests that this group

The literature also shows PIBSIs similar to B and I, but with longer PIB chains (M_n of 1300 vs 1000 and 750, respectively) to have been good deposit control additives.[87] However PIBSI I falls into the "very weakly interacting" Group 1. However, if the increased PIB chain length is assumed to have a similar impact to that found with PIBSI G and I, that is a longer PIB chain results in lower mobility and stronger interactions, this does not disprove the hypothesis.

Unfortunately, to the best of this authors knowledge, there is no currently published work discussing the efficacy of any other PIBSIs with similar structures to those studied in this project, although it is likely that unpublished data exists within industrial research settings. This difficulty in finding published information on the efficacy of these materials at deposit control is a serious hindrance in the research into these materials and the development of testing techniques.

As literature data using engine testing methods was not found for either PIBSI G or C, it is unclear as to whether these PIBSIs and the "very strongly" interacting Group 3, function well as deposit control additives. This being said, the literature

does reference both TEPA and AEEA as PIBSI headgroups that have been used for deposit control[87,88] and synthesis methods which may result in some bis functionality of PIBSI samples.[86,91,183] There it might be reasonable to think that these materials may perform well as deposit control additives. However, it is possible that an increase in interactions between the PIB tail and the surface might lead to lower solubility in fuels, and thus decreased effectiveness as DCAs. If this was the case, it might be expected to see the dispersions fall out of solution with hexane while standing. Although no dedicated investigation into this has occurred, this has not been observed during sample preparation.

From the information available and the theoretical background, it is suggested by the author of this work, that the grouping into which these PIB derivatives fall, by strength of interaction between the derivative and MicroCB in a dispersion, may possibly be considered an indication of the potential efficacy of the PIB derivatives as deposit control additives. Specifically, that the PIB derivatives that have a $\Delta H_{\frac{1}{2}}$ at 5 wt. % loading of PIB derivative on MicroCB, as determined by broadline ^{1}H NMR at 250 °C, of greater than 3000 Hz, may have use as deposit control additives in diesel fuels, whereas those that have a $\Delta H_{\frac{1}{2}}$ of below 3000 Hz under these same conditions are likely to be poor deposit control additives.

4.8 Further Investigations of PIBSIs and their Dispersions using Solid State NMR

Carbon-13 NMR spectra were acquired using a cross polarisation pulse sequence and magic angle spinning (CP MAS), unless otherwise specified. This method was selected over a single pulse excitation, due to the significantly reduced experiment time (hours rather than days). Having a fast experiment time is necessary to to develop a commercially viable testing method.

Rather than for characterisation, these methods were originally attempted in order to try and investigate T_2 at the sub-molecular level. Hence the continued use of NMR in the solid state. However, as is explained in the following sections, due

to limitations associated with the materials this was not achieved.

4.8.1 Characterisation of Liquid PIBSIs Using Solid State Carbon-13 NMR

Preliminary C experiments were performed on liquid PIBSI C and G as a control. The spectra acquired can be seen in Figures 4.31 and 4.32..

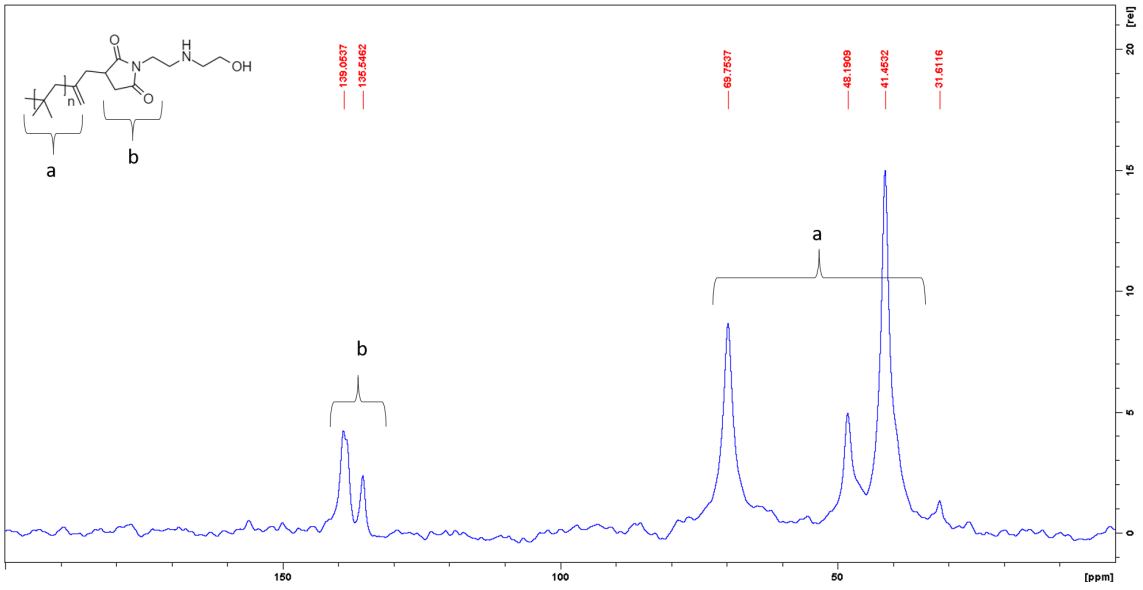


Figure 4.31: ^{13}C-^{1}H CP MAS NMR spectrum for PIBSI C, acquired at ambient temperature under a spinning speed of 1000 Hz, a contact time of 3000 ms, and with a spectrometer calibrated to TKS (at 3.5 ppm). The peaks at 135 and 138 ppm are likely to be the result of terminal isobutylene carbons and the peaks between 30-70 ppm are tentatively asssociated with carbons in the PIB chain.

These liquid CP ^{13}C NMR spectra were performed on the same spectrometer (Bruker ML300) as the solid samples, however due to the propensity of the liquid samples to leak from the capsule into the internal aspects of the spectrometer, the capsules were only half filled and the samples spun at 500-1000 Hz (rather than 5000 Hz for solid samples). Fortunately very high spinning speeds are unnecessary, as the sample is already somewhat isotropic.

There is no distinct difference between the C and G spectra which is likely due to the relatively small impact of the headgroup on the spectra, as it will be dominated

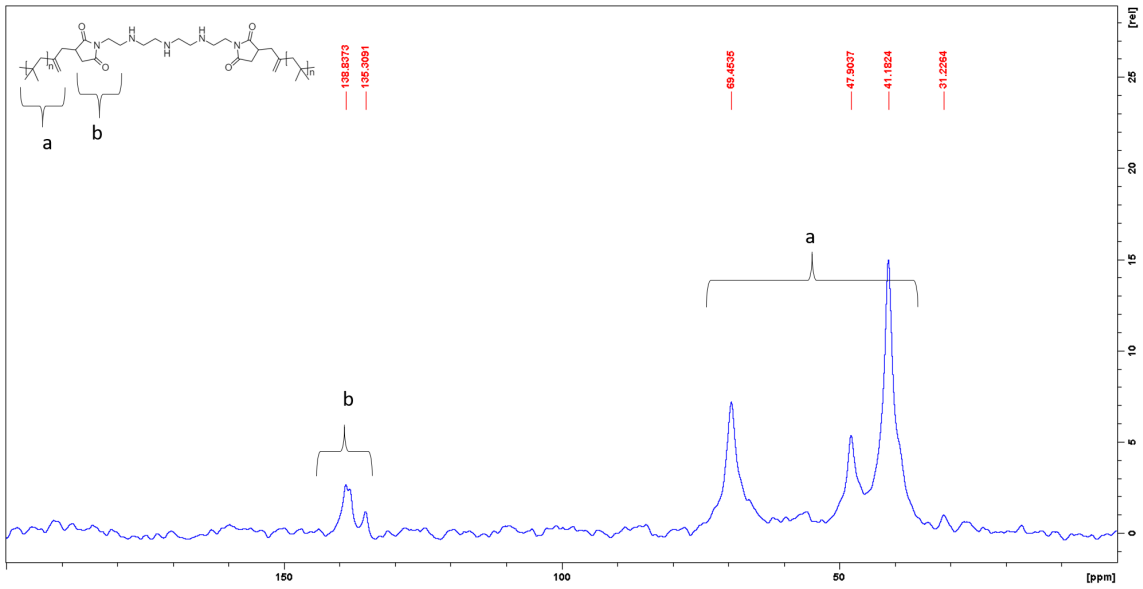


Figure 4.32: ^{13}C-^{1}H CP MAS NMR spectrum for PIBSI G, acquired at ambient temperature under a spinning speed of 750 Hz, a contact time of 3000 ms, and with a spectrometer calibrated to TKS (at 3.5 ppm). The peaks at 135 and 138 ppm are likely to be the result of terminal isobutylene carbons and the peaks between 40-70 ppm may result from the carbons in the PIB chain.

by the PIB chain. In addition, only small differences in chemical shielding between the headgroup carbon centres would be expected (all of the carbons in each of the headgroups would be expected to appear at 30-60 ppm).[184] When comparing these spectra (Figures 4.31 and 4.32) to the literature of polyisobutylenes and PIB derivatives, the chemical shifts of the peaks are in keeping with prior works however the spectra acquired here have less resolved peaks and are thus not able to be fully assigned.[185,186]

Comparison of SPE and CP Spectra

A single pulse excitation ^{13} spectra of PIBSI C was acquired to compare to the CP spectra.

The SPE (Figure 4.33) and CP (Figure 4.31) spectra both have intense peaks at 41 ppm, 48 ppm, 69 ppm and 138 ppm however the relative intensity of the vinylic peaks (130+ ppm) is significantly decreased in the CP spectra. This is to be expected

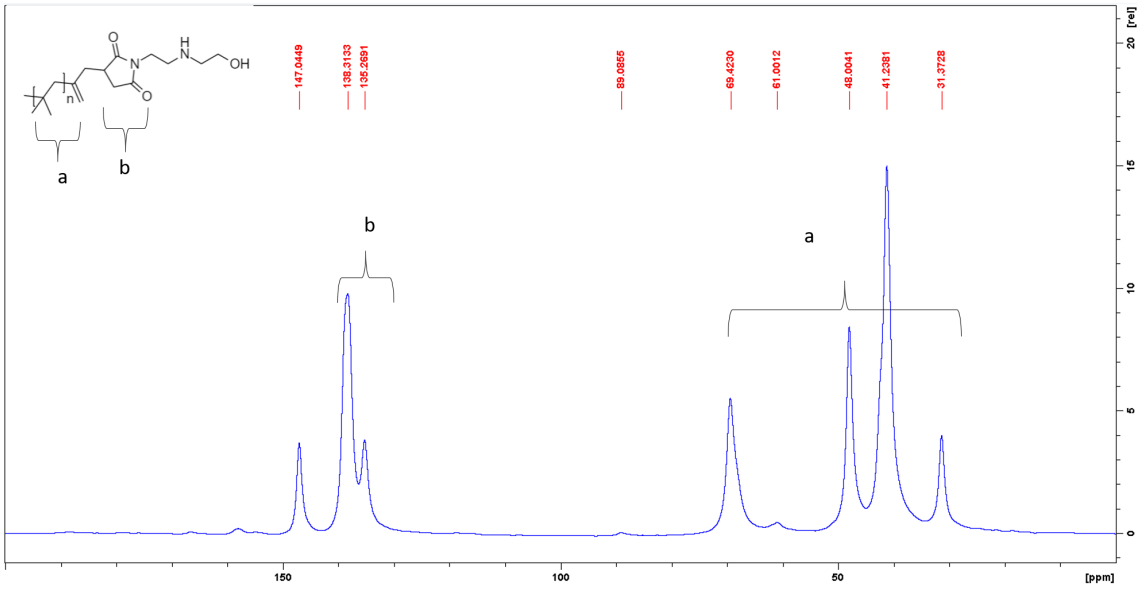


Figure 4.33: Single pulse excitation ^{13}C NMR spectrum for PIBSI C, acquired at ambient temperature under a spinning speed of 1000 Hz, a contact time of 3000 ms, and with a spectrometer calibrated to TKS (at 3.5 ppm)

as CP uses adjacent protons to the carbon centres to transfer magnetisation to the carbons, and thus carbons with a greater number of adjacent protons will have a greater intensity than those with fewer adjacent protons.

The signal to noise ratio is different between each of the spectra shown, this is most likely the result of uneven amounts of PIBSI used in each of the experiments and the variation in spinning speeds (as a result of using liquid samples).

4.8.2 Impacts of Carbon Black on CP MAS NMR Spectroscopy

A series of CP MAS NMR experiments were performed upon PIBSI-MicroCB dispersions however no discernible signal was observed for any of them. Initially spectra were acquired at different contact and acquisition times, however this had no effect on signal. Increasing the line broadening factor also had no impact. To ensure the specific sample used was not the issue, different samples were prepared at different target loadings (from 10 wt. % to 85 wt. % polymer loadings), PIBSI samples (PIBSI C and G) and samples using another carbon material (calcined coke). In addition a

sample of carbon black soaked in toluene, which has a strong NMR signal was investigated. As none of these methods resulted in a spectrum it was hypothesised that paramagnetic behaviour resulting from free radicals or delocalised electrons within the carbonaceous material was causing the signal to be disrupted.

In order to determine if this was an issue associated with the pulse programme (CP) used, a single pulse excitation experiment was performed, the resulting spectrum can be seen in Figure 4.34. In this spectrum, some signal is seen although the spectra has such low intensity and resolution that it is not possible to assign or obtain any useful information.

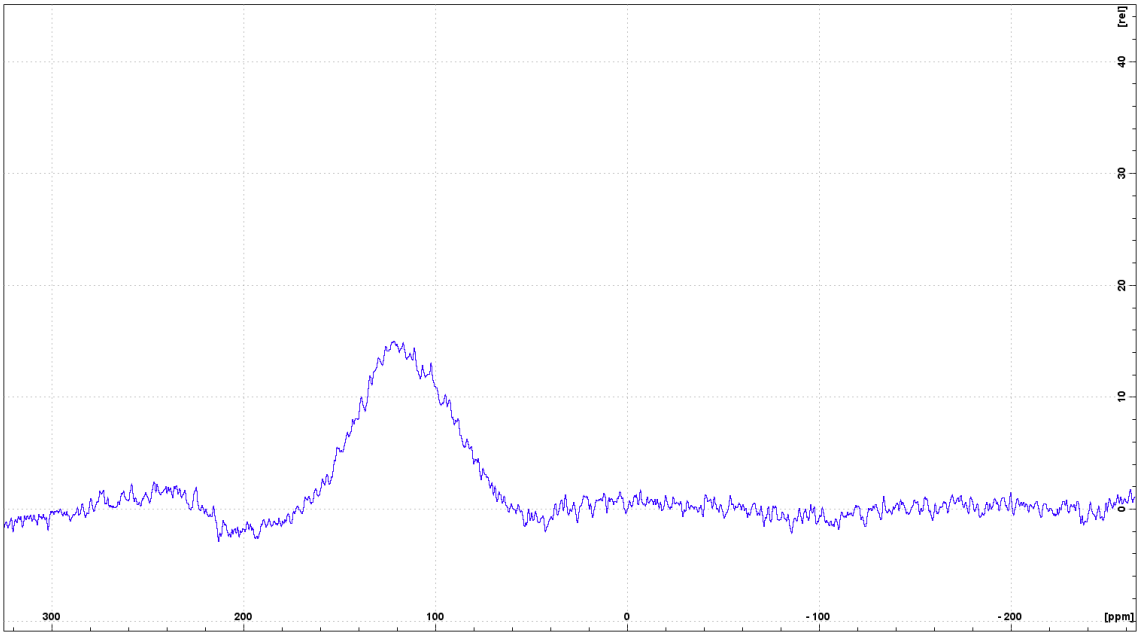


Figure 4.34: Single pulse excitation ^{13}C NMR spectrum for a 10 wt. % PIBSI G MicroCB dispersion, acquired at ambient temperature, under a spinning speed of 5000 Hz, a contact time of 3 ms and with the spectrometer calibrated to TKS (at 3.5 ppm).

Paramagnetic Behaviour of Carbon Black

An electron paramagnetic resonance (EPR) experiment was conducted on MicroCB to detect the presence of paramagnetism within the sample. The spectra can be seen in Figure 4.35. The broad linewidth unfortunately inhibits the calculation of a meaningful value for number of spins, this is likely due to the inhomogenous

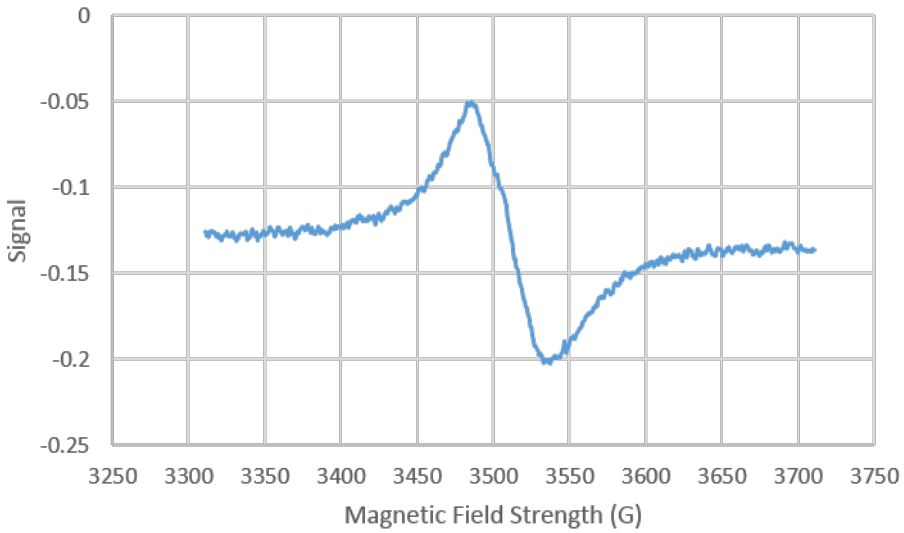


Figure 4.35: Electron Paramagnetic Resonance of MicroCB, at ambient temperature

nature of MicroCB. Although quantitative data was not able to be determined, it is thought that the strength of signal is indicative of enough paramagnetic behaviour to be interfering with the acquisition of CP MAS NMR spectra.

The effects of paramagnetic centres in the ^{13}C NMR spectra of soils has been investigated and these paramagnetic centres have been shown to cause signal loss, line broadening, increased relaxation times and changes in chemical shift of the signals.[187] The impacts of paramagnetic effects are related to the amount, type and distribution of the paramagnetic material with signal loss, caused by field inhomogenity as a result of the magnetism of the paramagnetic species, and/or interactions between spins (nuclear and electron). Nuclear and electron spin interactions have been shown to cause more signal loss in cross polarisation experiments due to the involvement of ^{1}H nuclei. ^{1}H nuclei are isotropically abundant and result in spin diffusion that is not seen in the significantly less abundant ^{13}C nuclei. This exacerbates the impact of the paramagnetic centres.[187] This is likely the source of much of the signal loss in the PIBSI-MicroCB samples, as we see some signal for bulk decay methods (SPE) and complete signal loss for cross polarisation. Much of the literature associated with this phenomenon is related to the impacts of paramagnetic metals (e.g. Cu^{2+}), however it is likely that the presence of delocalised electrons and free radicals would have similar effects.

Radical Removal

Two methods for radical removal on MicroCB were attempted, these were acid washing with 3 % HCl and the use of the hydrogen pyrolysis to expose the sample to high temperature and pressure hydrogen. Unfortunately both of these methods, when the MicroCB was prepared with PIBSI for NMR testing, did not result in CP MAS signal. It is therefore thought that the paramagnetic effects are as a result of delocalised electrons within aromatic structures in the MicroCB. It was decided to cease following this line of investigation and focus carbon-13 NMR work on other substrates.

4.8.3 The Use of Silica as a Deposit Model

Although carbon black is the preferred substrate for modelling the interactions of deposit control additives and deposit surfaces, it is unsuitable for use in CP MAS NMR due to the difficulties in obtaining a signal (as described in Section 4.8.2). Therefore a preliminary investigation into an alternate substrate was performed. Silica is widely used as a substrate, contains no carbon and is easily available in a series of different pore geometries.

Properties of Silica

The silica selected for this investigation was SBA-15. SBA-15 is the commercially available silica with the closest pore size to the MicroCB. A comparison of pore sizes and geometries can be seen in Table 4.8.

Sample Name	Surface Area (m^2 g^{-1})	Total Pore Volume (cm^3 g^{-1})	Avg. Pore Diameter (nm)
MicroCB	150-250	0.5	10
SBA-15	459-500	0.8-1	7-9

Table 4.8: Comparison of supplier provided data on the pore structure of MicroCB and potential silica analogue

Carbon-13 NMR Results

Initial investigation into the use of a silica substrate used an easily available mesoporous silica to confirm the acquisition of signal. The spectra for this experiment can be seen in Figure 4.36. The peaks at 130-140 ppm can be tentatively associated with the succinimide carbons, the peaks from 30-60 ppm with the PIB tail. As a signal was easily acquired, although the noise was significant, investigation proceeded with SBA-15.

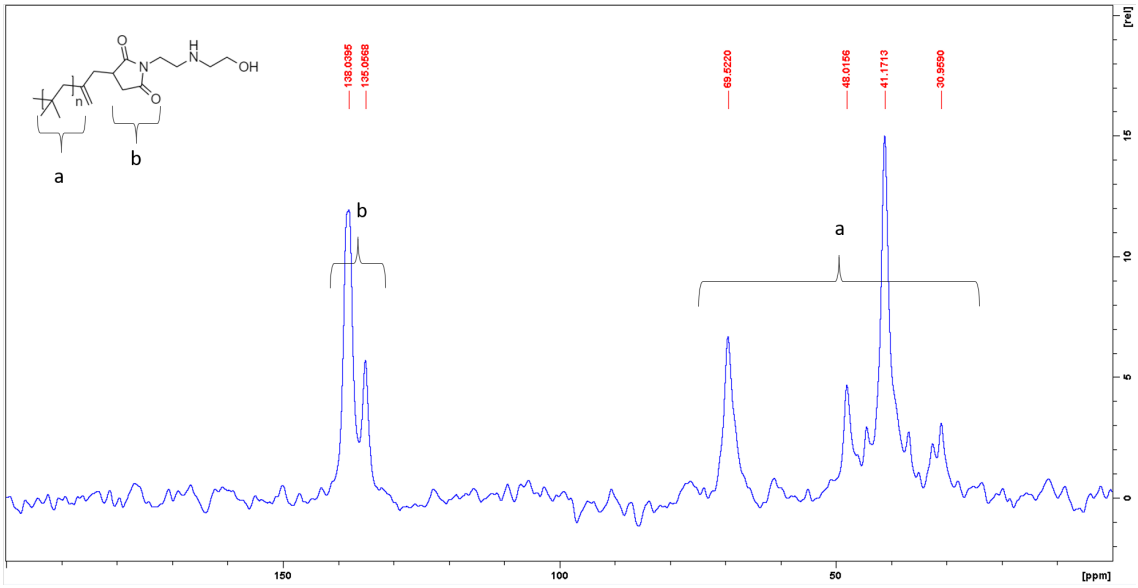


Figure 4.36: ^{13}C-^{1}H CP MAS NMR spectra of 50 wt. % PIBSI C mesoporous silica dispersion, acquired at ambient temperature, under a spinning speed of 5000 Hz, a contact time of 10 ms and with the spectrometer calibrated to TKS (at 3.5 ppm).

Figure 4.37 shows the CP MAS spectra of 30 wt. % PIBSI G on SBA-15, and Figure 4.38 shows the ^{13}C SPE MAS spectra, both including a standard TKS reference. The SPE spectra is more strongly resolved, however the standard peak is significantly stronger due to all of the carbon centres having 3 adjacent protons. Unfortunately as TKS has a weaker signal in CP than in SPE it may not be lost to high noise on certain spectra, fortunately the calibration of the spectrometer carries over well from one spectra to the next, so spectra without a TKS peak may still be considered calibrated against TKS.

Comparing these two spectra (Figures 4.37 and 4.38), both show many of the

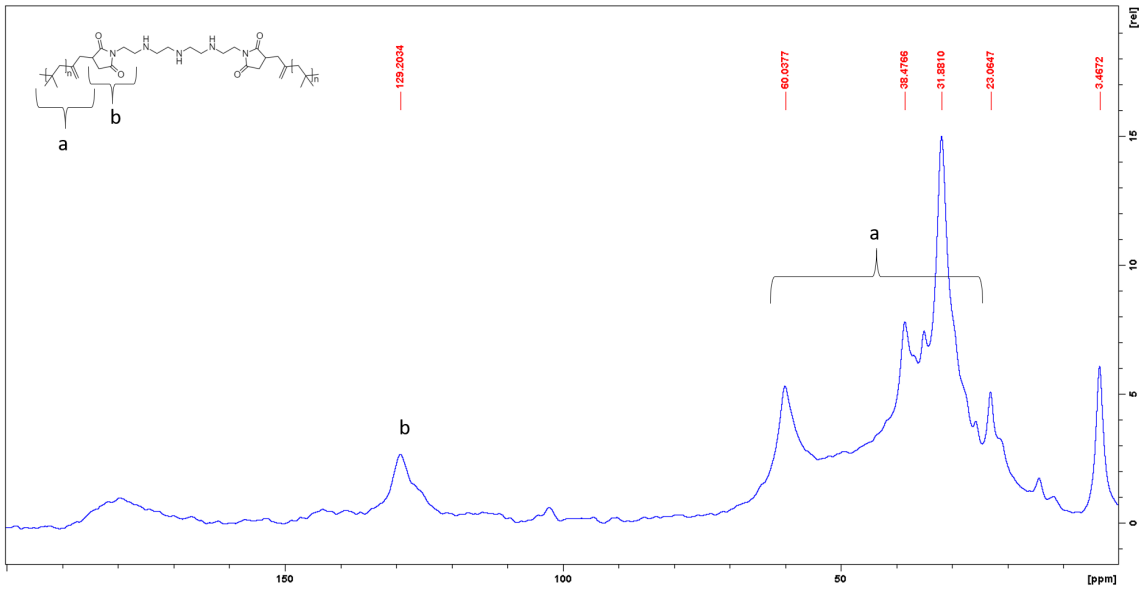


Figure 4.37: ^{13}C-^{1}H CP MAS spectra of 30 wt. % PIBSI G SBA-15 dispersion, acquired at ambient temperature, under a spinning speed of 5000 Hz and a contact time of 1 ms (TKS Standard at approximately 3.5 ppm).

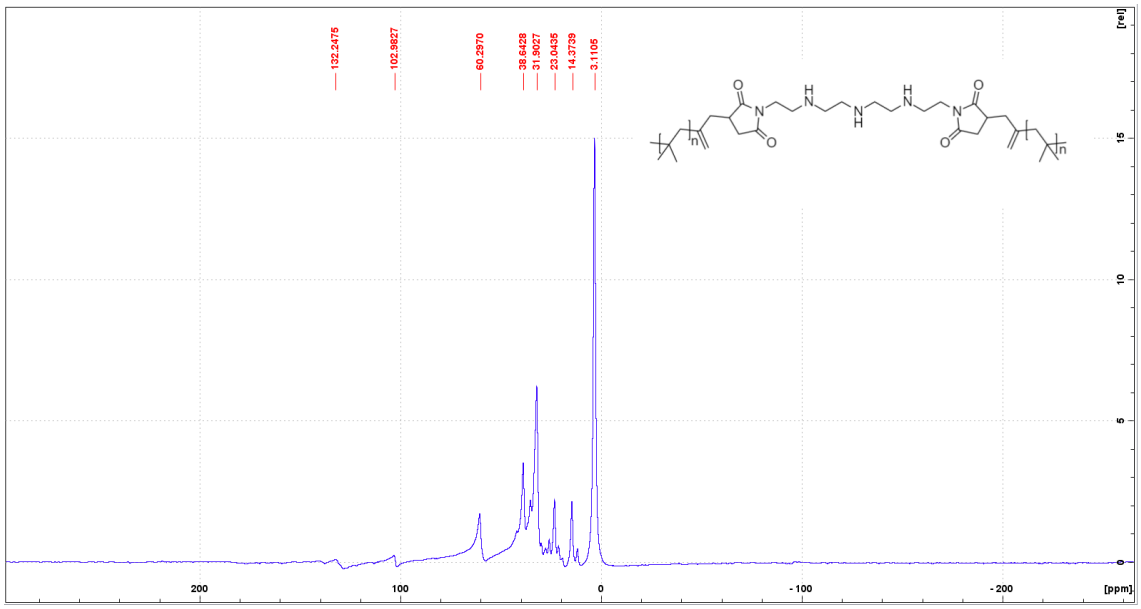


Figure 4.38: ^{13}C SPE spectra of 30 wt. % PIBSI G SBA-15 dispersion, acquired at ambient temperature, under a spinning speed of 5000 Hz and a contact time of 3 ms (TKS Standard at approximately 3.5 ppm).

same key peaks (e.g. peaks at approximately 31 ppm and 60 ppm), as would be expected. However, some of the minor peaks in the CP spectra, specifically those between 10 and 20 ppm are clearer in the SPE spectra due to the increased resolution and increased signal to noise. Some of the high ppm (> 100 ppm) peaks are not seen, or strongly reduced in the SPE spectra, this may simply be due to the high intensity of the other peaks (specifically TKS) in this spectra reducing them in size comparatively. The peaks in the region of 30-60 ppm can be tentatively assigned to the PIB tail. Due to the resolution and high number of carbon centres it is difficult to assign the peaks individually. However, the peak at at 129 ppm in Figure 4.37 is likely the result of carbon centers in succinimide group. This peak is not seen strongly in Figure 4.38, but is assumed to be lost to noise.

Proton NMR Results

To determine if the use of SBA-15 as a substrate is applicable in this way, proton NMR studies of PIBSI G on SBA-15 were undertaken to compare to the existing data with MicroCB as a substrate. Figure 4.39 shows the ^{1}H NMR data for PIBSI G at 10-40 wt. % loadings supported on SBA-15, over 30-250 °C, and Figure 4.40 shows $\Delta H_{\frac{1}{2}}$ at 250 °C with loading.

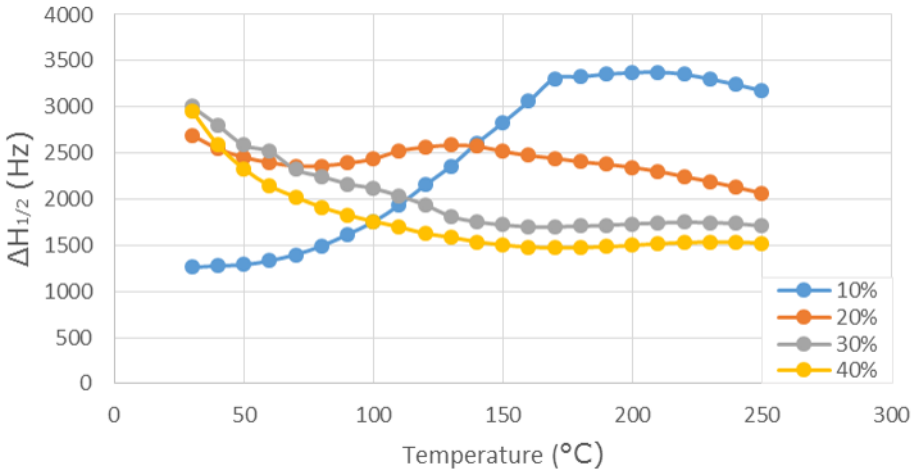


Figure 4.39: ^{1}H NMR data for PIBSI G supported on SBA-15 over 30-250 °C

The mobility tends to increase ($\Delta H_{\frac{1}{2}}$ decreases) with temperature, this is ex-

pected due to the increase in kinetic energy of the molecules would result in increased movement and mobility. This trend is seen by the 40 and 30 wt. % loadings over the whole temperature range, and the 20 wt. % loading at temperatures above 130 °C. At 10 wt. % loading the mobility decreases with temperature and then plateaus at about 170 °C. The high mobility of the 10 wt. % sample may be the result of residual solvent.

There is a general trend of increasing mobility with increasing polymer loading at high temperatures (above 170 °C) however at lower temperatures the lower loadings (5 and 10 wt. %) do not follow this trend.

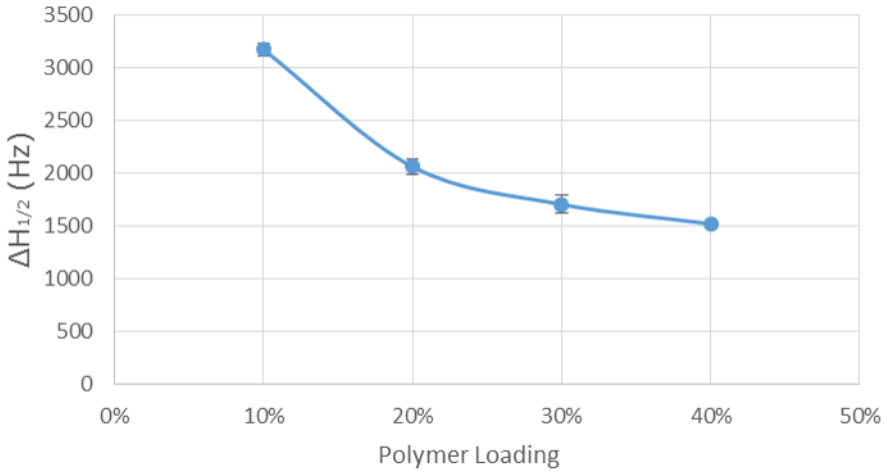


Figure 4.40: ^{1}H NMR data for PIBSI G supported on SBA-15 at 250 °C, with error bars of one standard deviation

The mobility data for 250 °C alone can be seen in Figure 4.40. The mobility consistently increases with polymer loading.

Comparison of PIBSI Dispersions on SBA-15 and MicroCB

Comparing this data for PIBSI G SBA-15 dispersions to that of the PIBSI G MicroCB dispersions seen in Figures 4.10 and 4.18 the numerical values of $\Delta H_{\frac{1}{2}}$ are significantly smaller for the polymer supported by SBA-15 than those supported on MicroCB, with a smaller change in $\Delta H_{\frac{1}{2}}$ over temperature. A similar trend in decreasing $\Delta H_{\frac{1}{2}}$ over 10-40 wt. % polymer loading is seen between the two dispersants.

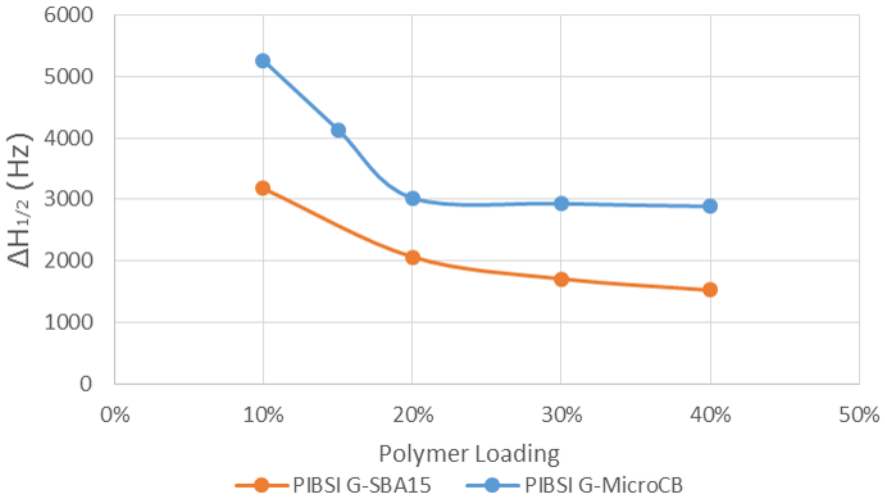


Figure 4.41: Comparison of PIBSI G dispersions on SBA-15 and MicroCB, at 10-40 % loading

The difference in $\Delta H_{\frac{1}{2}}$ between the two dispersions indicates the PIBSI impregnated on SBA-15 has a higher mobility than the PIBSI impregnated on MicroCB. This suggests that the the silica is interacting with the PIBSI less strongly than the carbon black. One reason for this is the different active sites of MicroCB and SBA-15, SBA-15 has hydroxide groups which are less likely to interact with the PIB tail than the oxide groups found on MicroCB.

4.9 Chapter Summary

- A simple ^{1}H NMR method to investigate the mobility of PIB derivatives on MicroCB was further developed and reproducibility and repeatability proven to a reasonable standard.

- The ^{1}H NMR derived monolayer loading of PIB derivatives on MicroCB does not correspond well with the PSA calculated monolayer, indicating a more complex adsorption than a simple comb regime.

- Mobility data derived from solid state proton NMR has shown the ability to distinguish between PIB derivatives adsorbed on MicroCB at low (monolayer)

loadings.

- PIBSI G and C have been shown to have much lower mobility than the other PIB derivatives. These are characterised as strongly interacting.
- PIB, PIBSA, PIBSI I and Y have high mobility with little difference between mobility at monolayer and higher loadings. These are characterised as very weakly interacting.
- PIBSI B and Z have a lower mobility than the very weakly interacting PIB derivatives, but much higher mobility than the strongly interacting samples. These are characterised as weakly interacting.
- Analogues to PIBSI B have good functionality as DCAs, indicating the "weakly" and "strongly" interacting groups may have potential use as DCAs.
- The impact of chain length the mobility of PIBSIs is seen through comparison of PIBSI G and Z. With the longer chain length of PIBSI G correlating with reduced mobility.
- The impact of bis and mono functionality on mobility is seen with PIBSI G and B, and PIBSI Y and I. Bis functionality correlates with a lower mobility.
- Solid state CP MAS NMR cannot be used to investigate PIB derivatives adsorbed on MicroCB due to the paramagnetic behaviour of the carbon black substrate.
- MicroCB and SBA-15 have somewhat similar porosity, and silicas do not interfere with CP MAS NMR. Therefore SBA-15 was trialled as an alternate substrate.
- Silica as a alternative substrate has enabled CP MAS NMR spectroscopy, although the resolution is not high. The broadline ^{1}H NMR of PIBSI G adsorbed on to SBA-15 has shown a higher mobility than that of PIBSI G-MicroCB dispersions indicating the PIBSI is not interacting as strongly with the silica as with carbon black.

Chapter 5

Mobility and Kinetics of CO_2 Adsorption of PEI-Silica

5.1 Introduction

This chapter will present and discuss the data obtained over the course of this study on PEI, silicas and the function and interactions of PEI-Silicas. Initially the development of the individual methods used will be discussed, followed by sample characterisation of the silicas and neat PEI. The mobility and kinetics results of the NMR and TGA analysis of the PEI-Silica samples is then presented and discussed, investigating the impact of both the PEI molecular weight and the pore structure of the silica substrate. This is followed by an investigation into pilot plant samples and the chapter closes with an investigation into the addition of antioxidants to PEI-Silicas.

As in the previous chapter, the figures displayed in this section show lines between points which are present as a visual aid and are not representative of further data points. Further to this, error bars are generally excluded for readability.

5.2 Method Development

5.2.1 Polyethylene Imine Samples

All of the PEIs selected are branched PEI (rather than linear) with molecular weights of 800-750000 g/mol. The weight average molecular weights for each PEI by product name can be seen in Table 5.1, however the PEIs will be referred to by their molecular weights in this chapter. An additional 1000000 g/mol molecular weight PEI was also the subject of a preliminary investigation, but high viscosity and inhomogenous water content resulted in study of this PEI being ceased.

Product Name	M_w (g mol^{-1})
FG	800
G20	1300
G35	2000
G100	5000
HF	25000
PS	750000

Table 5.1: PEI average molecular weights, as provided by the supplier. No information on error bands was provided.

5.2.2 Moisture Content of PEI

The PEI is provided from the supplier as a solution with water and also absorbs moisture from the air at ambient conditions, therefore it is necessary to determine the moisture content before use and adjust synthesis conditions accordingly. TGA was used to determine the moisture content and the method is described in Section 3.2.5. As some techniques, namely proton NMR, are sensitive to the presence of water, it may be necessary to remove as much water as possible from the samples. The presence of water in ^1H NMR samples is expected to result in line broadening, this is due to small fast moving molecules such as water having long T_2 times (relaxation is slow).

As packing the NMR capsule can take some time and it would be unrealistic to do under an inert atmosphere, in the current laboratory set up and on a larger scale, it was decided that the PEI-Silica samples would be dried in situ in the spectrometer. This was achieved by heating the spectrometer to approximately 100 °C for 30 minutes and then cooled before each experiment, a comparison of "wet" and "dry" 25000 PEI-Silica 1 samples can be seen in Figure 5.2. As the heat transfer gas for the spectrometer is nitrogen, there is no additional moisture added in the spectrometer. For neat PEI samples where this method would not be practical due to viscosity changes with temperature and the nature of keeping liquids in capsules designed for solid samples, moisture was removed from these samples by heating, as described in Section 3.2.1.

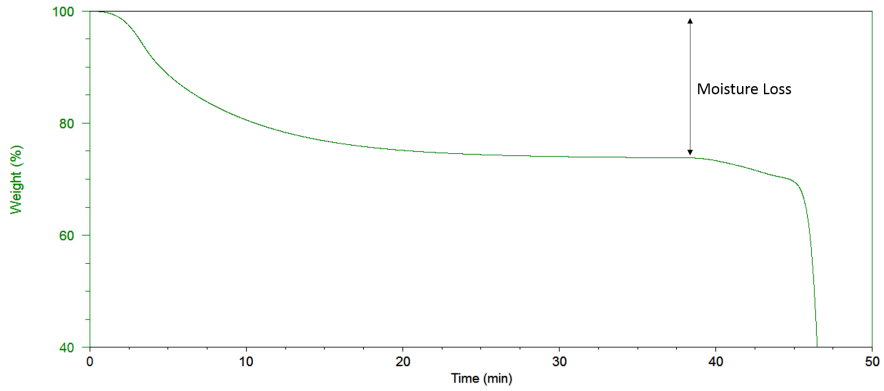


Figure 5.1: TGA thermogram for 25000 PEI, highlighting moisture loss after 30 min at 100 °C

An example TGA spectra can be seen in Figure 5.1, highlighting the moisture content of one sample of 25000 PEI, and Table 5.2 shows the moisture content of each PEI, as determined by TGA.

The low moisture content of 800 PEI compared to the other PEI samples is due to the 800 PEI sample being provided as a resin from the supplier whereas the remainder of the samples are provided in solution. The 1000000 molecular weight sample, due to its viscosity and tendency to separate, was difficult to obtain a consistent moisture measurement for, thus a range is given.

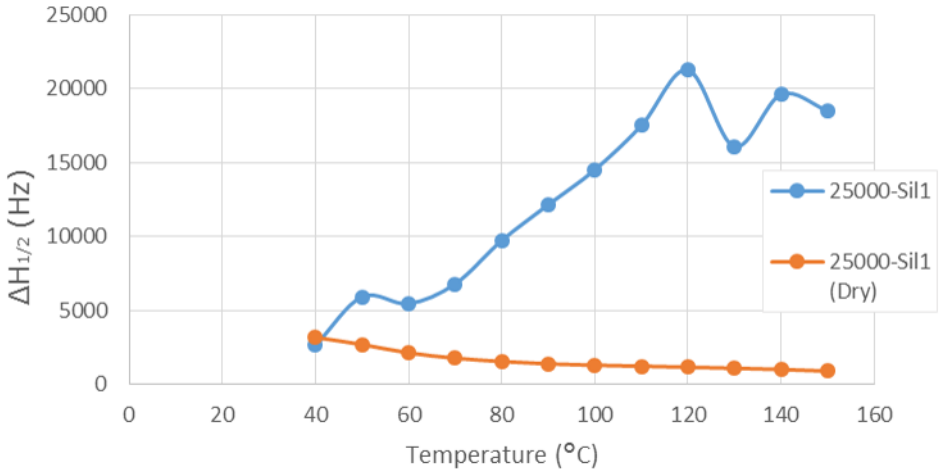


Figure 5.2: ^{1}H NMR data for a 25000 PEI-Silica 1 sample before and after drying in situ. Measurements acquired over 40-130 °C

PEI	Moisture Content (wt. %)
800 PEI	6 %
1300 PEI	47 %
2000 PEI	47 %
5000 PEI	48 %
25000 PEI	44 %
750000 PEI	63 %
1000000 PEI*	33-51 %

Table 5.2: TGA determined moisture content of PEI samples. * denotes that the moisture content may be inaccurate due to the inhomogeneous nature of the sample

5.2.3 Impregnation of Silica

Impregnation was shown by several authors to be the best method of adsorbing PEI onto silica when compared with grafting and direct condensation.[47,51–54] The method used to impregnate the silica with PEI is outlined in Section 3.2.1. As the PEI is provided in a solution with water, it is necessary to measure the moisture content and adjust the impregnation mixtures accordingly.

One issue faced with the sample preparation method used is that there is often solidification of the sample on the beaker walls as the sample dries, this can be seen in Figure 5.3. The sample tends to be strongly adhered to the walls, and difficult to remove with scraping, although effort was taken to ensure as much of the sample was reclaimed as possible.

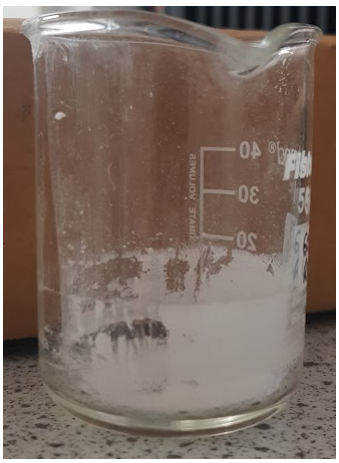


Figure 5.3: Photograph of a sample of 60 wt. % 750000 PEI-RH2 showing solidification of the PEI-Silica on the beaker walls

Determination of PEI Loading

Using thermogravimetric analysis (as described in Section 3.2.5) the PEI loading can be determined, Table 5.3 shows the target loadings and the experimentally (by TGA) determined loadings of the full range of loadings of PEI-Silicas prepared including those that are not free flowing powders. The discrepancy between the target loading and the actual loading is due to a variety of experimental errors, including loss of silica to the air, adhesion of PEI to the glassware and stirrer, weighing errors

and moisture changes in the PEI sample between moisture determination and impregnation as well as error in the TGA measurements as discussed in Section 5.3.1. It was determined that the level of error in impregnation was acceptable for the purposes as the key loadings (40-60 %) deviate from the target loading by less than 5 % of the target. PEI loading levels were also monitored throughout the study.

Table 5.3: PEI Loading of 25000 PEI on SBA15 (Dry Basis), *indicates an agglomerated sample

Target Loading (%)	Experimental Loading (%)	
	Average	Standard Deviation
10	12.9	0.25
20	21.7	1.24
30	33.2	1.76
40	41.7	0.82
50	49.3	1.00
60*	62.5	0.72
70*	72.2	1.11
90*	91.7	0.19

Determination of Optimum PEI Loading

To determine the optimum conditions for CO_2 uptake for PEI adsorbed onto each of the silicas in question, a range of loadings of 25000 PEI were tested using TGA as described in Section 3.2.5. 25000 PEI was selected for these measurements as it has one of the higher molecular weights and as such should ensure that the majority of the other PEI samples would be also able to adsorb onto the silica at the selected loading. The maximum CO_2 uptake at 75 °C (whilst the sample remained a free-form powder) for 25000 PEI on SBA-15 was 6.77 wt. %, on MCF it was 11.75 wt. %, on RH1 it was 11.15 wt. % and in RH2 it was 14.70 wt. %. All of of these were at 50 wt. % loading, except RH2 which was at 60 wt. %. This measurement was per-

formed at 75 °C as previous studies have shown this to be the optimum temperature for CO_2 adsorption on PEI-Silica samples (see Figure 5.4).

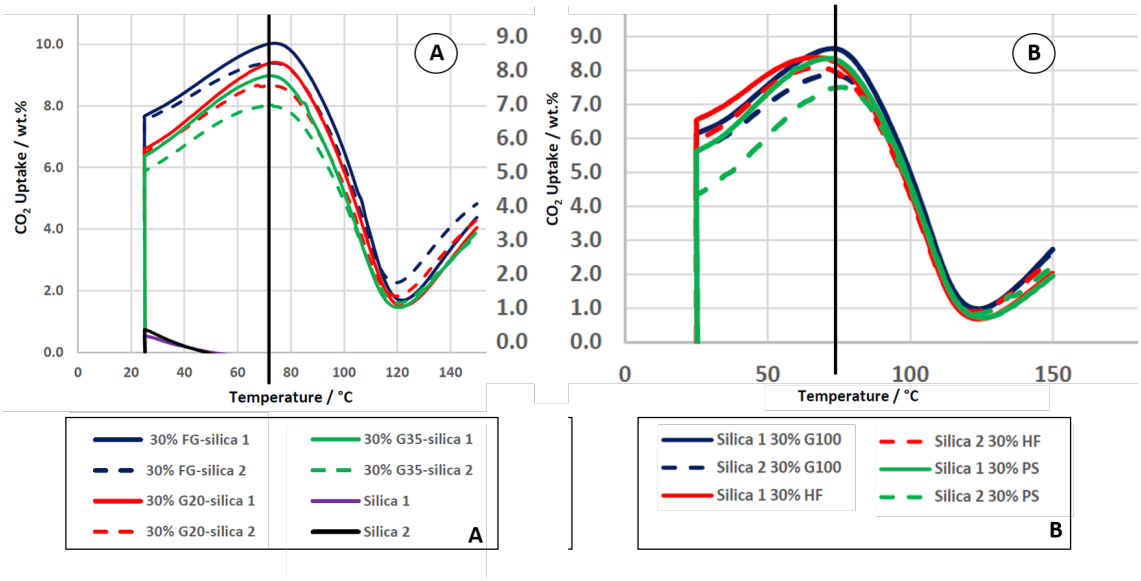


Figure 5.4: Adsorption and desorption of CO_2 on various PEI-Silicas as found by Abu-El-Haija (A) and Alhuaybi (B), 2016, with a line indicating 75 °C.[139,140]

It is important for the samples to remain free-form or free-flowing as once the particles begin to agglomerate, the interparticulate void space becomes blocked by the polymer restricting access of CO_2 into the pores. A free-form powder is also required for the material to be used in a fluidised or bubbling bed reactor. Figure 5.5 shows the maximum free-form loading of each of the samples where loading was determined in this study, as well as the agglomerated loadings for comparison. The free-form and optimum loading values can be seen in Table 5.4.

Interestingly all of the samples showed the optimum loading of PEI at the highest free-form loading except from MCF. This is concordant with previous studies which seem to suggest that maximum CO_2 capacity is seen at a point where pores are filled but not blocked.[134] The difference in optimum loading and the maximum free-form powder loading for MCF may result from highly filled pores restricting the access of CO_2 to the adsorption sites. As the difference between loading points investigated is 10 wt.%, it is possible that this point is missed for the other samples, occurring in between the samples loadings investigated.

Silica	Maximum Free-form PEI Loading (%)	Optimum PEI Loading(%)
Silica 1	40	40
SBA-15	50	50
MCF	60	50
RH1	50	50
RH2	60	60

Table 5.4: The maximum loading (wt.%) values at which 25000 PEI-Silica remains a free-form powder, and the loading at which these samples have the highest maximum CO_2 adsorption at 75 °C

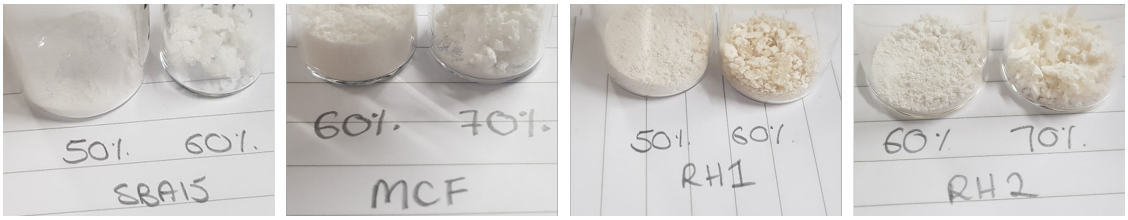


Figure 5.5: The maximum free-form loading of 25000 PEI-Silicas and the percentage loading which causes agglomeration

The first sample to be prepared was 25000 PEI-SBA15, this sample was prepared over the widest range of loadings, with subsequent samples prepared over smaller ranges, plots of the maximum TGA CO_2 capacity against loadings for each of the silicas can be seen in Figure 5.6.

The optimum loading for Silica 1 had already been determined in 2016 by Abu-El-Haija and Alhulaybi as 40 %, using a similar method, thus a plot of maximum TGA CO_2 capacity against loading is not shown for Silica 1.[139,140]

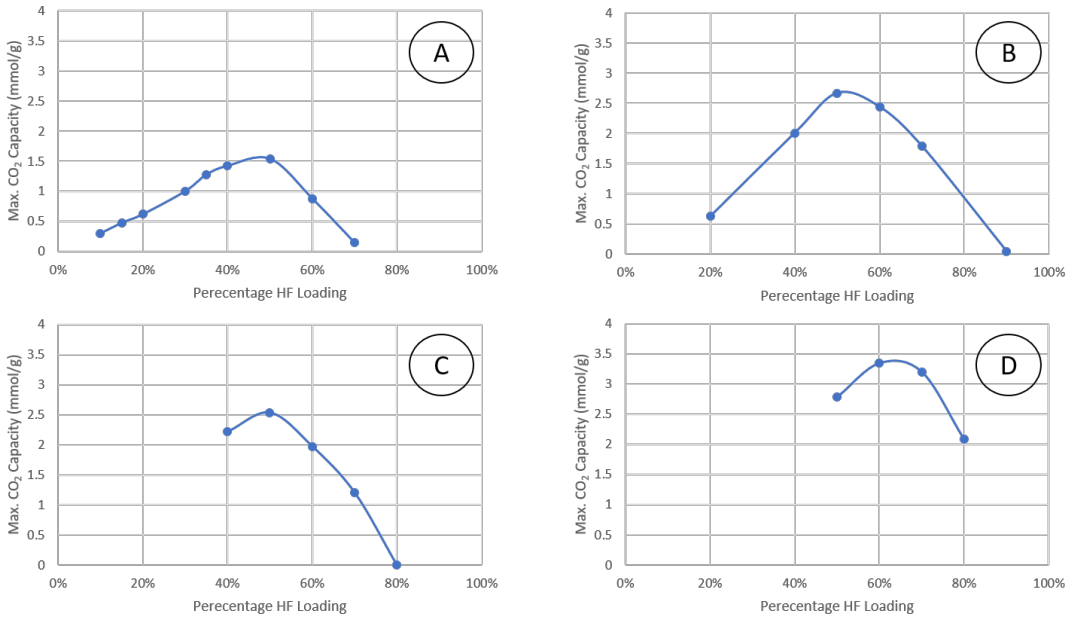


Figure 5.6: Plots of the CO_2 capacity at 75 °C against loading for 25000 PEI (HF) adsorbed onto SBA-15 (A), MCF (B), RH1 (C), and RH2 (D)

5.3 Measurements of Repeatability

5.3.1 Repeatability of Thermogravimetric Analyses

As with any experimental technique, there are potential sources of error in these thermogravimetric analyses. The sensitivity of the equipment is described in Section 3.2.5 and covers the error the temperature control and weight measurement. Other error sources include: inhomogeneous samples as a result of ineffective mixing in the impregnation step; insufficient quantities of sample; and inconsistencies or variation in the data processing.

In order to ensure data are not erroneous each sample was performed in duplicate, as a minimum. In addition to this, an initial repeatability test on 50 wt. % 25000 PEI-MCF was performed for both the PEI loading and CO_2 adsorption (at 80 °C) tests. The PEI loading repeatability test had a relative standard deviation of 1.7% and the CO_2 adsorption repeatability test had a relative standard deviation of 0.5 %.

5.3.2 Repeatability of Proton NMR Results

As the proton NMR investigation into PEI-Silica was started after the investigation into deposit control additives, much of the proof of reproducibility can be seen in Section 4.2.2.

However, due to the presence of water in the samples, which contributes significantly to the T_2 relaxation time, a simple repeatability check after drying the sample was performed. To dry the sample it was heated to 110 °C and then cooled in the spectrometer before taking measurements. The repeatability check consisted of repeating the process 3 times with the samples of 40 wt. % 5000 PEI-MCF. The results of which can be seen in Figures 5.7 and 5.8.

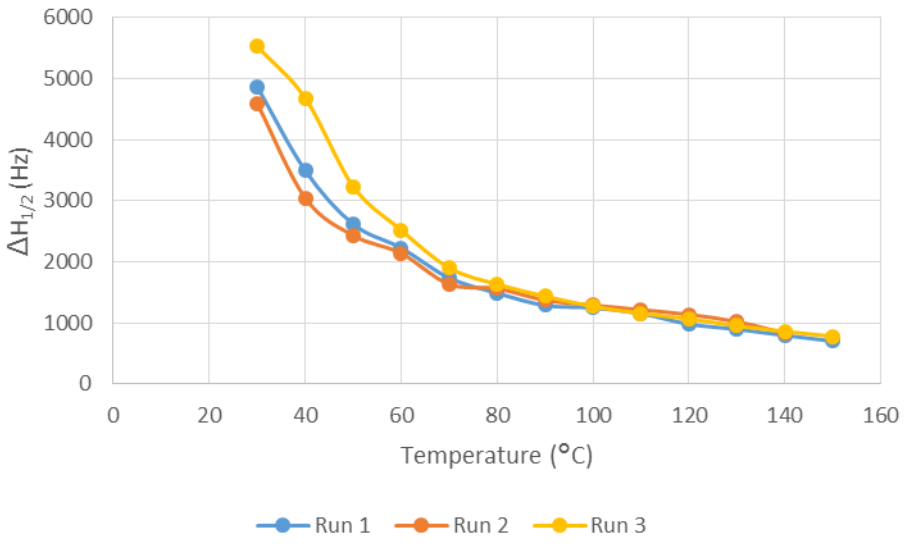


Figure 5.7: $\Delta H_{\frac{1}{2}}$ over 30-150 °C for repeat analysis of 40 wt. % 5000 PEI-MCF with drying in situ at 110 °C

The greatest deviation from the mean was 941 Hz (relative standard deviation of 18.45 %) at 40 °C. However at higher temperatures of over 70 °C, the greatest deviation from the mean was on average only 81 Hz (relative standard deviation of 6.07 %). On average over the whole range the deviation from the mean is 141 Hz (relative standard deviation of 6.40 %). At even higher temperatures (over 100 °C) this relative standard deviation further reduces to 3.81 %. Figure 5.7 shows the $\Delta H_{\frac{1}{2}}$ of each of these samples over 30-150 °C, and Figure 5.8 shows the average

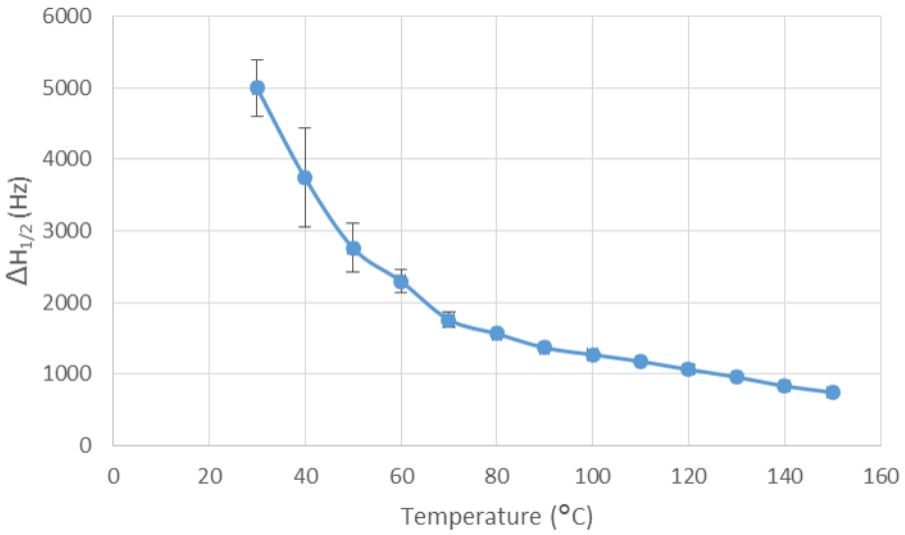


Figure 5.8: Average $\Delta H_{\frac{1}{2}}$ over 30-150 °C for repeat analysis of 40 wt. % 5000 PEI-MCF, dried in situ at 110 °C, with error bars of one standard deviation

with an error bar of one standard deviation. The higher errors at low temperatures (less than 70 °C) are likely due to the limits of the in-situ drying process.

These errors, particularly at higher temperatures are in keeping with those seen in the deposit control section of this research. However as this research has greater focus on the lower temperature results it is important to consider the higher error at low temperature. Fortunately the key areas of research are over the operational temperatures of the PEI-silica, with adsorption occurring at around 70 °C.

An example spectra can be seen in Figure 5.9 for reference. This spectra is of 40 wt. % 25000 PEI-Silica 1 at 80 °C and is representative of the line-shape seen for all of the samples.

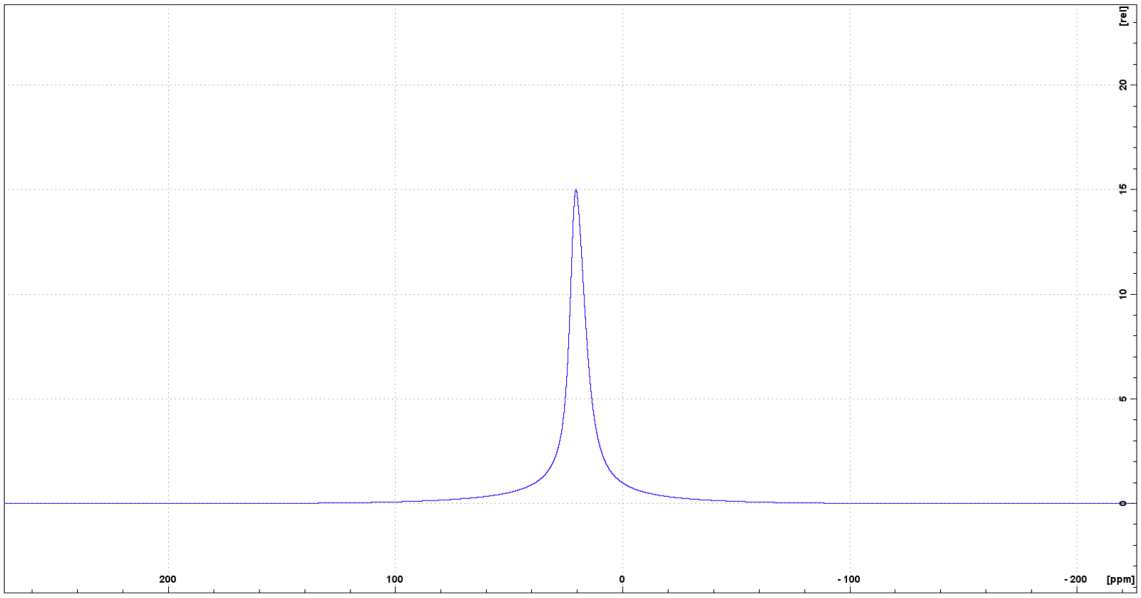


Figure 5.9: Example ^{1}H NMR spectra of PEI-Silica (40 wt. % 25000 PEI on Silica 1 at 80 °C)

Other Contributions to Signal

In order to determine if the PEI-Silica NMR signals are contributed to strongly by the silica substrate ^{1}H NMR and ^{13}C-NMR spectra were acquired on silica samples as a control. These samples did not show any observable signal.

5.4 N_2 Sorption Isotherms of Silica Samples

The N_2 sorption isotherms for each silica were acquired using an micromeritics ASAP 2420 analyser and processed using the BET model, BJH (Barrett-Joyner-Halenda) model and Hawkins-Jura correction (see Sections 3.2.4 and 3.1.4). The acquired data can be seen in Table 5.5.

The N_2 sorption instrument used in this study can only provide information for pores of up to 140 nm, as it is limited in the pressures that it can create to condense N_2 into the larger macro pores. It is therefore inaccurate for materials with a high proportion of macropores. In this case, as can be seen from the isotherm, both RH1 and RH2 silica pores were not completely filled (see Figure 5.12). This means that the N_2 sorption data is not completely accurate and is only an indicator of pore sizes.

It is likely that there is a significant amount of macroporosity at pore diameters of greater than 140 nm for these silicas. In addition to this the discrepancy between the total pore volume and the sum of micro- and mesopore volumes is high for these two samples showing high levels of volume between approximately 50 nm and 140 nm.

In addition to N_2 sorption, Dr. Lee Stevens at the University of Nottingham performed mercury intrusion porosimetry (MiP) on RH1, a method in which mercury is forced into the pores to determine porosity, in order to gain greater insight. However, this method is not very suitable for use with templated silicas, as it has been repeatedly reported that this technique has a tendency to crush the sample, bursting the pores and thus only really provides bulk density and total porosity measurements rather than a breakdown of meso- and macro- porosity as desired.[101,188] If the sample is crushed, the data provided will also include any closed pores which would not be available for adsorption. These data alongside data for Silica 1 (noted by Dr. Stevens as Old PQ Silica) determined by Dr. Stevens can be seen in Appendix B.2. These data shows the existence of macropores at pore sizes greater than detectable by the N_2 sorption instrument used in this study. The Silica 1 data shows significant discrepancies from the N_2 sorption data in the surface area and pore volume, however the average pore diameter is similar (27 nm for N_2 sorption and 24 nm for MiP). This is likely to be as a result of this method measuring macropores and interparticulate voids that N_2 sorption does not measure. Due to the measurement issues and discrepancies between the Silica 1 data of the two methods, the mercury intrusion porosimetry data is not considered a valid representation of the pore structure of these silicas, however the overall picture painted by this method does lend some additional support to the existence of significant macroporous structure in RH2 (and by association RH1).

As the SBA-15 sample was purchased from Sigma-Aldrich, the N_2 sorption data can also be compared with the specification provided, the data for this is shown in Appendix B.3. In this case we see that the specification shows a significantly larger pore diameter than the N_2 sorption isotherms (7-9 nm and 4.16 nm respectively). It is not known what characterisation methods were used by the supplier, although

N_2 sorption isotherms are a common commercial technique.

The N_2 sorption isotherms show that the SBA-15 silica has by far the greatest surface area at over 700 m^2/g, the lowest total pore volume of all of the silicas (0.8 cm^3/g), and the smallest average pore diameter (4.16 nm). It is often the case the pore volume and surface area are inversely related in this way, with smaller pores having a high surface area to volume ration than larger pores. Silica 1 and MCF have similar surface areas of around 300 m^2/g, but MCF shows a higher pore volume (2.47 cm^3/g). These silicas are mostly mesoporous however it can be noted that the sum of the microporous and mesoporous volumes are less than the total pore volume, this indicates additional macroporous structure. MCF has a slightly lower mesoporous and microporous volume than Silica 1 (0.659 and 0.005 cm^3/g vs. 1.903 and0.012 cm^3/g) but has a higher total pore volume. The two silicas derived from rice husks have lower surface areas compared to the other silicas (108 and 166 m^2/g for RH1 and RH2 respectively) with RH1 showing the smallest surface area of the two. The smaller surface area of RH1 indicates that most of the pore volume is in larger mesopores and macropores even though the total pore volume measured is lower than that of RH2 (1.02 cm^3/g for RH1 against 1.09 cm^3/g for RH2). This is supported by the larger average pore diameter of RH1 than RH2 (37.8 nm and 26.4 nm respectively). As the two rice husk derived silica show pores at greater than 140 nm it can be assumed however that the pore volume and average pore diameter are underestimated, and that these two silicas, are in fact in possession of the largest pores. With regards to which of the two rice husk silicas contain the largest accessible pore volumes to PEI, this can be inferred by the limit seen in PEI impregnation. RH1 was able to adsorb 50 wt.% of 25000 PEI while remaining a free form powder, where RH2 was able to remain freeform at loadings of 60 wt.%. This indicates that RH2 has the larger overall pore volume.

The comparison of adsorption and desorption pore diameter can give an indication of the pore shape, with the desorption pore diameter giving an indication of the pore neck size. From Table 5.5, it can be seen that SBA-15, Silica 1 and MCF all have higher desorption pore diameters than adsorption and the values of these are

very similar, this means the pores do not have a significant neck, and are more like channels than "ink-bottles" (see Figure 5.10). In contrast to these it can be seen that the rice husk silicas have larger adsorption than desorption pore diameters, indicating somewhat of an "ink-bottle" pore structure, with a pore neck that may restrict adsorption and desorption, especially with regards to molecules with higher molecular weights. However as these samples did not reach equilibrium it is difficult to say for certain that these results are accurate.

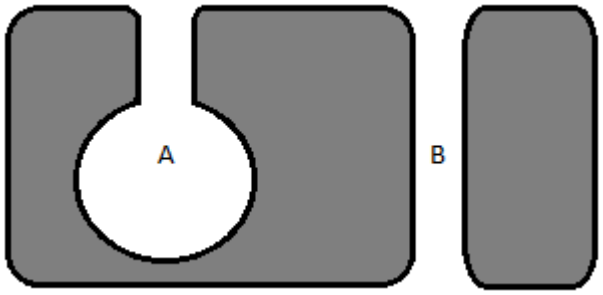


Figure 5.10: Inkbottle (A) vs channel (B) type pore shapes. Note that ink-bottle pores are not exclusively terminal as is shown in this image.

Examples of the N_2 sorption isotherms for silica samples can be seen in Figures 5.11 and 5.12 (the isotherms for the remaining silicas can be found in Appendix B.4).

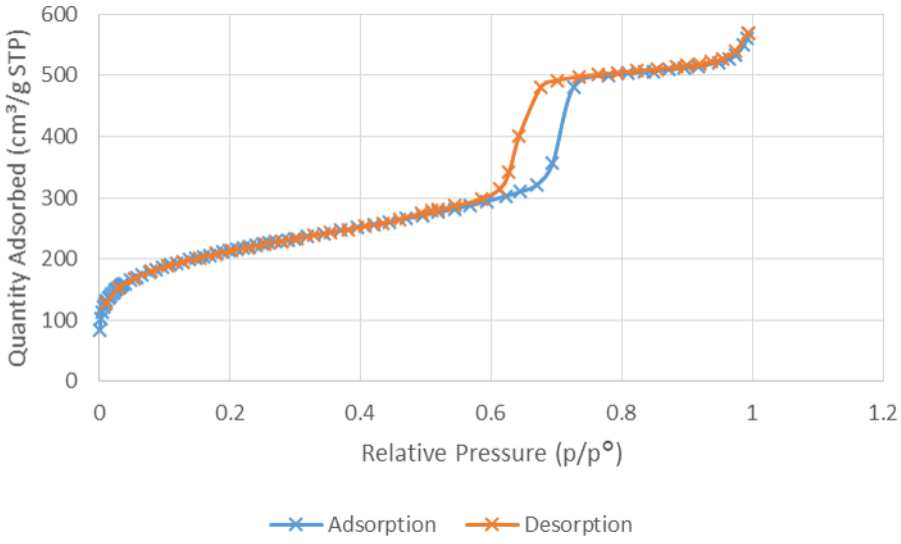


Figure 5.11: N_2 sorption isotherm for SBA-15 (at 200 °C)

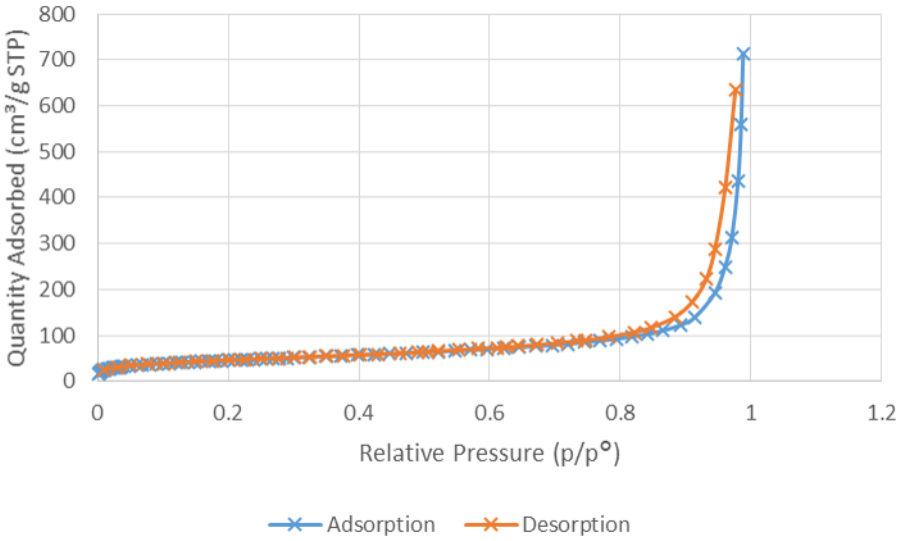


Figure 5.12: N_2 sorption isotherm for Rice Husk Silica 2 (at 200 °C)

From the example N_2 sorption isotherm for SBA-15 (Figure 5.11), the isotherm shape is a Type 4, specifically the hysteresis loop shows a H1 shape.[189,190] This means that the pore shape is likely cylindrical uniform mesopores. All of the silicas which reach saturation show a similar shape isotherm, and thus all have similar pore shapes. As the two rice husk silicas do not complete adsorption, it is more challenging to determine the isotherm shape. However the closest shape can also be assigned to Type 4 and either H1 or H3 (see Figure 5.12 for the N_2 sorption isotherm for Rice Husk Silica 2). This would correspond with cylindrical or slit-shaped pores.[189,190] It can be assumed, however, that the pores are cylindrical and the complete hysteresis loop would show a H1 shape, as the method of preparation of the two rice husk silicas (RH1 and RH2) is very similar to that of MCF (which shows H1 shape) and uses the same template material (P123). Images of the different isotherm and hysteresis loop classification can be found in Appendix B.5.[189]

It is expected that PEI will adsorb/impregnate into meso- and macro- pores, therefore materials with higher meso- and macro- pore volumes as well as a higher average pore diameter would be expected to be able to adsorb PEI at higher loadings while maintaining a free-form powder. The maximum loadings of 25000 PEI on the silicas, where each of the samples remained free-form, are shown in Table 5.4, and Figure 5.5.

Sample Name	BET Surface Area	Pore Volume (cm^3/g)			Average Diameter (nm)	
	(m^2/g)	Microporous[a]	Mesoporous[b]	Total	Pore[c]	Neck/Window[d]
Silica 1	288	0.012	1.903	1.92	26.6	27.7
SBA-15	771	0.072	0.659	0.80	4.16	4.29
MCF	298	0.005	1.838	2.74	36.8	38.2
RH1	108	0.013	0.188	1.02	37.8	28.9
RH2	166	0.008	0.314	1.09	26.4	23.6

Table 5.5: The N_2 sorption data for each of the silica samples obtained at 200 °C ([a] determined using t-plot model with Harkins Jura correction, [b] determined using BJH model with Harkins Jura correction, [c] Average Pore size using Total Pore Volume using adsorption isotherm and [d] Next/Window Pore size using Total Pore Volume using desorption isotherm data)

5.5 Viscosity Measurements of Neat PEI

Viscosity measurements (as described in Section 3.2.6) were performed on the neat "dried" PEI samples. The measurements were performed at temperatures of 25 °C, 30 °C, 50 °C, 70 °C, 90 °C, 110 °C and 130 °C for all of the samples except 750000 PEI which was too viscous at 25 °C for a measurement to be recorded using the same equipment. Apart from 800 PEI, which is provided at a concentration of 99 %, the viscosities of the samples at room temperature are not comparable to those provided in the specification which were measured at 20 °C (The values are significantly lower and can be found in Appendix B.6). This is likely to be related to the difference in water content between the dried samples and the samples as purchased. These measurements were not repeated due to restricted instrument time so the following observations may include anomalous results.

As seen in Figure 5.13, each of the samples shows a reasonably smooth curve (note that the lines present on the graph are as a guide for the eye only) with a decrease in viscosity over 25-110 °C and the beginnings of a plateau between 110 and 130 °C. However the measurements for 750000 PEI above 90 °C appear somewhat irregular and it is likely that one or more of the results is erroneous.

At low temperature the results were as expected with the viscosity directly following the molecular weight of the samples, with the lower molecular weight samples (e.g. 800 and 1300 PEI) tending to have a lower viscosity. As the temperature increases however the trends, among the lower molecular weight samples, become less clear. At higher temperatures (over 60 °C) the viscosity of 800 PEI is higher than that of 1300 PEI. The 1300, 2000 and 5000 PEI samples are also all very close in viscosity at 130 °C. These results are surprising and are likely to be related to some kind of instrumental or operational error.

These errors may be in part due to the tolerance of the equipment for low viscosity samples or perhaps related to the temperature control of the equipment. As the sample is mixed by the spindle, which also measures the viscosity, and the heat is applied from the outside of the sample container, it is possible that the heating of the sample is not even across the sample resulting in erroneous results. Any residual

moisture will also impact on the viscosity. A final source of error may be the amount of sample used. The standard method used for this analysis requires between 7 and 10 g of sample with each of the experiments each using differing amounts of sample (up to 30 %), additional error may be introduced. It would therefore be useful to repeat these measurements in the future.

However the general trends of increasing molecular weight and increasing viscosity can still be seen, especially at temperatures of 50 °C and under or with the higher molecular weight samples (e.g. 25000 PEI).

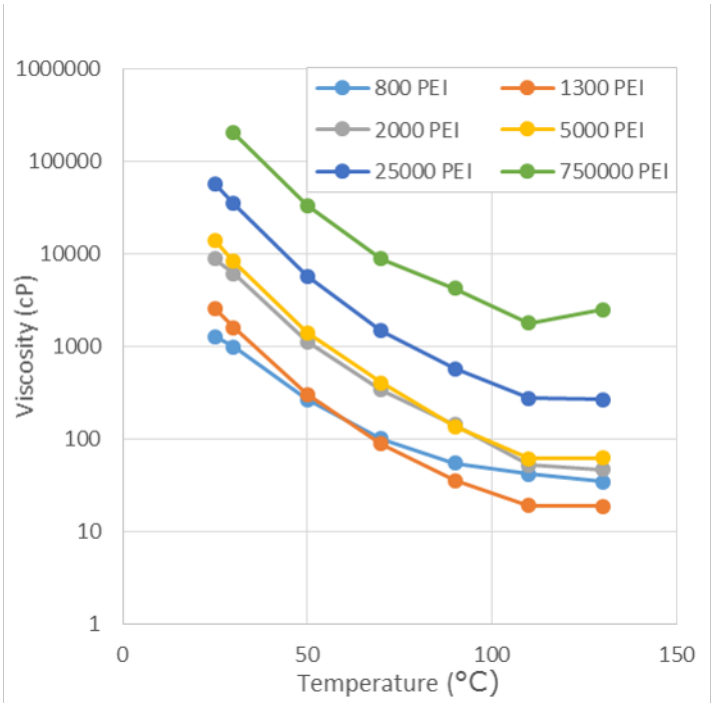


Figure 5.13: Viscosity measurements of PEI over 25-130 °C

5.6 Thermogravimetric Analysis of Thermal Decomposition and Volatilisation of PEI

The burnoff method described in Section 3.2.5 that was used to determine the loading of PEI on silica, and the moisture content of the PEI, also provides information about the temperatures at which the combustion of the samples occur. In addition to this method, the proximate analysis method provides information on the thermal

decomposition and volatilisation of the samples. Both of these methods can be used in conjunction to determine the maximum regeneration temperature of the samples. Figure 5.14 shows the burnoff TGA results for each of the neat PEI samples and Figure 5.15 shows the proximate analysis TGA results.

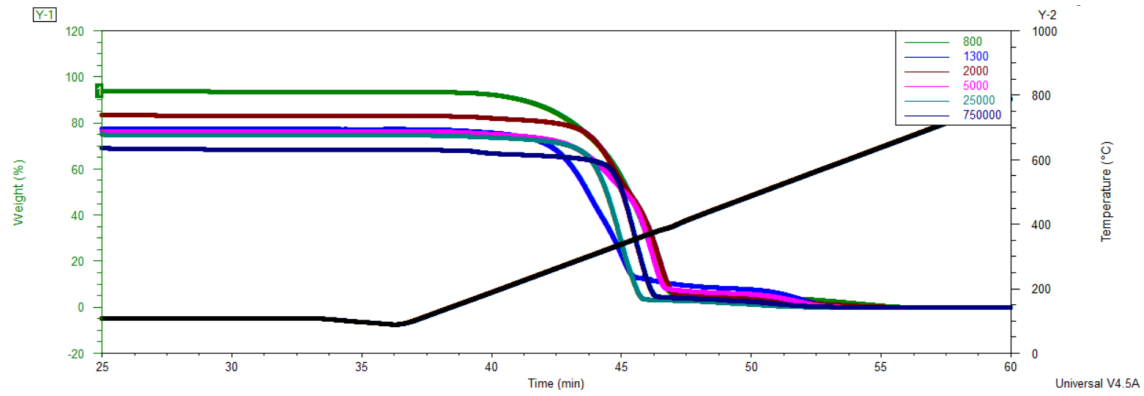


Figure 5.14: Burnoff TGA results for neat PEI samples under N_2/air

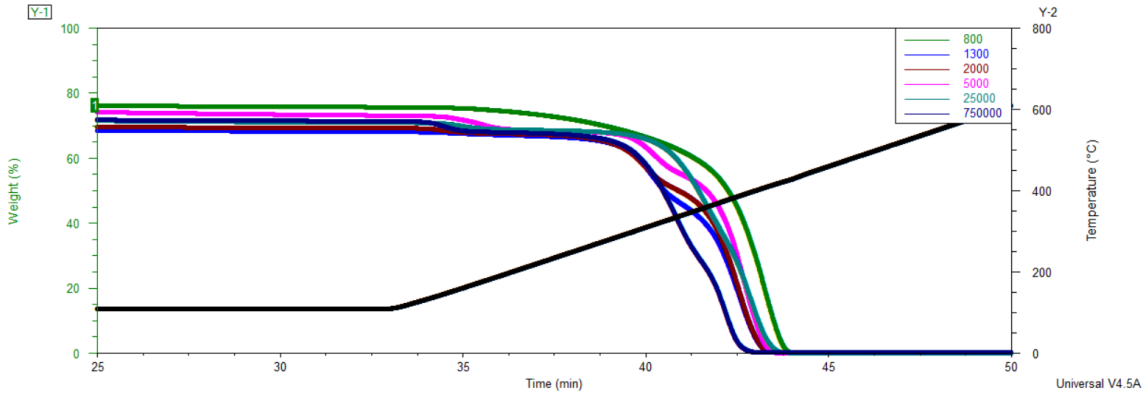


Figure 5.15: Proximate TGA results for neat PEI samples under N_2

The weight loss that occurs at around 200-400 °C (40-45 min) in Figure 5.14 can be associated with combustion of the PEI. The weight loss in the proximate analysis begins at around 150 °C with a steep decrease at 300 °C and complete weight loss by 425 °C. This weight loss can be associated with the thermal decomposition and volatilisation of PEI.

As all of the experimental work on these samples has been at or below 130 °C in the study, it is safe to assume negligible impacts of combustion, decomposition and volatilisation of the samples.

The TGA measurements performed on PEI-Silica samples described in Section 5.2.2, also show weight changes at around 200 °C and 225 °C, showing there to be little impact of the silica substrate on the thermal stability of PEI.

5.7 ^{1}H NMR Mobility Measurements of Neat PEI

Broadline ^{1}H NMR experiments were performed on liquid PEI samples. As some of these samples have considerable moisture content (see Table 5.2), which will impact the NMR signal, they were "dried" using the method described in Section 3.2.1. The "dried" PEI samples are referred to in this section as "neat PEI".

As neat PEI samples are all viscous liquids, it is possible to use the same experimental set up for broadline ^{1}H NMR as for the solid PEI-Silica samples discussed in previous sections. However, as the capsules are not completely sealed (there is a hole for the release of volatiles) at high temperatures the liquid PEI may escape the capsule and contaminate the probe. Therefore, the neat PEI samples were not subjected to as high temperatures as the PEI-Silica samples, with heating ceasing at 100 °C. In Figure 5.16 the mobility data for each of the PEIs is displayed over 30-100 °C.

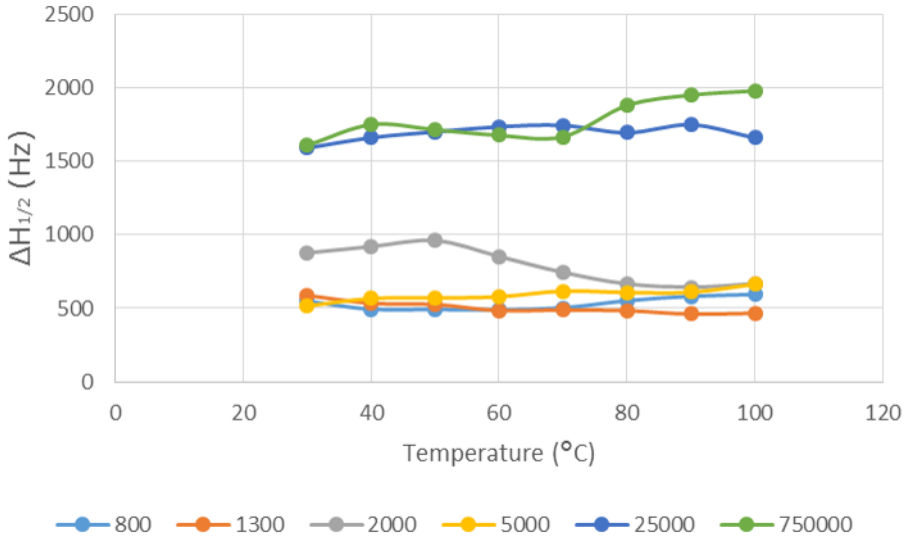


Figure 5.16: ^{1}H NMR data for different neat PEI samples over 30-100 °C

For readability, as with many of the other figures in this study, error bars have

not been included for these samples. However it is important to note that the error associated with these samples is significantly higher than those of the solid PEI-Silica samples. With 25000 and 750000 PEI samples having error ranges of approximately ± 200 Hz, and the remaining PEI samples having errors of approximately ± 50 Hz. This difference in errors is likely a result of the more viscous PEI samples presenting difficulty in loading into the NMR capsules, potentially resulting in under filled capsules or contamination.

In Figure 5.16 it can been seen that the PEI mobilities maintain a fairly consistent mobility over the temperature range, with the two highest molecular weight PEI samples (25000 and 750000 PEI) having a significantly lower mobility than the lower molecular weight PEI samples, with values of 1500-2000 Hz compared to those of around 500 Hz. These PEIs do have a significantly higher viscosity than their lower molecular weight counterparts (as can be seen in Figure 5.13), which may be the cause of this decreased mobility.

It might be expected to see an increase in mobility as temperature is increased, and this is seen to some extent with 2000 PEI, as the viscosity decreases (See Figure 5.13). However this is not observed for the majority of the samples and there is no obvious relationship between viscosity and mobility. This may due to the relatively small amounts of sample that can fit into the capsules, the temperature range investigated or increased errors associated with the liquid samples.

5.8 Impact of PEI Molecular Weight on Mobility and Kinetics of PEI-Silica

In this section the mobility and kinetics data for each PEI-Silica material are presented, categorised by the silica substrate used. This allows the comparison of each of the different PEIs. The mobility is shown as the $\Delta H_{\frac{1}{2}}$, the half peak width, of the broadline ^1H NMR peak, and the kinetics were measured through TGA. The kinetics data presented is in the form of the maximum CO_2 capacity and the time taken to reach 30, 60 and 90 % of that capacity (the t_{30}, t_{60} and t_{90}). The NMR

data were collected over 30-130 °C , and the kinetics data over 30-100 °C . The mobility temperature range covers the operational temperatures of PEI-Silica as a carbon capture material (60-80 °C adsorption and 120 °C desorption), and the kinetics data are collected over the adsorption temperature range. Higher temperatures than 130 °C were not studied due to the volatilisation of PEI at higher temperatures.

This section will present the data acquired with a brief discussion. More in depth discussion, general trends, interesting features and comparison of data sets will be discussed further in Section 5.10, and extended results may be found in Appendix B.7.

5.8.1 Impact of Molecular Weight of PEIs supported on Silica 1

PEI was adsorbed onto Silica 1 at 40 % loading. Silica 1 has a mostly mesoporous structure (see Table 5.5). These samples were studied using broadline ^{1}H NMR to measure proton mobility, the NMR was performed in 10 degree intervals from 40 to 130 °C after drying at 100 °C in the spectrometer for at least 10 minutes. The kinetics of CO_2 adsorption were also studied using TGA under a 15 % CO_2 stream at temperatures of 30, 40, 60, 75, 80 and 100 °C .

Kinetics of CO_2 Adsorption

The maximum CO_2 adsorption can be seen in Figure 5.17. The highest value of maximum adsorption of CO_2 is seen, for all PEI-Silica 1 samples, at 75 or 80 °C . The maximum adsorption of the PEI-Silicas tends to increase with decreasing molecular weight but the trend is not concrete. The kinetics of this adsorption can be seen in Figures 5.18, 5.19, and 5.20. Generally speaking, the t_{30} kinetics are fairly constant over the whole temperature range, especially compared to the t_{60} and t_{90} data, varying by no more than 0.4 s. This is commonly seen through all the samples and thus is presented in the appendix for the remaining silicas (See Appendix B.7). The t_{60} and t_{90} both tend to decrease with temperature. The t_{60} values plateau after 60 °C and the t_{90} data has some divergence from the trend around 75 °C . For

both t_{60} and t_{90} increasing PEI molecular weight tends to result in slower kinetics.

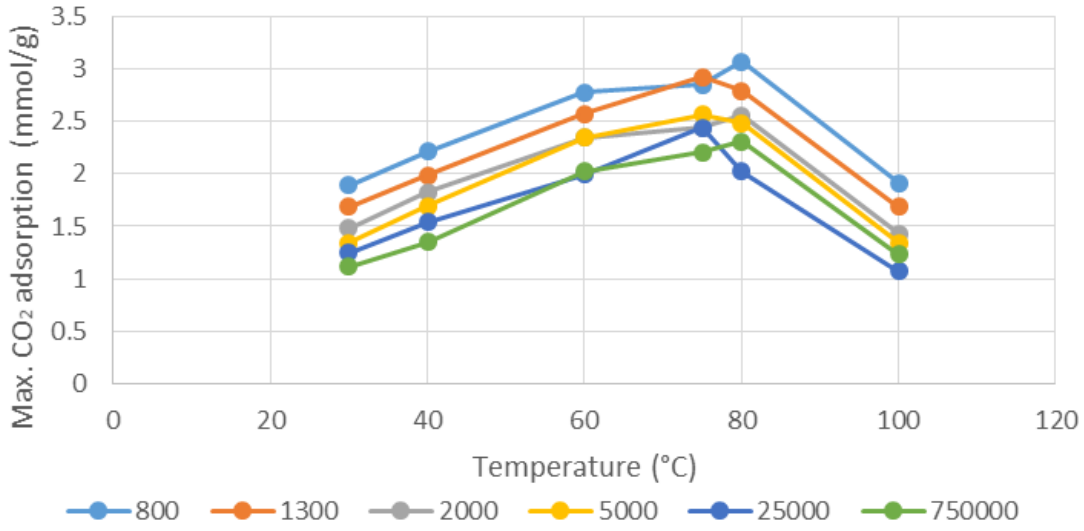


Figure 5.17: Maximum CO_2 capacity of different 40 wt. % PEI-Silica 1 samples over 30-100 °C, derived from TGA thermograms

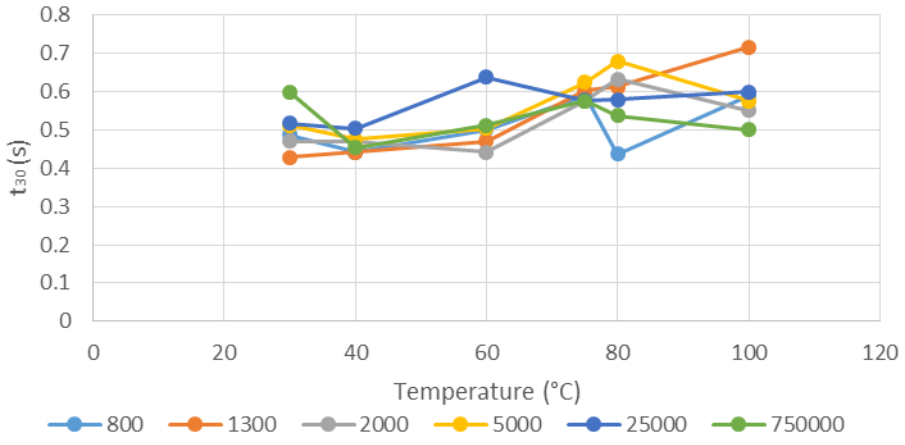


Figure 5.18: t_{30} of CO_2 adsorption on different 40 wt. % PEI-Silica 1 samples over 30-100 °C, derived from TGA thermograms

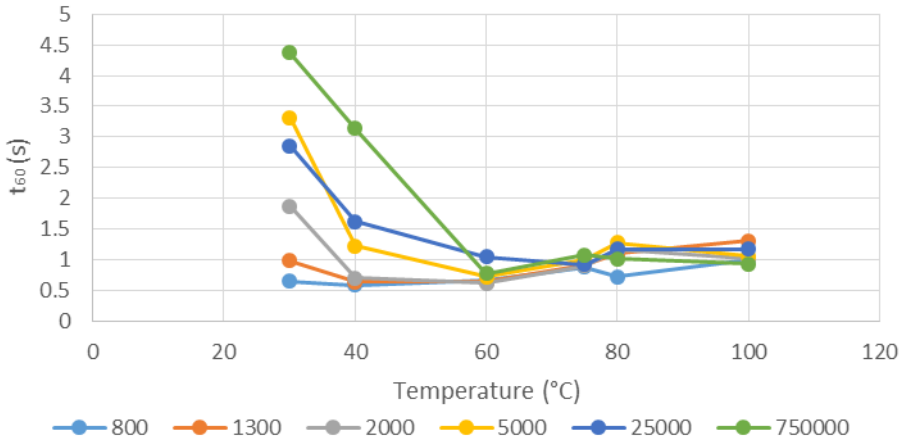


Figure 5.19: t_{60} of CO_2 adsorption on different 40 wt. % PEI-Silica 1 samples over 30-100 °C, derived from TGA thermograms

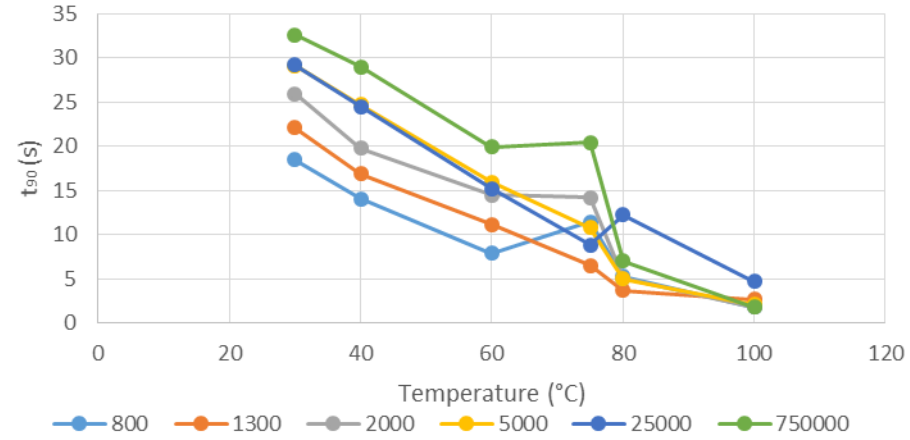


Figure 5.20: t_{90} of CO_2 adsorption on different 40 wt. % PEI-Silica 1 samples over 30-100 °C as determined by TGA

^{1}H NMR Determined Mobility

The mobility of all of the PEI-Silica 1 samples can be seen in Figure 5.21. The mobility of these samples increases with temperature, with the decrease in $\Delta H_{\frac{1}{2}}$ being steeper at lower temperatures and much more gradual at higher temperatures. The distinction between these two regimes seems to occur at approximately 80 °C . There does not seem to be a consistent order of the samples over the whole temperature range or any correlation between PEI chain length and mobility (information on each PEIs molecular weight can be seen in Table 5.1).

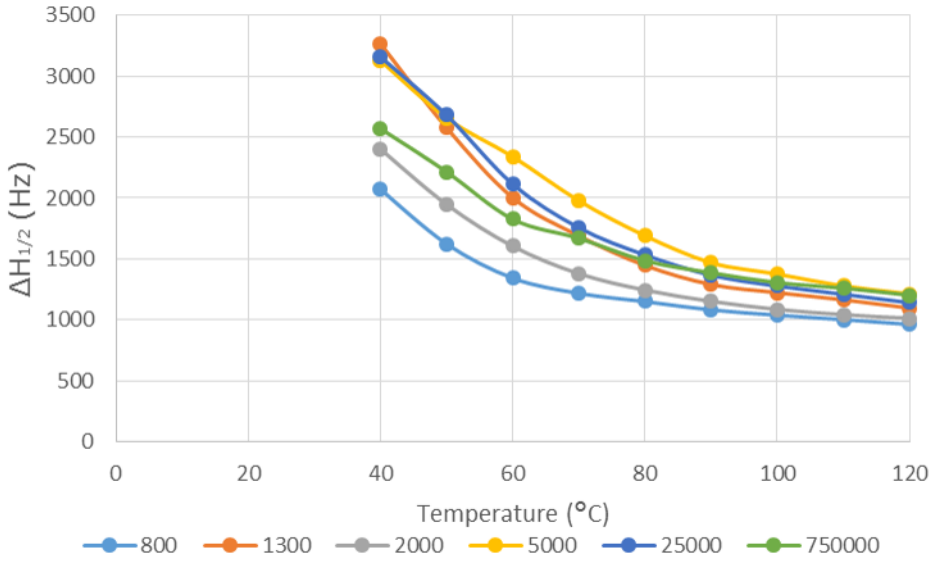


Figure 5.21: ^{1}H NMR data for different PEI-Silica 1 samples over 30-130 °C

5.8.2 Impact of Molecular Weight of PEIs supported on SBA-15

PEI was impregnated onto SBA-15 at 50 wt. % loading. SBA-15 has a significant proportion of micropores (see Table 5.5). These samples were studied using broadline ^{1}H NMR after drying in situ and TGA in a 15 % CO_2 stream as described in Section 5.3.2.

Kinetics of CO_2 Adsorption

The maximum CO_2 adsorption can be seen in Figure 5.22. The highest maximum adsorption of CO_2 is seen, for all PEI-SBA15 samples, at 80 °C . The lower molecular weight PEIs (800 PEI, 1300 PEI) have higher maximum adsorptions but there is no discernible trend over the whole range of PEIs. The kinetics of this adsorption can be seen in Figures 5.23, and 5.24 (the t_{30} data is fairly consistent and can be found in Appendix B.7) . The kinetics are fastest for the highest molecular weight PEI, 750000 PEI and generally decrease with decreasing molecular weight, this is expected as there the higher molecular weight PIBSIs tend to adsorb the smallest amount of CO_2. The t_{60} and t_{90} both tend to decrease with temperature.

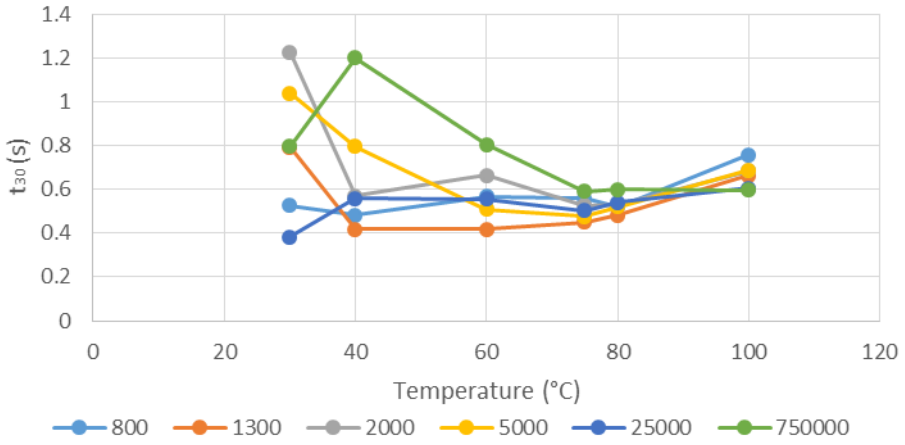


Figure 5.22: Maximum CO_2 capacity of different 50 wt. % PEI-SBA15 samples over 30-100 °C, derived from TGA thermograms

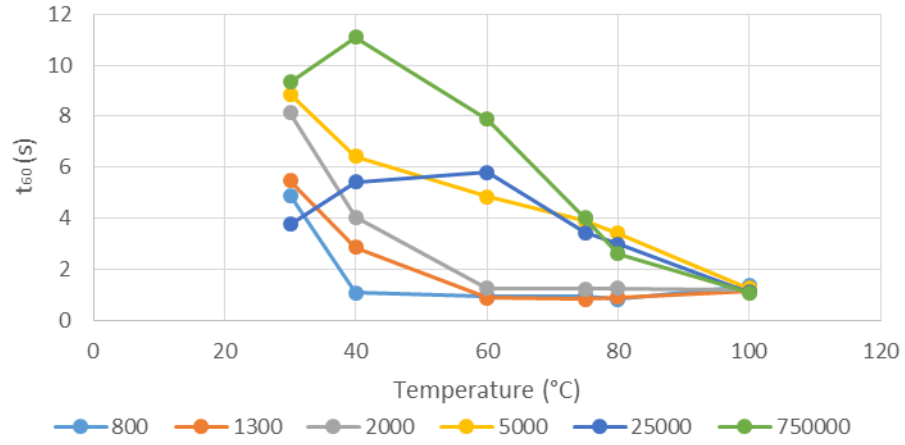


Figure 5.23: t_{60} of CO_2 adsorption on different 50 wt. % PEI-SBA15 samples over 30-100 °C, derived from TGA thermograms

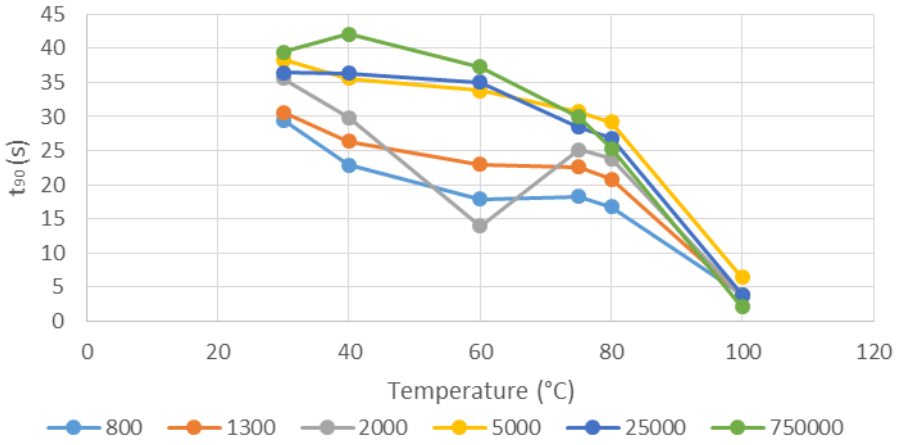


Figure 5.24: t_{90} of CO_2 adsorption on different 50 wt. % PEI-SBA15 samples over 30-100 °C, derived from TGA thermograms

^{1}H NMR Determined Mobility

The mobility of all of the PEI-SBA15 samples can be seen in Figure 5.25. The mobility of these samples increases with temperature, with the decrease in $\Delta H_{\frac{1}{2}}$ being steeper at lower temperatures and much more gradual at higher temperatures. The distinction between these two regimes seems to be approximately 70 °C. There does not seem to be a consistent order of the samples over the whole temperature range or any correlation between PEI chain length and mobility, but all samples show increasing mobility with temperature.

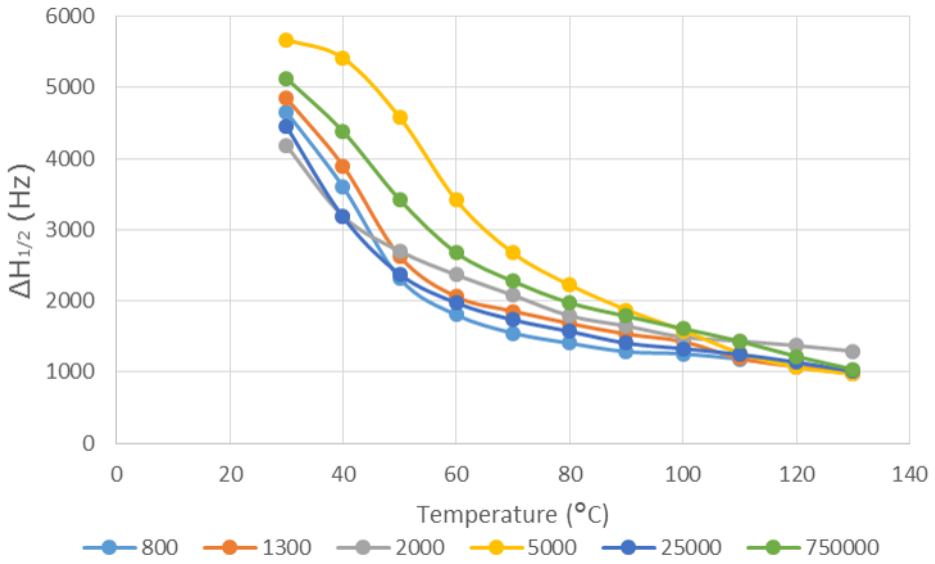


Figure 5.25: ^{1}H NMR data for different 50 wt. % PEI-SBA15 samples over 30-130 °C

5.8.3 Impact of Molecular Weight of PEIs supported on MCF

PEI was adsorbed onto MCF at 50 % loading. MCF has a mostly mesoporous structure with few micropores (see Table 5.5). These samples were studied using broadline ^{1}H NMR after drying in situ and TGA in a 15 % CO_2 stream as described above.

Kinetics of CO_2 Adsorption

The maximum CO_2 adsorption can be seen in Figure 5.26. The highest maximum adsorption of CO_2 is seen, for all PEI-MCF samples, at either 75 or 80 °C , apart from 800 PEI which shows a highest CO_2 capacity at 100 °C . There is no discernible trend between the molecular weight and maximum CO_2 capacity over the whole range of PEIs. The kinetics of this adsorption can be seen in Figures 5.27, and 5.28 (the t_{30} data is fairly consistent and can be found in Appendix B.7). The kinetics data do not show any discernible trend with PEI molecular weight, however, the t_{90} tends to decrease with temperature. The t_{60} for the lower molecular weight PEIs (800 PEI and 1300 PEI) is fairly constant over the whole temperature range and the t_{60} for the other PEIs initially decreases with temperature and then seems to plateau after 60 °C .

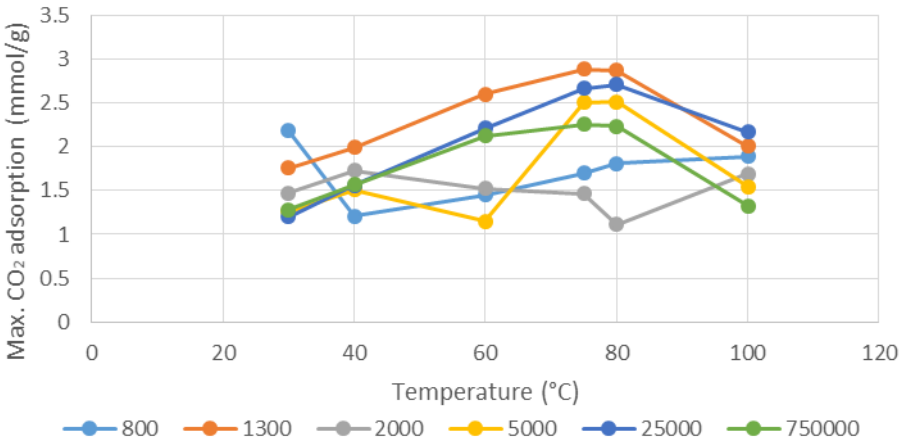


Figure 5.26: Maximum CO_2 capacity of different 50 wt. % PEI-MCF samples over 30-100 °C, derived from TGA thermograms

^{1}H NMR Determined Mobility

The mobility of all of the PEI-MCF samples can be seen in Figure 5.29. The mobility of these samples increases with temperature. The $\Delta H_{\frac{1}{2}}$ for 800 PEI is higher than expected at 60 °C , although still following this trend. This increase may simply be due to a temperature control issue on the NMR as it is only seen in one of the other 800 PEI samples or PEI-MCF samples. Again there are two regimes seen, with a

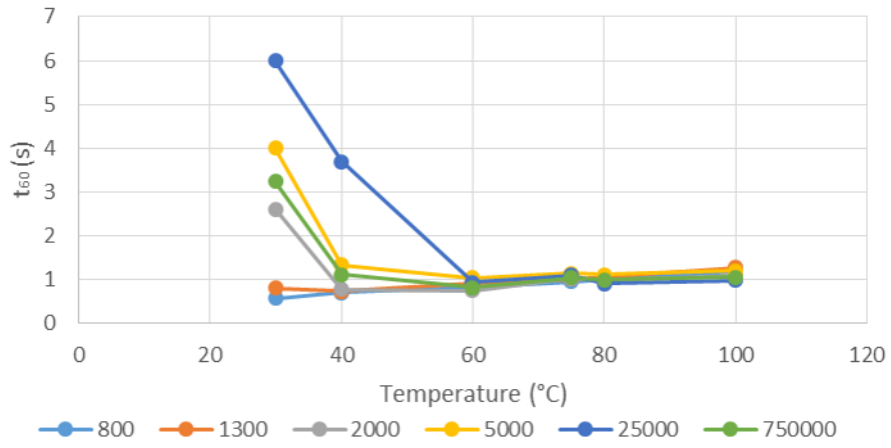


Figure 5.27: t_{60} of CO_2 adsorption on different 50 wt. % PEI-MCF samples over 30-100 °C, derived from TGA thermograms

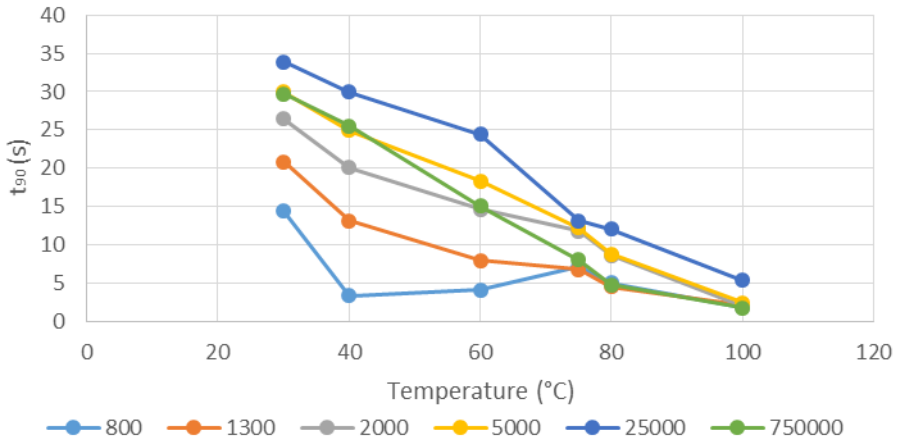


Figure 5.28: t_{90} of CO_2 adsorption on different 50 wt. % PEI-MCF samples over 30-100 °, derived from TGA thermogramsC

steeper decrease in $\Delta H_{\frac{1}{2}}$ being seen at temperatures up to approximately 70 °C and a gradual decrease seen above that. Again for this set of samples there does not seem to be a consistent order over the whole temperature range or any correlation between PEI chain length and mobility.

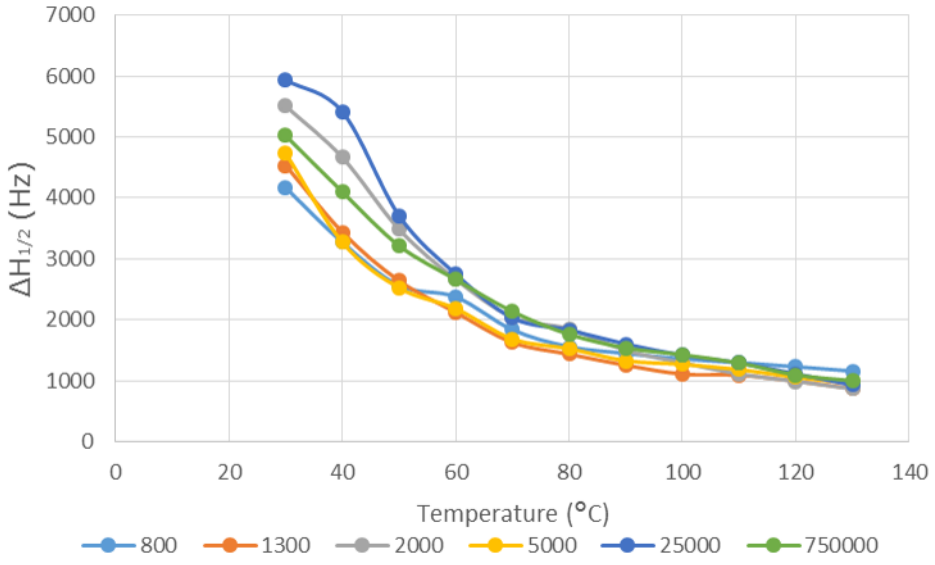


Figure 5.29: ^{1}H NMR data for different 50 wt. % PEI-MCF samples over 30-130 °C

5.8.4 Impact of Molecular Weight of PEIs supported on Rice Husk Silica 1

PEI was adsorbed onto Rice Husk Silica 1 at 50 % loading. Rice Husk Silica 1 has high mesoporosity and likely has a significant macroporous structure (see Table 5.5). These samples were studied using broadline ^{1}H NMR after drying in situ and TGA in a 15 % CO_2 stream as described above.

Kinetics of CO_2 Adsorption

The maximum CO_2 adsorption can be seen in Figure 5.30. The highest maximum adsorption of CO_2 is seen, for all PEI-RH1 samples, at either 75 or 80 °C . The lower molecular weight PEIs generally have higher maximum capacity but there is no strong trends over the whole data set. The kinetics of this adsorption can be seen in Figures 5.31, and 5.32 (the t_{30} data is fairly consistent and can be found in Appendix B.7). The t_{60} and t_{90} kinetics data shows a trend of decreasing t_{60} with decreasing PEI molecular weight. The t_{90} also tends to decrease with temperature. The t_{60} for the lower molecular weight PEIs (800 PEI and 1300 PEI) is fairly constant over the whole temperature range and the t_{60} for the other PEIs initially decreases with temperature and then seems plateau after 60 °C , this is the same as is seen

with MCF.

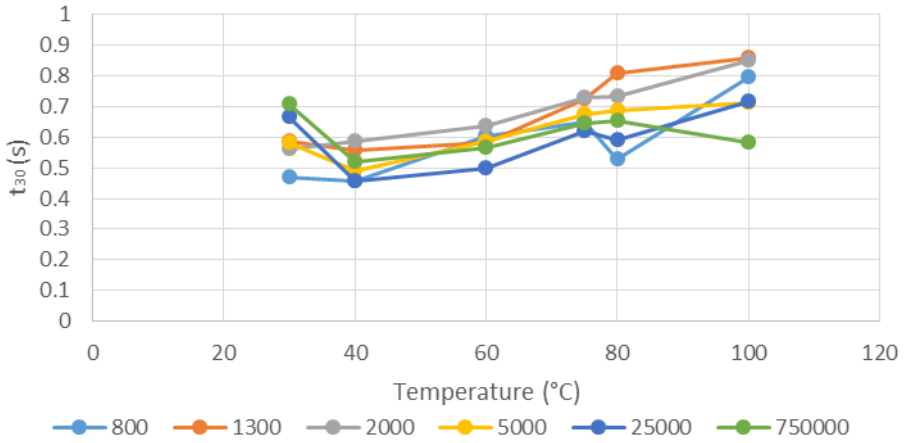


Figure 5.30: Maximum CO_2 capacity of CO_2 adsorption on different 50 wt. % PEI-RH1 samples over 30-100 °C as determined by TGA

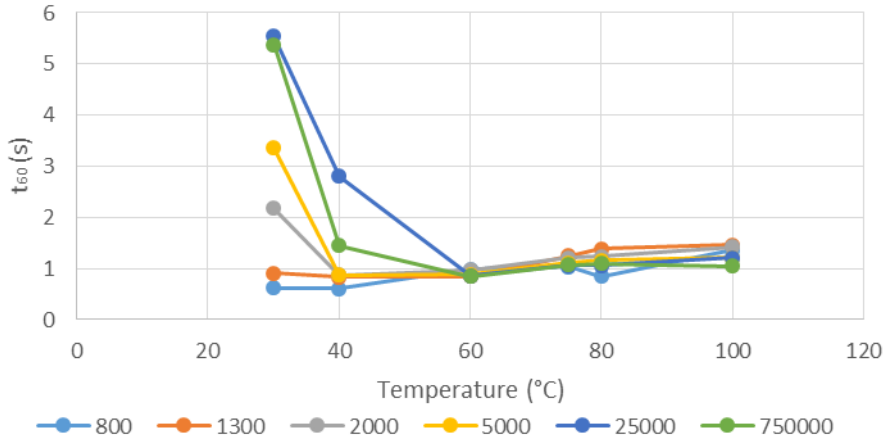


Figure 5.31: t_{60} of different CO_2 adsorption on 50 wt. % PEI-RH1 samples over 30-100 °C as determined by TGA

^{1}H NMR Determined Mobility

The mobility of all of the PEI-RH1 samples can be seen in Figure 5.33. The mobility of these samples increases with temperature. There are also two regimes seen with this substrate, with a steeper decrease in $\Delta H_{\frac{1}{2}}$ being seen at temperatures up to approximately 70 °C and a gradual decrease seen at temperatures above that. The 800 PEI-RH1 mobility data does not follow this regime pattern as closely, especially

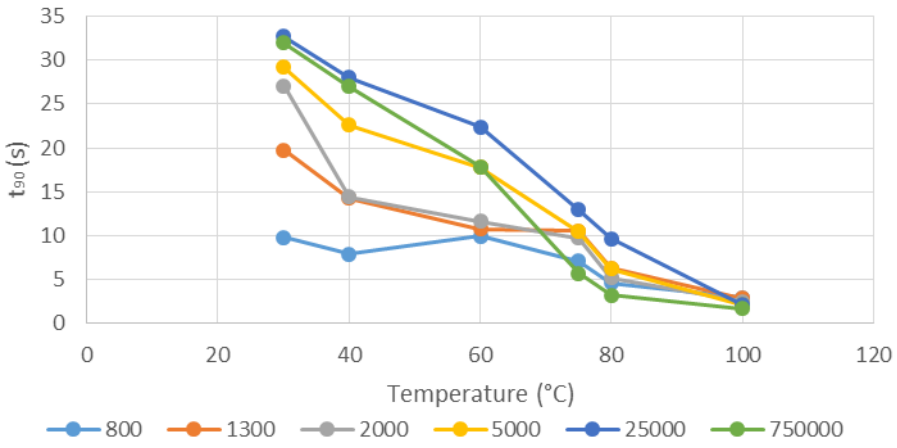


Figure 5.32: t_{90} of CO_2 adsorption on different 50 wt. % PEI-RH1 samples over 30-100 °C as determined by TGA

in the 50-60 °C region. Again for this set of samples there does not seem to be a consistent order over the whole temperature range or any correlation between PEI chain length and mobility.

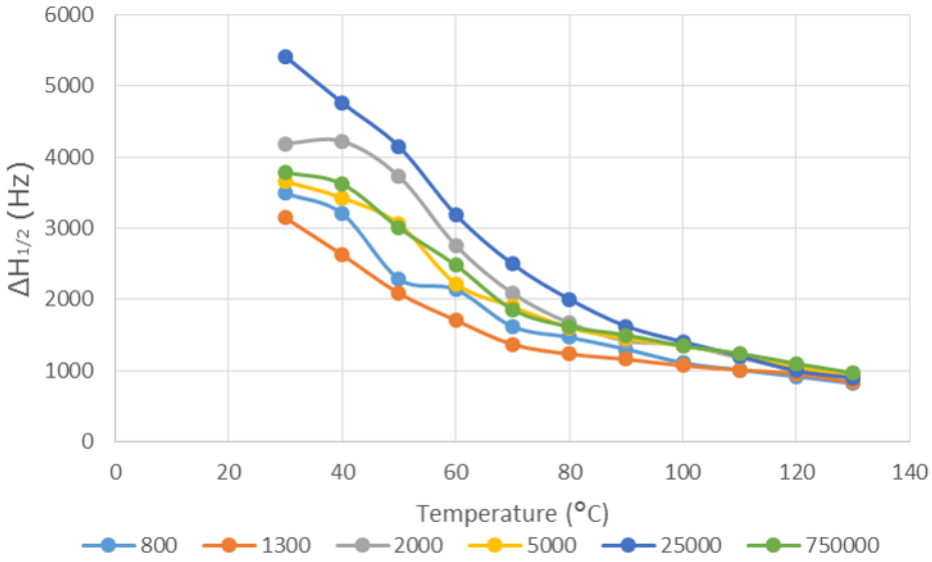


Figure 5.33: ^1H NMR data for different 50 wt. % PEI-RH1 samples over 30-130 °C

5.8.5 Impact of Molecular Weight of PEIs supported on Rice Husk Silica 2

PEI was adsorbed onto Rice Husk Silica 2, RH2, at 60 wt. % loading. Like RH1 Rice Husk Silica 2 has high mesoporous structure and likely has significant macroporous structure (see Table 5.5). These samples were studied using broadline ^{1}H NMR after drying in situ and TGA in a 15 % CO_2 stream as described above.

Kinetics of CO_2 Adsorption

The maximum CO_2 adsorption can be seen in Figure 5.30. The highest maximum adsorption of CO_2 is seen for 800 PEI-RH2 at 100 °C , for samples of 1300 PEI and 25000 PEI at 60 °C and for the higher molecular weight PEIs, 25000 PEI and 750000 PEI, at 75 °C . The kinetics of this adsorption can be seen in Figures 5.35, and 5.36 (the t_{30} data is fairly consistent and can be found in Appendix B.7). The kinetics data for 800 PEI samples is significantly higher over the entire temperature range for all three metrics, and decreases with temperature for t_{60} and t_{90}. The remaining PEIs show a trend of decreasing t_{90} with temperature but little correlation between kinetics and molecular weight.

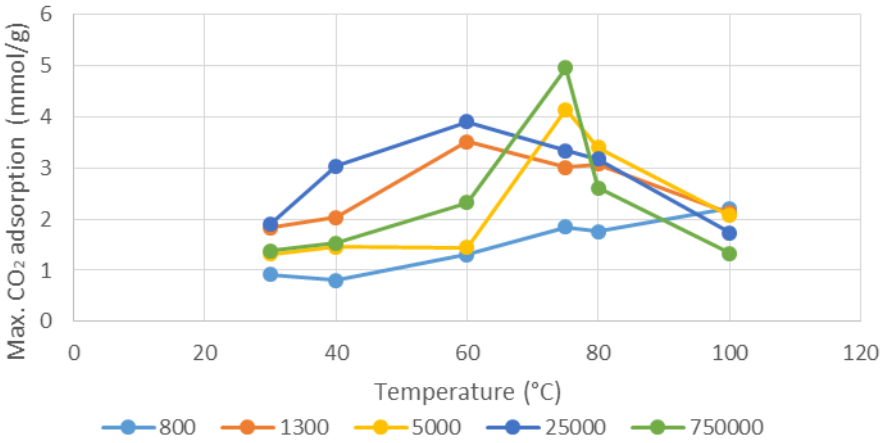


Figure 5.34: Maximum CO_2 capacity of different 60 wt. % PEI-RH2 samples over 30-100 °C, derived from TGA thermograms

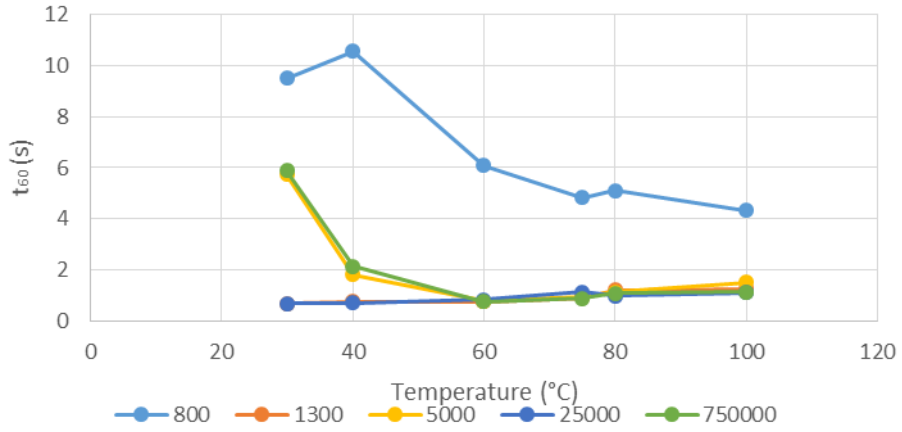


Figure 5.35: t_{60} of CO_2 adsorption on different 60 wt. % PEI-RH2 samples over 30-100 °C, derived from TGA thermograms

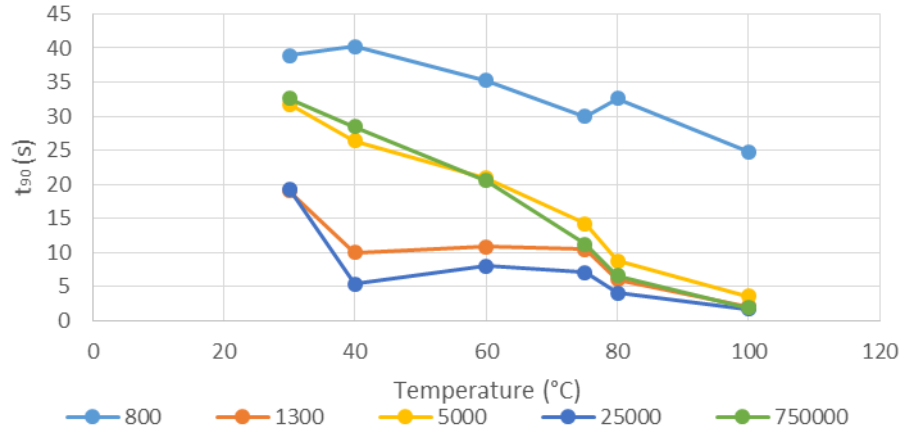


Figure 5.36: t_{90} of CO_2 adsorption on different 60 wt. % PEI-RH2 samples over 30-100 °C, derived from TGA thermograms

^{1}H NMR Determined Mobility

The mobility of all of the prepared PEI-RH2 samples can be seen in Figure 5.37. Unfortunately due to a limited amount of RH2 available, samples of all 6 PEIs could not be prepared in the quantities necessary for both NMR and TGA studies. Thus a sample of 2000 PEI-RH2 was not prepared. 2000 PEI was eliminated as it is a middling weight PEI.

The mobility of all of these samples increases with temperature, again generally following two regimes. An initial steeper decrease in $\Delta H_{\frac{1}{2}}$ being seen at temperatures

up to approximately 70 °C and a gradual decrease seen at temperatures above that. Again the 800 PEI sample does not follow this regime pattern as closely, in the 60 °C region. Again for this set of samples there does not seem to be a consistent order over the whole temperature range or any correlation between PEI chain length and mobility.

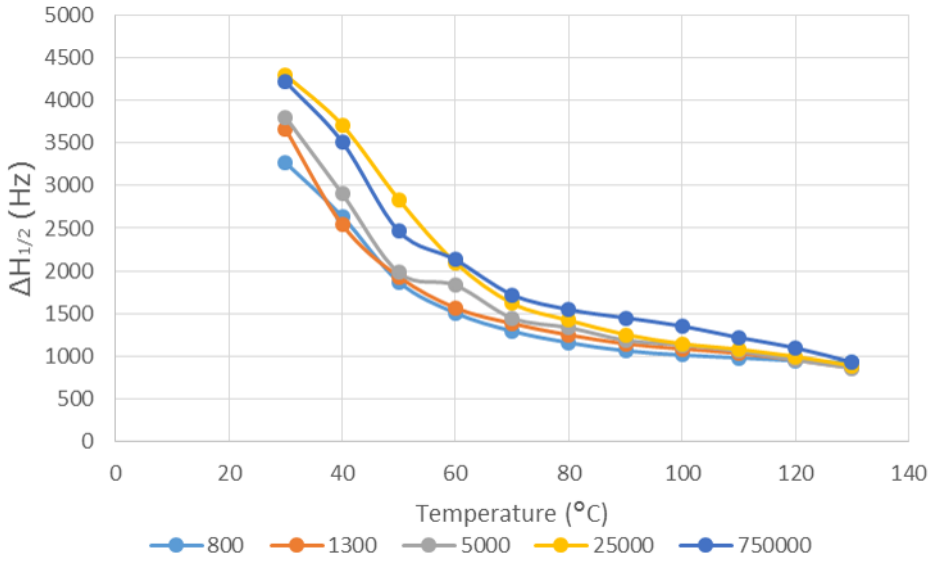


Figure 5.37: ^{1}H NMR data for different 60 wt. % PEI-RH2 samples over 30-130 °C

5.9 Impact of Silica Substrate on Mobility and Kinetics of PEI-Silica

In this section the mobility and kinetics results will be displayed by PEI, ordered by molecular weight, in order to compare the impacts and effects of the silica substrate. This section will also compare the neat PEI data with that of the PEI-Silicas. As with the previous sections, the t_{30} data has been omitted for brevity.

Observations on the overall lineshapes and the specific impacts of the PEI used (as opposed to the impact of the silica) are presented in Section 5.8.

In this section the term "pore size" will be used as a general term, with silicas of high surface area and microporous volume in conjunction with low mesoporous volume having a smaller pore size and those with lower surface areas and high

mesoporous volume having larger pore sizes. With evidence of macroporous structure being expected to result in larger pore sizes than suggested by N_2 sorption. Using this to categorise the silicas, SBA15 has a small pore size, MCF and Silica 1 have middling pore sizes, and RH1 and RH2 have larger pore sizes. More detailed information on the pore structure can be found in Section 5.4.

Mobility and Kinetics of CO_2 Adsorption of 800 M_w PEI Supported on Silicas of Varying Pore Sizes

For the 800 PEI samples, the silica which results in the highest CO_2 capacity is silica 1, at 40 wt. % loading and the higher loading (60 wt. %) RH2 shows one of the lowest loadings (see Figure 5.38). This is in opposition to the logical hypothesis that an increased number of adsorption sites (from higher loadings) would result in greater CO_2 capacity, and the findings of Sanz which found increased PEI content to increase CO_2 capacity.[144]

The kinetics results (Figures 5.39 and 5.40) show much slower rates of CO_2 adsorption for PEI supported on RH2 compared to the other silicas, this difference is especially noticeable for the t_{60} data.

The lowest mobility sample is that of 800 PEI-MCF and the highest mobility across the temperature range is seen in the sample prepared with Silica 1 (see Figure 5.41). The sample prepared with RH1 has a relatively low mobility at low temperatures (under 80 °C) when compared to the other samples and a comparatively high mobility at higher temperatures. The mobility of the RH2 sample is consistently one of the highest compared to the other 800 PEI-silicas. The mobility of the supported PEI tends towards that of the liquid PEI as the temperature increases, suggesting liquid-like behaviour in the pores.

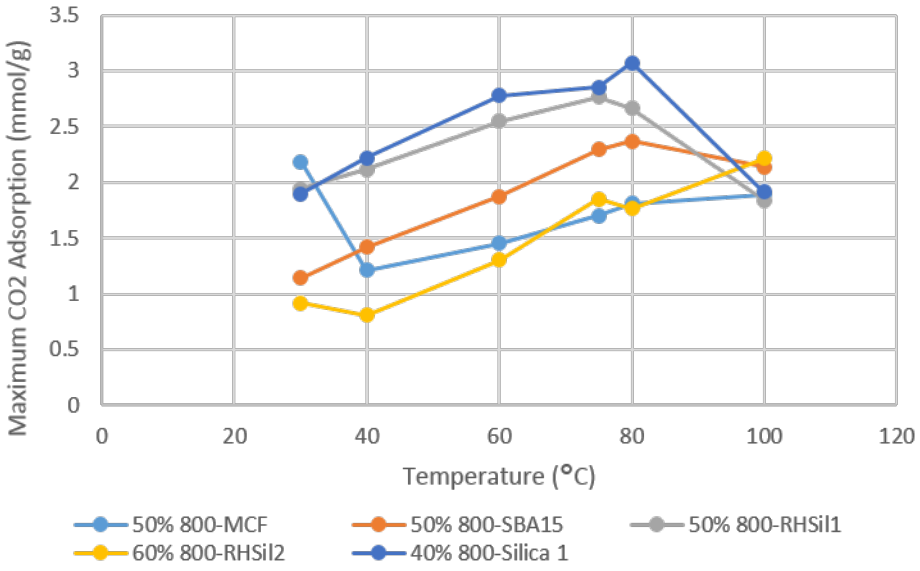


Figure 5.38: Maximum CO_2 capacity of different 800 molecular weight PEI-Silica samples over 30-100 °C, derived from TGA thermograms

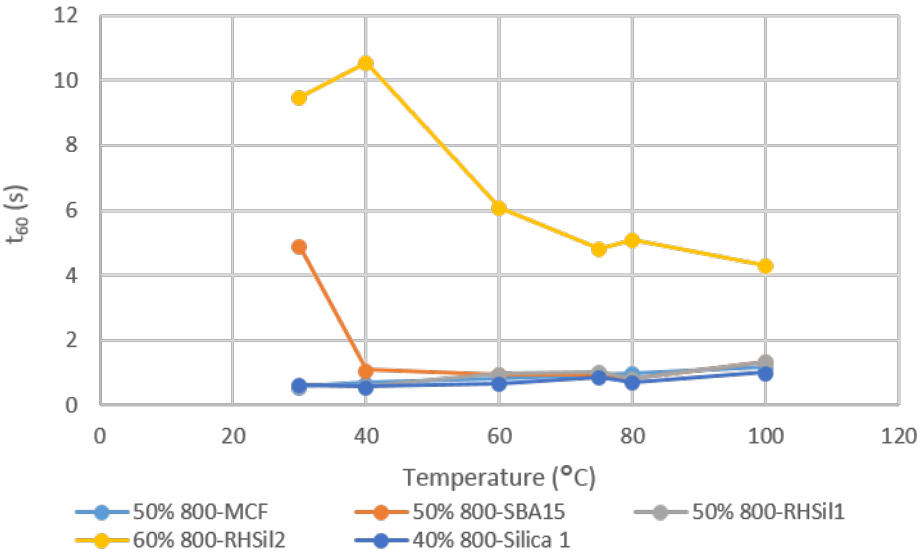


Figure 5.39: t_{60} of CO_2 adsorption on different 800 molecular weight PEI-Silica samples over 30-100 °C, derived from TGA thermograms

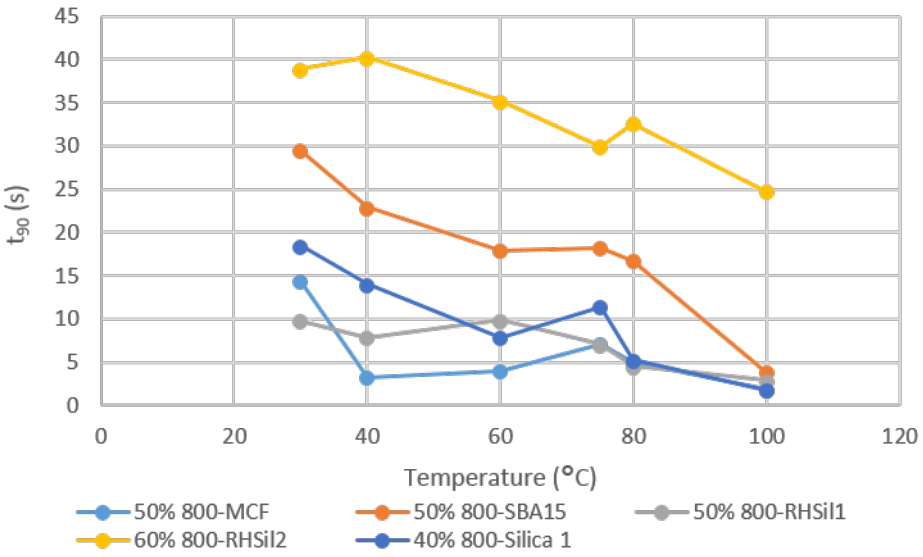


Figure 5.40: T_{90} of CO_2 adsorption on different 800 molecular weight PEI-Silica samples over 30-100 °C, derived from TGA thermograms

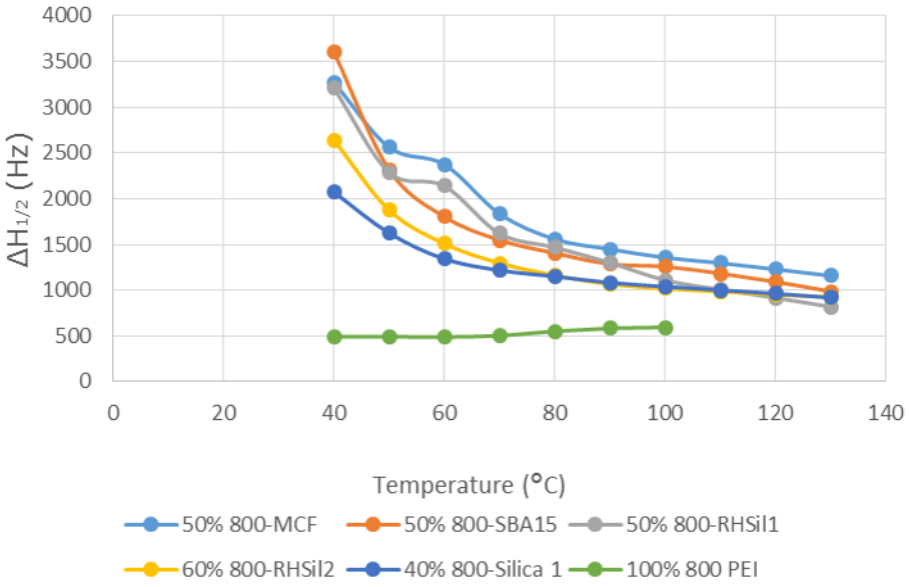


Figure 5.41: ^{1}H NMR data for different 800 molecular weight PEI-Silica samples over 30-130 °C, including neat PEI

Mobility and Kinetics of CO_2 Adsorption of 1200 M_w PEI Supported on Silicas of Varying Pore Sizes

For the 1300 PEI samples, the silica which results in the highest CO_2 capacity is RH2, at 60 wt. % loading (see Figure 5.42). RH2 has the highest loading and largest pore sizes (see Table 5.5). This is contrasted by the lowest CO_2 capacity being seen for the silica with the smallest pore size, SBA-15. This is somewhat expected as it logically follows that the highest PEI loading would result in higher CO_2 capacity as there are a greater number of adsorption sites and the smallest pore sizes might be expected to present a greater steric hindrance to CO_2 adsorption.

The RH2 sample also has a maximum CO_2 capacity at a lower temperature, 60 °C than the other samples, which tend to be 75 or 80 °C.

The kinetics results (Figures 5.43 and 5.44) show much slower rates of CO_2 adsorption for PEI supported on SBA-15 compared to the other silicas, although this difference is not present for t_{60} at higher temperatures.

In this sample set there seems to be a propensity for the silicas with smaller pores to have a lower mobility than those with larger pores, this is specifically seen in SBA-15 (the silica with the most microporous pore volume) having a consistently higher $\Delta H_{\frac{1}{2}}$ than the silicas derived from rice husk (RH1 and RH2, which have significant meso- macro- porous structure). This may be a result of increased pore confinement restricting the mobility of the PEI or the result of increased interaction between the PEI and the silica surfaces. This trend is also seen with several of the other PEI samples.

The mobility of these samples increases towards that of the liquid PEI sample at high temperatures, however the supported PEI maintains a lower mobility than that of the liquid.

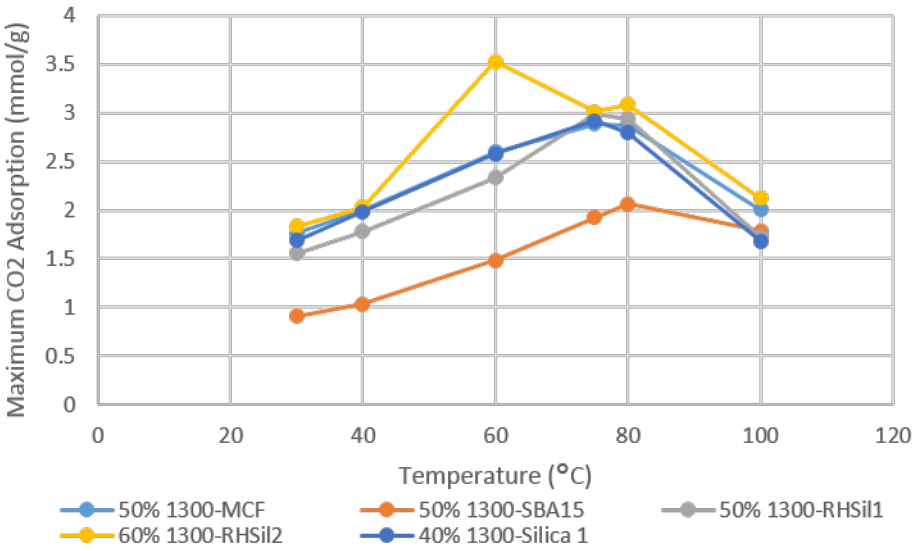


Figure 5.42: Maximum CO_2 capacity of different 1300 molecular weight PEI-Silica samples over 30-100 °C, derived from TGA thermograms

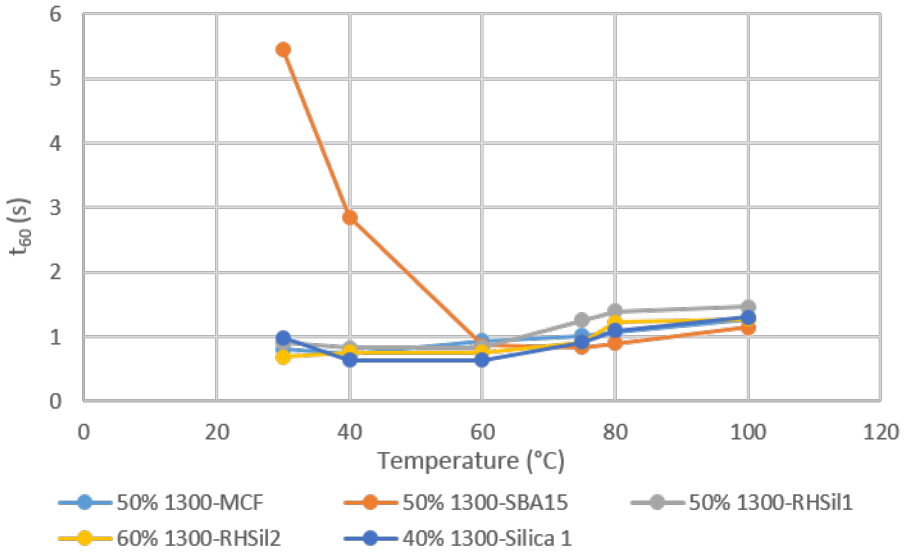


Figure 5.43: t_{60} of CO_2 adsorption on different 1300 molecular weight PEI-Silica samples over 30-100 °C, derived from TGA thermograms

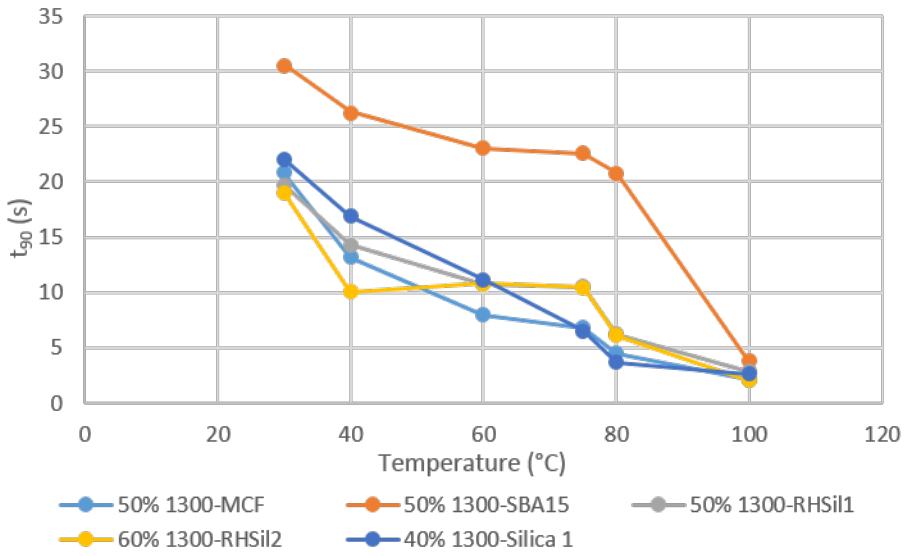


Figure 5.44: t_{90} of CO_2 adsorption on different 1300 molecular weight PEI-Silica samples over 30-100 °C, derived from TGA thermograms

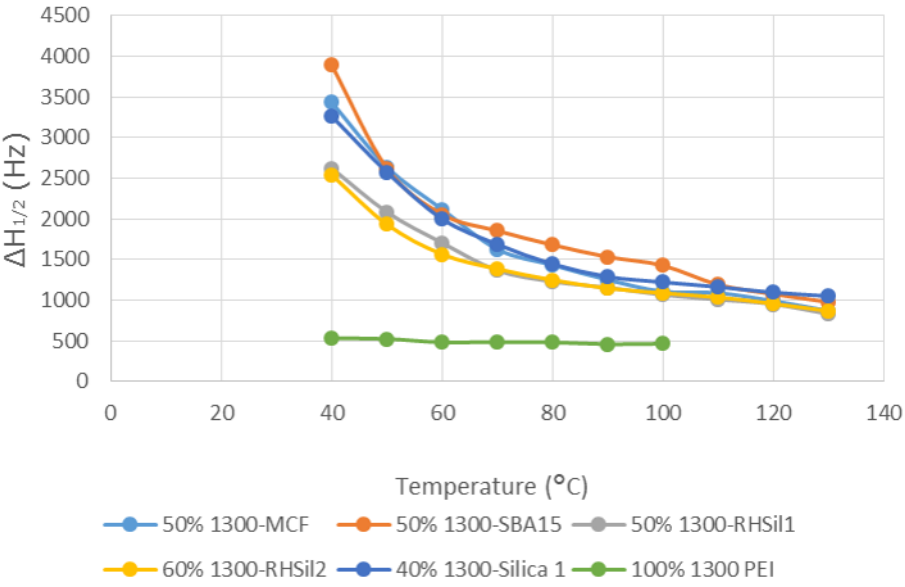


Figure 5.45: ^{1}H NMR data for different 1300 molecular weight PEI-Silica samples over 30-130 °C, including neat PEI

Mobility and Kinetics of CO_2 Adsorption of 2000 M_w PEI Supported on Silicas of Varying Pore Sizes

For the 2000 PEI samples, the silicas which results in the highest CO_2 capacity are Silica 1 and RH1 (with maximum capacities over 2.5 mmol/g, see Figure 5.46), however it was not possible to prepare a 2000 PEI-RH2 sample RH2 so it is unknown if the use of RH2 as the silica support would result in a higher maximum capacity as it has for other PEIs.

The kinetics results (Figures 5.47 and 5.48) initally show much slower rates of CO_2 adsorption for PEI supported on RH1 compared to the other silicas, with a RH1 having relatively high t_{60}. However SBA-15 has the highest t_{90}, and RH1 is comparative to the other silicas.

For samples of 2000 PEI supported on silicas (Figure 5.49 C), there is no discernible relationship between pore sizes and mobility. The lowest mobilities at low temperature of MCF and RH1 samples are comparatively high at high temperature. Again the mobility of these samples increases towards that of the liquid PEI sample at high temperatures with some of the samples at 130 °C having a comparative mobility to that of the neat PEI at 40-50 °C.

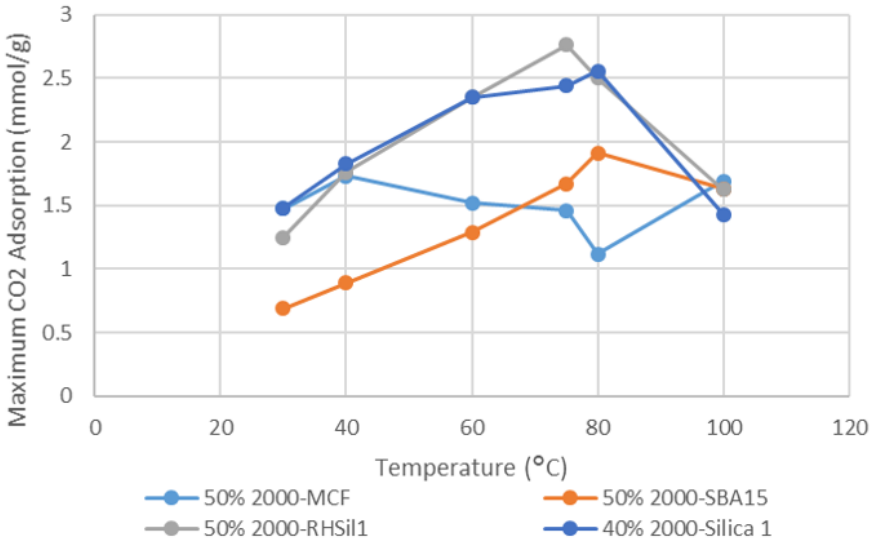


Figure 5.46: Maximum CO_2 capacity of different 2000 molecular weight PEI-Silica samples over 30-100 °C, derived from TGA thermograms

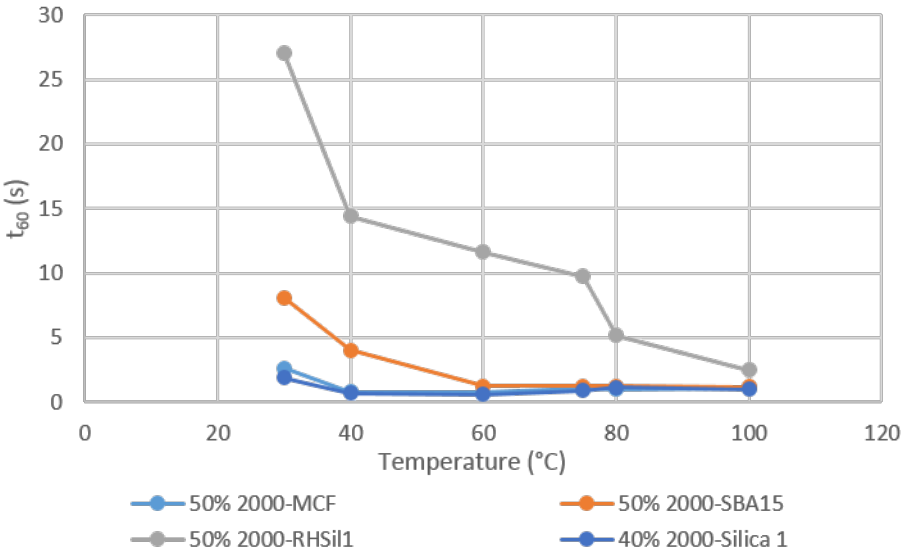


Figure 5.47: t_{60} of CO_2 adsorption on different 2000 molecular weight PEI-Silica samples over 30-100 °C, derived from TGA thermograms

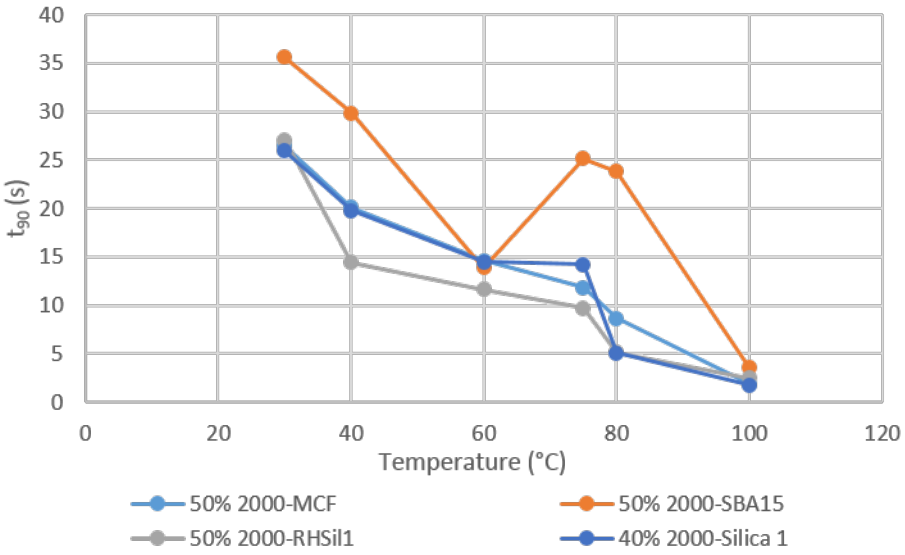


Figure 5.48: t_{90} of CO_2 adsorption on different 2000 molecular weight PEI-Silica samples over 30-100 °C, derived from TGA thermograms

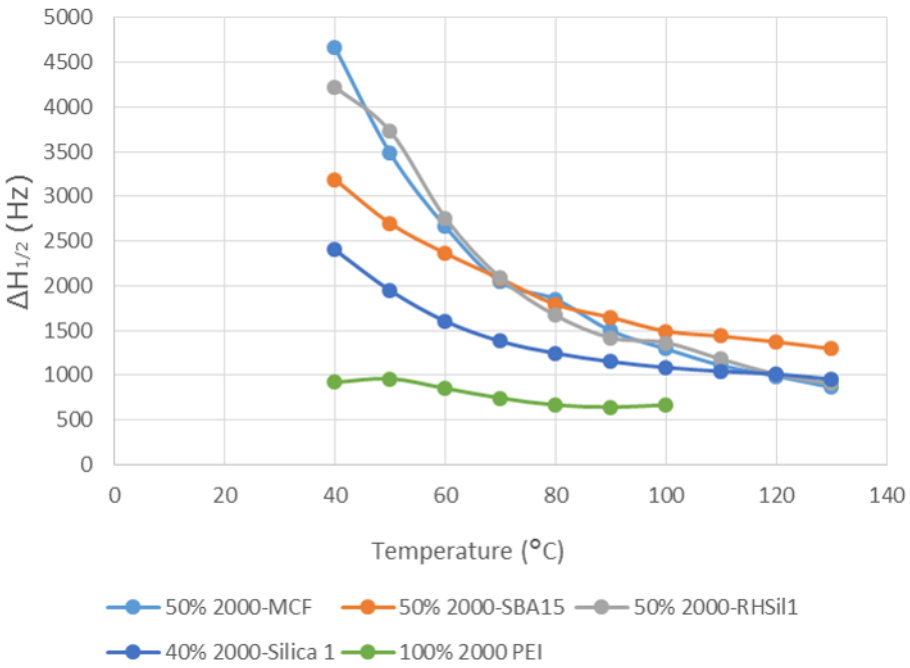


Figure 5.49: ^{1}H NMR data for different 2000 molecular weight PEI-Silica samples over 30-130 °C, including neat PEI

Mobility and Kinetics of CO_2 Adsorption of 5000 M_w PEI Supported on Silicas of Varying Pore Sizes

For the 5000 PEI samples, the silica which results in the highest CO_2 capacity is again RH2, and the lowest is SBA-15 (see Figure 5.50). However the RH2 samples maximum CO_2 capacity is at 75 °C for this sample.

The kinetics results again (Figures 5.51 and 5.52) show much slower rates of CO_2 adsorption for PEI supported on SBA-15 compared to the other silicas, which are very similar.

For these samples there is some correlation between pore size and mobility, with the smallest pore size (SBA-15) generally resulting in the lowest mobility and the one of the largest pore sizes (RH2) resulting in the highest (see Figure 5.53), however RH1 which also has a highly macroporous structure does not follow this trend. The mobility of the liquid PEI is again comparative to that of the high temperature supported PEI.

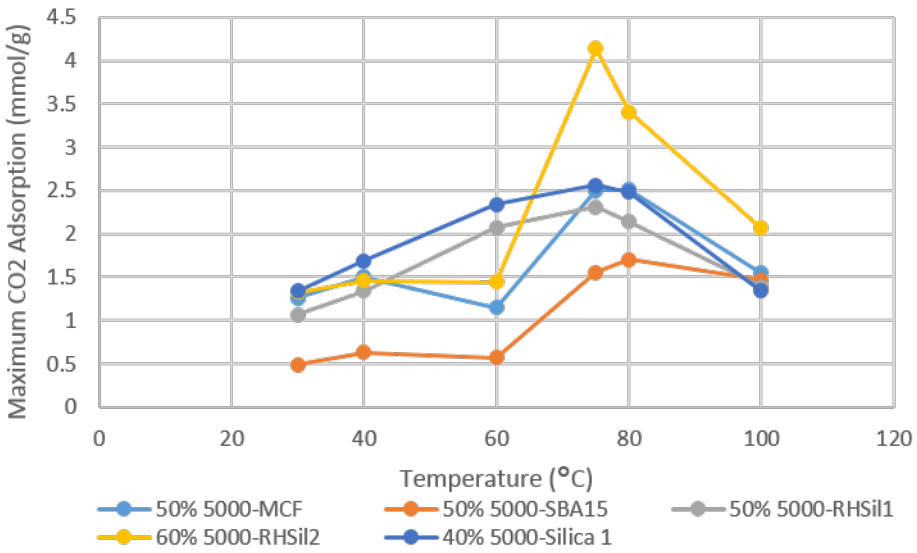


Figure 5.50: Maximum CO_2 capacity of different 5000 molecular weight PEI-Silica samples over 30-100 °C, derived from TGA thermograms

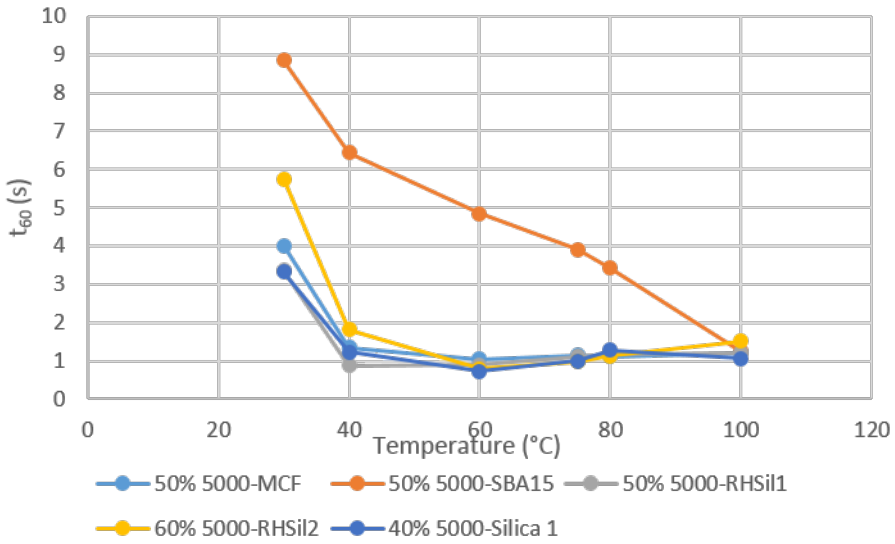


Figure 5.51: t_{60} of CO_2 adsorption on different 5000 molecular weight PEI-Silica samples over 30-100 °C, derived from TGA thermograms

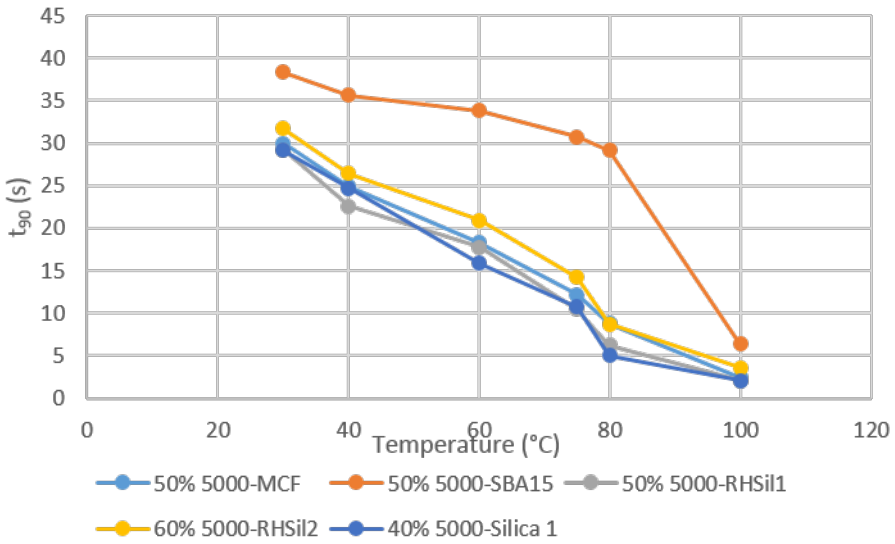


Figure 5.52: t_{90} of CO_2 adsorption on different 5000 molecular weight PEI-Silica samples over 30-100 °C, derived from TGA thermograms

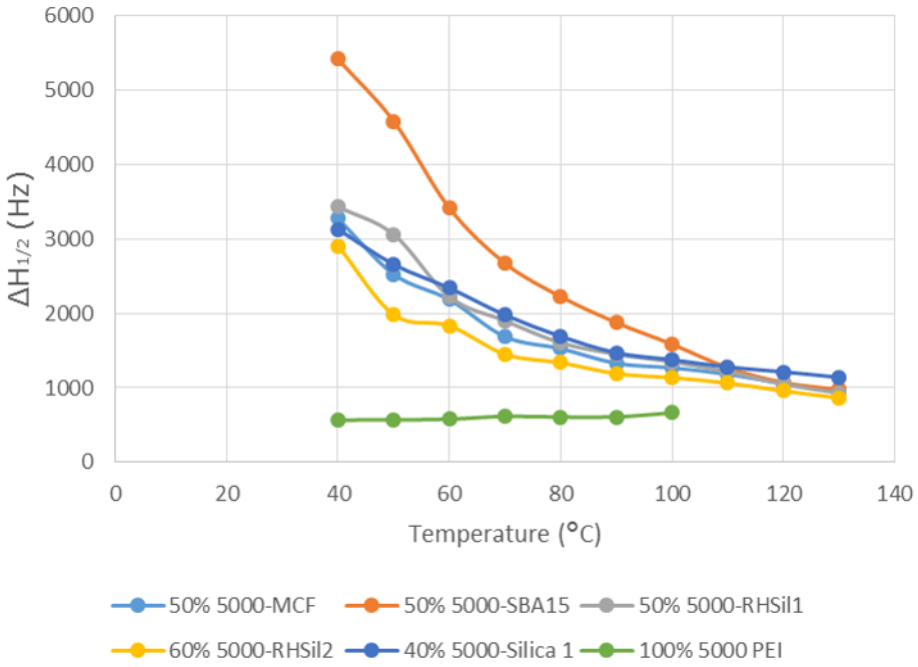


Figure 5.53: ^{1}H NMR data for different 5000 molecular weight PEI-Silica samples over 30-130 °C, including neat PEI

Mobility and Kinetics of CO_2 Adsorption of 25000 M_w PEI Supported on Silicas of Varying Pore Sizes

For the 25000 PEI samples, the highest and lowest CO_2 capacities are again seen by PEI supported on RH2 and SBA-15 (see Figure 5.54). Similarly to the 1300 PEI samples the maximum CO_2 capacity for the RH2 sample is again seen at 60 °C.

Again, the kinetics (Figures 5.55 and 5.56) show much slower rates of CO_2 adsorption for PEI supported on SBA-15 and PEI-RH2 shows the fastest kinetics.

The 25000 PEI-Silica samples do not show any obvious correlation between pore sizes and mobility, with the highest mobility shown by SBA-15 (50 wt % loading) and RH2 (60 wt % loading), the silicas with the smallest and one of the largest pore sizes, respectively (see Figure 5.57). The lowest mobility is seen for the 25000 PEI-RH1 sample which has significant meso- and macro- porous structure. The relative mobility of the neat PEI is significantly lower than with the lower molecular weight PEIs and at high temperatures the supported PEI shows higher mobility than that of the bulk liquid.

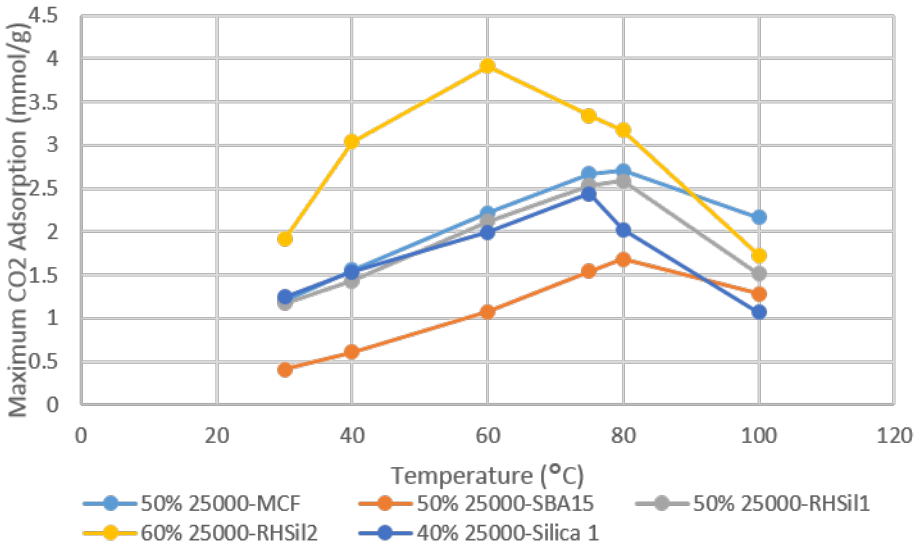


Figure 5.54: Maximum CO_2 capacity of different 25000 molecular weight PEI-Silica samples over 30-100 °C, derived from TGA thermograms

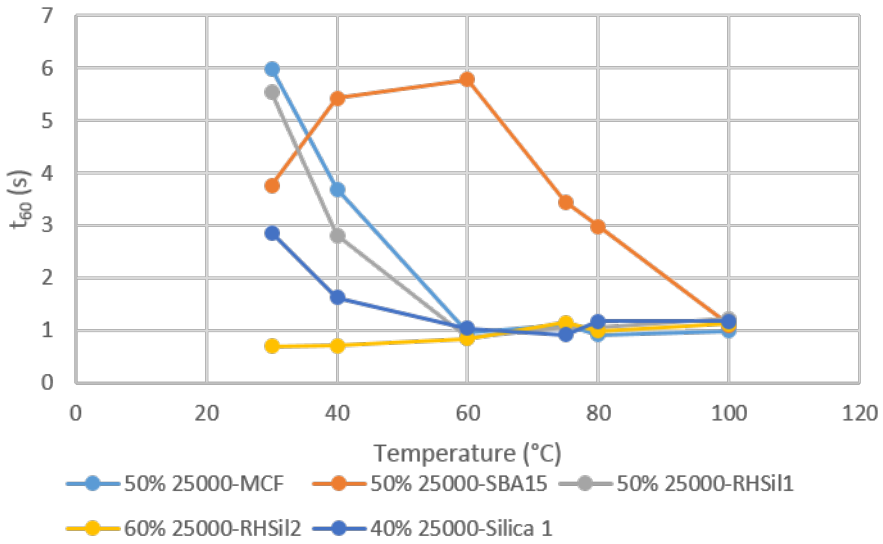


Figure 5.55: t_{60} of CO_2 adsorption on different 25000 molecular weight PEI-Silica samples over 30-100 °C, derived from TGA thermograms

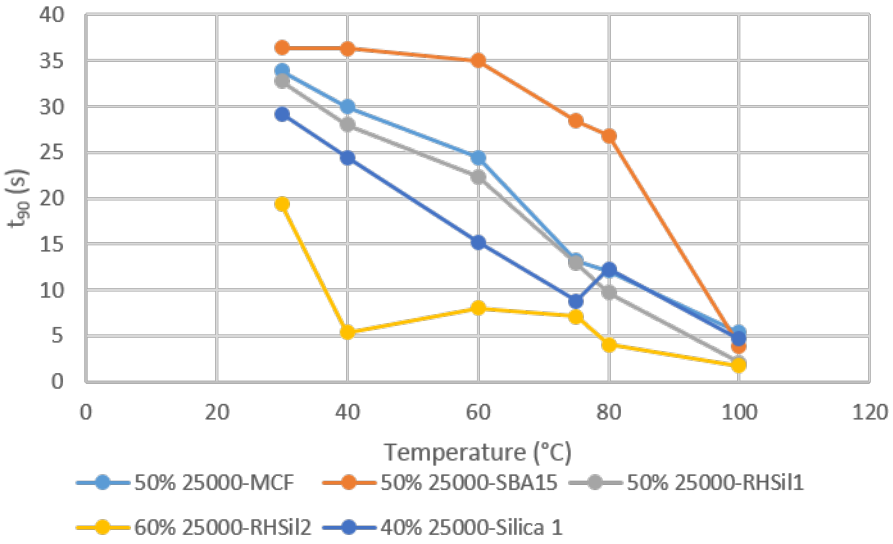


Figure 5.56: t_{90} of CO_2 adsorption on different 25000 molecular weight PEI-Silica samples over 30-100 °C, derived from TGA thermograms

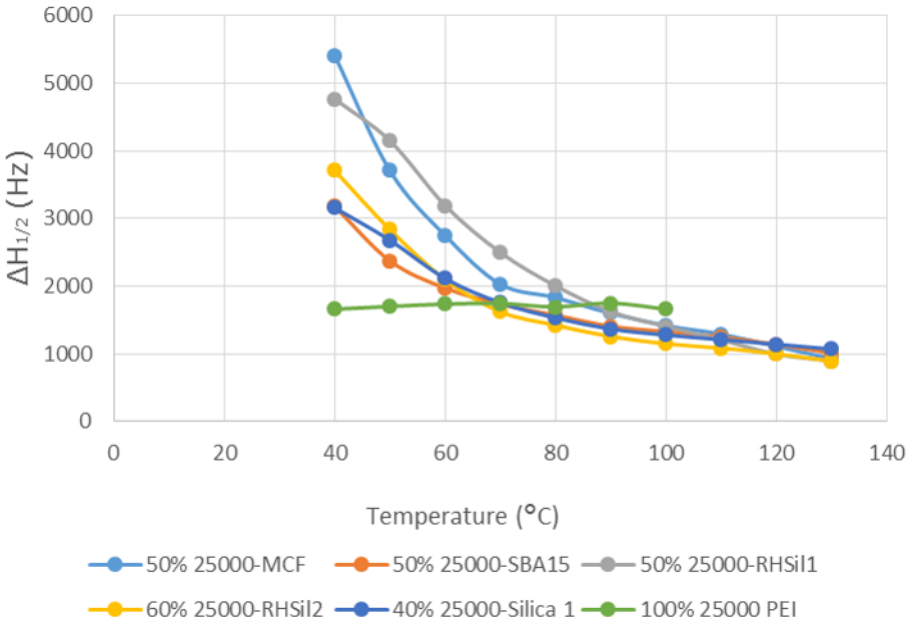


Figure 5.57: ^{1}H NMR data for different 25000 molecular weight PEI-Silica samples over 30-130 °C, including neat PEI

Mobility and Kinetics of CO_2 Adsorption of 750000 M_w PEI Supported on Silicas of Varying Pore Sizes

For the highest molecular weight PEI, the highest and lowest CO_2 capacities are again seen by PEI supported on RH2 and SBA-15 (see Figure 5.58). The maximum CO_2 capacity is seen at 75 °C and is significantly higher than the other samples.

Again, the kinetics (Figures 5.59 and 5.60) show much slower rates of CO_2 adsorption for PEI supported on SBA-15.

The 750000 PEI, there is a trend of increasing mobility with increasing pore size for all but Silica 1 which shows the highest mobility whilst having smaller pores and neck size than the other mesoporous silica, MCF (see Figure 5.61). This may simply be a result of the lower loading of Silica 1 (40 wt. %).

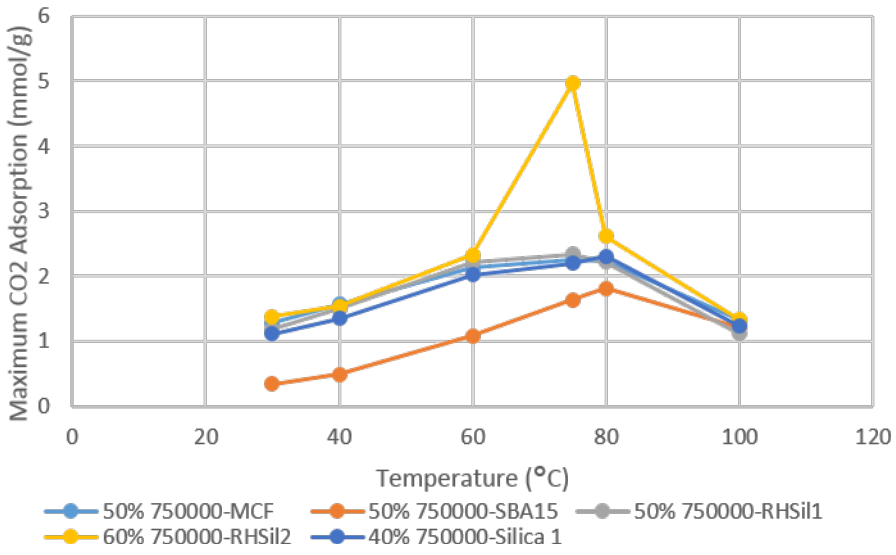


Figure 5.58: Maximum CO_2 capacity of different 750000 molecular weight PEI-Silica samples over 30-100 °C, derived from TGA thermograms

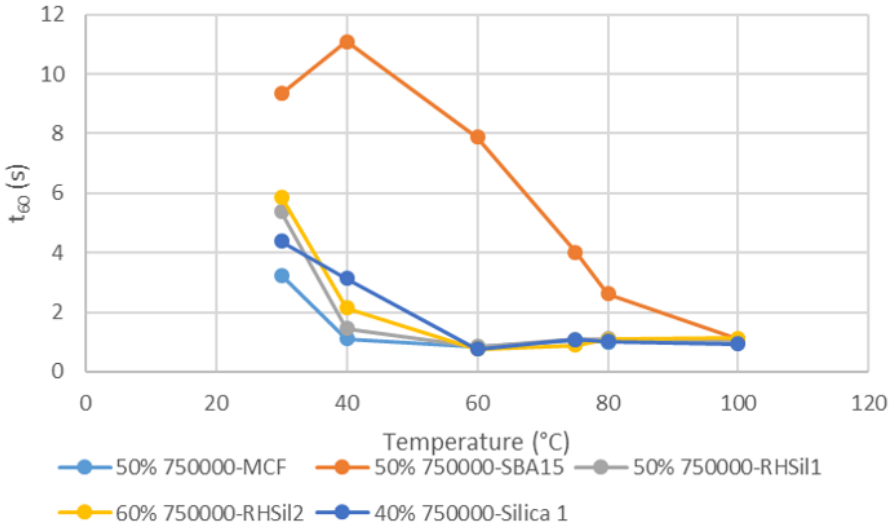


Figure 5.59: t_{60} of CO_2 adsorption on different 750000 molecular weight PEI-Silica samples over 30-100 °C, derived from TGA thermograms

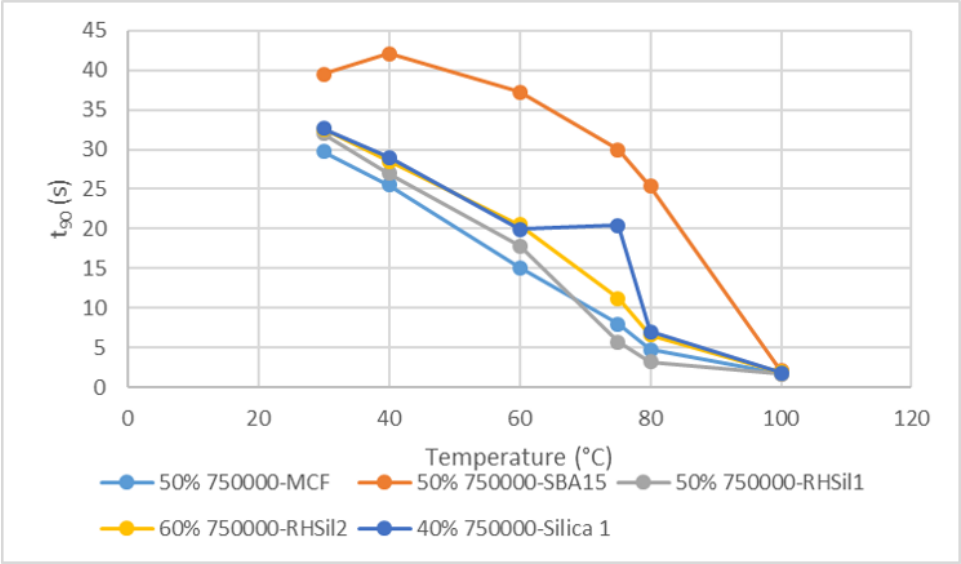


Figure 5.60: t_{90} of CO_2 adsorption on different 750000 molecular weight PEI-Silica samples over 30-100 °C, derived from TGA thermograms

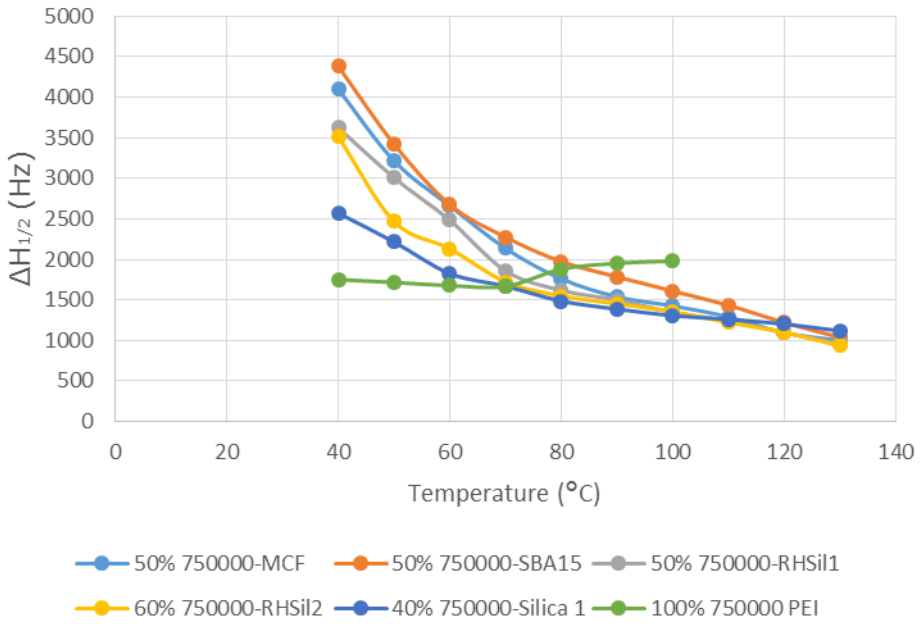


Figure 5.61: ^{1}H NMR data for different 750000 molecular weight PEI-Silica samples over 30-130 °C, including neat PEI

5.9.1 Kinetics of CO_2 Adsorption at Optimum PEI-Silica Loadings

The kinetics data for the temperature at which the highest maximum CO_2 adsorption was achieved (see Table B.6 in Appendix B.7) have been collated into Figures 5.62, 5.63, and 5.64, which display the t_{30}, t_{60} and t_{90}.

As can be seen from these figures, other than low adsorption rates for 800 PEI-RH2 and 800 PEI-RH1, the initial adsorption (t_{30}) is fast and fairly consistent across all PEI molecular weights and silicas. The t_{60}, however shows that for the higher molecular weight PEI samples the smallest pore size silica, SBA-15, has a much slower rate of adsorption after the initial fast adsorption. This is likely due to pore blockage and steric hindrance to CO_2 diffusion. The t_{90}, indicating the speed of the final stages or adsorption, is high for all SBA-15 samples.

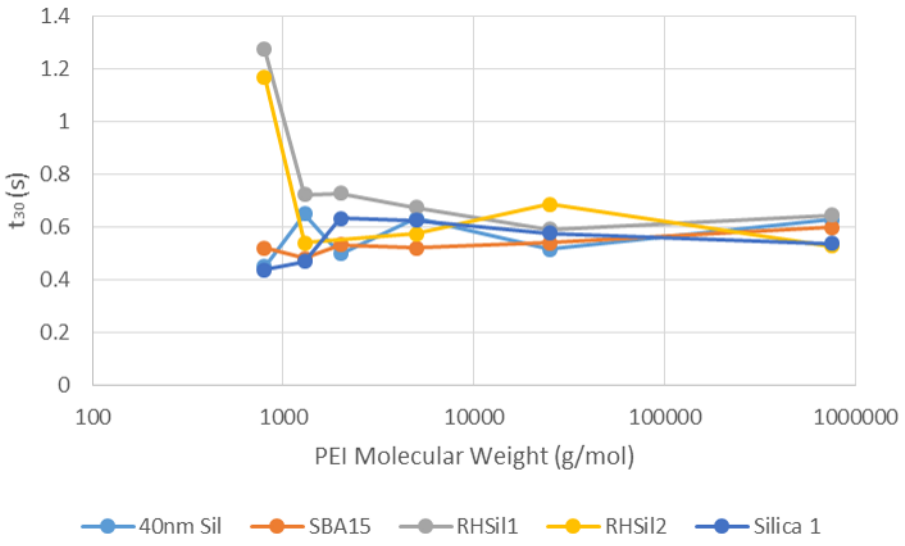


Figure 5.62: TGA determined t_{30} of CO_2 adsorption onto the highest capacity PEI-Silica materials with respect to the molecular weight of the PEI

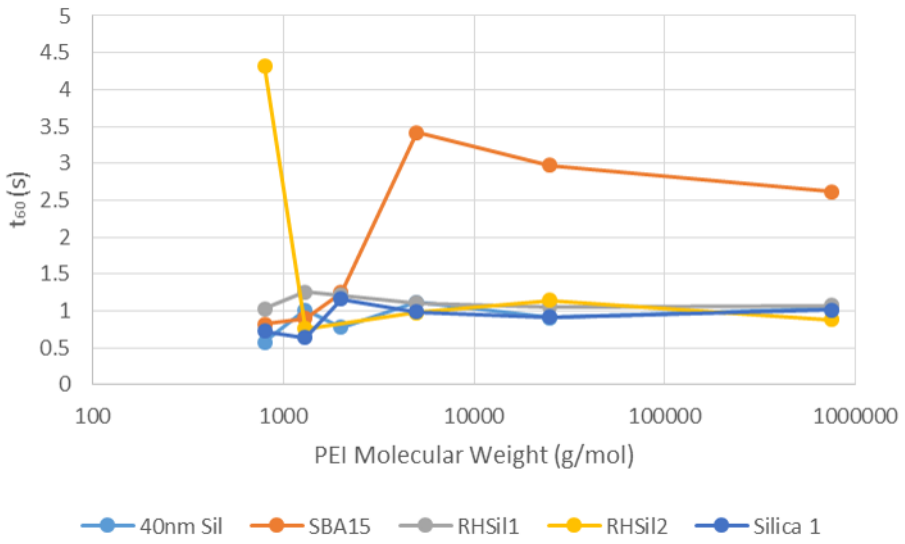


Figure 5.63: TGA determined t_{60} of CO_2 adsorption onto the highest capacity PEI-Silica materials with respect to the molecular weight of the PEI

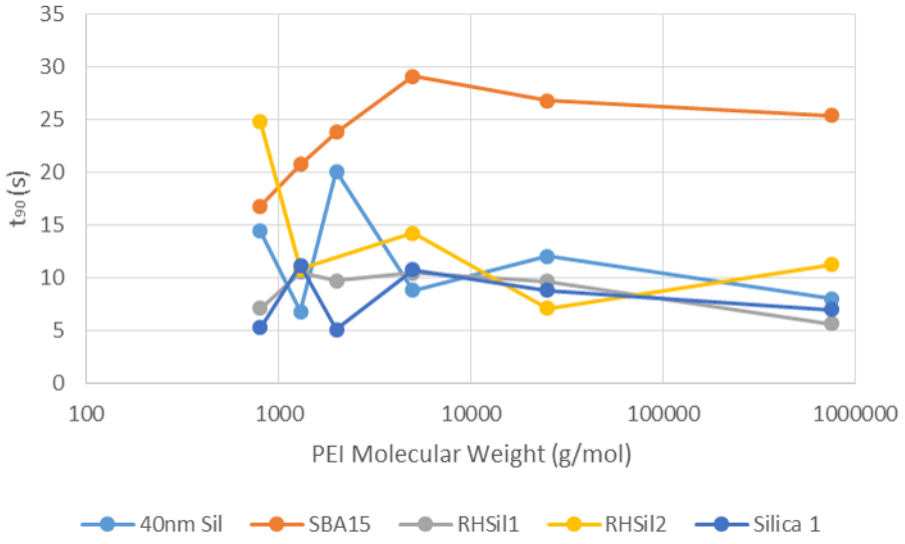


Figure 5.64: TGA determined t_{90} of CO_2 adsorption onto the highest capacity PEI-Silica materials with respect to the molecular weight of the PEI

5.10 Discussion of PEI-Silica Mobility and Kinetics Results

The kinetics and mobility data for each of the PEI-Silicas is discussed in the previous sections (5.8 and 5.9). In this section the two properties will be compared and discussed.

The adsorption of CO_2 on PEI-Silica as well as the mobility of the PEI hydrogen atoms in PEI-Silica may be impacted by both the pore shape/size and the molecular weight of the PEI adsorbent.

With regards to pore size, one key feature associated with pore size is the loading capacity of the silica. Increased loading will result in an increased number of adsorption sites and may be expected to lead to a higher maximum capacity. An examination of this can be seen in the first part of Section 5.10.2. Pore size and shape would also be expected to impact the kinetics of CO_2 adsorption, with small necks and ink-bottle pores resulting in an increased likeliness for pore blockage. This may be expected to result in slower rates and lower maximum capacity, this is also discussed in Section 5.10.2.

In addition to pore size, high pore volumes would be expected to facilitate passage of CO_2 to the adsorption sites, which in turn would increase the rate of adsorption. One facet of this may be that fewer larger pores would result in a shorter path length to adsorption. As high pore volumes are associated with larger pores, this supports the premise that the larger pores would have faster adsorption kinetics.

When considering the impact of PEI molecular weight, it was expected that both the mobility of the PEI and the adsorption of CO_2 would be impacted. The higher molecular weight PEIs were expected to have lower mobilities, as the branched chains result in steric hindrance and entanglement. This is discussed in Section 5.10.1. The higher molecular weight PEIs were also expected to have decreased maximum capacity, in keeping with literature findings shown in Table 2.1 and to have slower kinetics as the PEI restricted access for the CO_2 into the pores. This is discussed in the second part of Section 5.10.2.

5.10.1 Discussion of PEI and PEI-Silica Mobility

Neat PEI Mobility

At low temperatures it is clear that the mobility of the bulk PEI is vastly different to that of the confined PEI in the PEI-Silicas. However as temperature increases and the mobility of the confined PEI increases, the difference between the values of $\Delta H_{\frac{1}{2}}$ for the confined and free PEI decreases.

In the cases of the higher weight PEIs, 25000 and 750000 PEI, the mobility of the bulk PEI is, at higher temperatures, slightly lower than that of the adsorbed PEI, however it is important to note the high error in these measurements. Considering this error, it is still fair to observe that these PEIs show, at around 70-80 °C, very similar mobility between the adsorbed and bulk PEI. This indicates that the PEI inside the silica pores is behaving as a free liquid, for these PEIs.

The lower weight PEIs do not show such a correlation, however these PEIs are significantly less viscous. From the comparison it can still be seen that the high temperature PEI-Silica mobility is much closer to that of the bulk liquid.

PEI-Silica Mobility

The mobility of all of the PEI-Silicas is dependent on temperature, as temperature increases so does the mobility of the sample. This is simply due to the increase in kinetic energy in the samples. The PEI-Silica samples initially increase in mobility quickly and then this begins to plateau at around 70-80 °C. This is a result of the PEI-Silica interactions lessening and the PEI becoming more free and fluid-like within the pores. This is supported by the much more similar values of $\Delta H_{\frac{1}{2}}$ seen at high temperature for all of the PEI-Silicas, than at low temperature.

Generally speaking, the PEIs supported on SBA-15 have the lowest mobility (except for 25000 PEI-SBA15), this is a result of the confinement of the small pores, and those supported on Silica 1 have the highest (or at least fairly high) mobilities. The high mobilities of PEI supported on Silica 1 is probably a result of the lower loading of PEI-Sil1s, of 40 %. PEI-RH2s often have a fairly high mobility in spite of the high (60 %) loading of these samples, which is likely due to the large macropores.

An interesting feature can be seen with regards to the mobilities of several of the samples, specifically 25000 PEI-Sil1, 25000 PEI-RH1, 800 PEI-RH1 and 750000 PEI-RH2, a stability in $\Delta H_{\frac{1}{2}}$ is seen at 60 °C. A possible source of this deviation from the trend may be interactions between the silica surface and PEI restricting the mobility of the PEI until broken by high temperatures, however it is also possible that it may have resulted from inconsistencies in the heating rate.

There does not seem to be any correlation between the molecular weight of PEI and the mobility of PEI-Silicas over temperature. This is not unexpected as each of the samples (on the same silica) uses the same wt. % loading so it would be expected for each of the pores to be equally filled and thus the impact of the pore confinement should be fairly equal. However this is in contrast to Lin and Blum (1997) who found adsorbed polymers (poly(methyl acrylate)) to show molecular weight dependant mobility (specifically lower mobility for lower molecular weights), although this study only investigated two polymer samples.[182] The aformentioned study also finds mobility to increase with temperature, and finds the bulk polymer higher to be lower than that of the adsorbed polymer. There is no information available for the pore size of the silica substrate used in the investigation and thus it is difficult to draw significant comparisons between the two sets of data.

5.10.2 Discussion of PEI-Silica Kinetics

Maximum CO_2 Adsorption

The maximum CO_2 adsorption, for the majority of the samples, increases from 30 °C to 75-80 °C and then decreases at 100 °C. The peak in maximum CO_2 adsorption, most commonly occurs at 75 or 80 °C and correlates well with with previous studies, which have also found optimum conditions at 75 °C.[139,140] 800 PEI supported on MCF and RH2 are both significant deviations from this, with each of these samples showing an increase in maximum adsorption over 40-100 °C. One explanation for this is the small size of 800 PEI results in it being unconfined in the pores and thus more available for volatilisation at the higher temperatures. This would result in maximum capacities which do not accurately represent the adsorption capacity of

800 PEI. An alternate reasoning is that due to the lower viscosity and molecular size of 800 PEI, all adsorption site are available at lower temperature than the larger PEI samples.

As previously mentioned, it is expected that increased PEI loadings would lead to increased CO_2 adsorption. Therefore it is expected that PEIs supported on RH2 would show the highest maximum CO_2 adsorption.

The highest maximum CO_2 adsorption over all the samples was seen for 60 % 750000 PEI-RH2, at a value of 21.85 % at 75 °C. This is considerably higher than the next highest value of 15.50 % for 60 % 1300 PEI-RH2 at 60 °C. RH2 consistently showed the highest maximum adsorption for all PEIs bar 800 PEI. The high loading of 60 % of the PEI-RH2 samples is at least partially responsible for this, however the additional adsorption is greater than the expected 20 % (for 50 % loading PEI-Silicas) increase as a direct result of increased loading, for instance the maximum CO_2 adsorption for 50 % 750000 PEI-RH1 at 75 °C is less than half that of 750000 PEI-RH1 at 10.28 %. Therefore other facets must be considered, one potential cause for this higher adsorption seen on the RH2 samples is that the CO_2 has an increased ability to access the PEI inside the pores of RH2, this may be due to a large pore neck size compared to RH1, for instance, or larger macropores. However, the high adsorption seen on 750000 PEI-RH2 also corresponds to an increased t_{90}, which will be discussed in more detail below.

However loading is not the only controlling factor on the maximum CO_2 adsorption, as the Silica 1 samples do not show the lowest adsorption even though they are at the lowest loading (40 %). In fact, Silica 1 samples consistently shows a similar adsorbance to PEI-RH1s, and consistently out-performs SBA-15, both of which have loadings of 50 %. The similar results to PEI-RH1s is likely to be as a result of the small pore neck suggested by the N_2 sorption isotherms of RH1, resulting in pore blockage and decreasing the maximum adsorption of PEI-RH1s. Whereas the poor performance of SBA-15 may be as a result of its significantly larger proportion of micropores, which again restricts CO_2 adsorption.

The maximum adsorption of 800 PEI, the smallest PEI, was expected to be

high as has been seen previously with low molecular weight PEIs (See Table 2.1), and due to the reduced steric hindrance of molecular size and branching to CO_2 adsorption. The high capacity of low molecular weight PEI-Silicas is a result of low steric hindrances but is counteracted by the low stability of these samples. This is seen to some extent in the samples investigated in this study, with 800 PEI and 1300 PEI supported on Silica 1, SBA-15, RH1 and 1300 PEI on MCF all showing high maximum CO_2 adsorptions compared to the other PEIs adsorbed on the same silicas. However for RH2, 800 PEI has a very low loading, at the standard adsorption temperatures. However, when the slow rates of adsorption of 800 PEI-RH2 are considered, it may be that 800 PEI-RH2 does not reach equilibrium, this slow rate will be discussed further below.

5.10.3 Rate of CO_2 Adsorption

As previously mentioned, the higher molecular weight samples are expected to have longer adsorption times (particularly t_{90}). This is partly a result of the increased maximum adsorption but also of increased steric hindrance of the molecules. In practice a cut off for the t_{90} of under 10 minutes is used when considering PEI-Silicas for use in plant scale facilities. This is due to the sample only being present in the adsorber for a certain amount of time before being regenerated. The resonance times of the sample in the adsorber are variable and can be controlled by changing the flow rate of the PEI-Silica, however long resonance times and flow rates (e.g. ¿ 10 minutes) are not optimal for efficiency. Thus several of the samples, at 75 °C may not be suitable for scale up. These include 60 % 750000 PEI-RH2, the PEI-Silica with the highest maximum capacity, along with 5000 PEI-RH2 which has the second highest maximum adsorbance.

Surprisingly high adsorbance times (including t_{30}) are seen for 800 PEI-RH2, and may be responsible for the low CO_2 adsorbance of this sample. This slow rate may be a result of the small 800 PEI molecules not filling the large macropores of RH2, even at 60 % loading, resulting in a smaller contact area between the adsorbent gas mixture and the PEI, hindering diffusivity.

PEIs supported on SBA-15 show a slow rate of adsorption (specifically t_{90} but also t_{60} for high molecular weight samples). This slow CO_2 uptake of PEI-SBA-15s, compared to that of the other silica supports, may be due to the pore size and shape of SBA-15. The small pore size (pore diameter and volume) may be completely filled or blocked by PEI, restricting the access of CO_2 to the internal surfaces of the pores. This would also explain why the rate is somewhat faster for the lower molecular weight PEIs, which will be able to access a higher proportion of the pores than their larger counterparts, resulting in less pore blockage.

Almost all samples show similar kinetics (t_{60} and especially t_{90}) at 100 °C, this is due to a shift in the reaction with CO_2 towards desorption. As optimum desorption tends to occur at around 120 °C, it is probable that the desorption phase begins at around 100 °C. Thus the kinetics seem fast due to a reduced adsorption capacity and a quickly achieved equilibrium.

5.10.4 Relationship Between Kinetics and Mobility

A relationship between kinetics of CO_2 adsorption onto PEI-Silicas and the ^1H NMR determined proton mobility of PEI-Silicas can be seen by plotting the kinetics against the $\Delta H_{\frac{1}{2}}$. The same general trends are seen for all of the samples, Figures 5.65-5.67 show the results for 50 wt. % 5000 PEI-RH1. This sample is typical of many of the PEI-Silicas with the t_{90} increasing with increasing mobility, and the t_{30} decreasing with increasing mobility. The t_{60} data is more variable between samples but a common line shape is also illustrated by 5000 PEI-RH1 in Figure 5.66.

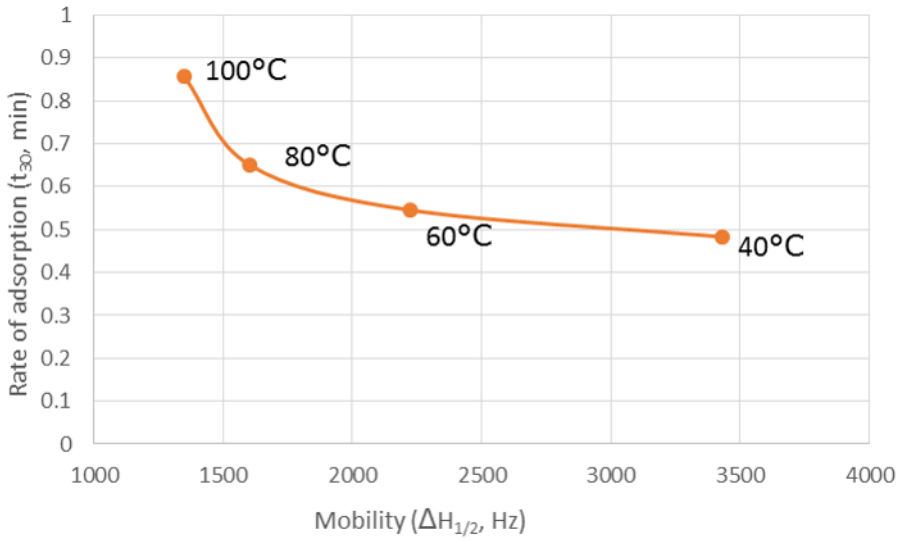


Figure 5.65: Rate of Adsorption, shown by t_{30}, against Mobility, shown by $\Delta H_{\frac{1}{2}}$, for 50 wt. % 5000 PEI-RH1 with the temperature of each measurement noted.

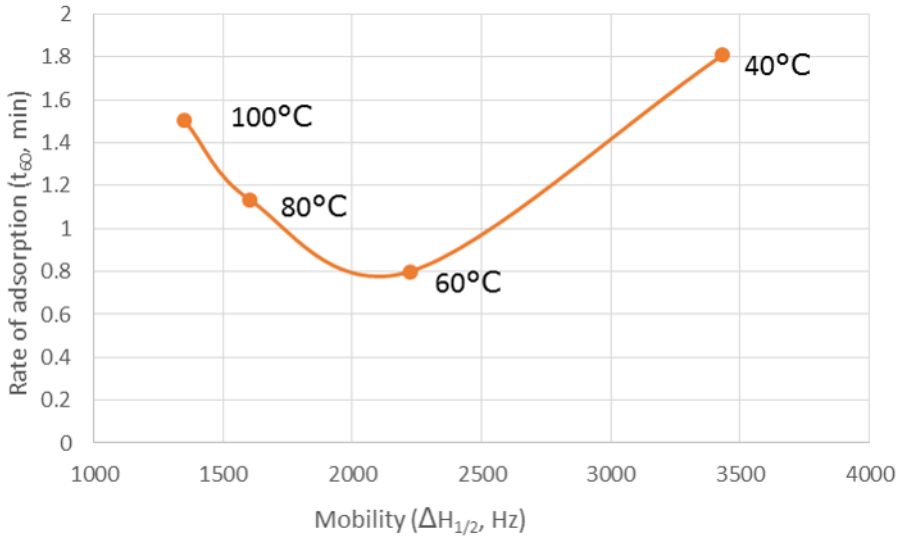


Figure 5.66: Rate of Adsorption, shown by t_{60}, against mobility, shown by $\Delta H_{\frac{1}{2}}$, for 50 wt. % 5000 PEI-RH1 with the temperature of each measurement noted.

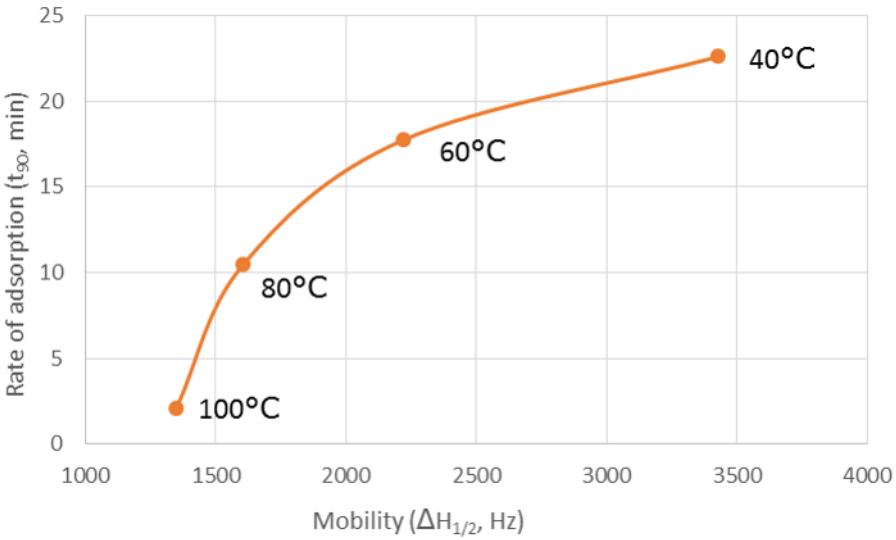


Figure 5.67: Rate of Adsorption, shown by t_{90}, against Mobility, shown by $\Delta H_{\frac{1}{2}}$, for 50 wt. % 5000 PEI-RH1 with the temperature of each measurement noted.

Another way to visualise the data, is to, rather than comparing individual data points, compare each data set. In Figure 5.68, this can be seen for all of the Silica 1 data. Using this method of visualisation, several correlations can be seen.

The change in regime at 70-80 °C in the mobility plots correlates with the maximum adsorption temperature shown by many of the PEI-Silica samples as well as fast rates of adsorption. In practice this is a correlation of mobility and optimum adsorption temperature. When comparing mobility of PEI-Silicas to that of the bulk material, it can be seen that the second regime, that of high mobility, is much more similar than the initial regime in $\Delta H_{\frac{1}{2}}$ to that of the bulk liquid. This indicates the behaviour of this second regime is closer to that of a free fluid and significantly less confined by the silica pores. Figure 5.68 compares the mobility and kinetics data for Silica 1, as an example of this correlation.

This higher mobility behaviour of the PEI in the silcia pores at 80-130 °C, correlating with the optimum adsorption temperature measured here and as reported in the literature, indicates that strong interactions between the PEI and silica surface restricts the adsorption of CO_2 and in order to facilitate ads- and de- sorption the PEI must be mobile within the pore systems. Mobile PEI would facilitate the diffusion of CO_2 within the pores facilitating adsorption and desorption. The diffusion of CO_2 being a limiting factor is supported by the work of Heydari-Gorji and Sayari (2011) who replicated experimental CO_2 capture of silica supported PEI in a computational model of kinetics.[154]

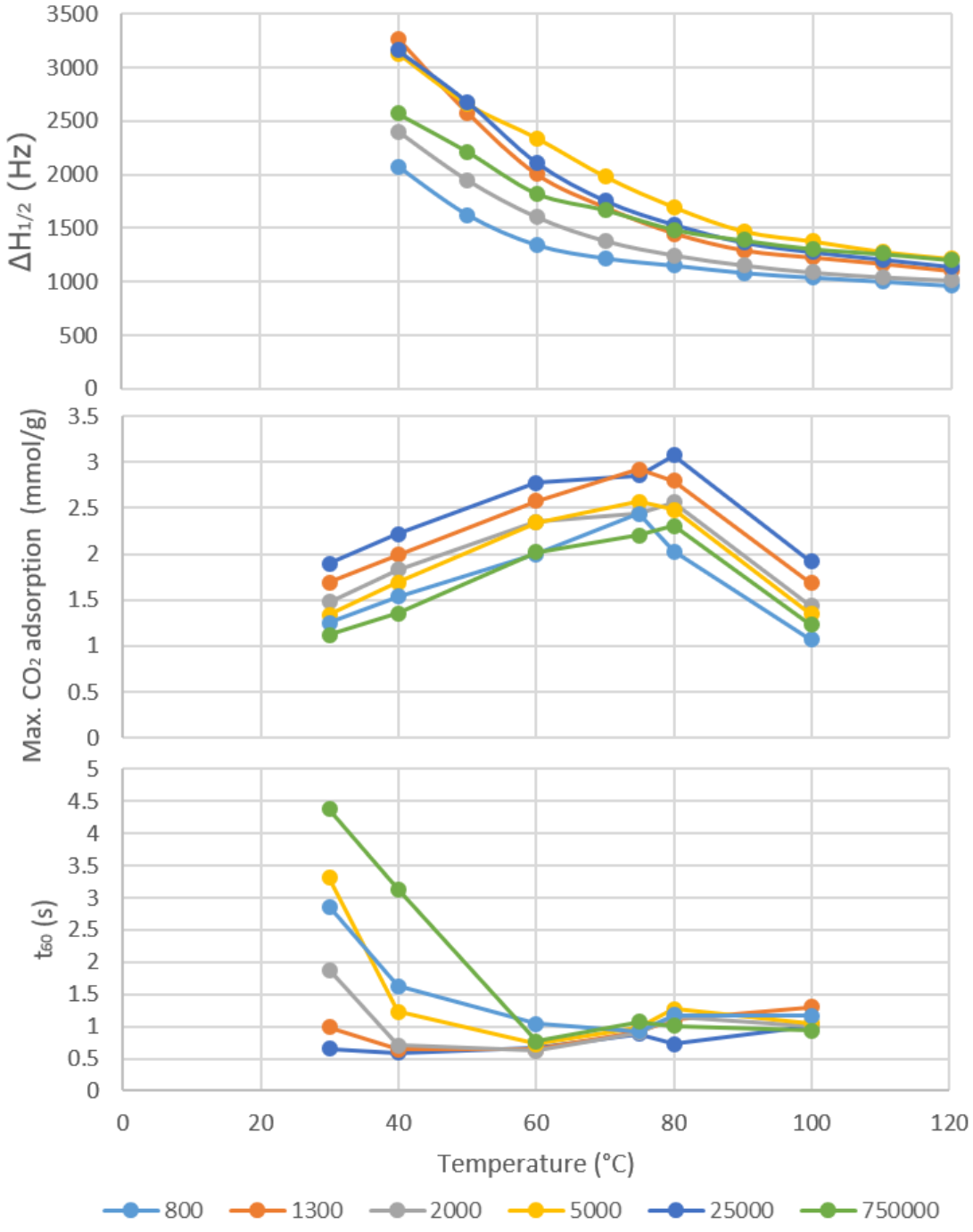


Figure 5.68: Comparison of ^{1}H NMR mobility and TGA maximum CO_2 adsorption and kinetics (t60) data of PEI-Silicas (Silica 1) over 20-120 °C

5.11 Chapter Summary

General Mobility and Kinetics Findings

- An increase in mobility is associated with an increase in temperature, with the rate of increase in mobility fitting into two regimes. At temperatures below 70 °C the rate is faster and at temperatures above 70 °C it is slower.
- Maximum CO_2 capacity commonly occurs at 60-80 °C, in line with previous research showing an optimum temperature for absorbance of 75 °C
- The kinetics data tends to show slower adsorption at lower temperatures, although the t_{30} data is fairly consistent over the temperature range studied.
- The change in regime of mobility data correlates well with the optimum adsorption temperature, and the increased rates of reaction suggesting a more fluid PEI is preferred for rapid CO_2 adsorption and desorption.

Impact of Changing the PEI or Silica in PEI-Silica Samples

- There is little correlation between mobility and PEI molecular weight.
- 800 PEI-Silicas (bar 800 PEI-RH2) have high CO_2 loading and fast kinetics, although this is expected to correspond with low stability over repeated cycles.
- PEI supported on SBA-15, due to the silica's small pore size, has slow kinetics, especially for the higher molecular weight PEI samples.
- 750000 PEI-RH2 and 5000 PEI-RH2 have higher than expected maximum loading, which corresponds with somewhat slower kinetics to the other samples. Further research on these samples, especially 750000 PEI-RH2 should be undertaken in order to understand the reasons behind this fully. This further work should include reproducing the loading on a larger scale, for example using the 5 kg test rig at the University of Nottingham.

Chapter 6

Additional Investigations into PEI-Silica

6.1 Introduction

In this chapter, additional research into PEI-Silicas as carbon capture materials is presented. This consists of an investigation into the CO_2 capacity of pilot plant samples and an investigation into the addition of antioxidants into PEI-Silica. All of the work in this chapter uses the 5000 molecular weight PEI, G100, supported on Silica 1 at 40 wt. % loading which will be referred to a G100-Silica throughout. This PEI-Silica is the type used at the KIER pilot plant.

As in the previous chapters, the figures displayed in this section show lines between points which are present as a visual aid and are not representative of further data points. Further to this, error bars are generally excluded for readability.

6.1.1 Method Development of The Preparation of PEI-Silicas with Antioxidants

This work was performed in collaboration with Wai Leung and Dr. Lee Stevens at the University of Nottingham as a preliminary investigation into the use of antioxidants to reduce degradation of PEI-Silica samples. Antioxidants were selected based on availability and existing literature on their use as antioxidants.[153] A method for

impregnating PEI-Silica with antioxidant was then determined, which can be found in Chapter 3.2.1 and the range of potential antioxidants was then narrowed to ensure suitability for the impregnation procedure. A simple method for determining the impact of the antioxidant was also developed.

During the preparation the antioxidants are combined with the PEI and this mixture impregnated onto silica. This was selected over other options, such as preparing the PEI-Silica and then impregnating with antioxidant, or impregnating the silica with antioxidant before the PEI, to minimise energy intensive preparation steps (heating, drying) and to try and ensure a even mixture of PEI and antioxidant through the silica. It was decided to maintain the same solvent, water, for this impregnation, as although it may limit antioxidant choices, it is low cost, and low risk, and therefore preferable for scale up. The base PEI-Silica used was G100-Silica 1 and samples were all prepared at 0-20 % antioxidant loading.

Water Solubility

In order to minimise expense on scale-up, it was decided to continue the use of water as a solvent for the preparation of antioxidant functionalised PEI-silica samples. The antioxidants selected were therefore required to be water soluble at 50 °C . This was done using quantities of 0.1 g antioxidant and 6 g water, with stirring at 50 °C for 30 minutes. Solubility was determined visually, an example for four of the samples can be seen in Figure 6.1 (the other two were performed at a later date and both fully dissolved so the image has been omitted).

Name	Water Soluble?
Sodium salicylate	Yes
Pyrogallol	Yes
3,3' Dithiodipropionic acid	Yes
2,2' Thiodiethanol*	Yes
2,6-Di-tert-butyl-4-(dimethylaminomethyl)phenol	No
Pentaerythritol tetrakis(3,5-di-tert-butyl-4-hydroxyhydrocinnamate)	No

Table 6.1: Solubility of Antioxidants. * denotes liquid sample



Figure 6.1: Solubility Test for (from left to right) Sodum Salicylate, 2,6-Di-tert-butyl-4-(dimethylaminomethyl)phenol, Pyrogallol and Pentaerythritol tetrakis(3,5-di-tert-butyl-4-hydroxyhydrocinnamate).

Oxidation Testing

To determine the impact of adding antioxidants to PEI-Silica Samples, a method of heating at 75 °C in a conventional oven for 1 to 10 days was initially used. This method is a simple way of simulating the main cause of oxidation of the samples in the plant, which is exposure to the adsorption temperature. The multiple day time scale reflects the lifespan of PEI-Silica in plant scale facilities where it will be recycled thousands of times. The samples were then analysed with TGA to determine the CO_2 capacity in 15 % CO_2. A "pure" PEI-Silica sample (with 0 % antioxidant) was used as a control.

6.2 Carbon-13 NMR Detection of Urea Formation

In addition to kinetics and mobility studies of various PEI-Silicas, experimental work using CP MAS ^{13}C NMR was performed in order to detect CO_2 chemically adsorbed on PEI-Silica samples from various sources and distinguish between adsorbed CO_2 and irreversibly bonded CO_2 (in the form of Urea).

For this, samples of PEI-Silica from the KIER pilot scale plant (40 % G100-Silica 3), which had undergone several cycles of adsorption and desorption were investigated. As a control these were compared to fresh samples. In addition to this, a spectrum was acquired for a pure silica sample to ensure there was no contribution to the signal, as expected there was no observable signal.

6.2.1 Carbon-13 NMR of a Control Sample

A control sample of G100-Silica 1 was used to obtain a spectrum for a CO_2-free sample. In Figure 6.2, the spectrum can be seen. There is a singular broad peak at 59 ppm. The spectrum was acquired at 5000 Hz on a spectrometer calibrated with TKS. Due to PEI being a polymer of repeating monomers, containing 1:1:1 ratio of primary, secondary and tertiary amines, there are many distinct but similar carbon environments which results in a singular broad peak at this resolution. Using higher resolution techniques it might be possible to get a more resolved spectra with individual PEI peaks but as this method is being used to detect the distinct C=O peak a more resolved spectrum was unnecessary.

A spectra was also acquired for the unsupported liquid PEI, G100, however as the same equipment was used the same difficulties of spinning a liquid sample as discussed in Section 4.8.1 were encountered. Therefore the spectra was acquired at a spinning rate of 1000 Hz. Unfortunately at this low a spinning speed the CP method was ineffective and did not show a resolved spectra, so a SPE method was used to try an obtain a usable spectra. This spectra can be seen in Figure 6.3. The spectra of this liquids sample is more resolved than that of the solid sample due

to the isotropic nature of a liquid sample, and the use of a more extended pulse programme. The peaks all occur with in the range of 45-80 ppm, which aligns well with the broad peak seen for the solid sample.

For the CP MAS NMR spectra the peaks can be broadly assigned to carbons adjacent to primary (43 ppm), secondary (51 ppm) and tertiary (54 ppm) nitrogen. The more complex SPE spectra may be assigned to also consider the nitrogen centres for which the carbons are in the β position.[191] Thus they can be loosely assigned as follows: 1) α-primary/β-tertiary (47 ppm), 2) α-primary/β-secondary (49 ppm), 3) α-secondary/β-tertiary (55 ppm), 4) α-tertiary/β-tertiary (57 ppm), 5) α-secondary/β-primary (60 ppm), 60 α-tertiary/β-secondary (62 ppm) and 7) α-tertiary/β-primary (65 ppm).

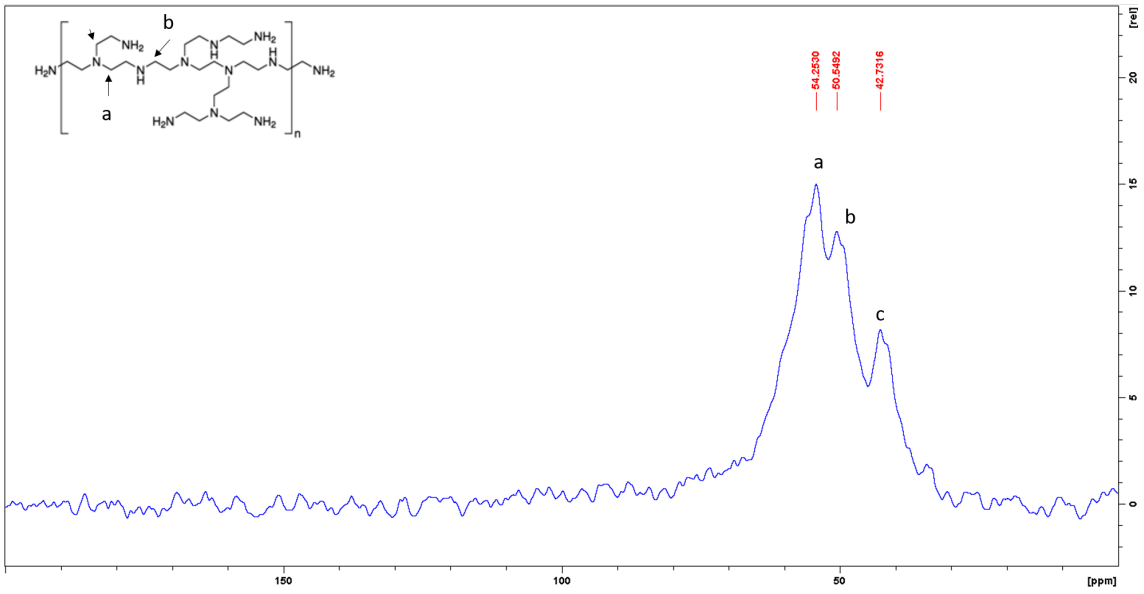


Figure 6.2: CP MAS ^{13}C-^{1}H NMR spectra of 40 % G100-Silica 1. The spectrum was acquired at a spinning speed of 5000 Hz and a contact time of 1 ms. The spectrometer was calibrated to TKS at 3.5 ppm.

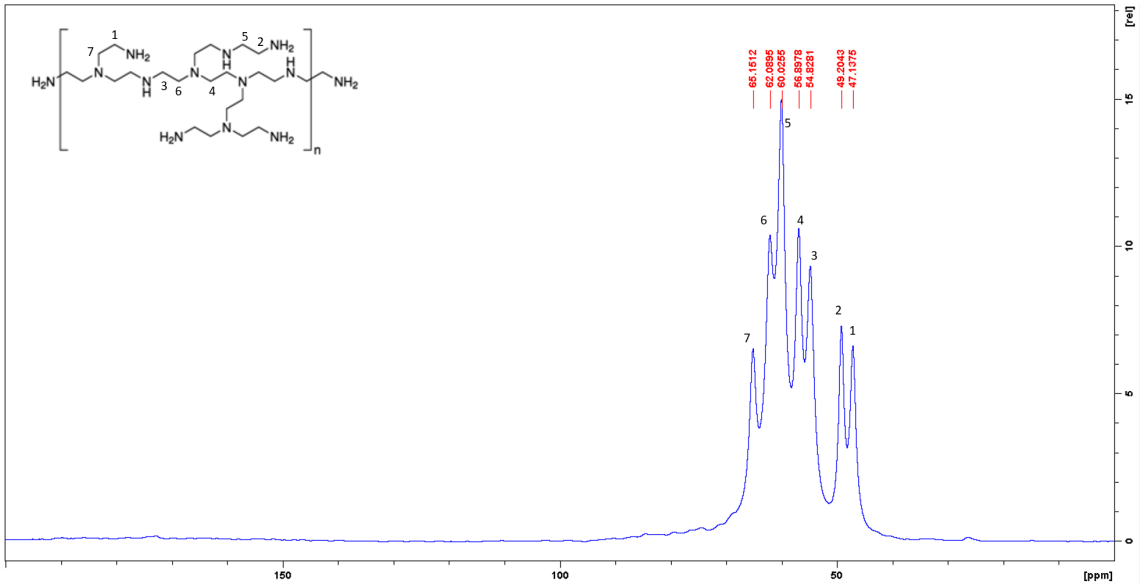


Figure 6.3: SPE MAS ^{13}C-^{1}H NMR spectra of neat G100, with a spinning speed of 1000 Hz. The spectrum was acquired at a spinning speed of 5000 Hz and a contact time of 3 ms. The spectrometer was calibrated to TKS at 3.5 ppm.

6.2.2 Carbon-13 NMR of Pilot Plant Samples

Several samples (in two sets) were provided from the KIER pilot plant, these samples are 40 % G100-Silica 1. They were taken from either after the adsorption stage (noted with an A) or after the regeneration stage (noted with an R). The samples were taken after different number of days of adsorption and regeneration cycles. A comparison of the two samples can be seen in Figure 6.4. The ^{13}C NMR experiments were performed at 5000 Hz and used TKS (chemical shift of 3.5 ppm) as a standard. These experiments were not possible to repeat due to a limited amount of sample.

The broad peaks at 47 ppm are the PEI and the narrow peaks at 164 ppm (this peak is very small on the regenerated sample) is a C=O peak, that corresponds with adsorbed CO_2. The CO_2 peak is significantly smaller (in comparison to the main PEI peak) in the regenerated sample, this is due to the majority of CO_2 desorbing in the regeneration process at 130 °C.

By taking the integral under the peaks and comparing the C=O integral to the PEI integral a ratio of CO_2 to PEI can be determined. This ratio is not necessarily representative of the actual ratio of molecules or by weight, as cross polarisation

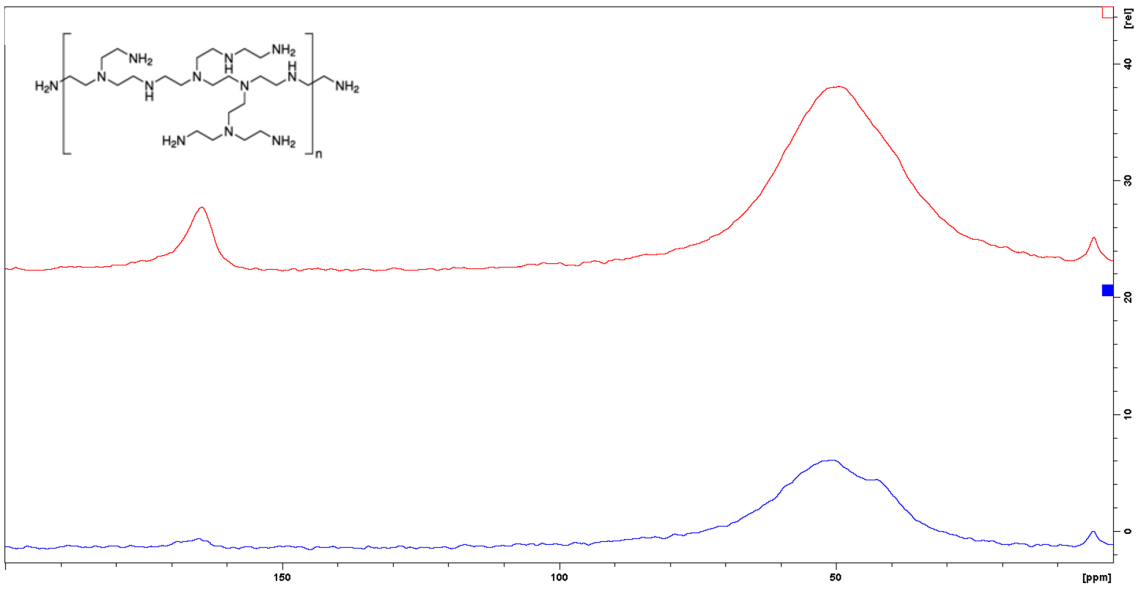


Figure 6.4: CP MAS ^{13}C-^{1}H NMR spectra of adsorbed (Top/Red) and regenerated (Bottom/Blue) PEI-Silica samples from the KIER pilot scale plant. Peaks are at 164 ppm (C=O), 50 ppm (PEI) and the reference peak is at 3.5 ppm (TKS). The spectrum was acquired at a spinning speed of 5000 Hz and a contact time of 1 ms.

methods give additional intensity to carbons with adjacent hydrogen atoms. Thus, the C=O peak will likely be smaller than in SPE, for example. In addition the ratio is only for CO_2 to PEI rather than the whole PEI-silica solid sorbent, as is more standard for the other methods. However, the ratio determined can be compared with the ratio of other samples, specifically comparing the adsorbed and regenerated samples, to give an indication of the difference in amount of CO_2 that has been adsorbed. This data can be found in Tables 6.2 and 6.3.

It is expected that complete regeneration of the PEI-Silica samples will not occur in the plant, as the efficiency of the CO_2 removal process is reduced as more CO_2 is removed over repeated samples. In practice this means that the length of time the sample is in the regenerator is not long enough to achieve saturation of CO_2.

From Tables 6.2 and 6.3, it can be seen that both of the samples show an increase in amount of CO_2 in the adsorber samples, over the first few days. The first sample shows a higher ratio of CO_2 to PEI for the regenerated sample than the adsorbed sample. This is not believed to accurately represent plant conditions and may be

Day	Adsorbed CO_2 (wt. %)	Regenerated CO_2 (wt. %)
1	4.9	5.1
2	9.1	2.2
3	11.1	3.7
4	11.6	3.1
5 (am)	10.2	3.6
5 (pm)	11.8	3.1
6	10.5	5.4
7	11.7	10.9

Table 6.2: Ratio of CO_2 peak integral (approx. 164 ppm) to PEI peak integral (approx. 50 ppm) displayed as a percentage for sample set 1

the result of an improperly sealed vial allowing adsorption of CO_2 from the air. This is supported by the results of sample set 2.

Neither of the samples show any significant change in amount of CO_2 in the adsorption samples, after this initial growth, over the course of the study (8 and 10 days). However the amount of CO_2 remaining on the regenerated sample tends to increase, so the amount of CO_2 that is effectively being captured by the PEI-Silica is decreasing. This may potentially be due to adsorber degradation, although no urea formation was detected (see Section 6.2.4 or the loss of PEI from the PEI-Silica, however the temperatures used are not high enough for significant amounts PEI to volatilise or decompose. The day 8 regeneration sample for sample set 1 is unexpectedly high, which again may be erroneous due to air capture.

Comparing the two sample sets, sample set 2 has consistently lower values of CO_2 adsorbed on both the adsorber and regenerator samples than sample set 1. These samples were collected approximately 6 months apart, but studied using NMR at the same time. This is likely the cause of the discrepancy between the data sets, sample set 1 had significantly longer to adsorb ambient CO_2 than sample set 2. The dates of the sample collection can be found in Appendix B.8.

Day	Adsorbed CO_2 (%)	Regenerated CO_2 (%)
1	5.5	0.0
3	7.4	2.7
5	8.6	2.1
6	9.4	2.9
7	8.1	2.4
8	8.1	2.4
10 (am)	9.3	3.8
10 (pm)	9.0	4.7

Table 6.3: Ratio of CO_2 peak integral (approx. 164 ppm) to PEI peak integral (approx. 50 ppm) displayed as a percentage for sample set 2

6.2.3 Thermogravimetric Analysis of Pilot Plant Samples

In order to gain further insight into the samples from the pilot plant, specifically the impact of cycled adsorption and regeneration on maximum CO_2 capacity. CO_2 adsorption TGA as described in Section 3.2.5 was performed on each of the samples. It was not possible to perform repeats of these experiments due to limited amounts of sample. The results are displayed in Tables 6.4 and 6.5.

Day	Adsorbed Max. CO_2 (wt. %)	Regenerated Max. CO_2 (wt. %)
1	9.9	9.8
2	9.7	8.6
3	9.1	9.0
4	9.0	9.0
5 (am)	9.0	8.9
5 (pm)	8.9	8.9
6	8.9	8.9
7	8.8	8.7

Table 6.4: Maximum CO_2 adsorption of the adsorbed and regenerated samples, as determined by TGA at 75 °C and 15 % CO_2, for sample set 1

From Table 6.4, sample set 1 shows a decrease in capacity over time, and a similar capacity between the adsorber samples and the regenerator samples (except for day 2). The loss of CO_2 capacity is fairly low at only 1.1-1.2 % over 7 days, especially compared to sample set 2 which showed a loss of capacity of 2.7-2.9 % over the sample time period.

Day	Adsorbed Max. CO_2 (wt. %)	Regenerated Max. CO_2 (wt. %)
1	9.8	9.8
3	9.6	9.9
5	9.2	9.2
6	7.6	7.2
7	6.9	7.1
8	6.4	6.5
10 (am)	5.4	5.3
10 (pm)	5.4	5.3

Table 6.5: Maximum CO_2 adsorption of the adsorbed and regenerated samples, as determined by TGA at 75 °C and 15 % CO_2, for sample set 2

From Table 6.5, sample set 2 also shows a consistent decrease in capacity over time, and a similar capacity between the adsorber samples and the regenerator samples.

Both of these features are to be expected. The decrease in capacity is expected as the samples will degrade and oxidise over time and this degredation will result in the PEI-Silicas being less effective carbon capture materials. In the case of the KIER facility, compressed gas is used to transport the 75 ° sample from the absorber to the desorber. This gas can be inert like N_2, however compressed air may also be used, with oxidation being expected to significantly worse if air is used for this process. There is also a possibility of air ingress into the system through leaks and the presence of residual air from loading which may result in oxidation. The similar capacity of the adsorber and regenerator samples is also expected as it follows logically that one cycle (the difference between the adsorber and regenerator samples)

would not have a significant impact on CO_2 capacity.

It would be expected that the two sample sets show similar maximum adsorptions if the hypothesis in Section 6.2.2 is correct, and the different adsorption seen in the NMR spectra is due to adsorption of CO_2 from the air. This is seen in the initial measurements over the first 3 days, however after this sample set 1 maintains higher maximum capacity than sample set 2. The cause of the more rapidly decreasing capacity of sample set 2, compared to sample set 1 is unknown as it is believed that the conditions in the pilot plant were the same for both sets.

Interestingly the maximum capacity shown by this method is lower than the capacity seen on the samples as provided. This may be the result of air adsorption of CO_2 over time, the impact of the residual CO_2 between cycles and/or oxidation of the samples due to air in the TGA system.

6.2.4 Determination of Urea Formation

As the expected chemical shift for a carbon in C=O double bond in a carbamate structure or a urea structure are very similar (around 160 ppm and 155-165 pmm), it was not possible assign the peak that occured at 164 ppm in these spectra with complete confidence. These values were estimated using several resources, predominantly: an online database from the University of Wisconsin, and the spectra prediction service www.nmrdb.org.[192–195] Therefore in order to determine if these peaks were associated with reversibly or irreversibly adsorbed carbon, a simple desorption process was performed to the sample and the NMR experiment performed again. This desorption process involved heating the samples to 150 °C as described in Section 3.2.1, a temperature at which any reversibly adsorbed CO_2 will desorb.

An example spectra acquired on the fully desorbed sample can be seen in Figure 6.5, this figure compares the regenerated, adsorbed and desorbed-regenerated samples. The desorbed sample does not show a peak at around 164 ppm, where a C=O peak would be expected. This indicates the C=O has been fully desorbed and was therefore reversibly adsorbed. Thus urea formation had not occurred in this sample. The peak for PEI in this sample seems distorted, which may be a

result of the desorption technique damaging the sample or volatilising off some of the low molecular weight PEI. This process was performed for the samples that had undergone the greatest number of cycles (longest time in the adsorber and desorber columns). Examination of both of the sample sets in this manor detected no urea formation.

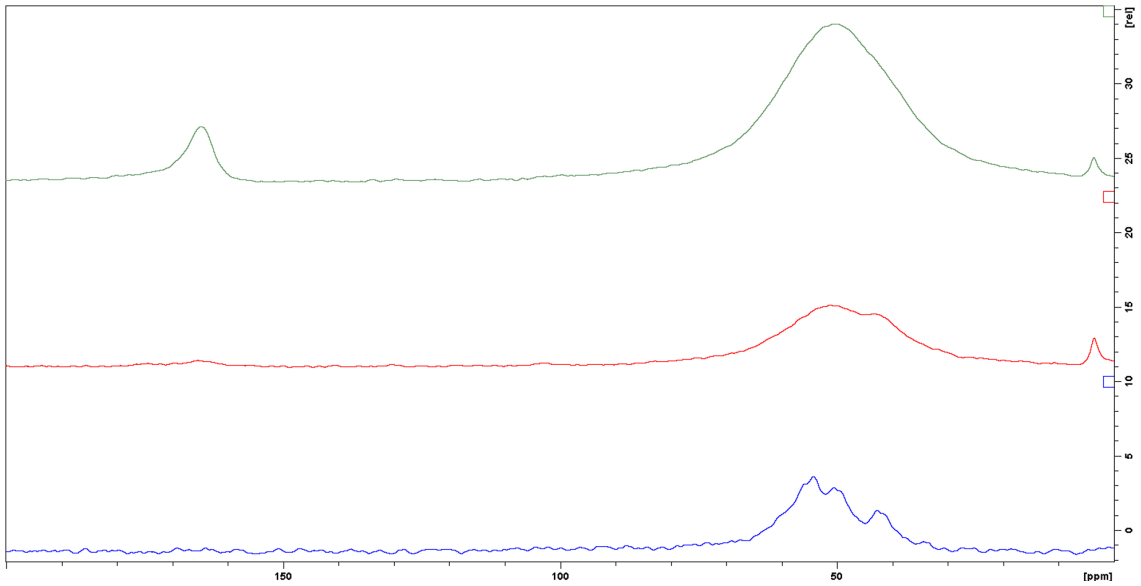


Figure 6.5: CP MAS ^{13}C-^{1}H NMR spectra of adsorbed (Top), regenerated (Middle) and desorbed-regenerated (Bottom) PEI-Silica samples from the KIER pilot scale plant. Peaks are at 164 ppm (C=O), 50 ppm (PEI) and the reference peak at 3.5 ppm (TKS). The spectrum was acquired at a spinning speed of 5000 Hz and a contact time of 1 ms.

6.3 The Impact of Antioxidants on PEI-Silica Performance

Oxidation is an ongoing issue impacting the lifetime of PEI-Silicas for carbon capture, with oxidation of the PEI resulting in reduced CO_2 adsorption and negatively impacting the efficiency of the plant. It is therefore pertinent to investigate ways of reducing this oxidation. One potential solution to this issue is the introduction of antioxidants to the PEI-Silica sample, which would combat the oxidation. Six an-

tioxidants were intially selected, however after solubility testing (see Section 6.1.1) only four were investigated further. These are:

- Sodium Salicylate
- Pyrogallol
- 3,3' Dithiodipropionic Acid
- 2,2' Thiodiethanol

The work in this section on sodium salicylate and pyrogallol was performed in collaboration with Wai Leung and Dr. Lee Stevens, University of Nottingham.[148]

6.3.1 Impact of Antioxidants on the CO_2 Capacity of G100-Silica 1

For the antioxidant testing, the PEI-Silica, 40 % G100-Silica 1 was used. This was selected as it was the PEI-Silica currently being tested in the pilot scale facility by KIER. Each of the antioxidant functionalised PEI-Silicas was prepared in a range of different concentrations from 0.25 % to 20 % (plus one control of 0 % antioxidant 40 % G100-PEI). This percentage, unlike the loading (e.g. 40 % PEI-Silica), refers to the weight of antioxidant as a percentage of the weight of the base PEI-Silica, i.e. for the sample of 1 % pyrogallol 40 % G100-Silica 1, 0.6 g Silica 1, 0.4 g G100 and 0.01 g of pyrogallol, to make a total of 1.01 g (so it would actually be 0.0099 wt.%). Although the weights are displayed as a percentage of the base PEI-Silica weight, the antioxidant was impregnated at the same time as the PEI. The actual weight percents of antioxidant in these samples can be seen in Appendix B.9.

After being subjected to oxidation conditions for a number of days, the CO_2 capacity of the samples was then measured using thermogravimetric analysis at 75 °C as described in Section 3.2.5. Due to limited amounts of sample it was not possible to repeat these experiments. For readability, only the data for key concentrations of each antioxidant are are shown in the following sections.

PEI-Silica Only Sample

A sample of 40 % G100-Silica 1 was prepared without the addition of an antioxidant, to use as a constant. The results of the oxidation testing for this sample can be seen in Figure 6.6.

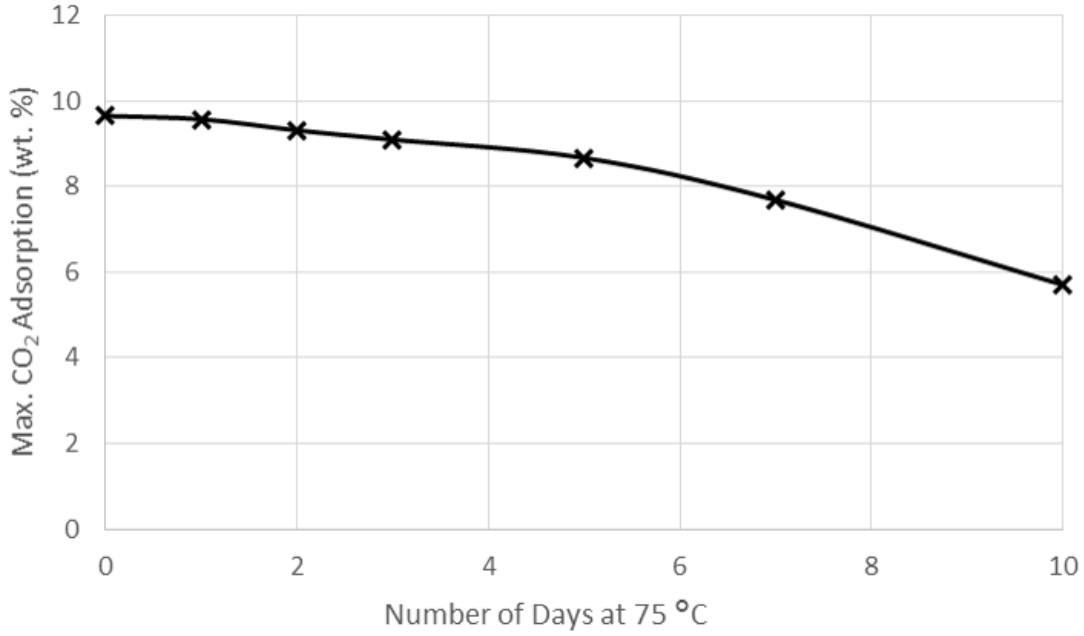


Figure 6.6: Oxidation results for a G100-Silica 1 sample with no added antioxidant

From this figure, it is clear that oxidative degradation occurs at a significant rate over the course of 10 days in air at 75 °C, with the initial capacity of G100-Silica 1 being 9.7 wt. % dropping to 5.7 wt. % after 10 days. The loss of carbon dioxide (CO_2) capacity seen seems to accelerate over time and would be expected to continue past the 10 day limit of this study.

Sodium Salicylate

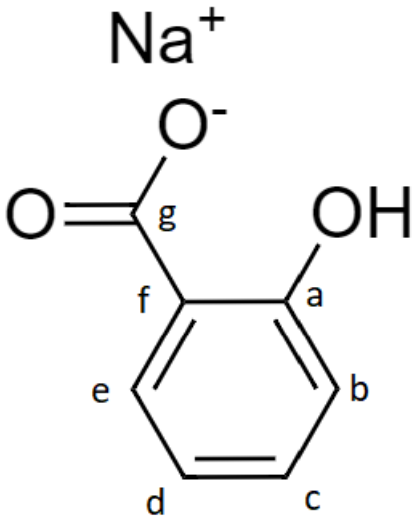


Figure 6.7: Labelled structure of sodium salicylate

Figure 6.8 shows the CP MAS ^{13}C NMR spectra of the base PEI-Silica (middle), sodium salicylate (bottom) and the PEI-Silica functionalised with sodium salicylate (top). These spectra show the presence of the antioxidant, sodium salicylate, is present in the functionalised sample and however some differences can be seen between the spectra (specifically seen in the 150-200 ppm range). An additional peak at 164 ppm on the functionalised sample is thought to be the result of of adsorbed CO_2 (this peak is also thought to be obscuring a peak at 159 ppm), although it is possible it is the result of an interaction between the sodium salicylate and PEI. Other differences (in the 100-150 ppm range) seem the result of poor resolution and high noise in the spectrum of the functionalised sample.

The peaks in the sodium salicylate spectrum can be assigned from left to right, using Figure 6.7 as a guide, as g (176 ppm), a (159 ppm), c and e (130 ppm), f (121 ppm), d (118 ppm) and b (114 ppm).

The oxidation testing of sodium salicylate functionalised PEI-Silica shows some reduction in oxidation for the 0.25 and 0.5 % samples. A comparison of the control PEI-Silica and the 0.25-1 % sodium salicylate samples can be seen in Figure 6.9. For all measurements taken after the samples were subjected to oxidation conditions the 0.5 % sodium salicylate sample shows a reduction in CO_2 capacity loss compared

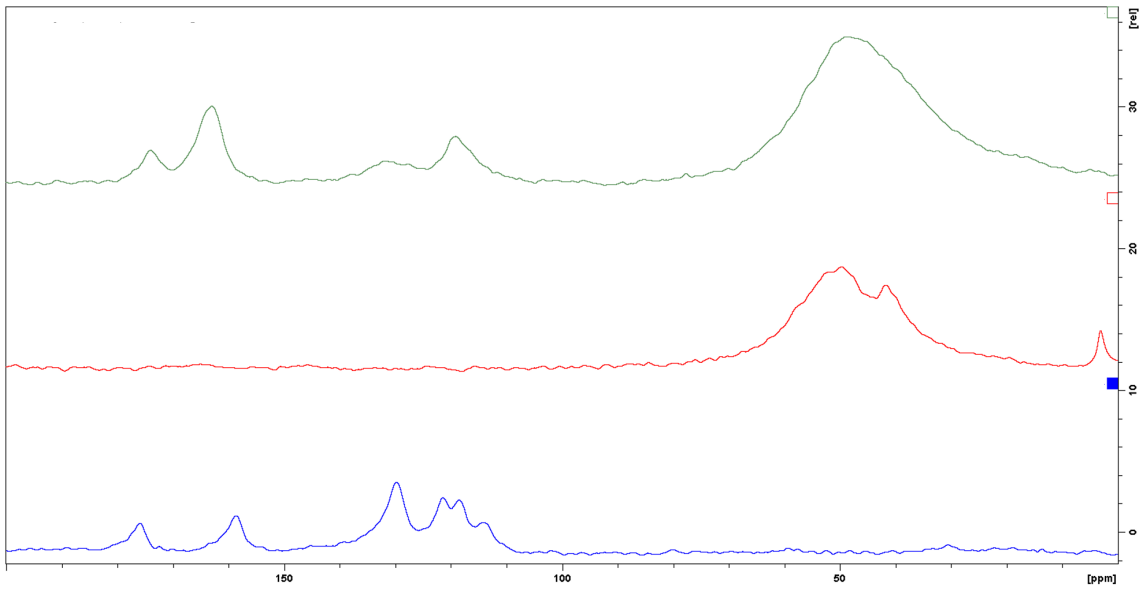


Figure 6.8: CP MAS ^{13}C-^{1}H NMR spectrum of 10 % sodium salicylate functionalised 40 wt. % G100-Silica 1 (top), 40 wt. % G100-Silica 1 (middle) and sodium salicylate (bottom). The spectrum was acquired at a spinning speed of 5000 Hz and a contact time of 1 ms. The spectrometer was calibrated using TKS at 3.5 ppm.

to that of the base PEI-Silica, however the difference in values between the control and the 0.5 % sample may not be significant. For the 0.25 % sample the capacity is similar to the control up to the 5th day, on the 7th and 10th day however the capacity is significantly higher than that of the control. The 0.75 and 1 % sodium salicylate samples both show a similar or lower capacity than the base silica at almost all times. Higher loadings, such as those for 4-10 % loadings seen in Figure 6.10, exacerbate this with CO_2 capacities of consistently lower values than the base PEI-Silica. Although at these loadings and above, no consistent trends between loading and CO_2 capacity over time are seen.

For samples with 0.25 and 0.5 % sodium salicylate, the total change in CO_2 capacity when compared with the base PEI-Silica was 8.9 and 2.5 % of the base PEI-Silica capacity.

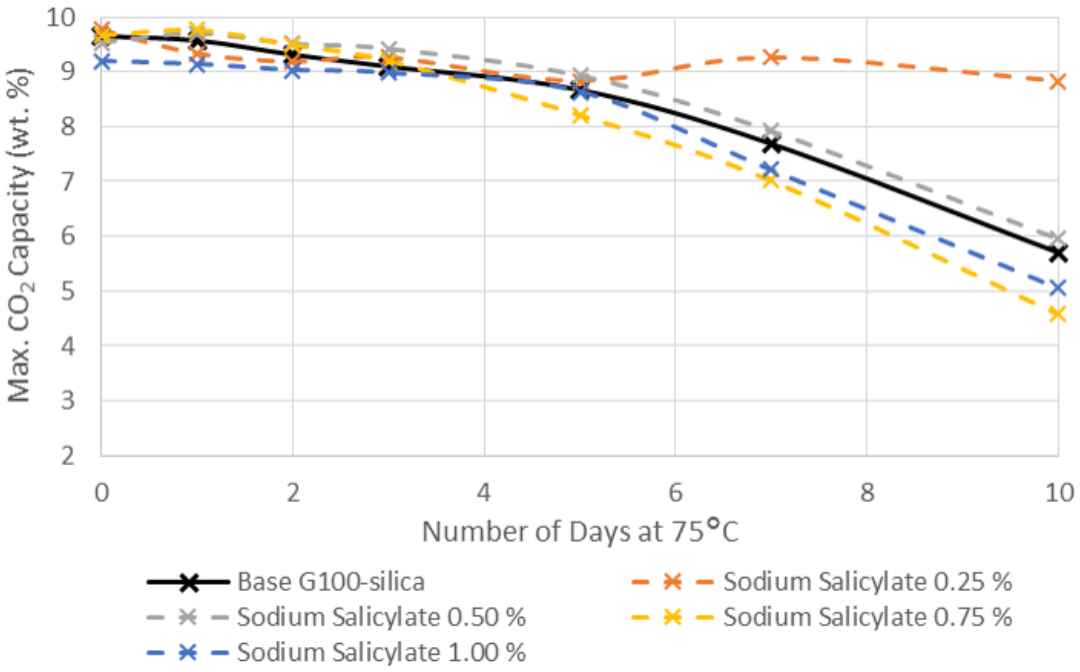


Figure 6.9: TGA determined maximum CO_2 capacity of G100-Silica 1 functionalised with 0.0, 0.25, 0.50, 0.75 and 1.0 % sodium salicylate, over 10 days under oxidation conditions[148]

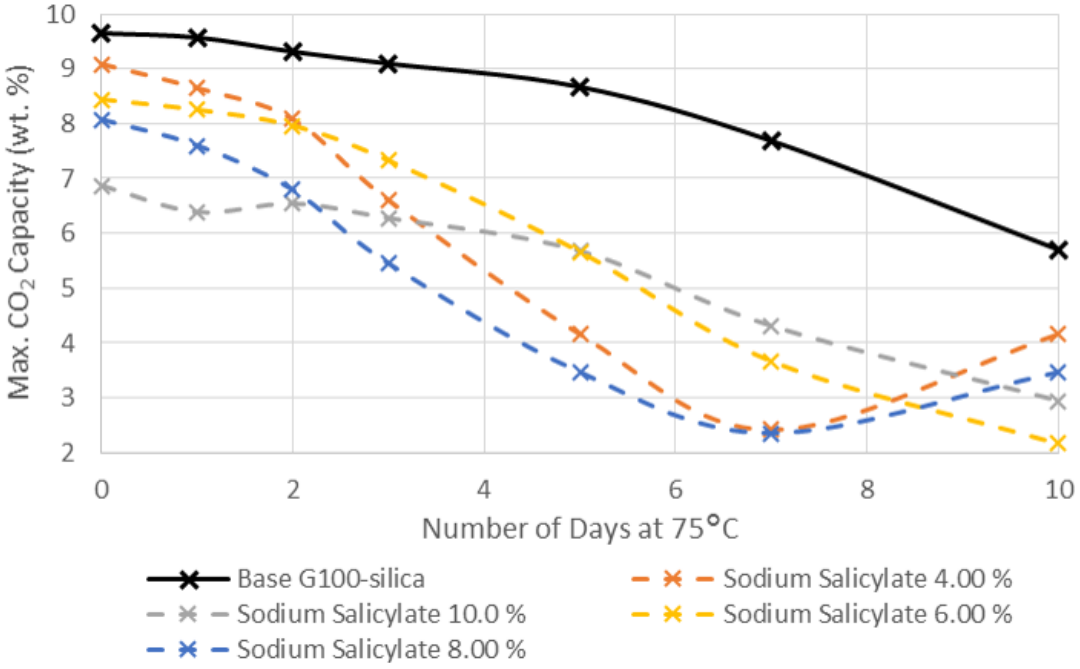


Figure 6.10: TGA determined maximum CO_2 capacity of G100-Silica 1 functionalised with 0, 4, 6, 8 and 10 % sodium salicylate, over 10 days under oxidation conditions[148]

Pyrogallol



Figure 6.11: Pyrogallol impregnated G100-Silica 1 using minimal added water (left) and using an additional 5 g added water (right).

In the preparation of pyrogallol functionalised PEI-Silica colour change was observed and a white precipitate formed when mixing pyrogallol and the PEI (G100). This precipitate was gel like and adhesive and the samples turned a dark brown-black colour (see Figure 6.11). In Figure 6.11 the white material in the left hand image is the white gel-like precipitate. In order to acheive impregnation this gel was dissolved in a further 5 g of water, even so samples above 16 % pyrogallol still produced the precipitate and therefore could not be prepared. It is hypothesised that this is the result of a reaction between the two materials which is supported by the CP MAS ^{13}C NMR spectra of the pyrogallol activated PEI-Silica (see Figure 6.13). The comparison of the spectrum of pyrogallol and the functionalised PEI-Silica shows an additional peaks at 163 pm on the latter spectra, which may be assigned to a C=O, possibly in a urea-type form, and a broadening and reduction in resolution of the peaks in the 100-160 ppm range. Due to these issues in preparing the samples a smaller range of loadings were prepared than for the other antioxidants.

The peaks in the pyrogallol spectrum can be assigned from left to right, using Figure 6.12 as a guide, as b (143 ppm), a (130 ppm), d (119 ppm), c (105 and 109 ppm).

As the antioxidant in this case is not simply impregnating onto the silica substrate but reacting with the PEI, it is expected to be detrimental to the PEI-Silicas capacity as a carbon capture material. This is seen in Figure 6.14, where increasing

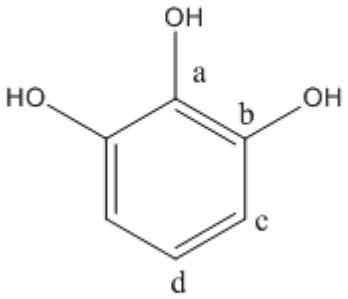


Figure 6.12: Labelled structure of pyrogallol

loading of pyrogallol decreases the maximum CO_2 uptake before oxidation testing. The negative impact of the addition of pyrogallol can be seen quite distinctly even at 0.5 %, where the CO_2 capacity is 6.18 % compared to 9.65 % for the control sample with no antioxidant. For most of the low loadings tested this was only exacerbated after time under oxidation conditions, however the 0.75 % and the higher loadings of 10 and 14 % shown in Figure 6.15 show an increase in capacity after 1 or 2 days. The 0.75 % antioxidant sample returns to a similar capacity as the base PEI-Silica after one day, and the higher loadings show significant increases CO_2 capacity after 2 days. An explanation for the differences shown by these samples is that the antioxidant did not properly impregnate and therefore reacted with the air leaving the PEI-Silica able to regain some or all of its CO_2 capacity. This may occur to a greater extent in the high loading samples due to the difficulties in sample preparation at these loadings, but why it occurs in the 0.75 % sample and not the 0.5 % or 1 % sample is unclear.

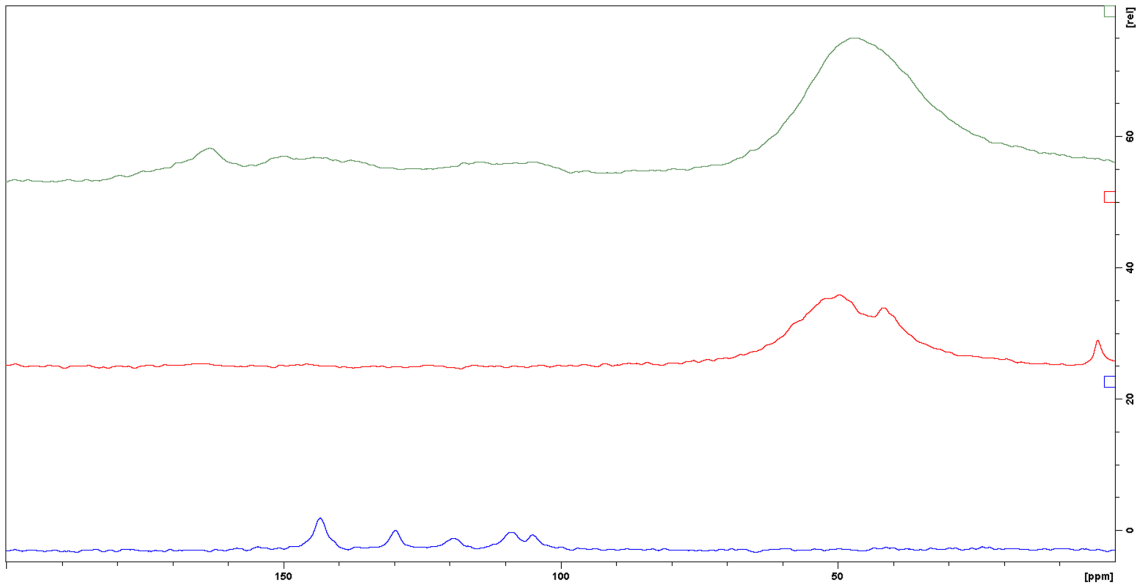


Figure 6.13: CP MAS ^{13}C-^{1}H NMR spectrum of 10 % pyrogallol functionalised 40 wt. % G100-Silica 1 (top), 40 wt. % G100-Silica 1 (middle) and pyrogallol (bottom). The spectrum was acquired with spinning at 5000 Hz and a contact time of 1 ms. The spectrometer was calibrated to TKS at 3.5 ppm.

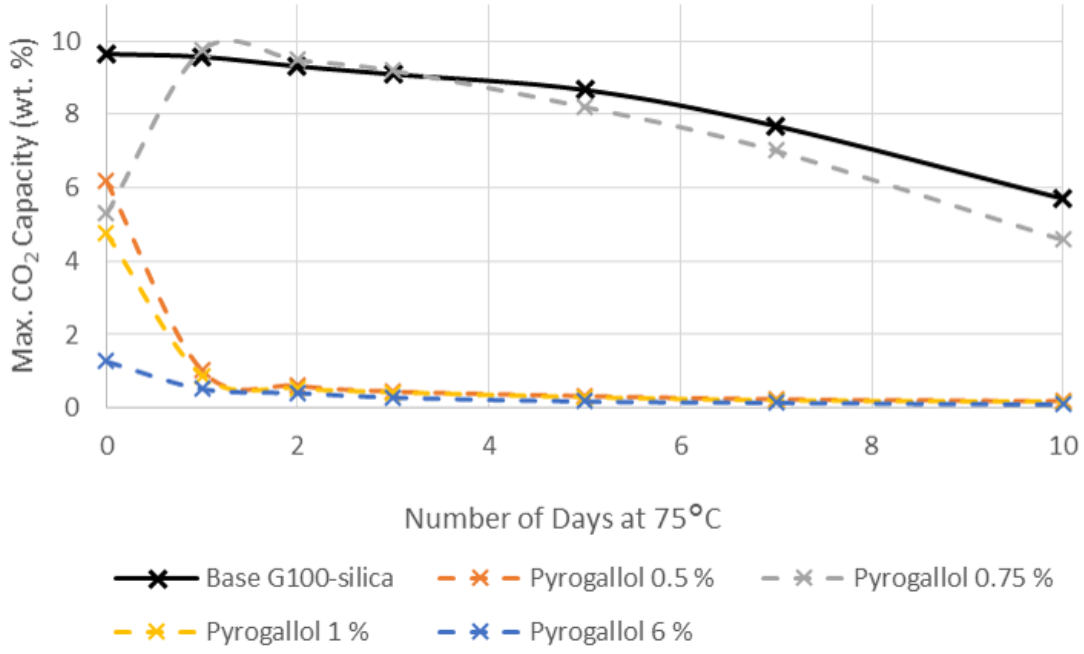


Figure 6.14: TGA determined maximum CO_2 capacity of G100-Silica 1 functionalised with 0, 0.5 1 and 6 % pyrogallol, over 10 days under oxidation conditions[148]

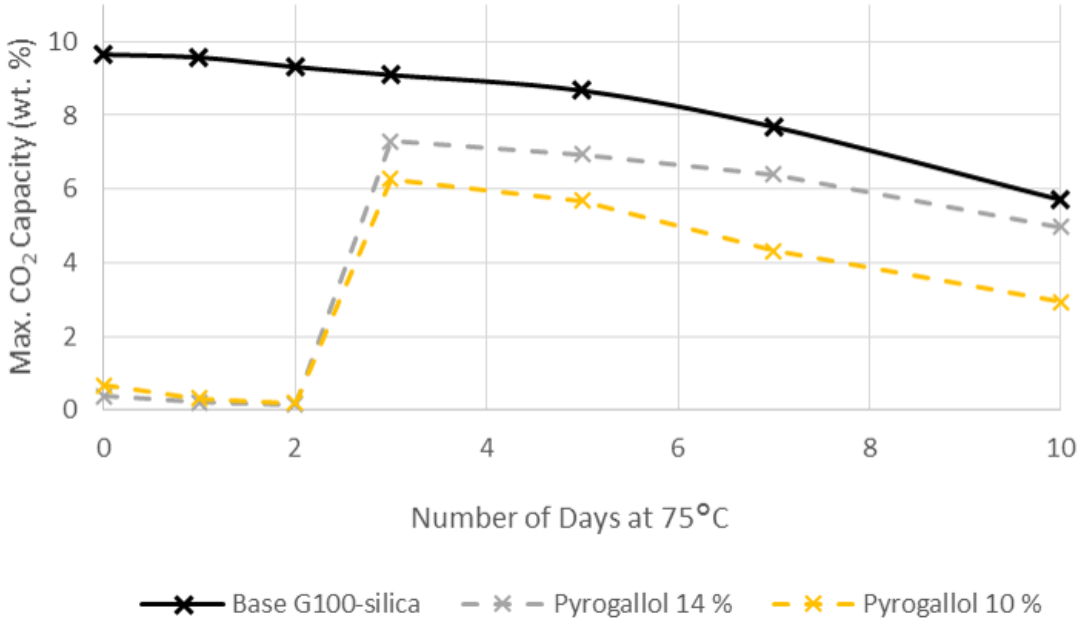


Figure 6.15: TGA determined maximum CO_2 capacity of G100-Silica 1 functionalised with 0, 10 and 14 % pyrogallol, over 10 days under oxidation conditions[148]

3,3' Dithiodipropionic Acid

The peaks in the 3,3' dithiodipropionic acid spectrum (Figure 6.17) can be assigned from left to right, using Figure 6.16 as a guide, as a (181 ppm), c (30 ppm) and b (26 ppm). By comparing the spectra of 3,3' dithiodipropionic acid and G100-Silica to the spectrum acquired on the 10 % 3,3' dithiodipropionic acid functionalised G100-Silica the 3,3' dithiodipropionic acid peaks at 25-30 ppm are adsorbed by the PEI peak in the functioanlised samples. The peak at 180 ppm is present in the functioanlised sample however, there is an additional peak at 167 ppm. This is likely to be a C=O peak as a result of air adsorption of CO_2. The peaks at 3.5 ppm are the standard, TKS. The comparision of these spectra show the presence of the 3,3' dithiodipropionic acid in the functionalised sample.

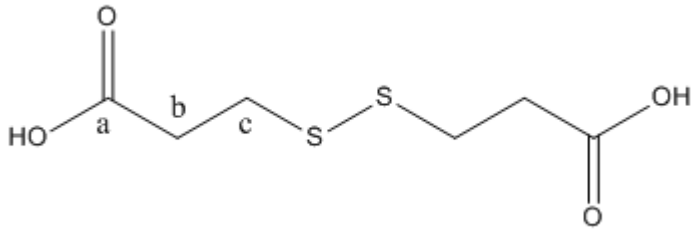


Figure 6.16: Labelled structure of 3,3' dithiodipropionic acid

In Figure 6.18 the samples with 0.25 and 0.5 3,3' dithiodipropionic acid show a similar CO_2 capacity to the base PEI-Silica over the first 5 days, and then show and relatively increased capacity on days 7 and 10. This increase shows the antioxidant is inhibiting the oxidation of the PEI-Silica and thus the samples are retaining their CO_2 capacity. The 0.75 % sample shows a similar capacity to the base sample over the first 3 days, however after this point it is reduced compared to the capacity of the base PEI-Silica sample. The 1 % sample has a consistently lower CO_2 capacity that the other samples. At higher loadings, of which the data can be seen in Appendix B.10, the samples consistently show lower capacity than the base PEI-Silica (except from 2 % which shows a similar capacity).

For samples with 0.25 and 0.5 % 3,3' dithiodipropionic, the total change in CO_2 capacity when compared with the base PEI-Silica was 2.6 and 1.4 % of the base

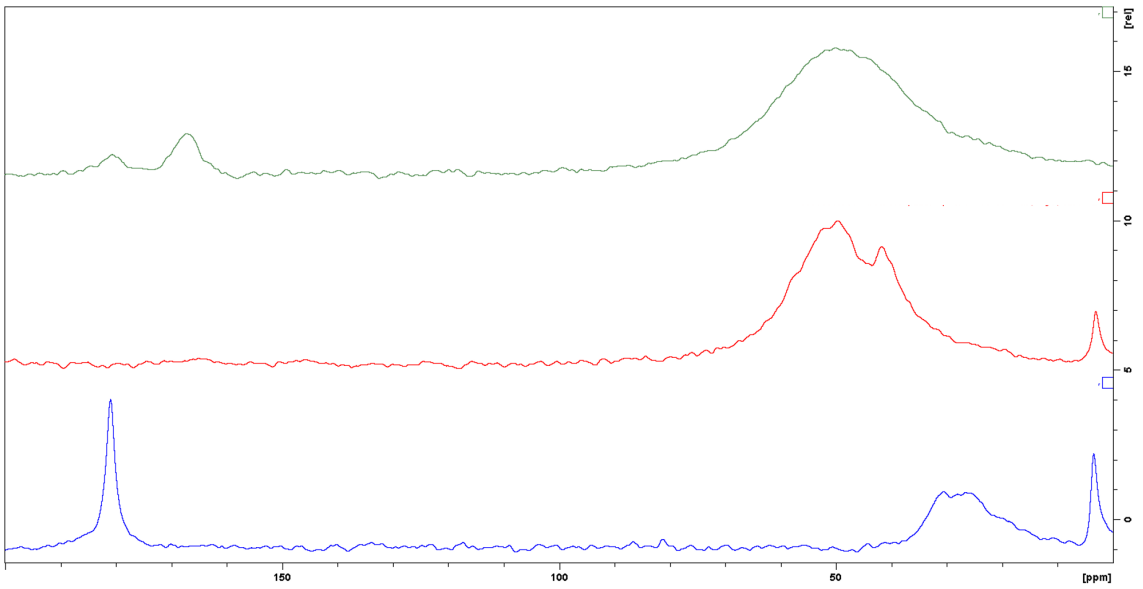


Figure 6.17: CP MAS ^{13}C-^{1}H NMR spectrum of 10 % 3,3' dithiodipropionic acid functionalised 40 wt. % G100-Silica 1 (top), 40 wt. % G100-Silica 1 (middle) and 3,3' dithiodipropionic acid (bottom). The spectrum was acquired with spinning at 5000 Hz and a contact time of 1 ms. The spectrometer was calibrated to TKS at 3.5 ppm.

PEI-Silica capacity.

A potential issue with this antioxidant is the presence of disulfide bonds which may be a route to decomposition, impacting the stability of this material. This is noted as a sulfur smell has been observed when performing TGA of samples of this material (at temperatures of up to 100 °C). The presence of sulfur gases coming off of the samples would result in the contamination of the CO_2 produced in this process, with potential side effects occurring along the CCS value chain.

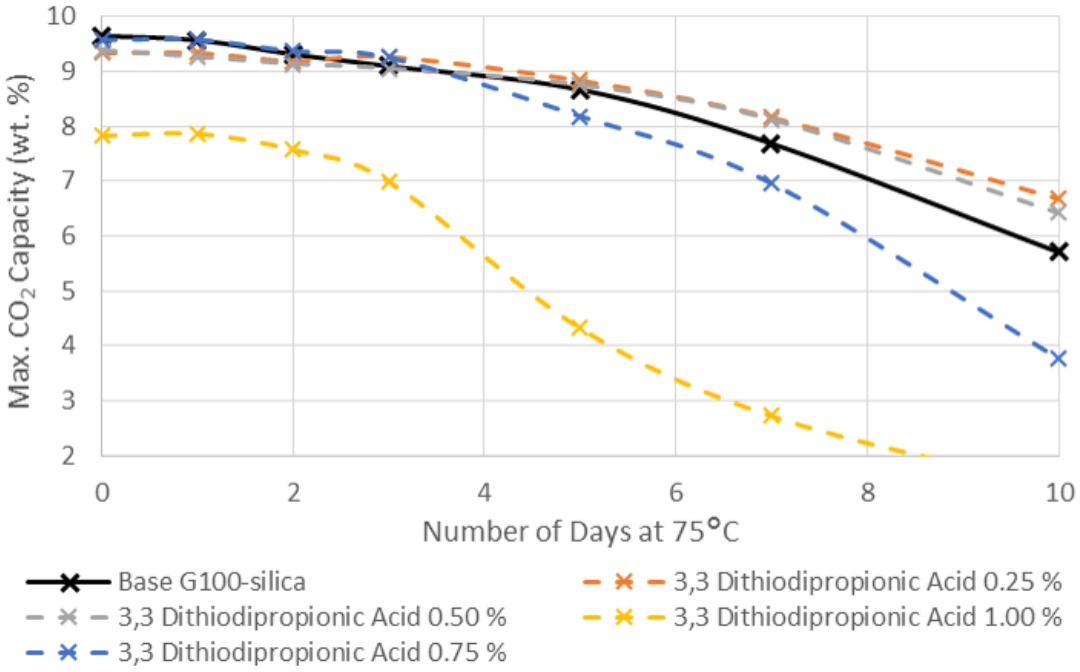


Figure 6.18: TGA determined maximum CO_2 capacity of G100-Silica 1 functionalised with 0, 0.25, 0.5, 0.75 and 1 % 3,3' dithiodipropionic acid, over 10 days under oxidation conditions

2,2' Thiodiethanol

As this sample is a liquid and therefore it would be difficult to perform CP MAS ^{13}C NMR and liquid ^{13}C NMR spectra of a multitude of materials are widely available online it was not deemed necessary to perform ^{13}C NMR on this sample. Figure 6.20 shows the spectrum of 2,2' thiodiethanol from SpectraBase.com (Bio-Rad Laboratories Inc.) assigned to the structure seen in Figure 6.19.[196]

By comparing the spectra of 2,2' thiodiethanol (Figure 6.20) with that of the functionalised G100-Silica 1 (Figure 6.21) the peaks at 63 ppm and 36 ppm can be seen both spectra, showing the presence of the antioxidant in the functionalised sample. There is an additional peak in the spectra of the functionalised sample at 165 ppm, this is likely adsorbed CO_2 from the air.

The 0.5, 1 and 2 % samples all show a similar level of CO_2 capacity to the base PEI-Silica over the first 5 days, however after day 5 these samples show higher capacity than the base sample. The 2 % sample has consistently lower CO_2 capacity than the other samples.

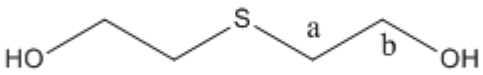


Figure 6.19: Labelled structure of 2,2' thiodiethanol

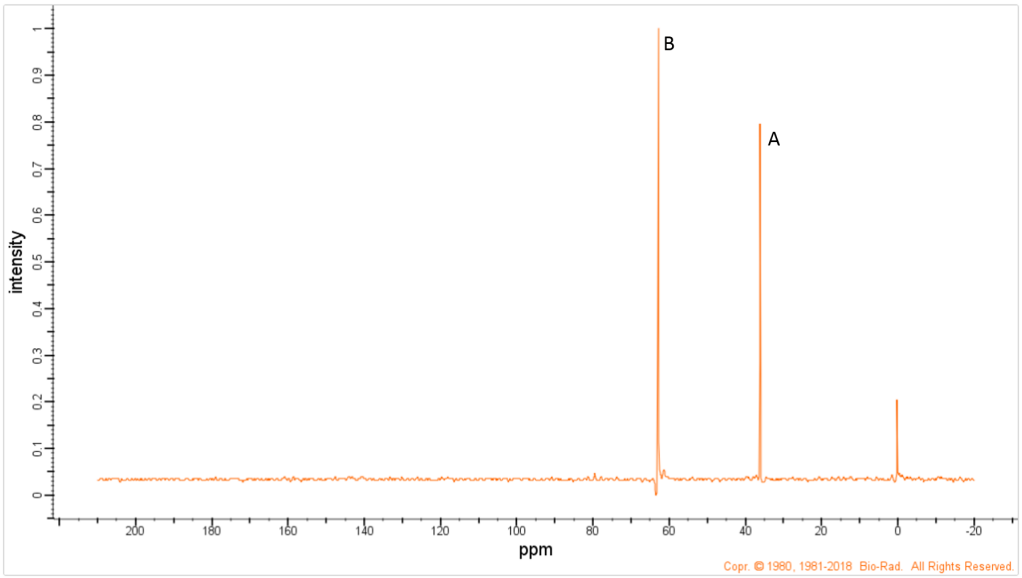


Figure 6.20: Liquid ^{13}C NMR spectrum of 2,2' thiodiethanol, with a TMS standard. From SpectraBase.com, courtesy of Bio-Rad Laboratories Inc.[196]

At higher loadings of antioxidant (2-20 %), for which the data can be seen in Appendix B.10, the samples consistently show lower capacity than the base sample over the first 5 days, however many samples show some increase in capacity after 10 days. This may be the result of additional antioxidant limiting the access of the CO_2 to the adsorption sites at higher loadings. In turn this may be reducing the CO_2 capacity of the samples. It is then only after significant oxidation occurs, between 5 and 10 days, to the base sample that the positive impact of the antioxidant counteracts the limited capacity imposed by the presence of additional loading.

For samples with 0.5, 1 and 2 % 2,2' thiodiethanol, the total change in CO_2 capacity when compared with the base PEI-Silica was 0.0, 2.9 and 6.8 % of the base PEI-Silica capacity. The 0.5 % 2,2' thiodiethanol sample although it showed higher capacity after several days, initially had a low capacity, which has limited its overall function.

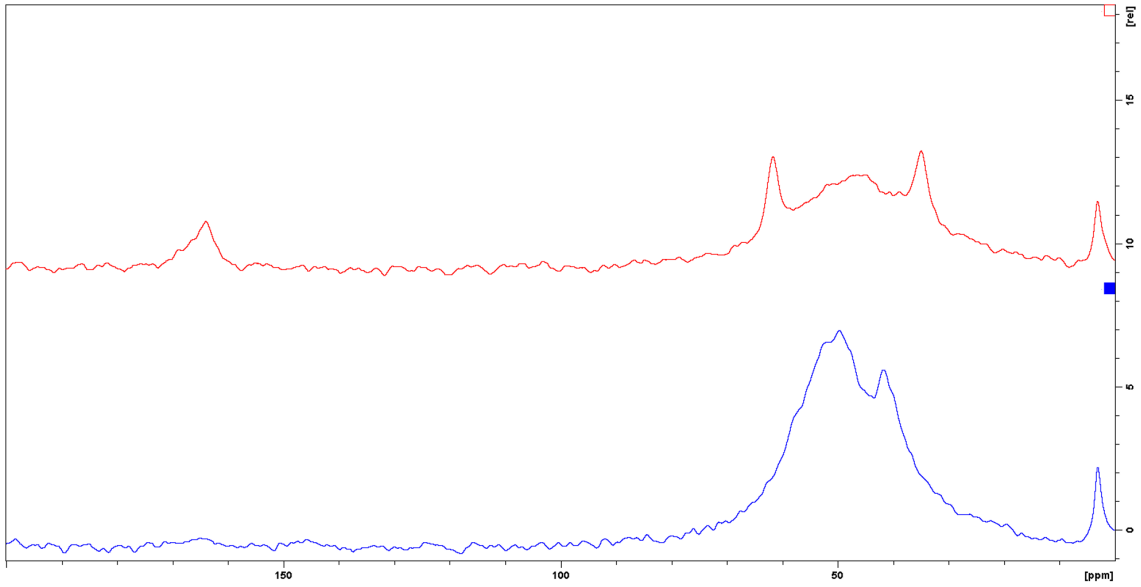


Figure 6.21: CP MAS ^{13}C-^{1}H NMR spectrum of 40 wt. % G100-Silica 1 (top) and 10 % 2,2' thiodiethanol functionalised G100-Silica 1 (bottom). The spectrum was acquired with spinning at 5000 Hz and a contact time of 1 ms. The spectrometer was calibrated to TKS at 3.5 ppm.

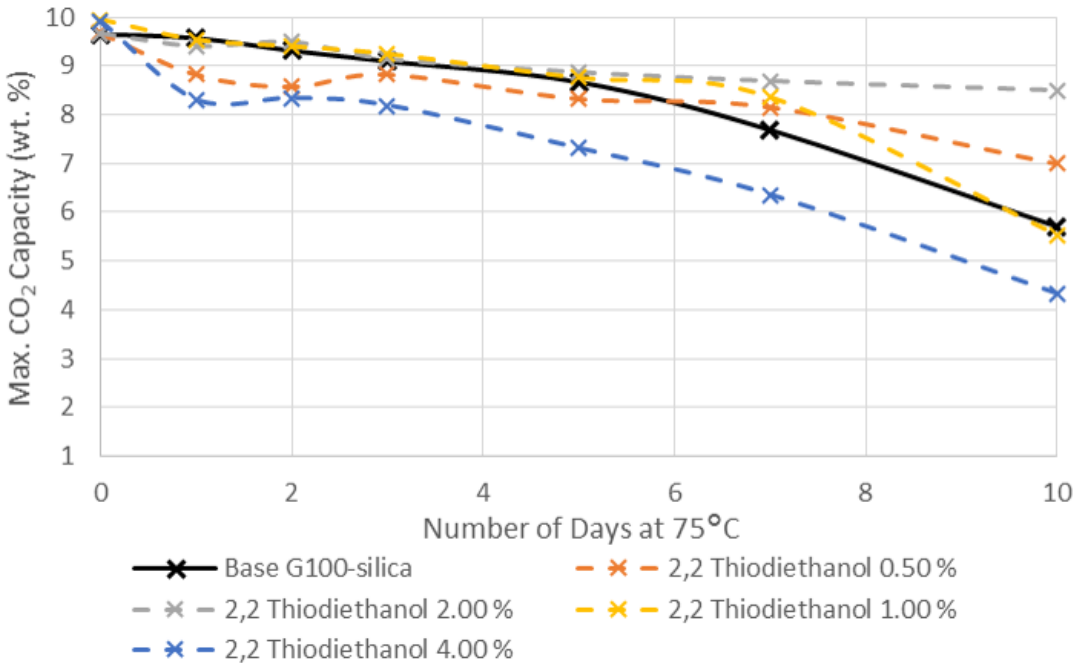


Figure 6.22: TGA determined maximum CO_2 capacity of G100-Silica 1 functionalised with 0.5, 1.0, 2.0, and 4.0 % 2,2' thiodiethanol, over 10 days under oxidation conditions

6.3.2 Potential for Use of Antioxidants in PEI-Silcia Carbon Capture

Low doses of 0.25 % of sodium salicylate and 3,3' dithiodipropionic acid, and higher doses of 1.0 % of 2,2' thiodiethanol may act as oxidation inhibitors in PEI-Silica exposed to air and CO_2 adsorption temperatures over 10 days. The ability of these materials over 10 days to reduce oxidation can be seen in Table 6.6. Pyrogallol, unlike the other antixodiants studied, does not seem to show any function as an antioxidant in PEI-Silicas and may detrimentally impact the ability of these materials to capture CO_2.

Antioxidant	Antioxidant Loading (%)	Average CO_2 Capacity (wt. %)	Average Capacity Increase (wt. %)
None	-	8.4	-
Sodium salicylate	0.25	9.2	8.9
	0.5	8.7	2.5
3,3' dithio-dipropionic acid	0.25	8.7	2.6
	0.5	8.6	1.4
2,2' thiodiethanol	1	8.7	2.9
	2	9.0	6.8

Table 6.6: Impact of the addition of antioxidant materials to 40 wt. % G100-Silica on the maximum CO_2 capacity as determined by TGA at 75 °C, under a 15 % CO_2 atmosphere

Suitability for Scale-up of Antioxidants

As stated in Section 6.1.1, two antioxidants were initially excluded from this study due to their insolubility in water, these were 2,6-di-tert-butyl-4-(dimethyl- aminomethyl)phenol and pentaerythritol tetrakis(3,5-di-tert-butyl-4-hydroxy-hydro- cinnamate). Other solvents, such a methanol, can be used to prepare PEI-Silica and may result in a greater range of potential antioxidants. However the additional cost of using methanol (for instance) as a solvent was deemed prohibitive when it comes to scale

up. In addition to this, other solvents may also have additional risks associated with them, methanol is highly flammable, for example.

When considering the use and further testing of these antioxidants in a larger scale process, it is important to consider the cost of the materials. Minimising cost is important for any commercial process and is especially so in this case, as the purpose of the addition of antioxidants to PEI-Silica is to maximise the efficiency of the system. It would be redundant to implement an antioxidant at a cost greater than that gained from efficiency improvements. It is therefore important that the antioxidant cost is evaluated when considering it's use in larger scale processes.

The prices for the antioxidants investigated in this study, as purchased from Sigma Aldrich, are listed per kg in Table 6.7. This costing is not representative of the real cost of bulk purchases of these materials, and an accurate costing would need to be performed on any sample taken further. However it is likely that the pricing of small quantities of these samples would somewhat reflect that of bulk materials.

An example of the quantities needed for scale-up is the newly commissioned facility at the University of Nottingham. At this facility 5 kg of PEI-Silcia sample is required per experiment for the smallest scale-up testing, with an additional 20 kg scale facility for larger tests. At 0.5 % loading of antioxidant on PEI-Silica, 250 g of antioxidant would be required per test on the smaller scale facility.

Antioxidant	Cost per kg (GBP)
Sodium salicylate	68.4
Pyrogallol	611
3,3' dithiodipropionic acid	441
2,2' thiodiethanol	61.2

Table 6.7: Cost per kg Antioxidant, from Sigma-Aldrich as of July 2019

From the results in the previous section (Section 6.3.1), it is clear that pyrogallol is not suitable for use as antioxidant in this case. In addition to this the prohibitive cost of pyrogallol (see Table 6.7) means that further investigations into solutions

to overcome the issues associated with this antioxidant are not being investigated further.

The remaining 3 antioxidants all showed higher CO_2 capacity compared to the base PEI-Silica over the 10 days of testing at various loadings (see 0.25 % in Figures 6.9 and 6.18, and 2 % in Figure 6.22). Although the results for 3,3' dithiodipropionic acid as an antioxidant for PEI-Silica were promising, the cost is significantly higher than the other antioxidants. At a loading of 0.25 % this would result in an additional cost of £1.10 per kg of PEI-Silica used for a reduction in oxidation of around 2.6 %.

Sodium salicylate and 2,2' thiodiethanol are both much more affordable, at £60-70 per kg. However with sodium salicylate being most effective at 0.25 % and 2,2' thiodiethanol being most effective at 2 % the additional cost of sodium salicylate will be much lower than that of 2,2' thiodiethanol. For each of these antioxidants, respectively, the additional cost is approximately £0.17 and £1.22 per kg of PEI-Silica for an average reduction in oxidation of 8.9 % and 6.8 % over 10 days.

Considering the significantly higher reduction in oxidation shown by sodium salicylate, in conjunction with it's low loading and cost, sodium salicylate is the most promising antioxidant for future work out of those studied. However, in the case that sodium salicylate is not suitable for a reason not foreseen here, the addition of 2 % 2,2' thiodiethanol has also shown promising results.

Other Considerations

As the results from this investigation into antioxidants in PEI-Silica are preliminary it would be important to perform more in depth studies into these materials and their interactions and a longer and more detailed assessment of these materials would be required in order to ensure that there are no unforeseen negative consequences of the use of these antioxidants in a CCS system.

Potential areas for further research into these materials can be found in Section 7.2.2.

6.4 Chapter Summary

^{13}C NMR of Pilot Plant Samples

- CP MAS ^{13}C NMR was used to investigate pilot plant PEI-Silica samples taken from the adsorber and regenerator.
- A method to determine the nature of CO_2 adsorbed onto the PEI-Silica was developed.
- CO_2 adsorption levels were measured on 2 sets of samples taken over 10 and 7 days. These measurements show a fairly stable CO_2 capacity over this time coupled with an increase in residual CO_2 on the regenerated samples resulting in an overall reduction in amount of CO_2 adsorbed.
- TGA of the samples showed a decrease in CO_2 capacity of the samples over time for one set of samples, however the other set showed consistent capacity over the whole time periof. No significant difference between adsorber and regenerator capacity was seen for either sample set.

Addition of Antioxidants to PEI-Silica

- Sodium salicylate has potential, at low concentrations of 0.25 % to limit the oxidation of PEI-Silica in air. It is low cost and highly effective at reducing CO_2 capacity loss.
- Pyrogallol is not a suitable antioxidant for addition to PEI-Silica.
- The cost of 2,2' thiodiethanol, 3,3' dithiodipropionic at the quantities required are prohibitive against scale up, unless a cheaper source is found.
- Further work investigating the addition of antioxidants to PEI-Silica is required, using techniques more representative of plant conditions.

Chapter 7

Conclusions

This work has focused on the interactions between polymers and surfaces on which they are adsorbed. These interactions have been predominantly investigated using solid state NMR, although other techniques have been employed to gain a greater understanding of the systems and in additional associated studies. The materials of interest have applications in cleaner fossil derived energies, with PIB derivatives improving the efficiencies of automobile fuels and PEI-Silica being a carbon capture material. In this section the conclusions of the research performed will be presented alongside suggestions for future work.

This section will consist of two halves, one on each of the major topics of study, starting with the investigations of solid state NMR as a testing method for PIB derivatives as deposit control additives.

7.1 Studies of PIBSI Dispersions As A Model of Deposit Control Additives

In this study, dispersions of various PIB derivatives on MicroCB were prepared at loadings of 2-50 wt. %. These dispersions were analysed by broadline solid state proton NMR and the mobility determined from the line width. From these data it is possible to categorise the PIB derivatives by their strength of interaction with the MicroCB surface at monolayer coverage, with low mobility corresponding to high

interaction strength. Three categories were determined: group 1 which are very weakly interacting and contains PIB derivatives which are expected to be poor deposit control additives, group 2 which are weakly interacting and contains derivatives expected to show some deposit control, and group 3 which are strongly interacting and for which the deposit control functionality is unclear. Providing there are no issues with solubility for the group 3 PIBSIs, the functionality as DCAs is expected to be good. Further investigation into the effectiveness of PIBSI G and C as DCAs would be of interest for this reason. This could be achieved through engine testing, measurement of adsorption isotherms or a number of other techniques. One technique of interest that was not persued in this study is atomic force microscopy (AFM) which may provide further insight into interaction strength.

Further to the categorisation of these PIB derivatives, some interesting impacts of different features of the PIBSIs that were supported on MicroCB were seen on the mobility of these materials. Increasing the PIB chain length was seen to result in a decreased mobility, likely as a result of chain entanglement and increased interactions with the surface. Likewise, bis functionality resulted in similarly decreased mobility compared with mono PIBSI. A mono- functionalised sample with a TEPA headgroup and a lower chain length was not investigated although this would be an interesting route to investigate the full impact of the PIB chain.

Polar surface area had been previously suggested as a method to determine monolayer coverage of these materials, however the ^{1}H NMR determined mobility suggests this is not accurate for these materials. In fact the monolayer seems to occur at a much lower level than PSA would suggest. This indicates an more complex interaction between the surface and PIB derivative than simply that of the headgroup and active site in a comb regime, for example a mushroom regime, or the polymer chain lying flat on the carbon surface.

Leading on from the use of ^{1}H NMR, solid state CP MAS ^{13}C NMR was attempted on the dispersions however obtaining a signal was not possible due to the paramagnetic features of MicroCB. Therefore a secondary deposit analogue, silica, was investigated. SBA-15 was selected as this analogue due to it's similar pore size

to MicroCB. The use of SBA-15 as an alternate substrate enabled CP MAS NMR spectroscopy however the mobility of PIBSI-SBA15 dispersions is significantly higher than that of PIBSI-MicroCB dispersions, indicating a weaker interaction between the silica and PIBSI.

7.1.1 Suggestions for Future Work

Verification of Results

Future work should include the verification of this study, specifically the relationship between ^{1}H NMR mobility and efficacy of PIBSI as a deposit control additive. This may be achieved through the use methods which test the strength of interaction, for example atomic force microscopy of the samples, or through method which directly test the function of the additive, such as engine testing. In the long term, if a test method for PIB derivatives as deposit control additives is to be developed, access to industrial testing methods such as the aforementioned engine tests, or data there from would be required. The current work is limited by the proprietary nature of these materials and it is likely that further study would be required to take place "in house".

In addition to confirming the trends seen using other techniques, further characterisation of PIBSI samples would ensure the conclusions drawn here are accurately representing the experimental results. One suggested method, would be solution state ^{1}H NMR of the neat PIBSI samples or ^{1}H MAS NMR in the solid state (of PIBSI-MicroCB samples), although other methods such as IR spectroscopy would also provide characterisation information.

Further to this, a greater number of PIBSI and other deposit control additives studied by broadline NMR would enable to expansion of the data set to greater solidify the findings seen here.

Continued ^{13}C NMR Investigations

Additionally, further investigations into silica as a substrate for PIB derivatives would provide opportunities to investigate mobility by CP MAS NMR. Which in

turn may enable the investigation of mobility at a sub-molecular level. This would be especially interesting if it could be combined with a high temperature (lazer heated) CP MAS probe. To achieve this, further work comparing the impacts of changing substrate on mobility as measured by ^{1}H NMR would be performed in order to determine if the trends of mobility seen with MicroCB are replicated.

Alternatively, investigations into other carbon substrates or into other ways to facilitate the carbon-13 NMR studies of PIBSI-MicroCB dispersions, for example the use of higher spinning speeds may have value.[197]

7.2 Investigations of PEI-Silica As Carbon Capture Materials

7.2.1 Conclusions of Research

In this study, branched polyethylene imine samples adsorbed onto mesoporous silicas, were investigated using various techniques. These techniques included both hydrogen and carbon-13 solid state NMR and thermogravimetric analysis. The primary focus of the research into these materials was the investigation and comparison of the mobility and kinetics data for PEI-Silicas with different molecular weights and silica pore sizes. To achieve this, 6 PEI samples of molecular weights from 800-750000 mol/g were investigated, along side 5 silica samples, over 30-150 °C.

All of the PEI-Silica samples generally show similar mobilities over 30-130 °C, with two regimes of mobility seen over this temperature range. The first saw mobility rapidly decreasing with temperature between 30-80 °C, and the second saw somewhat of a plateau in mobility over 80-130 °C as the PEI nears fluid-like behaviour inside the silica pores. The transition between these regimes line up well with the CO_2 adsorption temperature of the PEI-Silica of 70-80 °C.

From the change in mobility behaviour which correlates with the adsorption temperature, this work suggests that adsorption and desorption of CO_2 is facilitated by a fluid PEI in the silica pores.

The lowest molecular weight PEI (800), showed a high CO_2 adsorption on the majority of the silica substrates, this is attributed to a reduction in steric hindrance of the adsorption sites of the PEI as a result of the smaller molecules (the molecules are able to fit more easily into the pores). However the limitations of low molecular weight PEIs are that they often have low stability over time and are thus not ideal for industrial purposes.

The silica which could support the most PEI, RH2 at 60 % loading, showed the highest CO_2 adsorption due to the increased number of adsorption sites. This silica is prepared from rice husk and has significant macroporous structure.

In turn the silica with the smallest pores, SBA-15, showed very slow adsorption kinetics. This is thought to be the result of the narrow pores restricting the access of CO_2 to the adsorption sites.

Unexpectedly high CO_2 adsorption was seen for 750000 PEI-RH2 and 5000 PEI-RH2, of almost 22 % and 15 % respectively. This prompts further investigation into the use of these materials as a solid state CO_2 capture material, and further investigations into more macroporous silicas as supports for PEI and other amines. These Samples have slow kinetics so may not be suitable for scale-up, however continued work into these materials will hopefully gain insight into their expected affinity for CO_2.

Two other areas of research were also performed on PEI-Silica, specifically the 5000 molecular weight PEI supported on Silica 1, one investigating CO_2 adsorption and the other the use of antioxidants in the samples.

The use of CP MAS ^{13}C NMR to investigate the presence and nature of adsorbed CO_2 on KIER pilot plant PEI-Silcia samples was successful in that it showed the presence of C=O groups from adsorbed CO_2. However it was not immediately possible to determine if these groups were reversibly reacted (i.e. chemisorbed) or permanently bonded. It was possible to prove that the groups were chemisorbed using a process to desorb the CO_2, however this required additional stages and the NMR spectroscopy to be repeated. As this work progresses other methods such as IR spectroscopy may also be used to investigate the adsorption of CO_2.

Through the investigation of samples from the adsorber and regenerator of the pilot plant it was possible to get a image of the adsorption and desorption of CO_2 over several days and see presence of the residual CO_2 remaining after desorption. The NMR results showed the CO_2 adsorption levels to remain fairly stable over time, however this was accompanied by an increase in residual CO_2 remaining adsorbed onto the regenerated samples. In real terms this results in an overall reduction in CO_2 adsorbed per unit PEI-Silica as time goes on. CO_2 adsorption TGA was also carried out on these samples and the results of this analysis support the findings of the ^{13}C NMR, with the maximum CO_2 reducing over the length of time the samples were in the plant. TGA results showed no significant difference between adsorber and regenerator samples taken at the same time.

The use of antioxidants is a promising solution to the issue of sample oxidation. Restricting the selection of antioxidants to those that are water soluble for the sake of cost reduction on scale up, 4 potential antioxidants were investigated. Out of these antioxidants, sodium salicylate, 3,3' dithiodipropionic acid and 2,2' thiodiethanol show reduction in loss of CO_2 adsorption capacity over 10 days. Due to its higher impact on CO_2 capacity and the low cost of the chemical, sodium salicylate shows the most potential for application in the future. The antioxidant pyrogallol is unsuited to this work due to reactivity with PEI.

7.2.2 Suggestions for Future Work

Investigations of Silica Substrates

The rice husk used in this study was obtained from a private farm, rather than a large scale commercial supplier. If the use of rice husk to continue preparing these silicas was to be used at a larger scale, a commercial supplier would need to be sourced. However, as the samples are prepared by a templating method, it is very possible that an alternate organic feed stock would be suitable for this method. Thus, further investigations into potential silica sources and the features of silicas made through various techniques would be valuable. In addition, one area not considered by this study is the impact of particle size on the adsorption, Zhu et al. found increasing

particle size to decrease the adsorption capacity of PEI-Silicas, so it may be useful to specifically source silicas with small particle sizes.[155]

Futher Investigations of Anti-Oxidant Functionalisation of PEI-Silica

The University of Nottingham, in collaboration with KIER has constructed a new pilot scale carbon capture rig for use with solid adsorbents, specifically PEI-Silicas. This rig will, hopefully, be used in the future to further investigate these PEI-Silicas. One key area suggested to be investigated on this rig would be the addition of antioxidants (specifically sodium salicylate) to the PEI-Silica samples. This would be useful to test the ability of the antioxidants over time, and determine the resilience of the antioxidant to the cycling of adsorption and regeneration. It would be recommended to repeat the lab scale testing of these materials before scale up to confirm the findings of this study.

In addition, an investigation into different potential antioxidants, for instance ethylenediaminetetraacetic acid and N,N-diethanolglycine which have been used or investigated for use preventing the oxidation of MEA on submarines, would be of interest.[150]

Further NMR Experiments

Further investigation, using proton NMR, into the mobility of different solid supported amines may also provide further insight.

Using a CO_2 gas flow, it might be possible to investigate the adsorption of CO_2 with NMR in real time. This would be easier with broadline proton NMR as the acquisition/experiment time is so short (30 s), however would be most interesting using a high resolution technique in which the C=O peak could be resolved, however as these experiments tend to take much longer amounts of time further investigation into an appropriate technique would be required.

Experiments using Other Techniques

Other techniques of interest for PEI-Silica materials include IR spectroscopy, which may be useful to further investigate the presence of adsorbed CO_2 on the samples. Using IR, determination of whether the CO_2 was reversibly chemisorbed or irreversibly bonded to the PEI should be possible (with carbamate and urea functional groups being expected to show peaks at different wavenumbers). X-ray photoelectron spectroscopy may also be useful in investigating the surface chemistry of the samples and may be able to determine if a urea group is formed.[48]

Additionally the use of CO_2 gas sorption might be used to determine what, if any, adsorption of CO_2 is taking place directly onto the silica substrate.

Bibliography

[1] IPCC. *Fifth Assessment Report - Impacts, Adaptation and Vulnerability*. Tech. rep. Cambridge: Cambridge University Press, 2014. URL: https://www.ipcc.ch/report/ar5/wg2/.

[2] R Stuart Haszeldine. "Carbon capture and storage: how green can black be?" In: *Science (New York, N.Y.)* 325.5948 (Sept. 2009), pp. 1647–52. ISSN: 1095-9203. DOI: 10.1126/science.1172246. URL: http://www.ncbi.nlm.nih.gov/pubmed/19779187.

[3] Alfred Rudin and Phillip Choi. "Introductory Concepts and Definitions". In: *The Elements of Polymer Science & Engineering*. Elsevier, 2013, pp. 1–62. DOI: 10.1016/b978-0-12-382178-2.00001-8.

[4] Steven M. Kurtz. "A Primer on UHMWPE". In: *UHMWPE Biomaterials Handbook: Ultra High Molecular Weight Polyethylene in Total Joint Replacement and Medical Devices: Third Edition*. Elsevier Inc., 2016, pp. 1–6. ISBN: 9780323354011. DOI: 10.1016/B978-0-323-35401-1.00001-6.

[5] Nicholas P. Cheremisinoff. *Condensed Encyclopedia of Polymer Engineering Terms*. Elsevier, 2001. DOI: 10.1016/c2009-0-25687-x.

[6] Ulrich Steuerle and Robert Feuerhake. "Aziridines". In: *Ullmann's Encyclopedia of Industrial Chemistry*. Weinheim, Germany: Wiley-VCH Verlag GmbH & Co. KGaA, Dec. 2006. DOI: 10.1002/14356007.a03{_}239.pub2. URL: http://doi.wiley.com/10.1002/14356007.a03_239.pub2.

[7] Richard T. Cimino et al. "Mechanisms of chain adsorption on porous substrates and critical conditions of polymer chromatography". In: *Journal of*

Colloid and Interface Science 481 (Nov. 2016), pp. 181–193. ISSN: 10957103. DOI: 10.1016/j.jcis.2016.07.019.

[8] Alfred Rudin and Phillip Choi. "Practical Aspects of Molecular Weight Measurements". In: *The Elements of Polymer Science & Engineering*. Elsevier, 2013, pp. 89–148. DOI: 10.1016/b978-0-12-382178-2.00003-1.

[9] G. Fleer et al. *Polymers at Interfaces*. Springer, 1993, p. 491.

[10] C. J. Kuo and W. L. Lan. "Gel spinning of synthetic polymer fibres". In: *Advances in Filament Yarn Spinning of Textiles and Polymers*. Elsevier Ltd., 2014, pp. 100–112. ISBN: 9780857094995. DOI: 10.1533/9780857099174.2.100.

[11] Armando Maestro et al. "Reptation in langmuir polymer monolayers". In: *Soft Matter* 6.18 (Sept. 2010), pp. 4407–4412. ISSN: 1744683X. DOI: 10.1039/c0sm00250j.

[12] Kunio Miyazawa, Tetsuro Yokono, and Yuzo Sanada. "High temperature ^{1}H-NMR study of coal and pitch at the early stages of carbonization". In: *Carbon* 17.3 (Jan. 1979), pp. 223–225. ISSN: 0008-6223. DOI: 10.1016/0008-6223(79)90082-4. URL: https://www.sciencedirect.com/science/article/pii/0008622379900824.

[13] Karen M Steel et al. "Use of Rheometry and ^{1}H NMR Spectroscopy for Understanding the Mechanisms behind the Generation of Coking Pressure". In: *Energy & Fuels* 18.5 (2004), pp. 1250–1256. DOI: 10.1021/ef0340581. URL: http://dx.doi.org/10.1021/ef0340581.

[14] Anthony Dufour et al. "In Situ Analysis of Biomass Pyrolysis by High Temperature Rheology in Relations with 1 H NMR". In: *Energy & Fuels* 26.10 (Oct. 2012), pp. 6432–6441. DOI: 10.1021/ef301310x. URL: http://pubs.acs.org/doi/10.1021/ef301310x.

[15] Anthony Dufour et al. "The Origin of Molecular Mobility During Biomass Pyrolysis as Revealed by Insitu ^{1}H NMR Spectroscopy". In: *ChemSusChem* 5.7

(July 2012), pp. 1258–1265. ISSN: 18645631. DOI: 10.1002/cssc.201100442. URL: http://doi.wiley.com/10.1002/cssc.201100442.

[16] C. Denecker, J. J. Liggat, and C. E. Snape. "Relationship between the thermal degradation chemistry and flammability of commercial flexible polyurethane foams". In: *Journal of Applied Polymer Science* 100.4 (May 2006), pp. 3024–3033. ISSN: 0021-8995. DOI: 10.1002/app.23701. URL: http://doi.wiley.com/10.1002/app.23701.

[17] C Dick et al. "The flammability of urethane-modified polyisocyanurates and its relationship to thermal degradation chemistry". In: *Polymer* 42.3 (Feb. 2001), pp. 913–923. ISSN: 0032-3861. DOI: 10.1016/S0032-3861(00)00470-5. URL: https://www.sciencedirect.com/science/article/pii/S0032386100004705.

[18] The European Parliament and the Council of the European Union. *Regulation (EC) No 715/2007 of the European Union and of the Council of 20 June 2007 on type approval of motor vehicles with respect to emissions from light passenger and commercial vehicles (Euro 5 and Euro 6) and on access to vehicle repair and maintenance*. 2007. URL: http://eur-lex.europa.eu/LexUriServ/LexUriServ.do?uri=OJ:L:2007:171:0001:0016:EN:PDF.

[19] The European Parliament and the Council of the European Union. *Regulation (EC) No 443/2009 of the European Parliament and of the Council of 23 April 2009 setting emission performance standards for new passenger cars as part of the Community's integrated approach to reduce CO^2 emissions from light-duty vehicles*. 2009. URL: https://eur-lex.europa.eu/eli/reg/2009/443/oj.

[20] European Commission. *Air pollution from the main sources - Air emissions from road vehicles*. 2019. URL: http://ec.europa.eu/environment/air/transport/road.htm.

[21] Hu Jianqiang, Yao Junbing, and Du Zhanhe. "Opportunities for replacement of phosphorus and dithiophosphates in lubricating oil with borate ester addi-

tive containing nitrogen". In: *World Tribology Congress III*. Washington DC: The American Society of Mechanical Engineers, 2005, pp. 623–624.

[22] *Motorcycle Tech - Gasoline Direct Injection*. URL: https://www.rideapart.com/articles/249017/motorcycle-tech-gasoline-direct-injection/.

[23] Sean Bennett. "Injector Nozzles". In: *Modern Diesel Technology: Diesel Engines*. 2nd ed. Stamford: Cengage Delmar Learning, 2014. Chap. 14, pp. 267–278. ISBN: 978-1285442969.

[24] Darby Kozak, David Moreton, and Brian Vincent. "The adsorption of non-ionic surfactants on carbon black particles in hydrocarbon media". In: *Colloids and Surfaces A: Physicochemical and Engineering Aspects* 347.1-3 (2009), pp. 245–250. DOI: 10.1016/j.colsurfa.2009.07.020.

[25] Lubrizol. *The CEC DW10 Diesel Fuel Injector Fouling Test*. 2010.

[26] William Meredith et al. "Spectroscopic Studies of Internal Injector Deposits (IDID) resulting from the Use of Non-commercial Low molecular Weight Polyisobutylenesuccinimide (PIBSI)". In: *SAE Int. J. Fuels Lubr.* 7.3 (2014). DOI: doi:10.4271/2014-01-2720..

[27] J B Retzloff, L Plonsker, and R B Sneed. "Fuel Detergency - Effects on Emissions". In: *SAE National Fuels and Lubricants Meeting*. SAE International, 1972. DOI: 10.4271/720941. URL: http://dx.doi.org/10.4271/720941.

[28] Robert C Tupa and Donald E Koehler. "Intake Valve Deposits - Effects of Engines, Fuels & Additives". In: *SAE International Fall Fuels and Lubricants Meeting and Exhibition*. SAE International, 1988. DOI: 10.4271/881645. URL: http://dx.doi.org/10.4271/881645.

[29] Yves Chevalier et al. "Review: The adsorption of functional polymers from their organic solutions: applications to fuel additives". In: *Polymer International* 53.5 (2004), pp. 475–483. DOI: 10.1002/pi.1438.

[30] A Tomlinson et al. "Adsorption properties of succinimide dispersants on carbonaceous substrates". In: *Carbon* 38 (2000), pp. 13–28.

[31] Jim Barker et al. "A Novel Technique for Investigating the Nature and Origins of Deposits Formed in High Pressure Fuel Injection Equipment". In: *SAE* (2009). DOI: 10.4271/2009-01-2637.

[32] Gautam T Kalghatgi. "Deposits in Gasoline Engines - A Literature Review". In: *SAE International Fuels and Lubricants Meeting and Exposition*. SAE International, 1990. DOI: 10.4271/902105. URL: http://dx.doi.org/10.4271/902105.

[33] Allen A Aradi et al. "A Study of Fuel Additives for Direct Injection Gasoline (DIG) Injector Deposit Control". In: *SAE International Spring Fuels & Lubricants Meeting & Exposition*. SAE International, 2000. DOI: 10.4271/2000-01-2020. URL: http://dx.doi.org/10.4271/2000-01-2020.

[34] Sarah Angel Smith. "Characterisation of Diesel Injector Deposits Using Advanced Analytical Techniques". PhD thesis. University of Nottingham, 2017.

[35] Daniel T Daly et al. "Mechanism of Combustion Chamber Deposit Formation". In: *SAE Fuels & LUbricants Meeting & Exposition*. SAE International, 1994. DOI: 10.4271/941889. URL: http://dx.doi.org/10.4271/941889.

[36] Gequn Shu, Lihui Dong, and Xingyu Liang. "A review of experimental studies on deposits in the combustion chambers of internal combustion engines". In: *International Journal of Engine Research* 13.4 (2012), pp. 357–369. DOI: 10.1177/1468087411427661. URL: http://jer.sagepub.com/content/13/4/357.abstract.

[37] *ATC Document 113, Fuel Additives Uses and Benefits, 2013.*

[38] K L Kipp et al. "Ability of Gasoline Additives To Clean Engines And Reduce Exhaust Emissions". In: *SAE Mid-Year Meeting*. SAE International, 1970. DOI: 10.4271/700456. URL: http://dx.doi.org/10.4271/700456.

[39] Paul Richards et al. "The Emerging Market for Biodiesel and the Role of Fuel Additives". In: *JSAE/SAE International Fuels & Lubricants Meeting*. SAE International, 2007. DOI: 10.4271/2007-01-2033. URL: http://dx.doi.org/10.4271/2007-01-2033.

[40] Stephen A Rackley. *Carbon capture and storage*. eng. Ebook library. Amsterdam: Elsevier Butterworth-Heinemann, 2010. ISBN: 9780080951386.

[41] Bert Metz et al. *IPCC Special Report on Carbon dioxide Capture and Storage*. Tech. rep. Cambridge: Cambridge University Press, 2005. URL: https://www.ipcc.ch/report/srccs/.

[42] British Geological Survey. *INDUSTRIAL CARBON DIOXIDE EMISSIONS AND CARBON DIOXIDE STORAGE POTENTIAL IN THE UK*. Tech. rep. 2006. URL: https://webarchive.nationalarchives.gov.uk/20090703100908/http://www.berr.gov.uk/files/file35684.pdf.

[43] IEA GHG R&D Programme (IEA GHG). *CO^2 Capture in the Cement Industry*. Tech. rep. 2008. URL: www.ieagreen.org.uk.

[44] Jitong Wang et al. "Carbon dioxide capture using polyethylenimine-loaded mesoporous carbons". In: *Journal of Environmental Sciences* 25.1 (Jan. 2013), pp. 124–132. ISSN: 1001-0742. DOI: 10.1016/S1001-0742(12)60011-4. URL: https://www.sciencedirect.com/science/article/pii/S1001074212600114.

[45] Sunho Choi, Jeffrey H Drese, and Christopher W Jones. "Adsorbent Materials for Carbon Dioxide Capture from Large Anthropogenic Point Sources". In: *ChemSusChem* 2.9 (Sept. 2009), pp. 796–854. DOI: 10.1002/cssc.200900036. URL: http://doi.wiley.com/10.1002/cssc.200900036.

[46] Wenbin Zhang et al. "Performance of polyethyleneimine–silica adsorbent for post-combustion CO^2 capture in a bubbling fluidized bed". In: *Chemical Engineering Journal* 251 (Sept. 2014), pp. 293–303. ISSN: 1385-8947. DOI: 10.1016/J.CEJ.2014.04.063. URL: https://www.sciencedirect.com/science/article/pii/S1385894714004951#b0090.

[47] Kaimin Li et al. "Polyethyleneimine-nano silica composites: a low-cost and promising adsorbent for CO^2 capture". In: *Journal of Materials Chemistry A* (2015). DOI: 10.1039/c4ta04275a. URL: www.rsc.org/MaterialsA.

[48] T.C. Drage et al. "Thermal stability of polyethylenimine based carbon dioxide adsorbents and its influence on selection of regeneration strategies". In: *Microporous and Mesoporous Materials* 116.1-3 (Dec. 2008), pp. 504–512. ISSN: 13871811. DOI: 10.1016/j.micromeso.2008.05.009. URL: http://linkinghub.elsevier.com/retrieve/pii/S1387181108002369.

[49] Chungsying Lu et al. "Comparative Study of CO^2 Capture by Carbon Nanotubes, Activated Carbons, and Zeolites". In: *Energy & Fuels* 22.5 (Sept. 2008), pp. 3050–3056. ISSN: 0887-0624. DOI: 10.1021/ef8000086. URL: http://pubs.acs.org/doi/abs/10.1021/ef8000086.

[50] Watcharop Chaikittisilp et al. "Poly(allylamine)–Mesoporous Silica Composite Materials for CO^2 Capture from Simulated Flue Gas or Ambient Air". In: *Industrial & Engineering Chemistry Research* 50.24 (Dec. 2011), pp. 14203–14210. ISSN: 0888-5885. DOI: 10.1021/ie201584t. URL: http://pubs.acs.org/doi/abs/10.1021/ie201584t.

[51] Kaimin Li et al. "The influence of polyethyleneimine type and molecular weight on the CO^2 capture performance of PEI-nano silica adsorbents". In: *Applied Energy* 136 (Dec. 2014), pp. 750–755. ISSN: 0306-2619. DOI: 10.1016/J.APENERGY.2014.09.057. URL: https://www.sciencedirect.com/science/article/pii/S0306261914010058.

[52] Junya Wang et al. "Recent advances in solid sorbents for CO^2 capture and new development trends". In: (2014). DOI: 10.1039/c4ee01647e. URL: www.rsc.org/ees.

[53] Yi Zhao, Yanmei Shen, and Lu Bai. "Effect of chemical modification on carbon dioxide adsorption property of mesoporous silica". In: *Journal of Colloid and Interface Science* 379.1 (Aug. 2012), pp. 94–100. ISSN: 0021-9797. DOI: 10.1016/J.JCIS.2012.04.064. URL: https://www.sciencedirect.com/science/article/pii/S0021979712004687.

[54] Praveen Bollini et al. "Amine-oxide hybrid materials for acid gas separations". In: *Journal of Materials Chemistry* 21.39 (Sept. 2011), p. 15100. ISSN:

0959-9428. DOI: 10.1039/c1jm12522b. URL: http://xlink.rsc.org/?DOI=c1jm12522b.

[55] David S. Mebane et al. "Transport, Zwitterions, and the Role of Water for CO^2 Adsorption in Mesoporous Silica-Supported Amine Sorbents". In: *The Journal of Physical Chemistry C* 117.50 (Dec. 2013), pp. 26617–26627. ISSN: 1932-7447. DOI: 10.1021/jp4076417. URL: http://pubs.acs.org/doi/10.1021/jp4076417.

[56] Alain Goeppert et al. "Nanostructured silica as a support for regenerable high-capacity organoamine-based CO^2 sorbents". In: *Energy & Environmental Science* 3.12 (Nov. 2010), p. 1949. ISSN: 1754-5692. DOI: 10.1039/c0ee00136h. URL: http://xlink.rsc.org/?DOI=c0ee00136h.

[57] Sam Bailey. "A Study of Polyisobutylene and its Derivatives at High Temperatures". PhD thesis. University of Nottingham, 2016.

[58] Jack D Benson and Philip A Yaccarino. *The Effects of Fuel Composition and Additives on Multiport Fuel Injector Deposits*. 1986. DOI: 10.4271/861533. URL: http://dx.doi.org/10.4271/861533.

[59] T W Zerda, X Yuan, and S M Moore. "Effects of fuel additives on the microstructure of combustion engine deposits". In: *Carbon* 39.10 (2001), pp. 1589–1597. URL: http://www.sciencedirect.com/science/article/pii/S0008622300002876.

[60] Dairene Uy et al. "Characterization of gasoline soot and comparison to diesel soot: Morphology, chemistry, and wear". In: *Tribology International* 80 (2014), pp. 198–209. DOI: http://dx.doi.org/10.1016/j.triboint.2014.06.009. URL: http://www.sciencedirect.com/science/article/pii/S0301679X14002370.

[61] Robert C Tupa and Donald E Koehler. "Gasoline Port Fuel Injectors - Keep Glean/Clean Up With Additives". In: *SAE International Fuels and Lubricants Meeting and Exposition*. SAE International, 1986. DOI: 10.4271/861536. URL: http://dx.doi.org/10.4271/861536.

[62] Changsoo Kim, Spyros I Tseregounis, and Bruce E Scruggs. "Deposit Formation on a Metal Surface in Oxidized Gasolines". In: *SAE International Fall Fuels and Lubricants Meeting and Exhibition*. SAE International, 1987. DOI: 10.4271/872112. URL: http://dx.doi.org/10.4271/872112.

[63] Richard J DuMont et al. "Controlling Induction System Deposits in Flexible Fuel Vehicles Operating on E85". In: *SAE Powertrain & Fluid Systems Conference & Exhibition*. SAE International, 2007. DOI: 10.4271/2007-01-4071. URL: http://dx.doi.org/10.4271/2007-01-4071.

[64] *Carbon black manufacturing — What is carbon black? — Products and Technology — ASAHI CARBON CO., LTD.* URL: http://www.asahicarbon.co.jp/global_site/product/cb/manufacturing.html.

[65] International Carbon Black Association (ICBA). *General Information, What is Carbon Black? - International Carbon Black Association - ICBA*. 2016. URL: http://www.carbon-black.org/index.php/what-is-carbon-black.

[66] H P Boehm. "Some aspects of the surface chemistry of carbon blacks and other carbons". In: *Carbon* 32.5 (1994), pp. 759–769. DOI: http://dx.doi.org/10.1016/0008-6223(94)90031-0. URL: http://www.sciencedirect.com/science/article/pii/0008622394900310.

[67] A D H Clague et al. "A comparison of diesel engine soot with carbon black1". In: *Carbon* 37.10 (1999), pp. 1553–1565. DOI: http://dx.doi.org/10.1016/S0008-6223(99)00035-4. URL: http://www.sciencedirect.com/science/article/pii/S0008622399000354.

[68] Ann Y. Watson and Peter A. Valberg. "Carbon Black and Soot: Two Different Substances". In: *AIHAJ - American Industrial Hygiene Association* 62.2 (Mar. 2001), pp. 218–228. ISSN: 1529-8663. DOI: 10.1080/15298660108984625. URL: http://www.tandfonline.com/doi/abs/10.1080/15298660108984625.

[69] Solmaz Pirouz et al. "Chemical Modification of Polyisobutylene Succinimide Dispersants and Characterization of Their Associative Properties". In: *The Journal of Physical Chemistry B* 119.37 (2015), pp. 12202–12211. DOI: 10.

1021/acs.jpcb.5b04515. URL: http://dx.doi.org/10.1021/acs.jpcb.5b04515.

[70] J A Bert et al. "A Gasoline Additive Concentrate Removes Combustion Chamber Deposits and Reduces Vehicle Octane Requirement". In: *SAE Fuels and Lubricants Meeting*. SAE International, 1983. DOI: 10.4271/831709. URL: http://dx.doi.org/10.4271/831709.

[71] Yasunori Takei et al. "Effects of Gasoline and Gasoline Detergents on Combustion Chamber Deposit Formation". In: *SAE Fuels & Lubricants Meeting & Exposition*. SAE International, 1994. DOI: 10.4271/941893. URL: http://dx.doi.org/10.4271/941893.

[72] S R Kelemen et al. "Fuel, Lubricant and Additive Effects on Combustion Chamber Deposits". In: *SAE International Fall Fuels and Lubricants Meeting and Exposition*. SAE International, 1998. DOI: 10.4271/982715. URL: http://dx.doi.org/10.4271/982715.

[73] H Mach. "Highly reactive polyisobutene as a composition element for a new generation of lubricant additives". In: *Oil Gas-European Magazine* 22.2 (1996), pp. 38–40.

[74] The Lubrizol Corporation. *Polyisobutylene Succinimides in Engine Oil - Corporate Responsibility - The Lubrizol Corporation*. 2019. URL: https://www.lubrizol.com/Sustainability/HSES/Product-Stewardship/Polyisobutylene-Succinimides-in-Engine-Oil.

[75] R. M. Mortier and S. T. Orszulik, eds. *Chemistry and Technology of Lubricants*. Dordrecht: Springer Netherlands, 1997. ISBN: 978-94-017-1023-7. DOI: 10.1007/978-94-017-1021-3. URL: http://link.springer.com/10.1007/978-94-017-1021-3.

[76] M Dubois-Clochard et al. "Adsorption of polisobutenylsuccinimide derivatives at a sold-hydrocarbon interface". In: *Langmuir* 17.19 (2001), pp. 5901–5910. DOI: 10.1021/la010076o.

[77] S.D. Gurumayum Sharma, D. Moreton, and B. Vincent. "Adsorption isotherm and atomic force microscopy studies of the interactions between polymers and surfactants on steel surfaces in hydrocarbon media". In: *Journal of Colloid and Interface Science* 263.2 (2003), pp. 343–349. ISSN: 00219797. DOI: 10.1016/S0021-9797(03)00320-5.

[78] S.D. Gurumayum Sharma et al. "Studies of the adsorption of oligomers and surfactants on carbon and steel surfaces in a hydrocarbon medium". In: *Colloids and Surfaces A: Physicochemical and Engineering Aspects* 250.1 (2004), pp. 51–56. ISSN: 09277757. DOI: 10.1016/j.colsurfa.2004.04.100.

[79] Robert J Pugh, Toshiaki Matsunaga, and Frederick M Fowkes. "The dispersibility and stability of carbon black in media of low dielectric constant. 1. Electrostatic and steric contributions to colloidal stability". In: *Colloids and Surfaces* 7.3 (1983), pp. 183–207. DOI: http://dx.doi.org/10.1016/0166-6622(83)80046-8. URL: http://www.sciencedirect.com/science/article/pii/0166662283800468.

[80] Robert J Pugh and Frederick M Fowkes. "The dispersibility and stability of carbon black in media of low dielectric constant. 2. Sedimentation volume of concentrated dispersions, adsorption and surface calorimetry studies". In: *Colloids and Surfaces* 9.1 (1984), pp. 33–46. DOI: http://dx.doi.org/10.1016/0166-6622(84)80140-7. URL: http://www.sciencedirect.com/science/article/pii/0166662284801407.

[81] R. E. Kornbrekke, I. D. Morrison, and T. Oja. "Electrophoretic mobility measurements in low conductivity media". In: *Langmuir* 8.4 (Apr. 1992), pp. 1211–1217. ISSN: 0743-7463. DOI: 10.1021/la00040a032. URL: http://pubs.acs.org/doi/abs/10.1021/la00040a032.

[82] E. Georges, J.-M. Georges, and S. Hollinger. "Contact of Two Carbon Surfaces Covered with a Dispersant Polymer". In: *Langmuir* 13.13 (June 1997), pp. 3454–3463. ISSN: 0743-7463. DOI: 10.1021/la970065o. URL: http://pubs.acs.org/doi/abs/10.1021/la970065o.

[83] Andrew R. Cox et al. "The effect of polymer chain architecture on the adsorption properties of derivatised polyisobutylenes at the carbon n-heptane interface." In: *Colloids and Surfaces A: Physicochem. Eng. Aspects* 181 (2000), 205–213.

[84] A S Ramadhas et al. "Impact of Fuel Additives on Intake Valve Deposits, Combustion Chamber Deposits and Emissions". In: *SAE International Powertrains, Fuels and Lubricants Meeting*. SAE International, 2011. DOI: 10.4271/2011-01-1980. URL: http://dx.doi.org/10.4271/2011-01-1980.

[85] Jacqueline Reid and Vince Burgess. *Fuel composition comprising detergent and quaternary ammonium salt additive*. Mar. 2011. URL: https://patents.google.com/patent/WO2011110860A1.

[86] Anthony Cooney, Alan Ross, and Vince Burgess. *Additives for Fuels and Lubricants*. 2013. URL: http://patents.com/us-20130288937.html.

[87] L.O. Alemán-Vázquez and J.R. Villagómez-Ibarra. "Polyisobutenylsuccinimides as detergents and dispersants in fuel: infrared spectroscopy application". In: *Fuel* 80.7 (May 2001), pp. 965–968. ISSN: 0016-2361. DOI: 10.1016/S0016-2361(00)00167-8. URL: https://www.sciencedirect.com/science/article/pii/S0016236100001678.

[88] Yuri Kim et al. "Development of PIBSI type dispersants for carbon deposit from thermal oxidative decomposition of Jet A-1". In: *Fuel* 158 (2015), pp. 91–97. DOI: 10.1016/j.fuel.2015.05.008.

[89] Scott D. Schwab and Xinggao Fang. *Fuel additives for treating internal deposits of fuel injectors*. Mar. 2015. URL: https://patents.google.com/patent/US9249769B1/en.

[90] M. Bubálik et al. "Development of deposit control additives for diesel fuel". In: *Petroleum & Coal* 51.3 (2009), pp. 167–175.

[91] Trevor Russell et al. *Multi-functional gasoline detergent compositions*. May 1996. URL: http://www.freepatentsonline.com/5518511.html.

[92] Vincent Burgess, Jacqueline Reid, and Simon Mulqueen. *Gasoline composition, method and use*. Feb. 2015. URL: http://www.freepatentsonline.com/y2015/0034036.html.

[93] Peter J Choate and John C Edwards. "Relationship Between Combustion Chamber Deposits, Fuel Composition, and Combustion Chamber Deposit Structure". In: *SAE Fuels & Lubricants Meeting & Exposition*. SAE International, 1993. DOI: 10.4271/932812. URL: http://dx.doi.org/10.4271/932812.

[94] Farshid Owrang, Jim Olsson, and Jorgen Pedersen. "Solid-State ^{1}H NMR Spin-Lattice Relaxation in Combustion Chamber Deposits from a Gasoline Direct Injection Engine". In: *SAE World Congress*. SAE International, 2004. DOI: 10.4271/2004-01-0042. URL: http://dx.doi.org/10.4271/2004-01-0042.

[95] John A Ripmeester et al. "^{1}H NMR relaxation in bituminous coal and semicoke". In: *Fuel* 63.4 (1984), pp. 522–524. DOI: http://dx.doi.org/10.1016/0016-2361(84)90290-4. URL: http://www.sciencedirect.com/science/article/pii/0016236184902904.

[96] F Separovic, H D Chau, and M I Burgar. "Solid-state NMR study of aging of Colorbond polymer coating". In: *Polymer* 42.3 (2001), pp. 925–930. DOI: http://dx.doi.org/10.1016/S0032-3861(00)00436-5. URL: http://www.sciencedirect.com/science/article/pii/S0032386100004365.

[97] Young Joo Lee et al. "High-Resolution Solid-State NMR Studies of Poly(vinyl phosphonic acid) Proton-Conducting Polymer: Molecular Structure and Proton Dynamics". In: *The Journal of Physical Chemistry B* 111.33 (2007), pp. 9711–9721. DOI: 10.1021/jp072112j. URL: http://dx.doi.org/10.1021/jp072112j.

[98] Yuen-Han Lam et al. "A Solid-State NMR Study of Protein Mobility in Lyophilized Protein-Sugar Powders". In: *Journal of Pharmaceutical Sciences*

91.4 (2001), pp. 943–951. DOI: 10.1002/jps.10089. URL: http://dx.doi.org/10.1002/jps.10089.

[99] Kaung-T i Yung. "Mri measurements of T_1, T_2 and D for gels undergoing volume phase transition". In: *Magnetic Resonance Imaging* 21.2 (2003), pp. 135–144. DOI: http://dx.doi.org/10.1016/S0730-725X(02)00639-2. URL: http://www.sciencedirect.com/science/article/pii/S0730725X02006392.

[100] Mingming Guo. "Comments on the Structural Heterogeneity and Molecular Motion in Poly(vinyl chloride) (PVC) and Poly(ether-ester) Characterized by Solid State NMR". In: *Macromolecules* 30.4 (1997), pp. 1234–1235. DOI: 10.1021/ma961280z. URL: http://dx.doi.org/10.1021/ma961280z.

[101] Jovyn K.T. Ng et al. "Solid-state ^{13}C NMR study of the mobility of polysaccharides in the cell walls of two apple cultivars of different firmness". In: *Carbohydrate Research* 386 (2014), pp. 1–6. ISSN: 00086215. DOI: 10.1016/j.carres.2013.12.019.

[102] Tadao Ishii and Toshinori Abe. "Non-BPP ion dynamics—NMR-T1". In: *Solid State Ionics* 154–155 (2002), pp. 203–208. DOI: http://dx.doi.org/10.1016/S0167-2738(02)00430-7. URL: http://www.sciencedirect.com/science/article/pii/S0167273802004307.

[103] Philippe China and Jean-Pierre Rivere. "Development of a Direct Injection Spark Ignition Engine Test for Injector Fouling". In: *JSAE/SAE International Spring Fuels & Lubricants Meeting*. SAE International, 2003. DOI: 10.4271/2003-01-2006. URL: http://dx.doi.org/10.4271/2003-01-2006.

[104] Jacqueline Reid and Jim Barker. "Understanding Polyisobutylene Succinimides (PIBSI) and Internal Diesel Injector Deposits". In: *SAE/KSAE 2013 International Powertrains, Fuels & Lubricants Meeting*. SAE International, 2013. ISBN: 0148-7191. DOI: 10.4271/2013-01-2682.

[105] Ying Yang et al. "Temperature effects on the rheological properties of carbon nanotube-in-oil dispersions". In: *Colloids and Surfaces A: Physicochemical and Engineering Aspects* 298.3 (2007), pp. 216–224. DOI: 10.1016/j.colsurfa.2006.10.065.

[106] You-Yeon Won et al. "Effect of Temperature on Carbon-Black Agglomeration in Hydrocarbon Liquid with Adsorbed Dispersant". In: *Langmuir* 21.3 (2005), pp. 924–932. DOI: 10.1021/la047906t.

[107] S Yasin et al. "Interaction Forces Between Graphitic Carbon Black Surfaces Coated with Polymers Using Atomic Force Microscopy". In: *Journal of Dispersion Science and Technology* 35.8 (2014), pp. 1163–1168. DOI: 10.1080/01932691.2012.695964.

[108] S Yasin et al. "Adsorption and Rheology of Graphitic Carbon Black Nonaqueous Dispersions Prepared Using Nonionic Surfactants". In: *Journal of Dispersion Science and Technology* 34.5 (2013), pp. 737–746. DOI: 10.1080/01932691.2012.683978. URL: http://dx.doi.org/10.1080/01932691.2012.683978.

[109] Peter A Asseff. "Multifunctional Gasoline Additives Reduce Engine Deposits". In: *SAE West Coast Meeting*. SAE International, 1966. DOI: 10.4271/660543. URL: http://dx.doi.org/10.4271/660543.

[110] Kornelia Lau et al. "Analysis of Internal Common Rail Injector Deposits via Thermodesorption Photon Ionization Time of Flight Mass Spectrometry". In: *Energy & Fuels* 29.9 (2015), pp. 5625–5632. DOI: 10.1021/acs.energyfuels.5b01114. URL: http://dx.doi.org/10.1021/acs.energyfuels.5b01114.

[111] Global CCS Institute and Electric Power Research Institute (EPRI). *CO^2 Capture Technologies: Technology Options for CO^2 Capture*. Tech. rep. 2012. URL: http://hub.globalccsinstitute.com/sites/default/files/publications/29701/co2-capture-technologies.pdf.

[112] José D. Figueroa et al. "Advances in CO^2 capture technology—The U.S. Department of Energy's Carbon Sequestration Program". In: *International Journal of Greenhouse Gas Control* 2.1 (Jan. 2008), pp. 9–20. ISSN: 1750-5836. DOI: 10.1016/S1750-5836(07)00094-1. URL: https://www.sciencedirect.com/science/article/pii/S1750583607000941#fig1.

[113] Anders Lyngfelt, Bo Leckner, and Tobias Mattisson. "A fluidized-bed combustion process with inherent CO^2 separation; application of chemical-looping combustion". In: *Chemical Engineering Science* 56.10 (May 2001), pp. 3101–3113. ISSN: 00092509. DOI: 10.1016/S0009-2509(01)00007-0. URL: https://linkinghub.elsevier.com/retrieve/pii/S0009250901000070.

[114] Matthias A. Schnellmann et al. "Quantifying the role and value of chemical looping combustion in future electricity systems via a retrosynthetic approach". In: *International Journal of Greenhouse Gas Control* 73 (June 2018), pp. 1–15. ISSN: 1750-5836. DOI: 10.1016/J.IJGGC.2018.03.016. URL: https://www.sciencedirect.com/science/article/pii/S175058361730693X.

[115] Liang-Shih Fan. *Chemical looping partial oxidation : gasification, reforming, and chemical syntheses*, p. 444. ISBN: 1107194393. URL: https://books.google.co.uk/books?id=Lu9UDwAAQBAJ&q=intro#v=onepage&q=metal&f=false.

[116] Liang Zeng et al. *Coal Direct Chemical Looping Retrofit to Pulverized Coal Power Plants for In-Situ CO^2 Capture*. Tech. rep. Pittsburgh, PA, and Morgantown, WV (United States): National Energy Technology Laboratory, Sept. 2013. DOI: 10.2172/1149155. URL: http://www.osti.gov/servlets/purl/1149155/.

[117] Anders Lyngfelt and Bo Leckner. "A 1000 MWth boiler for chemical-looping combustion of solid fuels – Discussion of design and costs". In: *Applied Energy* 157 (Nov. 2015), pp. 475–487. ISSN: 0306-2619. DOI: 10.1016/J.APENERGY.2015.04.057. URL: https://www.sciencedirect.com/science/article/pii/S030626191500519X?via\%3Dihub.

[118] Daniel Jansen et al. "Pre-combustion CO^2 capture". In: *International Journal of Greenhouse Gas Control* 40 (2015), pp. 167–187. DOI: 10.1016/j.ijggc.2015.05.028. URL: http://dx.doi.org/10.1016/j.ijggc.2015.05.028.

[119] Min Wei et al. "Study on the integration of fluid catalytic cracking unit in refinery with solvent-based carbon capture through process simulation". In: *Fuel* 219 (May 2018), pp. 364–374. ISSN: 0016-2361. DOI: 10.1016/J.FUEL.2018.01.066. URL: https://www.sciencedirect.com/science/article/pii/S0016236118300759#f0010.

[120] Global CCS Institute and Electric Power Research Institute (EPRI). *CO^2 Capture Technologies: Post Combustion Capture (PCC)*. Tech. rep. January. 2012, pp. 1–16. URL: http://hub.globalccsinstitute.com/sites/default/files/publications/29721/co2-capture-technologies-pcc.pdf\%0Ahttp://cdn.globalccsinstitute.com/sites/default/files/publications/29721/co2-capture-technologies-pcc.pdf.

[121] Elif Erdal Ünveren et al. "Solid amine sorbents for CO^2 capture by chemical adsorption: A review". In: *Petroleum* 3.1 (Mar. 2017), pp. 37–50. ISSN: 24056561. DOI: 10.1016/j.petlm.2016.11.001. URL: https://linkinghub.elsevier.com/retrieve/pii/S2405656116301249.

[122] Justin C. Glier and Edward S. Rubin. "Assessment of solid sorbents as a competitive post-combustion CO^2 capture technology". In: *Energy Procedia* 37 (Jan. 2013), pp. 65–72. ISSN: 1876-6102. DOI: 10.1016/J.EGYPRO.2013.05.086. URL: https://www.sciencedirect.com/science/article/pii/S1876610213000969.

[123] Cheng-Hsiu Yu, Chih-Hung Huang, and Chung-Sung Tan. "A Review of CO^2 Capture by Absorption and Adsorption". In: *Aerosol and Air Quality Research* 12 (2012), pp. 745–769. DOI: 10.4209/aaqr.2012.05.0132.

[124] Masoud Jahandar Lashaki, Soheil Khiavi, and Abdelhamid Sayari. "Stability of amine-functionalized CO^2 adsorbents: a multifaceted puzzle". In:

Chemical Society Reviews 48.12 (June 2019), pp. 3320–3405. DOI: 10.1039/C8CS00877A. URL: http://xlink.rsc.org/?DOI=C8CS00877A.

[125] Lan Li et al., eds. *Materials and processes for CO^2 capture, conversion, and sequestration*. The American Ceramic Society, John Wiley and Sons, 2018, p. 384. ISBN: 9781119231066.

[126] Mai Bui et al. "Carbon capture and storage (CCS): the way forward". In: *Energy & Environmental Science* 11.5 (May 2018), pp. 1062–1176. ISSN: 1754-5692. DOI: 10.1039/C7EE02342A. URL: http://xlink.rsc.org/?DOI=C7EE02342A.

[127] Lalit A Darunte et al. "CO^2 capture via adsorption in amine-functionalized sorbents". In: *Current Opinion in Chemical Engineering* 12 (May 2016), pp. 82–90. ISSN: 2211-3398. DOI: 10.1016/J.COCHE.2016.03.002. URL: https://www.sciencedirect.com/science/article/pii/S2211339816300211?via\%3Dihub.

[128] Kartik Ramasubramanian and WS Winston Ho. "Recent developments on membranes for post-combustion carbon capture". In: *Current Opinion in Chemical Engineering* 1.1 (Oct. 2011), pp. 47–54. ISSN: 2211-3398. DOI: 10.1016/J.COCHE.2011.08.002. URL: https://www.sciencedirect.com/science/article/pii/S2211339811000074.

[129] Global CCS Institute and Electric Power Research Institute (EPRI). *CO^2 Capture Technologies: Pre Combustion Capture*. Tech. rep. January. 2012. URL: www.cdn.globalccsinstitute.com/sites/default/files/publications/29756/co2-capture-technologies-pre-combustion-capture.pdf..

[130] Global CCS Institute and Electric Power Research Institute (EPRI). *CO^2 Capture Technologies: Oxy Combustion with CO^2 Capture*. Tech. rep. 2012. URL: http://cdn.globalccsinstitute.com/sites/default/files/publications/29761/\%5Cn\%5Ctco2-capture-technologies-oxy-combustion.pdfC;2012c\%5Cn.

[131] Bryce Dutcher, Maohong Fan, and Armistead G. Russell. "Amine-Based CO^2 Capture Technology Development from the Beginning of 2013—A Review". In: *ACS Applied Materials & Interfaces* 7.4 (Feb. 2015), pp. 2137–2148. DOI: 10.1021/am507465f. URL: http://pubs.acs.org/doi/10.1021/am507465f.

[132] Xinhua Shen et al. "Polyethylenimine Applications in Carbon Dioxide Capture and Separation: From Theoretical Study to Experimental Work". In: *Energy Technology* 5.6 (June 2017), pp. 822–833. ISSN: 21944288. DOI: 10.1002/ente.201600694. URL: http://doi.wiley.com/10.1002/ente.201600694.

[133] Kuijun Li, Joel D. Kress, and David S. Mebane. "The Mechanism of CO^2 Adsorption under Dry and Humid Conditions in Mesoporous Silica-Supported Amine Sorbents". In: *The Journal of Physical Chemistry C* 120.41 (Oct. 2016), pp. 23683–23691. DOI: 10.1021/acs.jpcc.6b08808. URL: http://pubs.acs.org/doi/10.1021/acs.jpcc.6b08808.

[134] Won-Jin Son, Jung-Sik Choi, and Wha-Seung Ahn. "Adsorptive removal of carbon dioxide using polyethyleneimine-loaded mesoporous silica materials". In: *Microporous and Mesoporous Materials* 113.1-3 (Aug. 2008), pp. 31–40. ISSN: 1387-1811. DOI: 10.1016/J.MICROMESO.2007.10.049. URL: https://www.sciencedirect.com/science/article/pii/S1387181107006348.

[135] Tetsuo Tsuda and Tsuyoshi Fujiwara. *Polyethyleneimine and Macrocyclic Polyamine Silica Gels Acting as Carbon Dioxide Absorbents*. Tech. rep. 1992. URL: https://pubs.rsc.org/en/content/articlepdf/1992/c3/c39920001659.

[136] Sunita Satyapal et al. "Performance and Properties of a Solid Amine Sorbent for Carbon Dioxide Removal in Space Life Support Applications". In: *Energy & Fuels* 15 (2001), pp. 250–155. DOI: 10.1021/ef0002391. URL: https://pubs.acs.org/sharingguidelines.

[137] Chao Chen et al. "Amine-impregnated silica monolith with a hierarchical pore structure: enhancement of CO^2 capture capacity". In: *Chemical Communi-*

cations 0.24 (June 2009), p. 3627. ISSN: 1359-7345. DOI: 10.1039/b905589d. URL: http://xlink.rsc.org/?DOI=b905589d.

[138] Wenbin Zhang et al. "Capturing CO^2 from ambient air using a polyethyleneimine-silica adsorbent in fluidized beds". In: *Chemical Engineering Science* (2014). ISSN: 00092509. DOI: 10.1016/j.ces.2014.05.018.

[139] Nadine Abu-El-Haija. "The effect of polyethyleneimine molecular weight and loading level on the capture performance of porous silica adsorbents for CFB cement plant conditions". PhD thesis. University of Nottingham, 2016.

[140] Zaid Alhulaybi. "The Effect of Increasing Molecular Weight Polyethyleneimine on Carbon Dioxide Adsorption/Desorption Kinetics and Polymer Stability". PhD thesis. University of Nottingham, 2016.

[141] Hang Zhang et al. "CO^2 capture on easily regenerable hybrid adsorbents based on polyamines and mesocellular silica foam. Effect of pore volume of the support and polyamine molecular weight". In: *RSC Adv.* 4.37 (Apr. 2014), pp. 19403–19417. DOI: 10.1039/C4RA02145B. URL: http://xlink.rsc.org/?DOI=C4RA02145B.

[142] Chao Chen et al. "Carbon dioxide capture using amine-impregnated HMS having textural mesoporosity". In: *Chemical Engineering Journal* 161.1-2 (July 2010), pp. 46–52. ISSN: 1385-8947. DOI: 10.1016/J.CEJ.2010.04.019. URL: https://www.sciencedirect.com/science/article/pii/S1385894710003451?via\%3Dihub.

[143] Dirgarini J.N. Subagyono et al. "Amine modified mesocellular siliceous foam (MCF) as a sorbent for CO^{2}". In: *Chemical Engineering Research and Design* 89.9 (Sept. 2011), pp. 1647–1657. ISSN: 0263-8762. DOI: 10.1016/J.CHERD.2011.02.019. URL: https://www.sciencedirect.com/science/article/pii/S0263876211000876?via\%3Dihub.

[144] R. Sanz et al. "CO^2 adsorption on branched polyethyleneimine-impregnated mesoporous silica SBA-15". In: *Applied Surface Science* (2010). ISSN: 01694332. DOI: 10.1016/j.apsusc.2009.12.070.

[145] Kyungmin Min et al. "Oxidation-stable amine-containing adsorbents for carbon dioxide capture". In: *Nature Communications* 9.1 (Dec. 2018), p. 726. ISSN: 2041-1723. DOI: 10.1038/s41467-018-03123-0. URL: http://www.nature.com/articles/s41467-018-03123-0.

[146] Gary T Rochelle. "Thermal degradation of amines for CO^2 capture". In: *Current Opinion in Chemical Engineering* 1.2 (May 2012), pp. 183–190. ISSN: 2211-3398. DOI: 10.1016/J.COCHE.2012.02.004. URL: https://www.sciencedirect.com/science/article/pii/S2211339812000081.

[147] S.B. Fredriksen and Klaus-J. Jens. "Oxidative Degradation of Aqueous Amine Solutions of MEA, AMP, MDEA, Pz: A Review". In: *Energy Procedia* 37 (Jan. 2013), pp. 1770–1777. ISSN: 1876-6102. DOI: 10.1016/J.EGYPRO.2013.06.053. URL: https://www.sciencedirect.com/science/article/pii/S1876610213002968.

[148] Wai Leung. *Resistance and Rejuvenation of Polyethylenimine Degradation in Post Combustion Capture Processes*. 2018.

[149] Bruno Delfort, Pierre-Louis Carrette, and Leslie Bonnard. "MEA 40% with improved oxidative stability for CO^2 capture in post-combustion". In: *Energy Procedia* 4 (2011), pp. 9–14. ISSN: 18766102. DOI: 10.1016/j.egypro.2011.01.016. URL: https://linkinghub.elsevier.com/retrieve/pii/S1876610211000178.

[150] C H Blachly and H Ravneit. *The Stabilization of Monoethanolamine Solutions for Submarine Carbon Dioxide Serubb,rs HARD COPY MICROFICHE*. Tech. rep. Washington, D.C.: U.S. Naval Research Laboratory, 1964. URL: https://pdfs.semanticscholar.org/0007/4c64e063ba0f185083db3fcb1bd2b98a6f4c.pdf.

[151] B H Susanto et al. "The effect of pyrogallol antioxidant addition and storage temperature to the change of biodiesel quality during storage period". In: *IOP Conference Series: Earth and Environmental Science* 105.1 (Jan. 2018), p. 012021. ISSN: 1755-1307. DOI: 10.1088/1755-1315/105/1/012021. URL:

http://stacks.iop.org/1755-1315/105/i=1/a=012021?key=crossref.bbdb28c2fb74b47d77370fbd599ca84c.

[152] M T Baltazar et al. "Antioxidant properties and associated mechanisms of salicylates." In: *Current medicinal chemistry* 18.21 (2011), pp. 3252–64. ISSN: 1875-533X. URL: http://www.ncbi.nlm.nih.gov/pubmed/21671857.

[153] Michael. Ash and Irene. Ash. *Handbook of preservatives*. Synapse Information Resources, 2009, p. 1565. ISBN: 1890595667. URL: https://books.google.co.uk/books?id=XZ2QB7bu5LwC&printsec=frontcover&redir_esc=y#v=onepage&q&f=false.

[154] Aliakbar Heydari-Gorji, Yong Yang, and Abdelhamid Sayari. "Effect of the Pore Length on CO^2 Adsorption over Amine-Modified Mesoporous Silicas". In: *Energy & Fuels* 25 (2011), pp. 4206–4210. DOI: 10.1021/ef200765f. URL: https://pubs.acs.org/sharingguidelines.

[155] Tao Zhu et al. "Adsorption of carbon dioxide using polyethyleneimine modified silica gel". In: *Korean J. Chem. Eng* 27.6 (2010), pp. 1910–1915. DOI: 10.1007/s11814-010-0284-6. URL: https://link.springer.com/content/pdf/10.1007\%2Fs11814-010-0284-6.pdf.

[156] A. D. Ebner et al. "Suitability of a Solid Amine Sorbent for CO^2 Capture by Pressure Swing Adsorption". In: *Industrial & Engineering Chemistry Research* 50.9 (May 2011), pp. 5634–5641. DOI: 10.1021/ie2000709. URL: http://pubs.acs.org/doi/abs/10.1021/ie2000709.

[157] T.C. Drage et al. "Developing strategies for the regeneration of polyethylenimine based CO^2 adsorbents". In: *Energy Procedia* 1.1 (Feb. 2009), pp. 875–880. ISSN: 18766102. DOI: 10.1016/j.egypro.2009.01.116. URL: http://linkinghub.elsevier.com/retrieve/pii/S1876610209001179.

[158] Jeremy Moore. *Solid-State NMR Studies of Carbon Capture and Carbon Mineralization Reactions*. Tech. rep. 2015. URL: https://openscholarship.wustl.edu/art_sci_etds/555.

[159] Enrico Andreoli et al. "Cross-Linking Amine-Rich Compounds into High Performing Selective CO^2 Absorbents". In: *Scientific Reports* 4.1 (May 2015), p. 7304. ISSN: 2045-2322. DOI: 10.1038/srep07304. URL: http://www.nature.com/articles/srep07304.

[160] Eoghan P Dillon, Christopher A Crouse, and Andrew R Barron. "Synthesis, Characterization, and Carbon Dioxide Adsorption of Covalently Attached Polyethyleneimine-Functionalized Single-Wall Carbon Nanotubes". In: *ACS Nano* 2 (2008), pp. 156–164. DOI: 10.1021/nn7002713. URL: www.acsnano.org.

[161] Thomas O. Nelson et al. "Solid Sorbent CO^2 Capture Technology Evaluation and Demonstration at Norcem's Cement Plant in Brevik, Norway". In: *Energy Procedia* 63 (Jan. 2014), pp. 6504–6516. ISSN: 1876-6102. DOI: 10.1016/J.EGYPRO.2014.11.686. URL: https://www.sciencedirect.com/science/article/pii/S1876610214025016.

[162] Thomas Nelson. "Results and Future Perspective of RTI's Advanced Solid Sorbent Project". In: *International CCS Conference*. Langesund, Norway, 2015. URL: https://www.norcem.no/en/CCS-conference.

[163] Aker Solutions. *CO^2 Capture Technology Picked by Norcem for Use in Cement Production*. 2015. URL: https://akersolutions.com/news/news-archive/2015/aker-solutions-co2-capture-technology-picked-by-norcem-for-commercial-scale-use-in-cement-production/.

[164] Norcem (HeidelburgCement Group). *Carbon capture – a part of our zero vision*. URL: https://www.norcem.no/en/carbon_capture.

[165] Jacob Knudsen. "Results and Future Perspective of Aker Solutions' Amine project: Norcem CO^2 Capture Project [Powerpoint Presentation]". In: *International CCS Conference*. Langesund, Norway, 2015. URL: https://www.norcem.no/en/CCS-conference.

[166] Jae-Young Kim et al. "Continuous testing of silica-PEI adsorbents in a lab.-scale twin bubbling fluidized-bed system". In: *International Journal of Green-*

house Gas Control 82 (Mar. 2019), pp. 184–191. ISSN: 1750-5836. DOI: 10.1016/J.IJGGC.2019.01.007. URL: https://www.sciencedirect.com/science/article/pii/S175058361830728X.

[167] David C. Apperley. *Solid-state NMR : basic principles & practice*. eng. Momentum Press, LLC, 2012. ISBN: 9781606503522.

[168] Vladimír Mlynárik. "Introduction to nuclear magnetic resonance". In: *Analytical Biochemistry* 529 (July 2017), pp. 4–9. ISSN: 0003-2697. DOI: 10.1016/J.AB.2016.05.006. URL: https://www.sciencedirect.com/science/article/pii/S0003269716300719.

[169] *Classical Description of NMR Spectroscopy - Chemistry LibreTexts*. URL: https://chem.libretexts.org/Bookshelves/Analytical_Chemistry/Supplemental_Modules_(Analytical_Chemistry)/Analytical_Sciences_Digital_Library/Active_Learning/In_Class_Activities/Nuclear_Magnetic_Resonance_Spectroscopy/03_Text/06_Classical_Description_of_NM.

[170] Melinda J. Duer. "The Basics of Solid-State NMR". In: *Solid-State NMR Spectroscopy Principles and Applications*. Oxford, UK: Blackwell Science Ltd, Dec. 2007, pp. 1–72. ISBN: 9780470999394. DOI: 10.1002/9780470999394.ch1. URL: http://doi.wiley.com/10.1002/9780470999394.ch1.

[171] Ibrahim Karaman, Rui Climaco Pinto, and Gonçalo Graça. "Metabolomics Data Preprocessing: From Raw Data to Features for Statistical Analysis". In: *Comprehensive Analytical Chemistry*. Vol. 82. Elsevier, Jan. 2018, pp. 197–225. ISBN: 9780444640444. DOI: 10.1016/BS.COAC.2018.08.003. URL: https://www.sciencedirect.com/science/article/pii/S0166526X18300746.

[172] Lynn F. Gladden. "Magnetic resonance: Ongoing and future role in chemical engineering research". In: *AIChE Journal* 49.1 (Jan. 2003), pp. 2–9. ISSN: 00011541. DOI: 10.1002/aic.690490102. URL: http://doi.wiley.com/10.1002/aic.690490102.

[173] Harald Gunther. *NMR spectroscopy : basic principles, concepts and applications in chemistry*. eng. Third completely ... Wiley-VCH, 2013. ISBN: 9783527674756.

[174] A. J. Deese et al. "Proton NMR T_1, T_2, and $T_{1\rho}$ relaxation studies of native and reconstituted sarcoplasmic reticulum and phospholipid vesicles". In: *Biophysical Journal* 37.1 (1982), pp. 207–216. ISSN: 00063495. DOI: 10.1016/S0006-3495(82)84670-5.

[175] Alina Adams. "Analysis of solid technical polymers by compact NMR". In: *TrAC Trends in Analytical Chemistry* (2016). ISSN: 01659936. DOI: 10.1016/j.trac.2016.04.003.

[176] K.C. Khulbe, A.F. Ismail, and T. Matsuura. "Electron Paramagnetic Resonance (EPR) Spectroscopy". In: *Membrane Characterization* (Jan. 2017), pp. 47–68. DOI: 10.1016/B978-0-444-63776-5.00003-6. URL: https://www.sciencedirect.com/science/article/pii/B9780444637765000036.

[177] Patrick Schmidt-Winkel et al. "Microemulsion Templating of Siliceous Mesostructured Cellular Foams with Well-Defined Ultralarge Mesopores". In: *Chemical Materials* 12 (2000), pp. 686–696. DOI: 10.1021/cm991097v. URL: http://www.cchem.berkeley.edu/pdygrp/pub_files/pubpdf/026.pdf.

[178] Ronald Y. Dong. "NMR Spectroscopy in Liquid Crystalline and Ordered Phases". In: *Encyclopedia of Analytical Chemistry*. John Wiley & Sons, Ltd, 2006.

[179] The British Standards Institution. *Bitumen and bituminous binders - Determination of dynamic viscosity of bituminous binder using a rotating spindle apparatus*. 2018. URL: https://www.standardsuk.com.

[180] American Association of State Highway and Transportation Officials (AASHTO). *Standard Method of Test for Viscosity Determination of Asphalt Binder Using Rotational Viscometer*. 2019. URL: https://www.transportation.org/.

[181] * Peter Ertl et al. "Fast Calculation of Molecular Polar Surface Area as a Sum of Fragment-Based Contributions and Its Application to the Prediction

of Drug Transport Properties". In: *J. Med. Chem.* (2000). DOI: 10.1021/JM000942E. URL: https://pubs.acs.org/doi/10.1021/jm000942e.

[182] Wuu-Yung Lin and Frank D. Blum. "Segmental Dynamics of Bulk and Silica-Adsorbed Poly(methyl acrylate)-d_3 by Deuterium NMR: the Effect of Molecular Weight". In: *Macromolecules* 31.13 (June 1998), pp. 4135–4142. ISSN: 0024-9297. DOI: 10.1021/ma971725z. URL: https://pubs.acs.org/doi/10.1021/ma971725z.

[183] *Method for producing polyalkenyl succinimide products, novel polyalkenylsuccinimide products with improved properties, intermediate products*. 2002. URL: https://www.google.com/patents/US8263535.

[184] *Polyisobutylene - 13C NMR Spectrum - SpectraBase*. URL: https://spectrabase.com/spectrum/8voDzfHYb2E?a=SPECTRUM_8voDzfHYb2E.

[185] Marina M. van der Merwe et al. "Structural Assignment of Commercial Polyisobutylene Succinic Anhydride-based Surfactants". In: *Journal of Surfactants and Detergents* 20.1 (Jan. 2017), pp. 193–205. ISSN: 1097-3958. DOI: 10.1007/s11743-016-1893-9. URL: http://doi.wiley.com/10.1007/s11743-016-1893-9.

[186] Sandor Nemes, Jiaoshi Si, and Joseph P. Kennedy. "^{13}C NMR chemical shifts of polyisobutylene end groups and related model compounds". In: *Polymer Bulletin* 23.6 (June 1990), pp. 597–603. ISSN: 01700839. DOI: 10.1007/BF01033104.

[187] Ronald J Smernik and J.Malcolm Oades. "Effects of added paramagnetic ions on the ^{13}C CP/MAS NMR spectrum of a de-ashed soil". In: *Geoderma* 89.3-4 (May 1999), pp. 219–248. ISSN: 0016-7061. DOI: 10.1016/S0016-7061(98)00085-8. URL: https://www.sciencedirect.com/science/article/pii/S0016706198000858.

[188] Stanley M. Brown and Edwin W. Lard. "A comparison of nitrogen and mercury pore size distributions of silicas of varying pore volume". In: *Powder Technology* 9.4 (Apr. 1974), pp. 187–190. ISSN: 0032-5910. DOI: 10.

1016/0032-5910(74)80031-8. URL: https://www.sciencedirect.com/science/article/pii/0032591074800318.

[189] Matthias Thommes et al. "Physisorption of gases, with special reference to the evaluation of surface area and pore size distribution (IUPAC Technical Report)". In: *Pure and Applied Chemistry* 87.9-10 (Oct. 2015), pp. 1051–1069. ISSN: 1365-3075. DOI: 10.1515/pac-2014-1117. URL: http://www.degruyter.com/view/j/pac.2015.87.issue-9-10/pac-2014-1117/pac-2014-1117.xml.

[190] K. S. W. Sing et al. *Reporting Physisorption Data for Gas/Solid Systems with Special Reference to the Determination of Surface Area and Porosity (Reccomendations 1984)*. Tech. rep. IUPAC Physical Chemistry Division Commission on, Colloid and Surface Chemistry Including Catalysis, 1985. URL: http://publications.iupac.org/pac/pdf/1985/pdf/5704x0603.pdf.

[191] G. M. Lukovkin, V. S. Pshezhetsky, and G. A. Murtazaeva. "NMR ^{13}C study of the structure of polyethyleneimine". In: *European Polymer Journal* 9.6 (1973), pp. 559–565. ISSN: 00143057. DOI: 10.1016/0014-3057(73)90039-6.

[192] Hans J. Reich. *C-13 Chemical Shifts*. URL: https://www.chem.wisc.edu/areas/reich/nmr/c13-data/cdata.htm.

[193] Damiano Banfi and Luc Patiny. "www.nmrdb.org: Resurrecting and Processing NMR Spectra On-line". In: *CHIMIA International Journal for Chemistry* 62.4 (Apr. 2008), pp. 280–281. ISSN: 00094293. DOI: 10.2533/chimia.2008.280. URL: http://openurl.ingenta.com/content/xref?genre=article&issn=0009-4293&volume=62&issue=4&spage=280.

[194] Christoph Steinbeck, Stefan Krause, and Stefan Kuhn. "NMRShiftDB-Constructing a Free Chemical Information System with Open-Source Components". In: *Journal of Chemical Information and Computer Sciences* 43.6 (Nov. 2003), pp. 1733–1739. DOI: 10.1021/ci0341363. URL: https://pubs.acs.org/doi/10.1021/ci0341363.

[195] Andrés M. Castillo, Luc Patiny, and Julien Wist. "Fast and accurate algorithm for the simulation of NMR spectra of large spin systems". In: *Journal of Magnetic Resonance* 209.2 (Apr. 2011), pp. 123–130. ISSN: 10907807. DOI: 10.1016/j.jmr.2010.12.008. URL: https://linkinghub.elsevier.com/retrieve/pii/S1090780710004003.

[196] Bio-Rad Laboratories Inc. *2,2'-Thiodiethanol - ^{13}C NMR Spectrum - SpectraBase*. URL: https://spectrabase.com/spectrum/KHQumkwjONc?a=SPECTRUM_KHQumkwjONc.

[197] Andrew J. Pell, Guido Pintacuda, and Clare P. Grey. *Paramagnetic NMR in solution and the solid state*. Apr. 2019. DOI: 10.1016/j.pnmrs.2018.05.001.

[198] Waters. *Size exclusion chromatography (SEC) Gel Permeation Chromatography (GPC) Guide*. 2019. URL: https://www.waters.com/waters/en_GB/GPC---Gel-Permeation-Chromatography-Beginner\%27s-Guide/nav.htm?cid=10167568&locale=en_GB.

Appendix A

Deposit Control Additives

A.1 PIB Derivative Preparation

Target Loading (%)	Polymer (g)	Substrate (g)
5	0.05	0.95
7.5	0.075	0.925
10	0.10	0.90
15	0.15	0.85
20	0.20	0.80
30	0.30	0.70
40	0.40	0.60
50	0.50	0.50

Table A.1: Weights used to prepare 1 g of PIB derivative dispersions (not considering moisture content)

A.2 Example Monolayer Calculation Using the PSA Method

The calculation of PIBSI-G monolayer coverage of MicroCB by PSA provides a result of approximately 43 % polymer loading.

Atom Type	PSA Contribution (Å²)	Number of atoms per Headgroup	Total contribution (Å²)
N#R	23.8	0	-
NHR_2	12.0	3	36
NH_2R	26.0	2	52
OR_2	9.2	0	-
OHR	20.2	0	-
		Total	88.0

Table A.2: Atomic Contributions to PSA of PIBSI G

PIBSI Mass (g)	PIBSI M_n (g/mol)	PIBSI PSA (m^2)	No. PIBSI Molecules	Total PIBSI S.A. (m^2)	MicroCB Mass (g)	MicroCB S.A. (m^2)	Total MicroCB S.A. (m^2/g)
1.0			$3.13x10^{20}$	275.8	0		0
0.9			$2.82x10^{20}$	248.27	0.1		21.4
0.8			$2.51x10^{20}$	220.7	0.2		42.8
0.7			$2.19x10^{20}$	193.1	0.3		64.2
0.6			$1.88x10^{20}$	165.5	0.4		85.6
0.5	1921	$8.8x10^{-1}$	$1.57x10^{20}$	137.9	0.5	214	107
0.4			$1.25x10^{20}$	110.3	0.6		128.4
0.3			$9.40x10^{19}$	82.8	0.7		149.8
0.2			$6.27x10^{19}$	55.2	0.8		171.2
0.1			$3.13x10^{19}$	27.6	0.9		192.6
0.0			0.00	0.0	1.0		214

Table A.3: Example calculation of monolayer coverage for a 1 g sample of PIBSI G-MicroCB

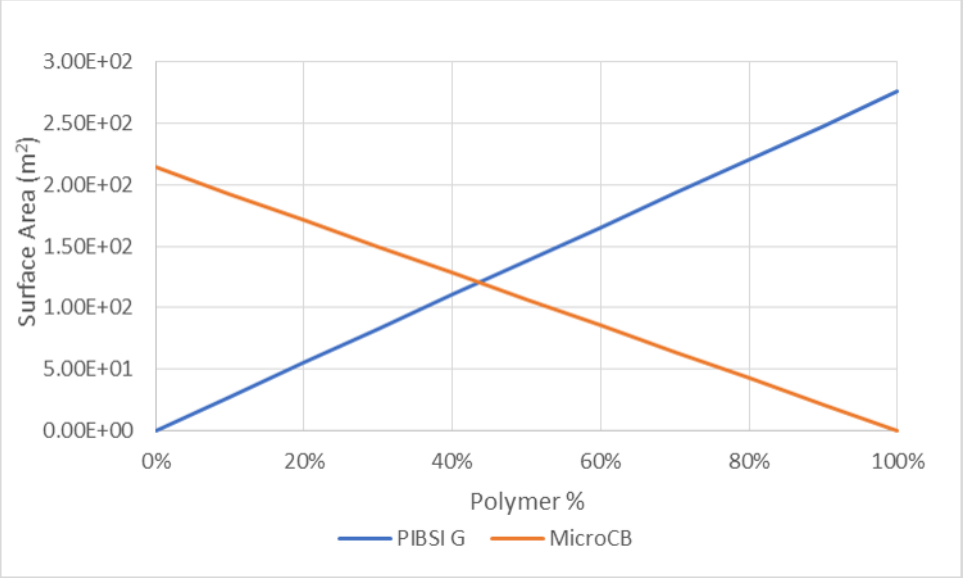


Figure A.1: Total surface area of PIBSI G and MicroCB at different polymer loadings of 1 g sample

Number of PIBSI molecules = (Mass/ Mn of PIBSI-A) x N_a

Total polymer surface area = Number of molecules x calculated polar surface area (PSA) of PIBSI head group

A.3 PIBSI structures

PIBSI Name	Headgroup	Headgroup structure
PIBSI B	tetraethylenepentamine (TEPA)	Figure A.2
PIBSI C	aminoethylethanolamine (AEEA)	Figure A.3
PIBSI G	tetraethylenepentamine (TEPA)	Figure A.2
PIBSI I	ethylenediamine (EDA)	Figure A.4
PIBSI Y	ethylenediamine (EDA)	Figure A.4
PIBSI Z	tetraethylenepentamine (TEPA)	Figure A.2

Table A.4: PIBSI Headgroup Structures

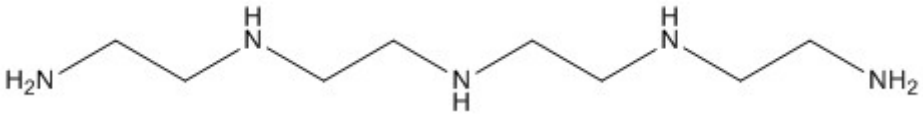


Figure A.2: Structure of tetraethylenepentamine (TEPA), head group of PIBSI B and G

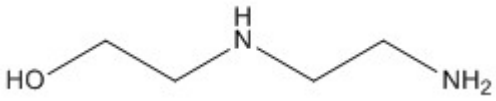


Figure A.3: Structure of aminoethylethanolamine (AEEA), head group of PIBSI C



Figure A.4: Structure of ethylenediamine (EDA), head group of PIBSI I



Figure A.5: Structure of ethanolamine

A.4 Supplementary Methods

A.4.1 Gel Permeation Chromatography Methodology

Gel permeation chromatography (GPC) is an analytical technique used to characterise polymers. It can determine molecular weight (both number average and weight average) and the distribution of the polymer by molecular weight. It is a size exclusion chromatography technique, separating molecules by size. It consists of a column packed with porous beads, with smaller molecules passing through the porous material increasing their path length and thus retention time, while larger molecules spend less time in pores and are eluted more quickly.[198]

The results referenced in this work, were carried out at Innospec Inc. by Dr. Jim Barker using a Waters Alliance 2695 system with a PIB standard as reference. The system used was equipped with a Waters refractive index Detector 2414 and four Waters Syragel® gel columns (HR 4, 2, 1, 0.5 (7.8 x 300 mm)) were used.

The eluent used was GPC grade tetrahydrofuran (THF) delivered at 1.0 mL min-1. 0.1-0.2 g of sample was made up to 25 mL with THF, the injection volume used was 100 μL and the samples were analysed at 39 °C. The samples were run against a calibration graph and the molecular weights and polydispersity calculated using Empower Pro software.

.

Appendix B

Carbon Capture Materials

B.1 Characterisation of Rice Husk Samples

The precursor material for the two rice husk silicas (RH1 and RH2) is a rice husk obtained from a small private farm in the the Hunan Province of China. Several experimental methods were performed on the Rice Husk in order to characterise the sample, these include thermogravimetric analysis, elemental analysis and X-Ray fluorescence (XRF).

Thermogravimetric Analysis of Rice Husk

Both burnoff and proximate TGA methods as described in Section 3.2.5 were performed on the Rice Husk sample. Prior to analysis the sample was ground to a powder in order to achieve a somewhat homogenous sample. The burnoff TGA analysis shows the rice husk to have a moisture content of 7.6 % and an ash content of 12.3 % on a wet basis or 13.3 % on a dry basis. This can be seen in Figure B.1. The dry basis ash content was calculated using Equation B.1.

$$Ash\%(dry) = \frac{Ash\%(wet)}{100\% - Moisture\%} \times 100\% \tag{B.1}$$

The proximate analysis shown in Figure B.2 shows a the volatile content of the rice husk of around 66 %, on a dry basis.

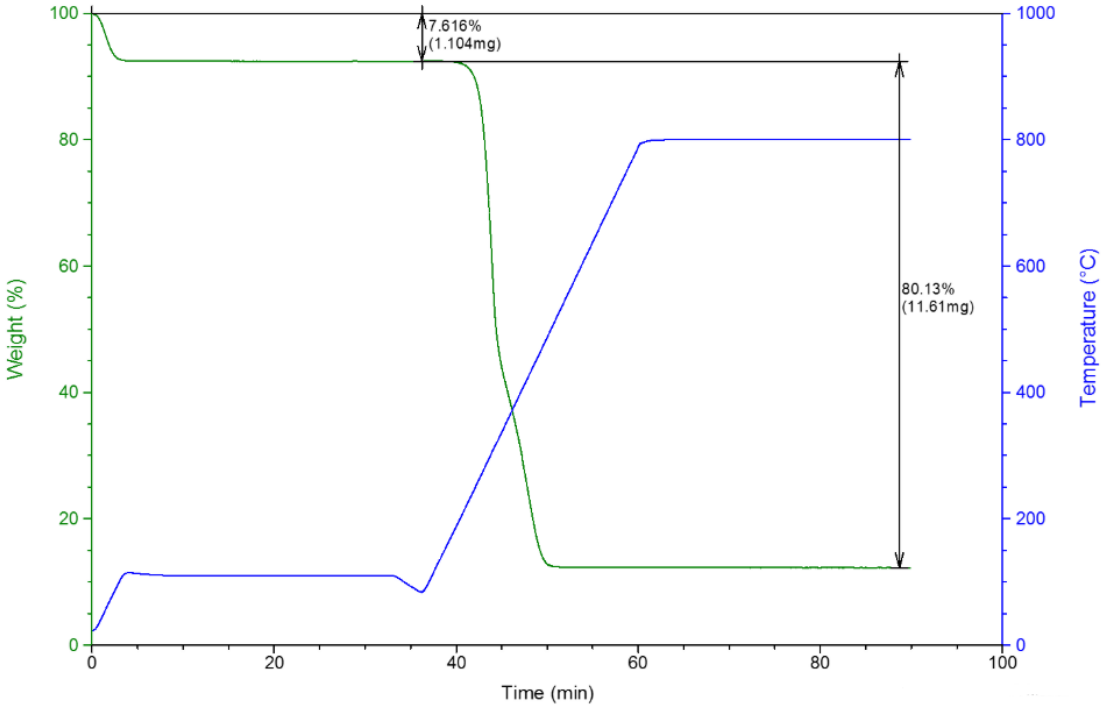


Figure B.1: Burnoff thermogravimetric analysis of Rice Husk under a nitrogen/air atmosphere

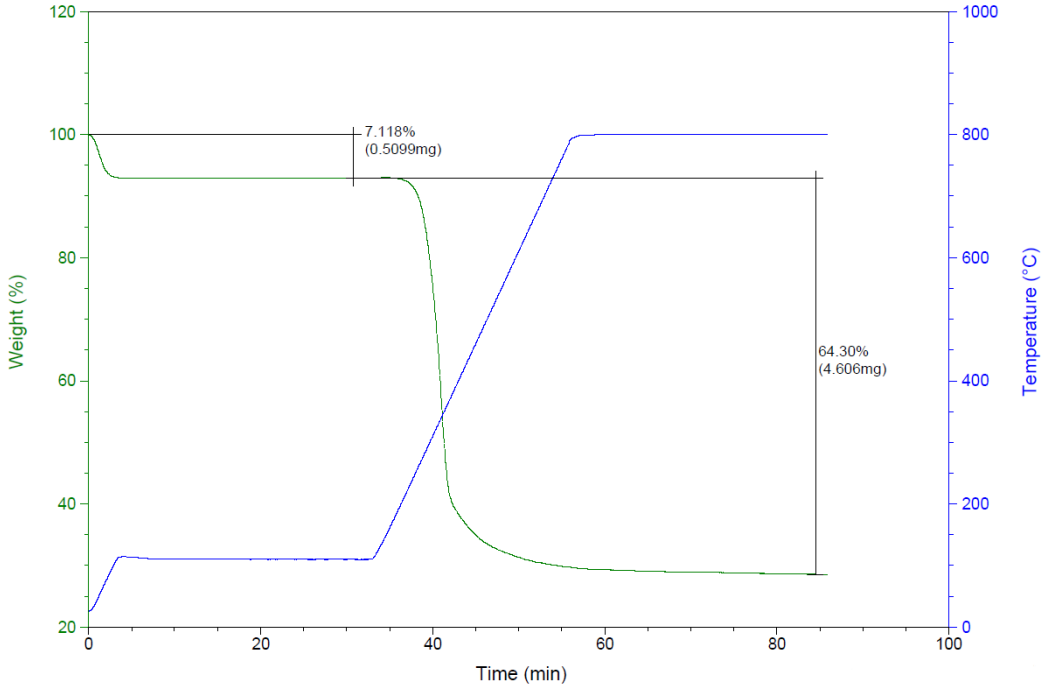


Figure B.2: Proximate thermogravimetric analysis of Rice Husk under a nitrogen atmosphere

Elemental Analysis of Rice Husk

Elemental analyses were performed in duplicate as described in Section B.11.2. The carbon. hydrogen and nitrogen content can be seen in Table B.1.

Element	Percentage (%)	Error
Carbon	40.3325	±0.2905
Hydrogen	5.87935	±0.00885
Nitrogen	0.47327	±0.01342

Table B.1: Elemental composition of rice husk

The CHN content only makes up 46.7 % of the total weight of the rice husk. The remaining 53.3 % of the sample will consist of oxygen and the ash which will be the basis for the silica. By subtracting the amount of ash found by the TGA measurements from this value of 53.3 %, the amount of oxygen, 40 %, is determined.

X-Ray Fluorescence Spectroscopy of Rice Husk

X-Ray fluorescence was performed in duplicate as described in Section B.11.1. The average content of silica, as well as other species with concentrations of greater than 0.5 % are shown in Figure B.2. The silica content determined by this method is higher than the ash content determined by the other methods. The content of the element silicon can be calculated as approximately 8.1 %. The error on these measurements is fairly high, measuring about 10 % of the average concentration, this is indicative of the non-homogeneity of the rice husk sample.

Species	SiO_2	SO_3	K_2O
Avg. Concentration (%)	17.12	0.57	1.49
Error	± 1.86	± 0.03	± 0.11

Table B.2: Average concentrations of significant species ($\geq$ 0.5 %) in Rice Husk sample, as determined by XRF

B.2 Mercury Intrusion Porosimetry of Silicas by Dr. Lee Stevens

	RH2	Silica 1
Total Pore Area (m^2/g)	357	521
Total Pore Volume (cm^3/g)	11.59	3.13
Average Pore Diameter (μm)	0.13	0.024
Vmacro (cm^3/g)	8.1	1.88
Vmeso (cm^3/g)	1.2	1.29
Bulk Density (g/cm^3)	0.077	0.269
Skeletal Density (g/cm^3)	2.275	2.158
% Porosity	97	88

Table B.3: Porosity data of Rice Husk Silica 2 and Silica 1 as determined by mercury intrusion porosimetry. This method has an intrusion accuracy of ± 1 %. Further data on error is unavailable.

B.3 Supplier Specification of SBA-15

Surface Area (m^1/g)	450-550
Pore Volume (cm^3/g)	0.8-1.0
Average Pore Diameter (nm)	7-9

Table B.4: Specification of SBA-15 as supplied by Sigma Aldrich

B.4 N_2 Sorption Isotherms for Silica Samples

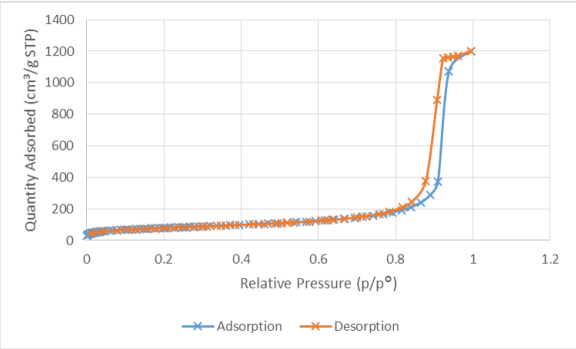


Figure B.3: N_2 sorption isotherm for Silica 1, at 200 °C

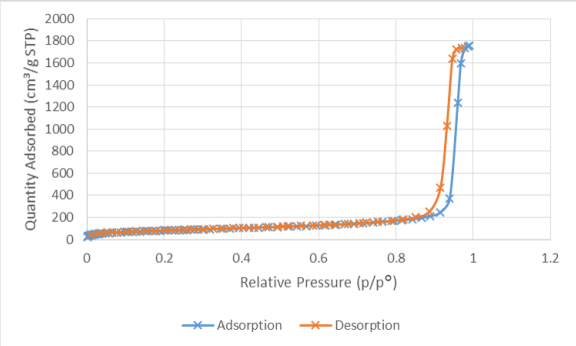


Figure B.4: N_2 sorption isotherm for 40 nm Silica, at 200 °C

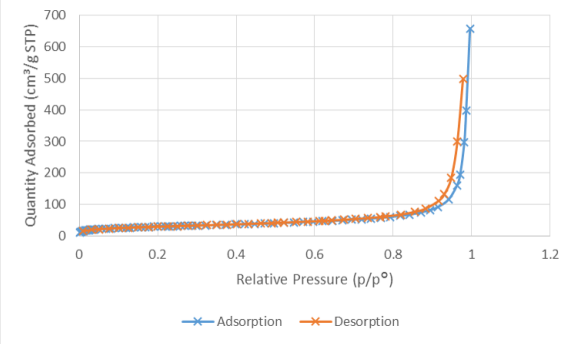


Figure B.5: N_2 sorption isotherm for Rice Husk Silica 1, at 200 °C

B.5 Physisorption Isotherms and Hysteresis Loop Classifications

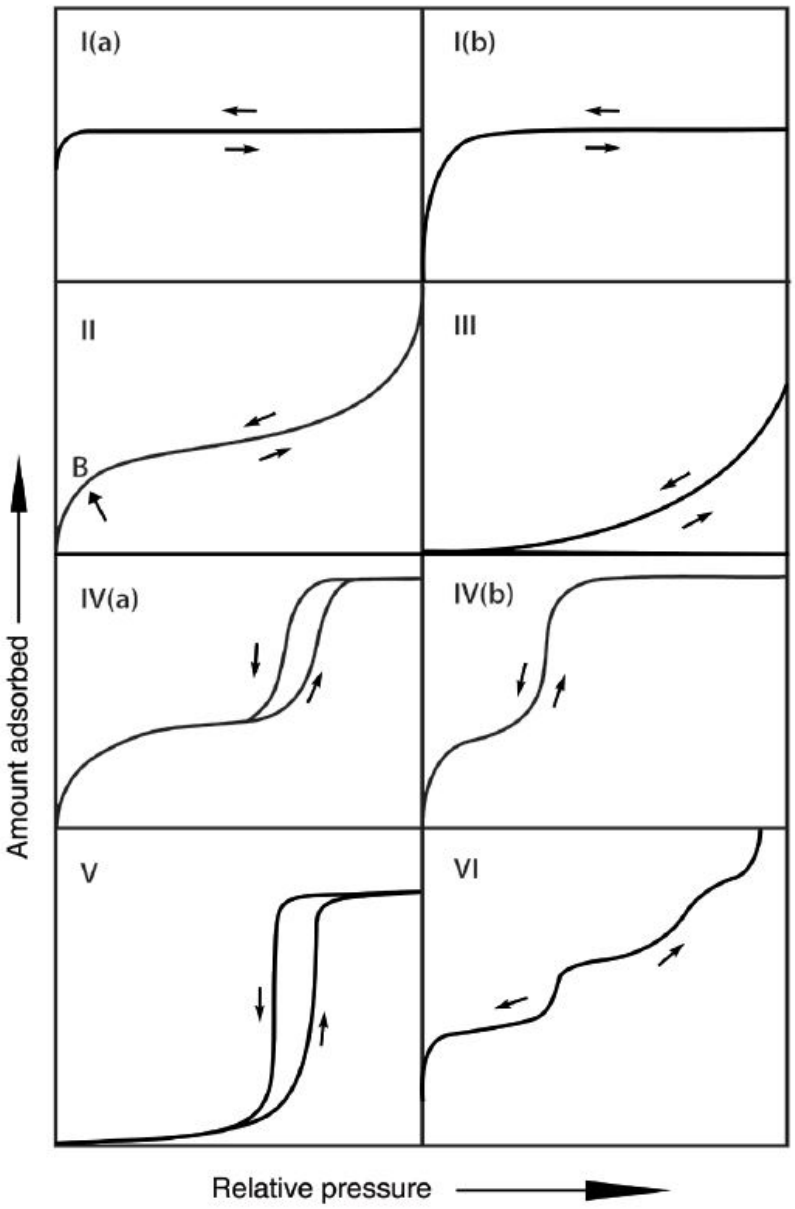


Figure B.6: Classification of physisorption isotherms[189]

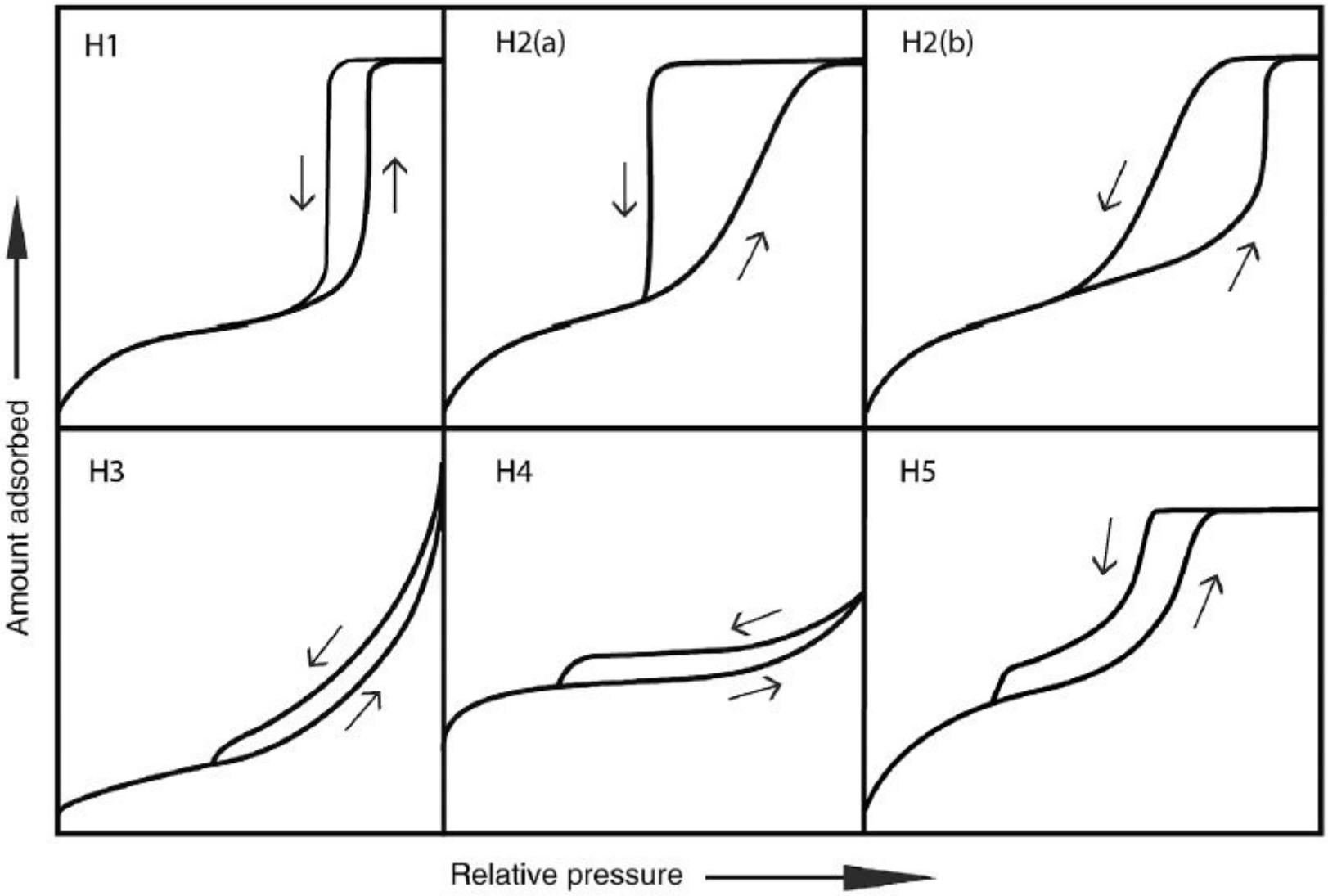


Figure B.7: Classification of hysteresis loops[189]

B.6 Viscosity of PEI Samples (From Specification)

B.7 PEI-Silica Kinetics

PEI sample	Moisture Content* (%)	Viscosity* at 20 °C (cps)	Viscosity of neat sample at 25 °C (cps)
800 PEI	99	800-5000	1300
1300 PEI	50	200-500	2600
2000 PEI	50	250-650	8800
5000 PEI	50	1100	14000
25000 PEI	56	11000	57000
750000 PEI	33	1000-2500	20000[(1)]

Table B.5: Viscosity measurements of PEI samples (*according to the product specification, [(1)]measurement taken at 30 °C)

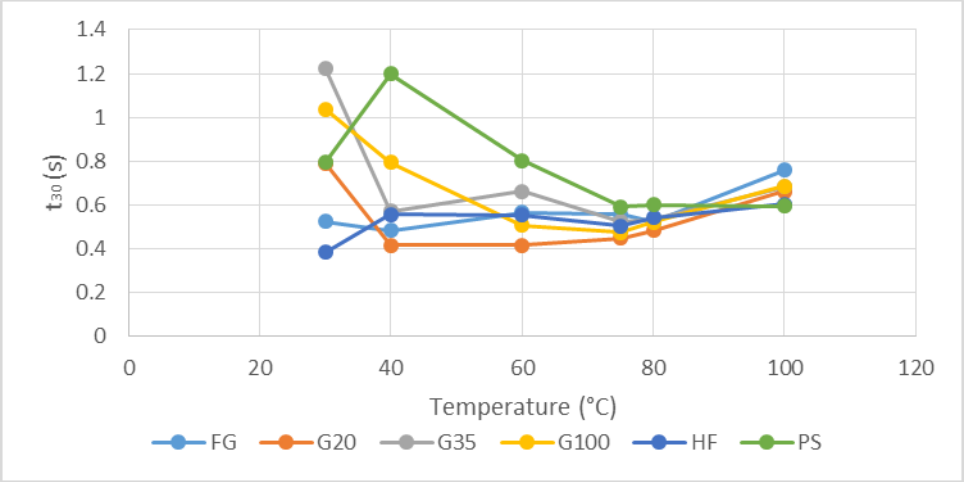


Figure B.8: T_{30} of different PEI-SBA15 dispersions over 30-100 °C

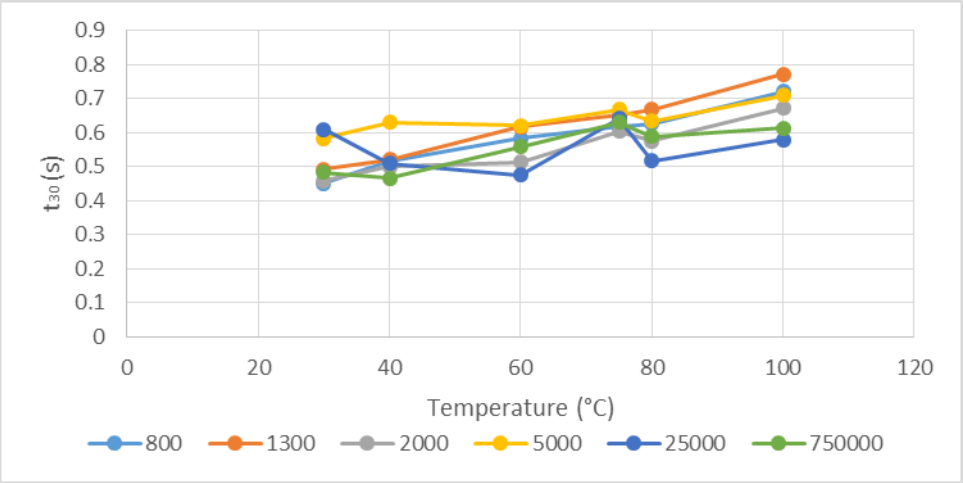


Figure B.9: T_{30} of different PEI-MCF dispersions over 30-100 °C

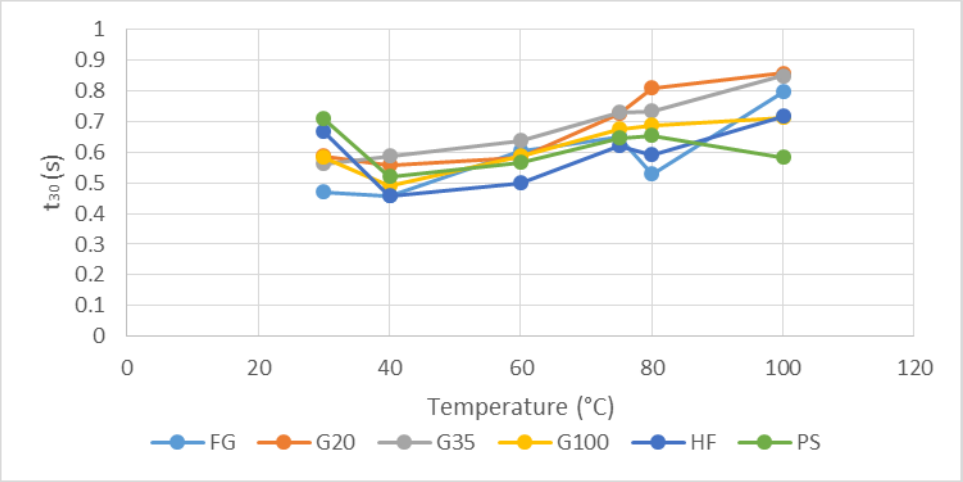


Figure B.10: T_{30} of different PEI-RH1 dispersions over 30-100 °C

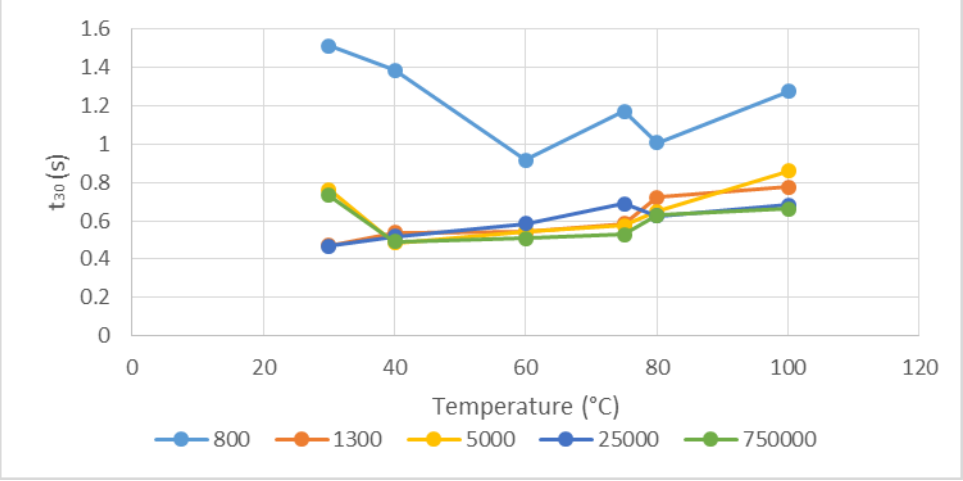


Figure B.11: T_{30} of different PEI-RH2 dispersions over 30-100 °C

PEI	Silica	Temperature of Maximum CO_2 Uptake (°C)	CO_2 Uptake (%)
800 PEI	SBA-15	80	10.4
	Silica 1	75	12.55
	MCF	30	9.60
	RH1	80	11.71
	RH2	100	9.73
1300 PEI	SBA-15	80	9.08
	Silica 1	60	11.31
	MCF	75	12.69
	RH1	75	13.17
	RH2	60	15.50
2000 PEI	SBA-15	80	8.42
	Silica 1	80	11.26
	MCF	40	8.78
	RH1	75	12.15
5000 PEI	SBA-15	80	7.48
	Silica 1	75	11.29
	MCF	80	11.06
	RH1	75	10.17
	RH2	75	15.00
25000 PEI	SBA-15	80	10.41
	Silica 1	75	10.74
	MCF	80	11.91
	RH1	80	11.38
	RH2	75	14.70
750000 PEI	SBA-15	80	8.00
	Silica 1	80	8.90
	MCF	75	9.92
	RH1	75	10.28
	RH2	75	21.85

Table B.6: The maximum CO_2 capacity of each PEI-Silica material and its associated adsorption temperature

B.8 KIER Pilot Plant Samples

Sample Date (day/month)	Sample Name
12/01	Sample 1 Day 1
14/01	Sample 1 Day 3
15/01	Sample 1 Day 4
16/01	Sample 1 Day 5
17/01	Sample 1 Day 6
18/01	Sample 1 Day 7
15/06	Sample 2 Day 1
17/06	Sample 2 Day 3
19/06	Sample 2 Day 5
20/06	Sample 2 Day 6
21/06	Sample 2 Day 7
22/06	Sample 2 Day 8
24/06	Sample 2 Day 9

Table B.7: Date of sample extraction (in 2017) and sample name

B.9 Antioxidant Loadings

Sample Name (%)	Weight Antioxidant in 1 g Sample (g)	Actual wt.% Antioxidant
0	0.000	0.000
0.25	0.00250	0.249
0.5	0.00500	0.498
0.75	0.00750	0.744
1	0.0100	0.990
2	0.0200	1.96
4	0.0400	3.85
6	0.0600	5.66
8	0.0800	7.41
10	0.100	9.09
12	0.120	10.7
14	0.140	12.3
16	0.160	13.8
18	0.180	15.3
20	0.200	16.7

Table B.8: Weight percent of antioxidant in antioxidant functionalised PEI-Silicas

B.10 Additional Oxidation Testing Results

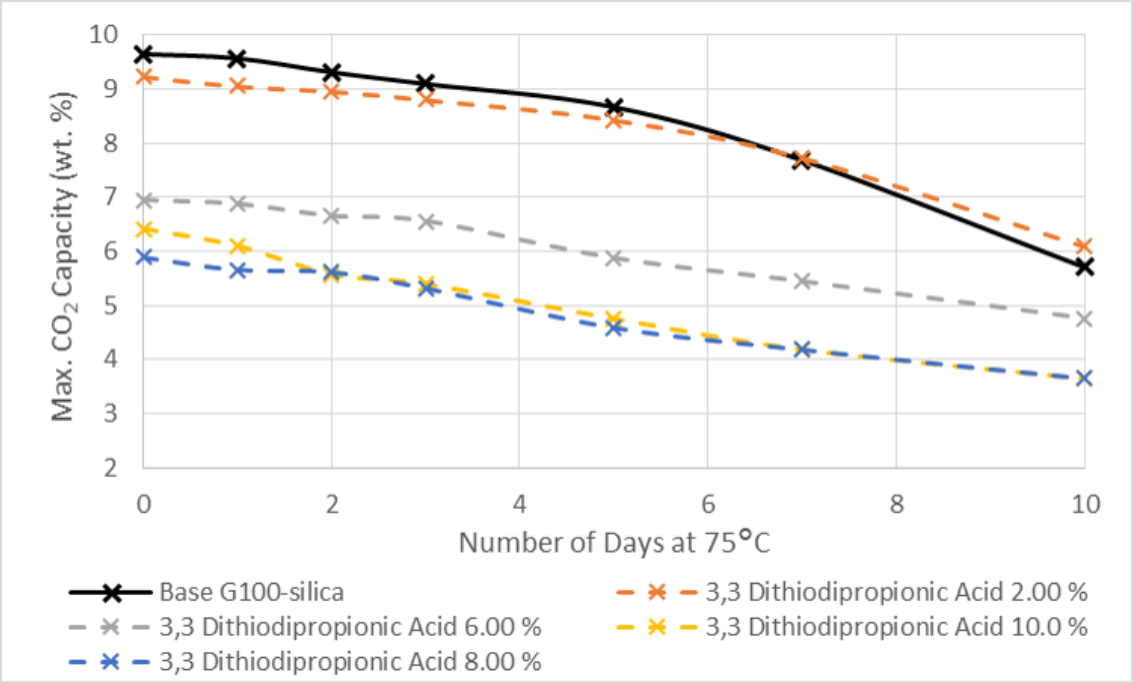


Figure B.12: TGA determined maximum CO_2 capacity of G100-Silica 1 functionalised with 0, 2, 6, 8 and 10 % 3,3' dithiodipropionic acid, over 10 days under oxidation conditions

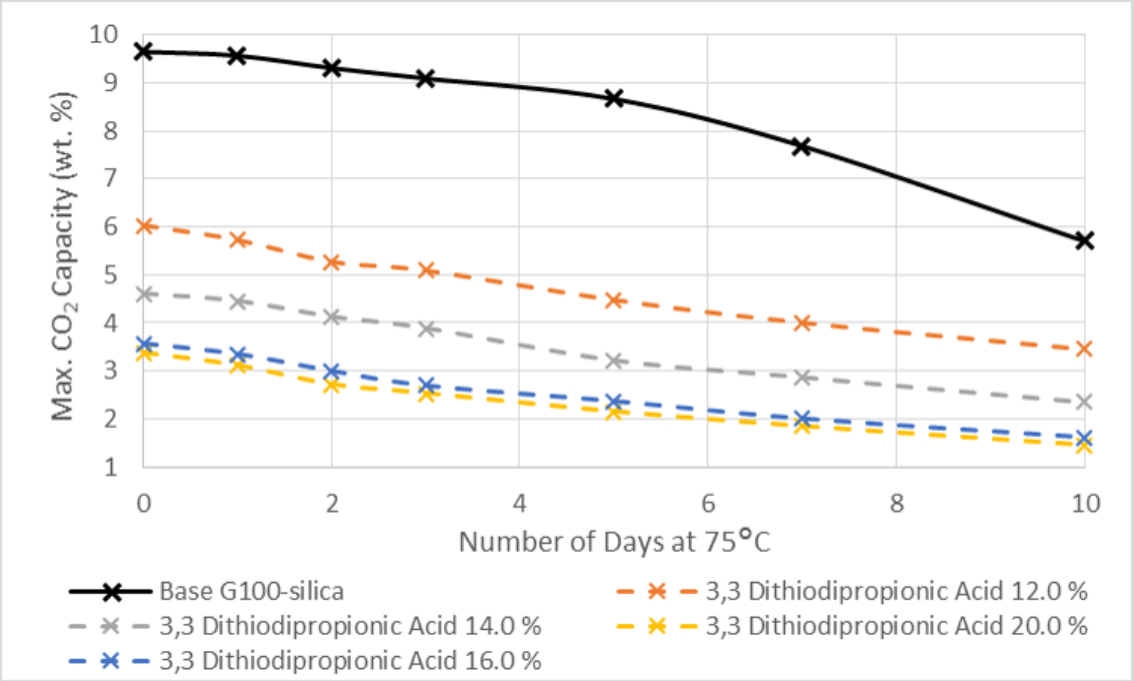


Figure B.13: TGA determined maximum CO_2 capacity of G100-Silica 1 functionalised with 0, 12, 14, 16 and 20 % 3,3' dithiodipropionic acid, over 10 days under oxidation conditions

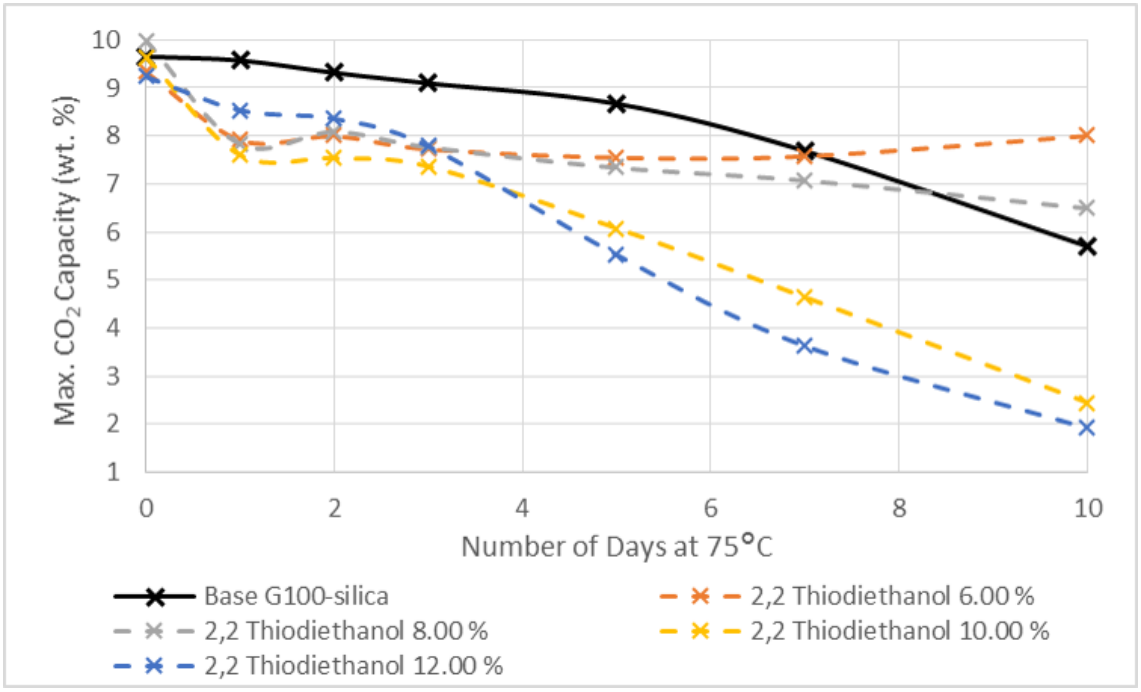


Figure B.14: TGA determined maximum CO_2 capacity of G100-Silica 1 functionalised with 0, 6, 8, 10 and 12 % 2,2' thiodiethanol, over 10 days under oxidation conditions

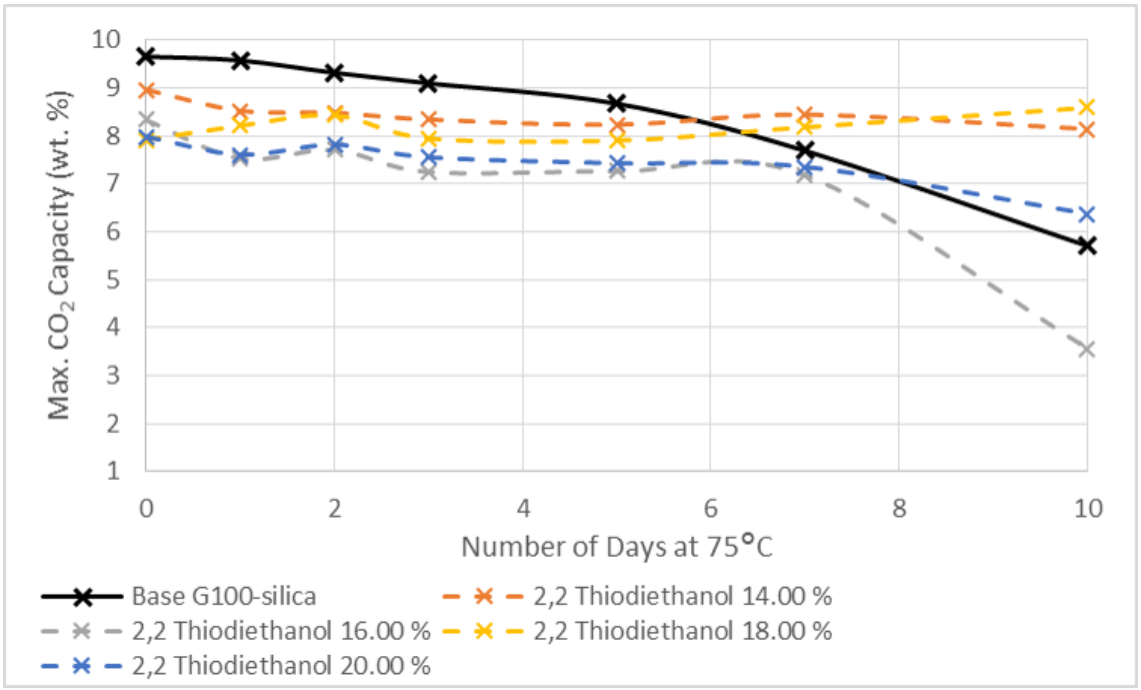


Figure B.15: TGA determined maximum CO_2 capacity of G100-Silica 1 functionalised with 0, 14, 16, 18 and 20 % 2,2' thiodiethanol, over 10 days under oxidation conditions

B.11 Supplementary Methods

B.11.1 X-Ray Fluorescence

X-ray fluorescence (XRF) is an analytical technique which can be used to determine elemental composition of samples. On excitation of a material by an X-ray source, the primary X-ray, the material will emit secondary X-Rays (fluorescent X-rays) which can be detected and measured. As each elements produces it's own distinct set of characteristic fluorescent X-rays, also known as a fingerprint, the different elements in a sample can be determined and quantified.

The secondary X-rays emitted by the sample occur due to the primary X-ray dislodging an electron from an inner orbital shell of an atom, this results in a higher energy electron dropping into the lower energy space left by this electron. To do this the electron releases it's excess energy as an X-ray. The energy of this X-ray will correspond with the energy difference between these two quantum states, and is specific to the atom of interest. When measured, the intensity of the peak at this energy indicates the concentration of that atom in the sample.

This method was used to characterise the rice husk sample. These measurements were performed on a Panalytical Epsilon 3 XL high performance benchtop energy dispersive X-ray fluorescence spectrometer system. This system can measure elements from sodium to uranium on the periodic table. The rice husk was dried under vacuum for 24 hours at 110 °C and then ground to a powder, quantities of approximately 3-4 g were used for the analysis.

This work was carried out with the assistance of Teresa Needham, University of Nottingham.

B.11.2 Elemental Analysis

Elemental analysis, also known as CHN or CHNX (where X is a hetero-atom such as sulphur) analysis, is a quantitative technique used to determine the elemental composition of various materials. There are various forms of elemental analysis but in this study, combustion analysis was used to determine the carbon, hydrogen

and nitrogen composition of a material. This technique combusts the sample in oxygen and collects the combustion products of carbon dioxide, water, and nitric oxide in traps. The masses of each of the products are measured and the percentage composition of the original material calculated.

These measurements were carried out on a LECO 628 CHN elemental analyser, with combustion at 950 °C. The analyser was calibrated by performing the analysis numerous times without a sample loaded, until the values generated by the analyser approached zero. The rice husk sample was ground lightly and 75 mg of sample weighed into aluminium foil cups which were folded and sealed before loading into the analysers auto-sampler. The analysis was performed and the resulting elemental composition recorded.

This work was carried out with the assistance of Prof. Will Meredith.

B.11.3 University of Nottingham Strata Technology CO_2 Capture Pilot Plant

Although this reactor was not used in this study as it was commissioned in the summer 2019, it is commented on briefly for costings and future work, therefore a brief description of this facility is as follows.

The unit consists of two reactors, a circulating fluidised bed (20 kg adsorbent) and a bubbling fluidised bed system (5 kg adsorbent). The adsorbers in these systems can be supplied with simulated flue gases or filtered and cooled flue gases from a biomass boiler system. The regeneration gas of the bubbling fluidised bed is a mixture of water saturated CO_2 and N_2 and for the circulating fluidised bed either the simulated gas stream or recycled gas from the desorber outlet that has been saturated with water is used. The transfer gas used is water saturated N_2.

The temperature of the gases are maintained by band heaters and the temperature of columns is controlled using cooling jackets. The solid/gas mixtures are separated with cyclones. The samples are fed into and removed from the vessels manually.